UNIVERSITÉ DE STRASBOURG

ÉCOLE DOCTORALE DE PHYSIQUE ET CHIMIE-PHYSIQUE

Institut de Physique et de Chimie des Matériaux de Strasbourg

THÈSE présentée par :

Dominik METTEN

soutenue le : **29 janvier 2016**

pour obtenir le grade de : **Docteur de l'Université de Strasbourg**

Discipline / Spécialité : Physique / Nanophysique

Probing the opto-electronic and mechanical properties of suspended graphene membranes by Raman spectroscopy

THÈSE dirigée par:

M. Stéphane BERCIAUD	Maître de conférences, Université de Strasbourg

RAPPORTEURS :

M. Christoph STAMPFER	Professeur, RWTH Aachen
M. Christophe VOISIN	Professeur, Université Paris Didérot (Paris 7)

EXAMINATEURS :

M. Florian BANHART	Professeur, Université de Strasbourg
Mme Nedjma BENDIAB	Maître de conférences, Université Joseph Fourier (Grenoble 1)
M. Pierre VERLOT	Maître de conférences, Université Claude Bernard (Lyon 1)

Contents

Acknowledgements vii

Publications ix

Résumé en langue française xiii

1 Introduction 1

2 General theoretical background on graphene 9
- 2.1 Atomic structure . . . 9
- 2.2 Electronic properties . . . 10
  - 2.2.1 Band structure . . . 11
  - 2.2.2 Band structure in the vicinity of the Dirac point . . . 13
  - 2.2.3 Tuning of the electronic properties by field effect . . . 16
  - 2.2.4 Substrate influences and the interest of suspended graphene . . . 17
- 2.3 Optical properties . . . 19
- 2.4 Phonons in graphene layers . . . 22
  - 2.4.1 Atomic displacement . . . 22
  - 2.4.2 Phonon dispersion . . . 24
- 2.5 Suspended graphene as a two dimensional membrane . . . 26
- 2.6 Conclusion . . . 34

3 Raman scattering spectroscopy of graphene 37
- 3.1 The Raman process . . . 38
- 3.2 Raman modes of graphene and few layer graphene . . . 40
  - 3.2.1 G mode . . . 43
  - 3.2.2 2D mode . . . 44
- 3.3 Sensitivity to external perturbations . . . 51
  - 3.3.1 Influence of doping . . . 51

3.3.2 Influence of strain . . . 54
3.4 Correlation of the Raman frequencies . . . 56
3.5 Optical interference effects in graphene multilayered systems . . . 62
3.5.1 One layer interferences: Fabry-Pérot . . . 64
3.5.2 Multilayer interferences . . . 65
3.5.3 Interference of the Raman interaction within a graphene layer . . . 65
3.5.4 Refractive indices . . . 67
3.5.5 Theoretical prediction for suspended graphene systems . . . 68
3.6 Conclusion . . . 72

4 Device fabrication and experimental setup 73
4.1 Device fabrication and fabrication techniques . . . 73
4.1.1 Optical lithography . . . 73
4.1.2 Wet and dry etching . . . 74
4.1.3 Mechanical exfoliation and determination of number of layers . . . 74
4.1.4 Contacting: Metal deposition and bonding . . . 76
4.2 Experimental setup . . . 76
4.2.1 Confocal micro-Raman setup . . . 76
4.2.2 Measurements at room and cryogenic temperatures . . . 78
4.3 Data acquisition and treatment . . . 80
4.4 Conclusion . . . 81

5 Built-in strain in suspended graphene 83
5.1 Raman spectra and hyperspectral mapping . . . 84
5.2 Estimating built-in strain in suspended graphene devices . . . 87
5.3 Comparing doping and strain in suspended and supported graphene . . . 92
5.4 Conclusion . . . 93

6 All optical blister test of suspended graphene 97
6.1 Strain induced phonon softening . . . 100
6.2 Raman intensities and blister height . . . 104
6.2.1 Blister height and maximal deflection . . . 105
6.2.2 Intrinsic value of I_{2D}/I_G . . . 106
6.2.3 Reconstruction of the blister profile . . . 109
6.3 Determination of the Grüneisen parameters . . . 112
6.4 Determination of the Young's modulus . . . 113
6.4.1 Hencky's description of a membrane blister test . . . 114
6.4.2 Application of Hencky's solution to graphene blisters . . . 115

6.5 Pressurized 2L, 3L and 4L graphene . . . 116
6.6 Discussion . . . 121
6.7 Conclusion . . . 124

7 Suspended graphene under electrostatic pressure 127
7.1 Optical probing of the gate induced deflection . . . 128
7.1.1 Determination of the deflection . . . 132
7.1.2 Intrinsic value of I_{2D}/I_G . . . 134
7.2 Theory of graphene sheet deformation due to electrostatic pressure . . . 136
7.2.1 Forces in electrostatic gating . . . 137
7.2.2 Mechanical deformation . . . 138
7.2.3 Comparison of three models to determine the electrostatic pressure load 142
7.3 Theory near collapse . . . 145
7.3.1 Maximal deflection and its critical value . . . 145
7.3.2 Charge density and its maximal value . . . 147
7.4 Analysis of phonon-softening . . . 150
7.5 Conclusion . . . 155

8 Conclusion and perspectives 157

Appendix 161
A Laser spot and defocusing influences . . . 161
B Calibration of the pressure load . . . 161
C Supplementary data of samples A . . . 163
D Data of samples B and C . . . 163
E Other supplementary data . . . 166

List of Figures 169

List of Tables 173

Bibliography 175

Acknowledgements

First I would like to acknowledge **Prof. Christoph Stampfer** (RWTH Aachen) and **Prof. Christophe Voisin** (Université Paris Didérot) for having been the referees of my thesis manuscript, and **Prof. Florian Banhart**, **Dr. Nedjma Bendiab** and **Dr. Pierre Verlot** for having participated to my defense as jury members. I enjoyed the scientific discussion with you and I am thankful for your comments.

The most important acknowledgement goes to my thesis supervisor, **Dr. Stéphane Berciaud**, who did not hesitate to accept me as a PhD student after my short visit in Strasbourg in summer 2012. My *Doktorvater* had (and still has) a lot of confidence in me, and I really thank him for the liberty he gave me to make our project evolve. His support has been invaluable. It has been a great pleasure to be part of his young and dynamic research group.

I furthermore thank **Prof. Bernard Doudin**, who has been my second thesis supervisor during my first year as PhD.

Without the STNano cleanroom facility or its staff, **Dr. Hicham Majjad**, **Sabine Siegwald**, **Romain Bernard** and **Alain Carvalho**, the sample fabrication would not have been straightforward, and the days spent in the cleanroom would have passed much slower. In particular, I appreciated the fresh fruits and nuts from Sabine's garden (kept outside the cleanroom, of course!) ... and I am not afraid of piranhas anymore!

Important technical support was provided by **Fabien Chevrier** (the Helium, pump, cable and security specialist), **Arnaud Boulard** (the metal piece specialist) and **Nicolas Beyer** (the lab and energy saving specialist).

I am grateful to **Michelangelo Romeo** for his help with Labview programming. He is a virtuoso in hardware connections and their synchronization.

Then I would like to acknowledge the other permanent members of the group, **Bohdan Kundys** and **Jean-François Dayen** for interesting scientific discussions and loaning pumps and other equipment to me.

Thanks to all the permanent staff of IPCMS who have always been available for me: **Véronique Wernher** for administrative help, **Béatrice Masson** for sharing organic vegetables, **Xavier Ledoux** and **Dominique Quince** for their informatics help, and many others. It has always been a pleasure to collaborate and chat with all of you.

The other PhD students of Stéphane's young up-and-coming group, **Dr.** (a brand new!) **François Federspiel**, **Guillaume Froehlicher** and **Etienne Lorchat** have always been available for mutual help and daily discussions about theoretical aspects and experimental issues. Thank you, François, for making me sensitive to a crucial optical alignment, and Guillaume, for being there when I needed help.

Also with the PhD students in the department, I have created strong social ties, notably with my office mates **Ather**, **Céline**, **Donald**, **Florian**, **Peter**, **Silvia**, **Tindara** and **Vina**. Thank you for having supported me and my puns (of increasing quality, you should admit!) and for your open ear in case of an emergency :-)

Thanks to all the other students of *Place du Café*, **Benjamin**, **Christian**, **Déborah**, **Dimitra**, **Gaël**, **Kerstin**, **Manuel**, **Michael**, **Nicolas**, **Olga**, **Ondrej**, **Vadym**, ... It has been a pleasure to share the lunch break and some *Feierabendbier(e)* with you!

Finally I thank my **parents** who accepted my leaving to launch myself into the PhD adventure. My **family** and **friends** from Bonn supported me a lot and my "old home" has always been a warm refuge.

The PhD period of three years has also been rich in personal events, in particular it has been a challenge to combine it with the organization of the wedding with my beloved **Marie-Astrid**, who has been always at my side with her daily encouragements and deep love.

Publications

Papers related to the work of this thesis

- Dominik Metten, François Federspiel, Michelangelo Romeo, and Stéphane Berciaud, *Probing built-in strain in freestanding graphene monolayers by Raman spectroscopy*, Physica Status Solidi B **250**, 2681–2686 (2013) / DOI: 10.1002/pssb.201300220

- Dominik Metten, François Federspiel, Michelangelo Romeo and Stéphane Berciaud, *An all-optical blister test on suspended graphene*, Physical Review Applied **2**, 054008 (2014) / DOI: 10.1103/PhysRevApplied.2.054008

- Dominik Metten, Guillaume Froehlicher, Stéphane Berciaud, *Doping- and interference-free measurement of I_{2D}/I_G in suspended monolayer graphene blisters*, Physica Status Solidi B **252**, 2390-2394 (2015) / DOI 10.1002/pssb.201552314

- Dominik Metten, Guillaume Froehlicher and Stéphane Berciaud, *Results of chapter 7, in preparation*

- Dominik Metten, Guillaume Froehlicher and Stéphane Berciaud, *Review on suspended graphene, in preparation*

Papers related to other works

- Florian Godel, Emmanuelle Pichonat, Dominique Vignaud, Hicham Majjad, Dominik Metten, Yves Henry, Stéphane Berciaud, Jean-François Dayen and David Halley, *Epitaxy of MgO magnetic tunnel barriers on epitaxial graphene*, Nanotechnology **24**, 475708 (2013) / DOI: 10.1088/0957-4484/24/47/475708

- Caitlin Morgan, Dominik Metten, Claus M. Schneider and Carola Meyer, *Effect of contact geometry on magnetoresistance in CoPd-contacted carbon nanotubes*, Physica Status Solidi B **250**, 2622–2626 (2013) / DOI: 10.1002/pssb.201300068

- Ather Mahmood, Cheol-Soo Yang, Jean-François Dayen, Serin Park, M. Venkata Kamalakar, Dominik Metten, Stéphane Berciaud, Jeong-O. Lee and Bernard Doudin, *Room temperature dry processing of patterned CVD graphene devices*, Carbon **86**, 256-263 (2015) / DOI: 10.1016/j.carbon.2015.01.040

- Caitlin Morgan, Maciej Misiorny, Dominik Metten, Sebastian Heedt, Thomas Schäpers, Claus M. Schneider and Carola Meyer, *Impact of tunnel barrier strength on magnetoresistance in carbon nanotubes*, submitted to Physical Review Applied (2015), available on arXiv: 1511.03058

Oral presentations related to the work of this thesis

- *Probing the vibrational and mechanical properties of freestanding graphene using Raman scattering spectroscopy*, Mid-term presentation, Scientific meeting at the Institut de Physique et de Chimie des Matériaux de Strasbourg, 10th of June 2014, Strasbourg (France)

- *All optical determination of the Young's modulus of graphene*, Condensed Matter in Paris (JMC14-CMD25), 24th to 29th of August 2014, Paris (France)

- *In-situ probing of electrostatically induced deflection of suspended graphene by Raman scattering spectroscopy*, Annual meeting of the GDRI Graphene Nanotubes, 29th of November to 3rd of December 2015, Aussois (France)

Posters related to the work of this thesis

- Dominik Metten, François Federspiel, Michelangelo Romeo, and Stéphane Berciaud, *Probing residual doping and built-in strain in freestanding graphene monolayers by Raman spectroscopy*
  presented at

  ▷ *Journées Néel*, Institut de Physique et de Chimie des Matérieux de Strasbourg, 3rd to 4th of September 2013, Strasbourg (France)

  ▷ Winter school *Surface-Confined Synthesis of Nanostructures*, Collège doctoral franco-allemand (Karlsruher Institut für Technologie and Université de Strasbourg), 17th to 20th of February 2014, Baden-Baden (Germany)

- Dominik Metten, François Federspiel, Michelangelo Romeo, and Stéphane Berciaud, *An all-optical blister test on freestanding graphene*
  presented at

  ▷ *Annual meeting of the GDRI Graphene Nanotubes*, 21th to 25th of February 2014, Strasbourg (France)

- *XXVIIIth International Winter School on Electronic Properties of Novel Materials*, 8th to 15th of March 2014, Kirchberg in Tirol (Austria)

Résumé en langue française

Le département de Formation Doctorale de l'Université de Strasbourg exige un résumé d'une longueur de 10 % du manuscrit de thèse en langue française. Ce résumé ne peut pas être considéré comme un document donnant des analyses et résultats avec une rigueur scientifique, mais doit être vu comme un document qui donne seulement les idées et résultats principaux, souvent en se référant à des analyses plus précises et à des figures présentées dans le manuscrit.

Introduction

Beaucoup de recherches ont été effectuées sur le graphène depuis son isolation en 2005, notamment en termes de transport électronique et de propriétés mécaniques. Un outil rapide et non-invasif, qui a bien servi à caractériser et comprendre le graphène, est la spectroscopie Raman. En effet, les principaux modes Raman sont sensibles aux contraintes, au dopage et au nombre de couches. Dans ce travail, nous nous servons de la spectroscopie Raman pour étudier en détails le graphène en tant que membrane suspendue, ce qui permet de partir d'un système propre et bien défini et ensuite étudier la réponse mécanique du graphène, qui sera soumis à une pression, soit par différence de pression d'air soit par une grille électrostatique. Les résultats présentés dans cette thèse s'alignent dans une volonté de comprendre les contraintes natives dans des membranes suspendues pour des applications telles que des résonateurs ou des détecteurs, et les méthodes utilisées peuvent être appliquées à d'autres matériaux bidimensionnels. Elles sont d'autant plus intéressantes que les mesures peuvent être faites *in situ*.

Généralités sur le graphène

En 1962, des couches très minces de carbone ont été observées par Boehm *et al.* sur du graphite réduit, à l'aide d'un microscope électronique en transmission [Boehm62]. Les auteurs ne s'imaginaient probablement pas l'engouement immense que ces couches ont engendée plus 40 ans après. En effet, il a fallu jusqu'en 2005 pour que Novoselov et Geim réussissent à isoler une monocouche de graphite d'épaisseur mono-atomique, appelée le *graphène* [Novoselov05a]. Novoselov

et Geim ont utilisé une technique simple: le dépôt sur un substrat par l'exfoliation à l'aide d'un ruban adhésif.

Le matériau ainsi obtenu est alors une monocouche qui est composée d'atomes de carbone arrangés en une structure bidimensionnelle hexagonale, dite de nid d'abeille. Cette structure n'est pas un réseau de Bravais puisque, d'un point de vue cristallographique, il y a deux types d'atomes de carbone, A et B (voir figure 2.1a). Il en résulte, dans l'espace réciproque, une zone de Brillouin qui est caractérisée par quatre points de haute symétrie, Γ, M, K et K' (voir figure 2.1b) [Castro Neto09]. La structure de bandes électroniques est calculée en utilisant le modèle des liaisons fortes [Wallace47, Reich02] en prenant compte les sauts des électrons d'un atome à l'atome plus proche. Pour affiner les calculs, on peut tenir compte des atomes plus loins, par exemple jusqu'à l'ordre 5, ce qui donne une structure de bande représentée en figure 2.2a. Les bandes de valence et de conduction se touchent aux points de symmétrie K et K', ce qui veut dire que la physique des électrons (et des trous) est gouvernée par la structure de bande au voisinage de ces points. Puisque la structure de bande y est linéaire, les électrons peuvent être considérés comme des particules de Dirac avec une masse effective, ces points sont alors nommés *points de Dirac*.

Du fait de la bidimensionalité du graphène et de sa dispersion linéaire, la densité des états est linéaire avec l'énergie des électrons, E_e et la densité de charges n est proportionnelle à E_e^2. Cette densité de charges peut être modifiée en mettant le graphène dans une géométrie à effet de champ, qui sera utilisée dans cette thèse en déposant le graphène sur un substrat de silicium dopé, couvert d'une couche de dioxyde de silicium qui sert comme espaceur diélectrique.

Dans ce genre de dispositif, des mobilités de porteurs de charge relativement élevées ont été mesurées [Geim07, Bolotin08b]. Pour des études de physique fondamentale proche du point de Dirac, mais aussi pour augmenter la mobilité des porteurs de charges, le graphène *suspendu* entre en jeu, parce qu'il n'est pas affecté par des interactions avec le substrat, qui, en particulier, crée des zones de charges inhomogènement répandues. Bolotin *et al.* ont mesuré des mobilités de plus d'un ordre de grandeur élevé par rapport au graphène supporté.

Le graphène suspendu est alors un système beaucoup plus propre, sans inhomogénité de densité de charges, très peu dopé et est ainsi dans une configuration idéale pour étudier ses propriétés au voisinage du point de Dirac.

Phonons et spectroscopie Raman du graphène neutre

Constitué de deux atomes par cellule unitaire, le graphène a six modes de phonons : trois optiques et trois acoustiques. Pour connaître leurs énergies, il faut regarder la dispersion des phonons, qui a été mesurée par diffusion de rayons X et calculée théoriquement par DFT [Maultzsch04b,

Mohr07, Lazzeri08]. Cette dispersion est représentée dans la figure 2.7. Pour les résultats de cette thèse, on se limite aux phonons des deux points de haute symmétrie, Γ et K.

L'effet Raman permet, entre autre, de sonder l'énergie des phonons par le couplage de ceux-ci avec des paires électron-trou (d'une énergie bien définie). Ces derniers ont été créés par des photons (lumière laser). Après avoir été diffusés inélastiquement, les photons sont détectés, leur perte d'énergie correspond à l'énergie des phonons (voir chapitre 3 pour plus de détails).

Au point Γ (les phonons ne transfèrent pas d'impulsion), seulement un mode est Raman actif, et ceci est dû à la dégénérescence des phonons longitudinaux et transversaux dans le plan. Ce mode est appelé mode G, qui est un mode non-résonant parce qu'il implique des états virtuels. Ce mode est le seul mode Raman actif au point Γ, tous les autres pics Raman qu'on observe dans le spectre du graphène (voir par exemple les figures 3.2a et b pour des spectres typiques) sont de l'ordre supérieur.

Le mode le plus éminent d'ordre supérieur est le mode 2D [Thomsen00]. Ce mode est un processus impliquant deux phonons d'impulsions opposées, au voisinage du point K. On rapelle que la conservation d'énergie et d'impulsion est toujours requise. Dans du graphène sans inhomogénité de densité de charges et neutre, ce mode est légèrement asymmétrique à cause d'effets de déformation trigonale (*trigonal warping* en anglais), qui commencent à jouer un rôle si on s'éloigne des points de haute symmétrie [Berciaud13].

En allant d'une monocouche de graphène à quelques couches, la forme du mode 2D change parce qu'il est très sensible à la structure de bande électronique, et parce qu'il est un mode résonant [Ferrari06, Gupta06, Graf07].

Effets de contraintes et de dopage sur le spectre Raman

Le spectre Raman d'une monocouche de graphène pésente alors deux pics, G et 2D, qui évoluent avec le dopage et des contraintes mécaniques dans le cristal de graphène.

Effets de contraintes

Sous contrainte biaxiale, soit extensive ou compressive, on attend une baisse ou une augmentation de l'énergie des phonons, respectivement. Ceci a été observé, par exemple, par Zabel *et al.* sur des bulles de graphène. Ces bulles, contrairement aux bulles pressurisées dans cette thèse, encapsulent de l'air entre le substrat et le graphène et sont présentes *as exfoliated*. Néanmoins, de fortes contraintes biaxiales extensibles ont été mesurées et, par conséquent, les pics Raman (au centre des bulles) sont observés à plus basse énergie (voir figure 3.7c et d).

Pour les contraintes uniaxiales, le mode G perd sa dégénérescence, ce qu'on peut voir dans la figure 3.7b, où un monofeuillet de graphène supporté par un substrat flexible est soumis à une

contrainte uniaxiale jusqu'à presque 1 % (extension par rapport à sa longueur initiale). On note que pour des contraintes inférieures à 0.5 %, cette division de pics n'est pas observable et que le mode 2D n'est pas affecté.

Une question difficile est de calibrer correctement les contraintes et d'attribuer un décalage Raman à une certaine valeur de contrainte. Cette calibration est déterminée par les fameux paramètres de Grüneisen γ [Mohiuddin09], qui seront déterminés dans cette thèse (voir sections 3.3.2 et 6.3).

Effets de dopage

Quand on ajoute des électrons, on attend intuitivement, que la maille cristalline s'étende, et inversement, qu'elle se réduise quand on dope avec des trous. Ceci a pour effet que les phonons auront moins ou plus d'énergie, respectivement (adoucissement et raidissement, *softening* et *hardening* en anglais). Cette évolution (sur les modes G et 2D) peut être observée comme une tendance (voir par exemple les données de G. Froehlicher *et al.* [Froehlicher15a]), et est appelée la renormalisation adiabatique des phonons.

Un autre terme, non-adiabatique, joue un rôle important dans le processus Raman, et c'est ce terme qui domine l'évolution des fréquences Raman à des niveaux de dopage accessibles avec les substrats utilisés dans nos travaux. Le terme non-adiabatique provient du couplage électron-phonon, qui est particulièrement fort au point Γ. On observe alors une superposition de ce couplage avec un terme adiabatique [Ando06, Lazzeri06, Pisana07] (voir figure 3.3). Notons que l'évolution exacte ne peut être résolue qu'à basse température et dans du graphène propre (inhomogénité de densité de charges très faible), et que l'effet non-adiabatique est moins prononcé pour le mode 2D, puisqu'il fait intervenir des phonons seulement à proximité du point K et pas au point K même.

Curieusement, la largeur à mi-hauteur du mode G, qui finalement représente le temps de vie des phonons, dépend fortement de la densité de charges. En effet, pour des énergies plus élevées que la moitié de l'énergie des phonons, le canal de déclin des phonons en paires électron-trou est bloqué par le principe de Pauli [Lazzeri06, Das08].

Les intensités Raman sont l'empreinte de la probabilité du processus Raman. Pour des énergies plus petites que la moitié de l'énergie des photons (laser), l'intensité du mode G est constant, mais celle du mode 2D dépend du taux de diffusion des électrons entre eux. C'est pourquoi, dans des échantillons de graphène non-dopé, on attend des intensités constantes [Das08, Basko09b, Basko09a, Kalbac10, Chen11].

Découplage des décalages Raman liés aux contraintes et dopage

À la fois le pic G et le pic 2D se décalent sous contraintes et dopage. Existe-t-il une manière de découpler ces deux effets ? Lee *et al.* ont mesuré les fréquences Raman sur du graphène supporté (en partie contraint) et ont changé le niveau de dopage en faisant un recuit. Les taux de décalage ($\partial\omega_{2D}/\partial\omega_{G}$) trouvés étant différents, les auteurs ont proposé un modèle basé sur une décomposition vectorielle dans le plan des fréquences ω_{G} et ω_{2D} [Lee12a], à l'aide duquel il est possible d'attribuer à une paire de fréquences mesurées une valeur de contrainte et une valeur de dopage (voir figure 3.8). Ce modèle n'est cependant valable que dans certaines conditions (voir la section 3.4 pour une discussion détaillée).

Le graphène comme membrane

Dans les travaux effectués pour cette thèse, des membranes de graphène pressurisées ont été étudiées. Pour connaître la déformation d'une telle membrane, on peut se référer à la théorie d'élasticité [Landau70]. Deux cas doivent être distingués : la déflection ξ_{max} (déflection maximale au centre) d'une *membrane* d'épaisseur négligeable, qui suit une loi $\Delta p \propto \xi_{max}^3$ (Δp étant la différence de pression), et la déflection d'une plaque fine, qui suit une loi $\Delta p \propto \xi_{max}$. On ne peut imaginer une membrane plus fine que le graphène, on attend alors que la réponse suit la loi $\propto \xi_{max}^3$. Or, des contraintes initiales peuvent agir en opposition à la flexion, considérer comme une rigidité effective et ainsi contribuer avec un terme linéaire.

Fabrication d'échantillons et montage expérimental

Fabrication d'échantillons

Pour obtenir des substrats préstructurés de tranchées (*trench* en anglais) ou de fossés (*pit* en anglais), une technique standard impliquant un processus de lithographie optique est utilisée (voir figure 4.2). Ensuite, sur des substrats propres, le graphène est exfolié à l'aide d'un ruban adhésif, qui permet de raffiner un cristal de graphite et à la fois de déposer le graphène sur le substrat (voir figure 4.1). Puis, les monocouches suspendues sont localisées à l'aide d'un microscope optique, grâce au contraste que le graphène présente sur des substrats d'une épaisseur d'oxyde de silicium optimisée [Blake07].

Le graphène suspendu peut alors être contacté électriquement en évaporant du métal (titane et or) avec des grilles TEM comme pochoir, ce qui évite tout contact avec des solvants ou résines avec le graphène. Le graphène contacté ainsi obtenu est alors très propre.

Montage expérimental

La conception et le montage d'un dispositif expérimental permettant des mesures de spectroscopie Raman faisait partie des travaux effectués pour cette thèse. À l'aide d'un montage optique de microscopie confocale, un faisceau laser ($\lambda_{\text{laser}} = 532\,\text{nm}$) est focalisé sur l'échantillon. L'objectif (nous disposons de deux objectifs différents : grandissement $\times 20$, ouverture numérique 0.45 et gr. $\times 50$, o.n. 0.65) sert à la fois à injecter la lumière excitante et à collecter la lumière diffusée. Cette dernière est filtrée spectralement (filtre dichroïque bloquant toute longueur d'onde inférieure à $535\,\text{nm}$, en particulier la lumière du laser et la diffusion Rayleigh) et spatialement (trou de confocalité conjugué avec le spot laser). Ensuite, la lumière diffusée est dispersée sur une caméra CCD (dispositif à transfert de charges) à l'aide d'un réseau. La figure 4.4a montre schématiquement les élements principaux du montage expérimental. Il est important d'ajouter que l'objectif est monté sur une platine Piezo, donnant la possibilité de scanner un échantillon et d'enregistrer des spectres Raman point par point.

Les spectres Raman peuvent être acquis sur des échantillons à température ambiante (voir photo de la figure 4.4b) ou alors sous vide et à basse température (voir figure 4.4c). Pour cela, un cryostat équipé d'une fenêtre pour l'accès optique est utilisé. Dans le cryostat, l'échantillon se trouve sous vide et est connecté thermiquement avec un bain d'hélium par un doigt froid, ce qui permet de refroidir l'échantillon jusqu'à une température de $4\,\text{K}$. De plus, par un accès électrique, des mesures de source, drain et de grille peuvent être réalisées.

L'acquisition des données se fait à l'aide du logiciel commercial *WinSpec* (pour une acqusition simple) ou alors à l'aide d'une interface *Labview*, qui permet de commander en même temps la platine Piezo pour acquérir des cartes Raman. Le traitement des spectres, notamment pour extraire la position spectrale, la largeur à mi-hauteur et l'intensité des principaux pics Raman, se fait à l'aide d'un programme personnalisé sous *Matlab*, permettant le traitement de plusieurs spectres à la fois.

Contraintes initiales dans graphène suspendu

Introduction

Dans des monofeuillets de graphène, qu'ils soient supportés par un substrat ou alors suspendus sur des tranchées ou des trous, des contraintes peuvent être présentes. Le graphène suspendu est une plateforme idéale pour étudier l'effet des contraintes sur les principaux modes Raman, sans qu'il y ait des effets liés au dopage induit par le substrat [Berciaud09]. Les résultats sont présentés dans le chapitre 5 du manuscrit.

Détermination de niveaux de contraintes initiales

En utilisant la décomposition vectorielle dans l'espace des fréquences ω_G et ω_{2D}, proposée par Lee *et al.* [Lee12a], on peut alors estimer le niveau de contraintes dans les membranes de graphène suspendu. Pour faire ceci, nous analysons des cartes de fréquences Raman (un exemple de carte peut être consulté dans la figure 5.3) d'une dizaine d'échantillons de graphène suspendu et calculons la moyenne de ces fréquences avec leurs écarts-types. Cette corrélation est montrée dans la figure 5.4b. Un ajustement linéaire de cette corrélation donne une pente de 2.2, ce qui est la valeur proposée par Lee *et al.* pour des contraintes. Les différences de fréquences d'un échantillon à l'autre sont alors purement liées aux contraintes. En effet, la largeur à mi-hauteur du mode G, Γ_G est de $(14 \pm 1)\,\text{cm}^{-1}$ sur tous les échantillons de graphène suspendu, ce qui indique que le niveau de dopage est faible et inférieur à $3 \times 10^{11}\,\text{cm}^{-2}$ (voir figure 5.4a).

La moyenne de ω_G des valeurs moyennées sur les échantillons est de $1581\,\text{cm}^{-1}$. Cette valeur correspond à la valeur de la bande G mesurée sur du graphite. Pour cette valeur de ω_G^0 on trouve une valeur de $\omega_{2D}^0 = 2667 \pm 1\,\text{cm}^{-1}$ (pour $\lambda_{laser} = 532\,\text{nm}$), ce qui est utilisé dans la suite comme valeur de référence pour du graphène suspendu non dopé et non contraint.

Avec ce point de référence, on voit que les contraintes peuvent être compressives ou extensives (fréquences plus élevées ou moins élevées), et en ajoutant la calibration de contraintes, qui est déterminée par les paramètres de Grüneisen (voir équation 3.11), on peut même donner une valeur quantitative aux contraintes.

Pour avoir plus de connaissances sur ces contraintes, en particulier sur leur distribution spatiale, on peut représenter la corrélation de ω_G et ω_{2D} de chaque pixel des cartes Raman acquises (voir figure 5.5a). La distribution des données dans le plan des fréquences dépend fortement des échantillons. Dans certaines membranes, les fréquences (et par conséquent les contraintes) sont homogènes ; ceci est surtout le cas dans les membranes suspendues sur des trous. D'autres membranes montrent une distribution qui s'aligne sur une pente de $\partial\omega_{2D}/\partial\omega_G = 2.2$, ce qui veut dire que les contraintes ne sont pas homogènement réparties sur la membrane. L'échantillon T2 (voir figure 5.5a) montre la plus grande dispersion de données dans le plan des fréquences le long de la pente 2.2. Cette exemple indique que certaines membranes peuvent avoir, par endroit, à la fois des parties contraintes de manière extensive et compressive. Les contraintes initiales varient alors d'un échantillon à l'autre.

Conclusion

Avec les paramètres de Grüneisen de $\gamma_G = 1.8$ et $\gamma_{2D} = 2.4$ (voir section 6.3) et le point de référence de ($\omega_G^0 = 1581\,\text{cm}^{-1}$, $\omega_{2D}^0 = 2667\,\text{cm}^{-1}$) (pour le graphène non dopé et non contraint), on peut alors conclure que les valeurs de contraintes initiales (absolues et moyennées)

peuvent atteindre 0.1 %. Quant à la dispersion des contraintes, elle peut également varier dans une gamme/zone de 0.1 %.

Bulle de graphène pressurisé

Introduction

Une manière élégante d'appliquer et de contrôler des contraintes dans une membrane de graphène est de pressuriser les membranes qui ont été exfoliées sur des trous. L'air sous la membrane est enfermé dans la microcavité (voir schéma dans la figure 6.1). En mettant ce genre de dispositif sous vide, une différence de pression Δp fait gonfler la membrane, ce qu'on appelle un *blister test* en anglais. On peut alors étudier, par spectroscopie Raman, la déformation et les contraintes pures, sans avoir d'effet de dopage sur les fréquences Raman.

En plus du décalage des pics Raman dû aux contraintes, on s'attend à observer un changement d'intensité en variant Δp, puisque la distance entre la membrane et le fond du trou varie et, à la fois la lumière incidente et diffusée (Raman) sont soumises à des effets d'interférences optiques.

De ces deux informations, les variations en décalage et intensité Raman, on peut extraire des informations sur les contraintes et sur la topographie de la membrane. Ces mesures ont été menées sur trois échantillons différents. Par la suite seront discutés les résultats d'un échantillon, comme cela a été fait dans le chapitre 6.

Adoucissement de phonons induit par contraintes

Des spectres Raman ont été mesurés au centre de la bulle de graphène pour différentes valeurs de Δp. Trois spectres (pour $\Delta p = 0$, $\Delta p = 30$ kPa et $\Delta p = 74$ kPa, la valeur maximale de Δp qui a été appliquée) sont présentés dans la figure 6.2. Par rapport à la position initiale des fréquences ω_{G} et ω_{2D} à $\Delta p = 0$, les décalages Raman sont $-15\,\mathrm{cm}^{-1}$ et $-33\,\mathrm{cm}^{-1}$, respectivement, à $\Delta p = 74$ kPa. Le quotient est 2.2, en accord avec la valeur proposée par Lee *et al.* pour des contraintes.

En traçant ω_{2D} en fonction de ω_{G} pour toutes les valeurs de Δp au centre de la membrane (voir figure 6.3b), on voit que les données s'alignent sur une droite avec une pente de 2.2. En particulier, l'évolution des valeurs ne suit pas de pente de 0.55 ou de 0.2, ce qui indiquerait un décalage Raman lié au dopage. Cette hypothèse est confirmée par le fait que la forme des pics ne change pas, et que la largeur à mi-hauteur du pic G reste à $15 \pm 1\,\mathrm{cm}^{-1}$ (voir figure 6.3a).

Des cartes Raman ont également été acquises sur les bulles. Pour les fréquences Raman, ces cartes sont représentées sur les figures 6.4a et b. On voit que l'adoucissement des phonons est maximal au centre et qu'il est centrosymétrique. En comparant des coupes des cartes Raman le long d'une ligne qui traverse le centre pour la membrane pressurisée et non-pressurisée (voir figure 6.4c), on voit que la partie supportée par le substrat n'est pas affectée par la différence de

pression. En traçant la corrélation des fréquences ω_{2D} en fonction de ω_G pour une vingtaine de valeurs de Δp et pour différentes distances du centre, la pente reste 2.2, même dans un rayon de $3\,\mu$m (voir figures 6.4d et e). Si proche du bord, une composante de contrainte uniaxiale est certainement présente, mais pour le cas d'une contrainte uniaxiale faible (pas de *splitting* de la bande G), la pente est proche de 2.2, ce qui est en accord avec les résultats d'autres groupes, assemblés dans la figure 3.10.

Intensités Raman et topographie de la bulle de graphène

On peut maintenant examiner les variations des intensités Raman qui sont liées aux interférences optiques entre la membrane de graphène et le fond du trou. Le système optique [Si - air/vide - graphène] agit comme une cavité optique, et l'intensité Raman est modulée par les interférences de la lumière du laser et de la lumière diffusée en changeant la distance h entre graphène et Si. Un facteur d'exaltation peut alors être calculé en considérant une cavité de Fabry-Pérot pour une couche et de l'appliquer pour le cas de plusieures couches (voir section 3.5 pour les détails). Ce facteur d'exaltation est montré dans la figure 6.6a pour le système [Si - air/vide - graphène] en fonction de h.

L'évolution des intensités Raman du mode G et 2D, I_G et I_{2D}, en fonction de Δp au centre de la membrane est montrée dans la figure 6.6b. En identifiant les maxima et les minima de cette évolution avec les maxima et les minima correspondants au facteur d'exaltation (la profondeur du trou est connue par mesures de profilométrie), il est alors possible de déterminer h, et ainsi la hauteur de la bulle.

Bien-sûr, la détermination de h est également possible pour des mesures Raman ailleurs qu'au centre. Pour des scans et des cartes Raman, la topographie de la bulle a été réconstruite, comme on peut voir dans les figures 6.10a et b.

Détermination des paramètres de Grüneisen

Connaissant la topographie, on peut estimer les contraintes ϵ_p, induites par la différence de pression. Ces contraintes atteignent une valeur maximale de $0.33\,\%$. Dans la figure 6.11, ω_G et ω_{2D} sont tracés en fonction de ε_p, ce qui permet de déterminer directement les paramètres de Grüneisen, qui sont définis comme $\gamma_x = \partial\omega_x/(2\omega_x^0\partial\epsilon_p)$ (x étant G ou 2D).

Dans la gamme de contraintes de 0.1 à $0.33\,\%$ (on néglige les valeurs de faibles contraintes parce que des effets de *self-tensioning* y peuvent jouer un rôle), on trouve les valeurs $\partial\omega_G/\partial\epsilon_p = -57\,\text{cm}^{-1}/\%$ et $\partial\omega_{2D}/\partial\epsilon_p = -128\,\text{cm}^{-1}/\%$. Avec le point de référence défini dans la section précédente ($\omega_G^0 = 1581\,\text{cm}^{-1}$, $\omega_{2D}^0 = 2667\,\text{cm}^{-1}$), on trouve alors $\gamma_G = 1.8 \pm 0.2$ et $\gamma_{2D} = 2.4 \pm 0.2$.

Détermination du module de Young

Pour une membrane, l'évolution de la hauteur de la bulle, ξ_{max}, avec une différence de pression appliquée, Δp, suit une loi $\Delta p \propto Et\xi_{\text{max}}^3/a^4$ (E étant le module de Young, t l'épaisseur du grapène et a un facteur lié à la géométrie). Pour le cas d'une membrane pressurisée circulaire, on peut prendre la solution proposée par Hencky en 1915 [Hencky15], où le facteur de proportionnalité, K est de 3.09 pour le graphène, et a est le rayon du trou [Bunch08, Koenig11].

Comme Δp et ξ_{max} sont connus, la détermination du module de Young est possible. En effet, en traçant ξ_{max}^3 en fonction de Δp (voir figure 6.12a), les données suivent une droite, dont on peut extraire la pente et ensuite le module de Young. Nous trouvons ainsi une valeur de $E = 1.05 \pm 0.10$ TPa.

Une contrainte initiale agirait comme une rigidité à la flexion (comparable aux plaques avec une épaisseur finie) et il faudrait ajouter un terme qui serait proportionnel à ξ_{max}. Les valeurs des fréquences Raman à $\Delta p = 0$ nous indiquent qu'une contrainte initiale de l'ordre de 0.05 % est présente dans la membrane. Cette contrainte n'est pas prise en compte dans l'ajustement linéaire. Il s'avère que la valeur exacte du rayon de la bulle, qui est difficle à déterminer [Lu10, Barton11], est un facteur qui est assez sensible aux ajustements. En effet, la figure 6.12b montre un ajustement avec un rayon légèrement plus grand et une contrainte initiale de 0.05 % qui suit bien la courbe.

Les résultats des deux autres échantillons que nous avons mesurés sont similaires (voir figure 6.13 par exemple). Ce genre de *blister test* a aussi été appliqué à des membranes de deux, trois et quatre couches de graphène. Les modules de Young ainsi obtenus sont de l'ordre de 1 TPa (pour les détails, voir la discussion dans la section 6.5).

Discussion et conclusion

La valeur de $\partial\omega_{\text{2D}}/\partial\omega_{\text{G}}$ que nous avons obtenue correspond à la valeur proposée par Lee *et al.* en 2012 [Lee12a]. Depuis, des valeurs similaires ont été publiées, notamment sur des bulles qui se sont auto-formées sur un substrat de SiO_2 [Zabel11] et sur des bulles pressurisées de diamètre différent (ce qui résulte en une contrainte différente à Δp égal) [Lee12b]. Notre valeur de 2.2 s'aligne bien parmi ces valeurs dans la littérature (voir figure 6.16).

Quant à la détémination des paramètres de Grüneisen, des valeurs proches des nôtres ont été trouvées récemment, mais toujours en utilisant au moins deux techniques de mesures différentes (par exemple AFM et Raman [Metzger09, Zabel11]) ou alors des calculs théoriques [Thomsen02, Mohiuddin09]. Nos mesures permettent d'extraire *in situ* à la fois la topographie (et les contraintes) et les fréquences des modes Raman, ce qui résulte en un ensemble de données cohérent. Les paramètres de Grüneisen permettent alors, pour du graphène non dopé dont on ne

connait pas les contraintes, d'attribuer à chaque valeur de fréquence Raman mesurée une valeur de contrainte.

L'extraction *in situ* du module de Young par des moyens purement optiques est aussi une nouveauté, puisque celui d'une monocouche de graphène a été uniquement mesuré par une technique de nanoindentation en utilisant une pointe d'AFM [Lee08] ou une combinaison de Raman et de simulations à base d'images SEM [Lee12b]. Les valeurs disponibles dans la littérature et la comparaison aux nôtres sont montrés dans le tableau 6.2.

Graphène suspendu sous pression électrostatique

Introduction

Une autre manière de faire bouger une membrane de graphène suspendu est d'appliquer une tension de grille, où le SiO_2 agit comme diélectrique. Le Si dopé et le graphène peuvent être considérés comme deux plaques d'un condensateur. Dans ce genre d'expérience, la maille du cristal de graphène est soumise à des contraintes, parce que la force électrostatique tire sur la membrane. Si l'on regarde les fréquences Raman, on s'attend à voir un effet lié aux contraintes, mais aussi lié à l'ajout de porteurs de charges.

Une grande partie du chapitre 7 est focalisée sur la détermination de la déflection (à partir des changements d'intensité des pics Raman liés aux interférences optiques) et sa valeur limite avant que la force électrostatique devienne assez forte pour que la membrane s'effondre. Cette analyse est particulièrement intéressante pour des mesures de transport électronique, qui, habituellement, n'offrent aucune possibilité d'observer *in situ* la déflection de la membrane. De plus, nous proposons un modèle qui prédit la tension de grille maximale à appliquer avant que la membrane ne s'effondre. Finalement les fréquences Raman sont analysées en détail.

Mesure optique de la défléction induite par la tension de grille

Dans le cas de la bulle de graphène pressurisée, la distance h entre le graphène et le fond du trou change avec Δp, pour le graphène soumis à une tension de grille, la distance h change avec V_g. La membrane étudiée ici, à basse température, est en partie suspendue sur une tranchée, la mise sous vide n'entraîne alors aucune déformation (voir figure 7.2a et f). Il y a également un résidu de SiO_2 au fond de la tranchée ($d_{SiO_2} = 212$ nm, l'épaisseur initiale totale d'oxyde étant 500 nm). Ceci résulte en une évolution du facteur d'exaltation qui est représentée dans la figure 7.3b.

L'évolution de I_G et I_2D en fonction de V_g est montrée dans la figure 7.3a. Comme dans le cas de la bulle, on peut tout de suite attribuer les valeurs d'intensité Raman à une hauteur (voir figure 7.8). Curieusement, en passant de $+19$ à $+20$ V, le changement des intensités n'est plus lisse mais abrupte. En regardant les spectres bruts correspondants (voir figure 7.2g et h), on voit

que la forme des pics Raman ne change pas pendant le balayage de la tension de grille, jusqu'à atteindre les $+20$ V, où un décalage important vers de plus basses fréquences est observé ainsi qu'une levée de dégénérescence de la bande G. Ce *splitting* est une première indication d'une forte contrainte uniaxiale, donc un effondrement de la membrane, qui semble être irreversible puisque l'intensité des pics Raman ne change plus en balayant à nouveau V_{g}.

Théorie sur la déformation d'une membrane de graphène due à la pression électrostatique

Pour comparer les données obtenues (la déflection au centre, ξ_{max}, en fonction de V_{g}) avec un modèle théorique, nous considérons la pression électrostatique entre deux plaques qui s'exprime comme $P_{\mathrm{el}} = c^2 V_{\mathrm{g}}^2/(2\varepsilon_0)$, où c est la capacitance par unité de surface du système SiO_2-air/vide. En calculant l'énergie libre d'une membrane contrainte, cette pression est en compétition avec l'énergie d'étirement (*stretching*) et de flexion (*bending*) [Medvedyeva11]. Si l'on suppose un profil parabolique de la membrane déflectée, on arrive à une expression qui lie P_{el} à la contrainte initiale T_0 et la déflection ξ_{max} (voir section 7.2.2 pour les détails):

$$P_{\mathrm{el}} = \frac{8T_0}{L^2}\,\xi_{\mathrm{max}} + \frac{64Et}{3(1-\nu^2)L^4}\,\xi_{\mathrm{max}}^3,$$

où ν est le ratio de Poisson et L la longueur de la tranchée.

On peut déterminer P_{el} de différentes manières (voir section 7.2.2 pour les détails). Ici, on se restreint sur une intégration le long du profil parabolique, ce qui donne une valeur moyennée pour P_{el}. Dans les figures 7.8a et b sont montrés les ajustements des données avec l'équation précédente (en noir et rouge pour l'extraction des données à partir de I_{G} et I_{2D}, respectivement), où la contrainte initiale a été laissée libre comme paramètre d'ajustement.

Trois choses remarquables sont à signaler ici: 1) Le modèle suit très bien l'évolution de ξ_{max}, en particulier autour de $V_{\mathrm{g}} = 0$, où T_0 a un impact considérable (la ligne pointillée montre $T_0 = 0$ pour comparer). 2) Le modèle prédit l'effondrement de la membrane proche de $+20$ V. 3) La valeur de T_0 trouvée par l'ajustement est de 0.07 %. Cette valeur correspond à la valeur qu'on peut extraire des données Raman acquises à température ambiante. Cette dernière observation est surprenante car les coefficients d'expansion thermique pour le substrat et le graphène ne sont pas les mêmes et un changement de température de 290 K devrait changer les contraintes dans la membrane.

Théorie près de l'effondrement

Les résultats du modèle sur la membrane soumise à une tension de grille par le bas peuvent être généralisés pour différentes géométries pour prédire l'effondrement, une information im-

portante pour les expériences de transport. On suppose que la membrane est fixée aux bords de la tranchée, la déflection et la contrainte initiales sont négligées et que le profil de la membrane est parabolique.

Pour un substrat d'épaisseur initiale de SiO_2 de 500 nm, la tension de grille à appliquer pour avoir une certaine déformation en fonction de l'épaisseur de l'air dans les 500 nm est montrée dans la figure 7.9a (pour $L = 5\,\mu$m). Deux régimes peuvent être identifiés: un régime où la membrane se dépose doucement au fond de la tranchée (ce qui est le cas pour des valeurs d_{air} (nm)/500 nm < 40 %) et un autre régime où la membrane s'effondre abruptement (pour des valeur de d_{air} plus élevées).

De ce graphe, on peut extraire une ligne critique en longeant la limite de l'effondrement. Les valeurs critiques de ξ_{max} et V_{g} ainsi obtenues sont représentées dans la figure 7.9b, pour différentes longueurs de tranchées. Les graphes pour $d_{SiO_2} = 285$ nm et 90 nm, substrats habituellement utilisés, sont reportés dans la figure 7.10.

Par la formule $n_{\text{max}} = c(\xi_{\text{max}})V_{\text{g}}(\xi_{\text{max}})$, le nombre de porteurs de charges peut être calculé au centre de la membrane et on peut estimer pour chaque géométrie ces valeurs n (voir section 7.3.2 pour les détails). Notamment au centre de la membrane mesurée, on attend une valeur de l'ordre de 6×10^{11} cm^{-2}.

Analyse de l'adoucissement des phonons

La variation des fréquences Raman avec la tension de grille est montrée dans les figures 7.14a et b et suit une évolution parabolique avec un adoucissement de -5 cm^{-1} et -11 cm^{-1} à $V_{\text{g}} = +19$ V pour ω_{G} et ω_{2D}, respectivement, par rapport aux valeurs initales à $V_{\text{g}} = 0$. Le rapport de ces adoucissements est de 2.2 (valeur pour une contrainte biaxiale ou uniaxiale faible), ce qui indique, à première vue, un décalage Raman dû aux contraintes. Pourtant, pour des valeurs de $n \approx 6 \times 10^{11}$ cm^{-2}, on s'attend à voir une variation des fréquences Raman due à l'ajout des porteurs de charges [Lazzeri06]. De plus, la corrélation des données (voir figure 7.14e) ω_{2D} en fonction de ω_{G} montre bien une pente de 2.2.

Pour interpréter ces observations, on peut regarder l'évolution de la largeur à mi-hauteur du pic G, Γ_{G}, qui change avec le nombre de porteurs de charges [Lazzeri06, Pisana07]. La corrélation de $\Delta\Gamma_{\text{G}}$ (par rapport à la valeur à $V_{\text{g}} = 0$) en fonction de n (calculé) est montrée dans la figure 7.14f. En traçant également les courbes théoriques (équation 3.10) pour différentes inhomogénités de densité de charges dans le même graphe, on s'aperçoit que les points expérimentaux sont mieux décrits par une inhomogénité de densité de charges finie de l'ordre de 1×10^{11} cm^{-2}. À cette valeur d'inhomogénité, l'évolution de ω_{G} en fonction de n ne présente qu'une petite variation de l'ordre de 0.5 cm^{-1}. La raison pour laquelle une inhomogénité de densité de charges est observée s'explique quand on regarde la convolution de la taille du spot laser

et de dérives thermiques avec la distribution des charges sur le profil parabolique. Pour la déflection maximale de la membrane, cette convolution ($0.7\ \mu\text{m}^2$ pour le spot laser et $2\ \mu\text{m}^2$ pour les dérives thermiques) est montrée dans les figures 7.15a et b. La valeur de l'inhomogénité de densité de charges qu'on peut en extraire est justement la valeur qui serait en accord avec une valeur constante de ω_G dans la gamme de n que nous avons étudiée.

On peut alors calculer les contraintes induites par la force électrostatique, qui sont de 0.1 %, en utilisant les paramètres de Grüneisen que nous avons déduits dans le chapitre précédent.

Conclusion

L'extraction de la déflection est une question importante dans le cadre d'expériences de transport électronique. Ici, nous avons montré que cette extraction peut se faire *in situ* à l'aide d'effets d'interférences, et qu'en même temps, les fréquences Raman donnent des informations sur les contraintes et le dopage. Le modèle théorique développé aide à comprendre à quelle amplitude de force électrostatique la membrane s'effondre. Le modèle peut notamment être considéré comme une directive pour la conception de nouveaux échantillons de graphène suspendu.

Conclusion et perspectives

Dans ce manuscrit, nous avons étudié en détails la réponse mécanique d'une monocouche de graphène à une pression externe, et ceci par des techniques purement optiques. L'utilisation de la spectroscopie Raman offre une vue d'ensemble approfondie sur le matériau étudié, puisqu'elle est sensible à la qualité cristalline de la membrane, au dopage, aux contraintes et elle permet aussi d'identifier les monocouches de graphène.

La première partie expérimentale est consacrée à l'étude de contraintes initiales dans des membranes de graphène issues d'un processus d'exfoliation mécanique, qui sont initialement non-dopées si elles sont découplées du substrat, ce qui est le cas dans le graphène suspendu. Nous trouvons que ces contraintes dépendent fortement de l'échantillon, peuvent être homogènes ou inhomogènes, compressives ou extensives, mais ne dépassent pas la valeur de 0.1 % dans nos échantillons.

L'étude détaillée d'une bulle de graphène pressurisée nous a permis de comprendre l'évolution des fréquences Raman en appliquant une contrainte extensive biaxiale de manière contrôlée. De plus, à l'aide de la théorie d'élasticité de membranes et des changements d'intensité des modes Raman liés à des interférences optiques, nous avons pu déterminer des paramètres mécaniques importants tels que ceux de Grüneisen et le module de Young. La reconstruction de la topographie par des moyens purement optiques est un point fort de notre étude, parce que l'obtention de cette information nécessite d'habitude un montage expérimental plus sophistiqué

(*e.g.* AFM sous vide). En particulier, cette approche pourrait être utilisée pour d'autres matériaux deux-dimensionnels.

Les changements d'intensités des modes Raman ont été utilisés pour déterminer également le déplacement d'une membrane suspendue sur une tranchée sous pression électrostatique, à basse température. Dans ce genre d'expérience, un effondrement de la membrane a été observé. L'évolution de la déflection avec la tension de grille a été modélisée ainsi que l'effondrement. Avec ce modèle, le déplacement de la membrane pour différentes géométries de dispositif a été prédit, information utile pour des mesures de transport. L'évolution des fréquences Raman est surtout due aux contraintes.

Ce contrôle précis de la déflection ouvre la voie pour des expériences qui cherchent à sonder des interactions entre une membrane de graphène et un nano-objet, *e.g.* un nano-émetteur [Federspiel15, Reserbat-Plantey15], qui dépend sensiblement de la distance graphène - nano-émetteur.

Les applications ne sont pas limitées à des tensions de courant continu (DC), au contraire, récemment le potentiel du graphène comme résonateur mécanique a été révélé [Bunch07, Chen09a, Barton11]. Le mouvement induit par l'activation électrique peut être lu soit électriquement [Chen09a, Eichler11] soit optiquement [Bunch07, Cole15]. La fréquence de résonance est très sensible à des perturbations extérieures; avec la petite masse du graphène, ces caractéristiques sont très favorables pour des applications telles que des détecteurs [Wong10, Hill11, Puller13].

De plus, on pourrait résoudre en temps l'oscillation d'un résonateur de graphène par spectroscopie Raman, ce qui permettrait de sonder à la fois le mouvement du résonateur (dans la gamme de MHz à GHz) et le mouvement des phonons (dans la gamme de THz).

1 Introduction

Dünnste Kohlenstoff-Folien (thinnest carbon films) have been observed by Boehm *et al.* in 1962 by transmission electron microscopy (TEM) [Boehm62]. The authors were certainly not aware of the research rush this ultra-thin material would have generated more than 40 years after its first observation. Graphite, which is the bulk crystal of these films, is a planar structure consisting of single layers with carbon atoms arranged in a honeycomb lattice (see figures 1.1a and d). It has been studied in detail in between, *inter alia* because of its importance as moderating material in nuclear reactors. A lot of understanding of the electronic and phonon band structure has been achieved during this period [Wallace47, Blakslee70, Tuinstra70, Nicklow72, Nemanich77, Vidano78].

However, the unambiguous isolation of a single layer, named *graphene* [Boehm94], has been achieved only at the beginning of the 21st century, and that by reducing the thickness of graphite crystals down to few and single layers with the help of a simple scotch tape exfoliation technique (top-down approach) [Novoselov04, Novoselov05b], for which the Nobel prize of physics has been attributed to Novoselov and Geim in 2010. Optimized substrates favored the localization of monolayer graphene [Blake07], and the observation of an electric field-effect modulated electrical conductivity pushed research group to focus on this material, which turned out to be endowed with an unusual electronic bandstructure [Reich04, Geim07, Castro Neto09, Narula14], an excellent electron transport [Novoselov04, Das Sarma11], optical [Nair08b], vibrational [Mohr09, Ferrari13], thermal [Balandin11, Pop12] and mechanical properties [Lee08, Bunch12, Tan13].

Graphene is the building block of the sp2 quasi zero- and one-dimensional (0d and 1d) nanostructures, *i.e.* fullerenes [Iijima80, Chuvilin10] and carbon nanotubes [Iijima93] (see figures 1.1a, b and c) and of graphite (see figure 1.1d). Thus, fundamental studies on these materials of different dimensionalities are very enriching because one can probe physics in quasi-1d and 2d systems. Furthermore, these materials form a good platform for spin injection [Tsukagoshi99, Sahoo05, Tombros07, Dlubak12].

There are several methods to isolate single graphene sheets. The main approaches are (1) mechanical exfoliation from graphite [Novoselov04, Novoselov05b], (2) graphene growth on metals

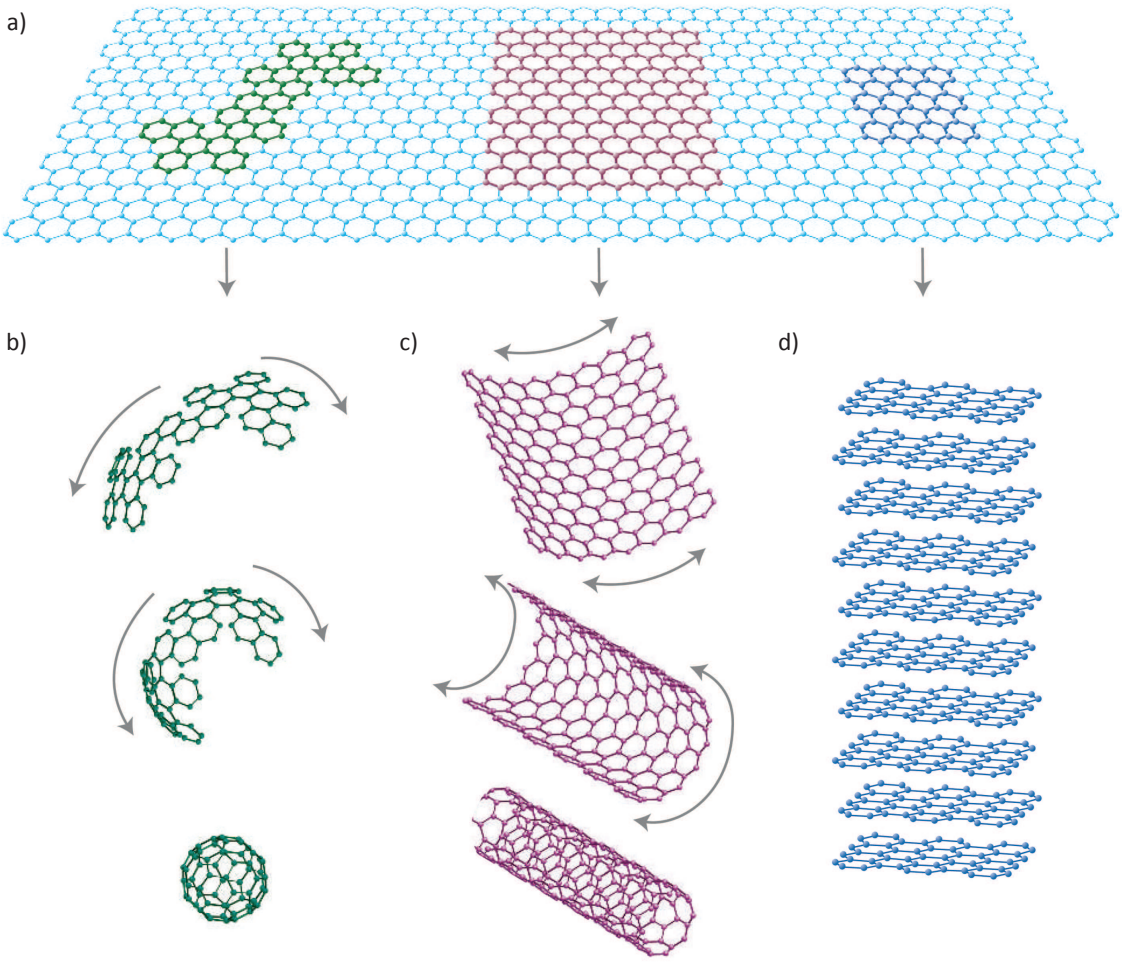

Figure 1.1: a) Graphene consists of carbon atoms forming a tightly packed honeycomb lattice and is the 2d building material for carbon materials of all other dimensionalities. It can be wrapped up into 0d fullerenes **(b)**, rolled into 1d nanotubes **(c)** or stacked into 3d graphite **(d)**. Image taken from ref. [Geim07].

by chemical vapor deposition [Land92, Kim09, Li09, Reina09], (3) epitaxial growth on silicon carbide [Berger04] and (4) liquid phase exfoliation [Hernandez08]. Furthermore, some transfer techniques exist [Dean10], *e.g.* by wet transfer of CVD grown graphene [Suk11] or by exfoliation on PDMS with further deposition on the target substrate [Martins13]. Graphene used in the work of this thesis requires high quality. Since graphene from a natural graphite source still has the best prerequisites, graphene from that source will be mechanically exfoliated by the scotch tape method.

Soon, researchers realized that, in spite of its exceptional characteristics, the electric properties of graphene were limited by an influence of the Si/SiO_2 substrate, on which graphene is usually deposited on. Indeed, supported graphene suffers from a substrate induced hole doping and an inhomogeneous charge carrier distribution, reducing the electron mobility in transport measurements [Casiraghi07b, Martin08, Xue11]. Hence, the suspension of graphene membranes (see figures 1.2a, b and c) allowed for a probing of electrical conductivity and mechanical strength a cleaner and more accurate way, and, in particular, led to an improvement of the electron mobility by more than one order of magnitude [Bolotin08b, Du08].

Suspended graphene has not only been used for transport measurements but soon has been identified as an ideal system for studying its mechanical properties, which is particularly appealing because graphene membranes are atomically thin and of ultralight weight. Soon after its first suspension (see figure 1.2a and ref. [Meyer07]), the pioneering work of Bunch *et al.* on pressurized graphene revealed its impermeability to standard gases and affirmed its strong adhesion to Si/SiO_2 substrates (see figures 1.2d, e and f) [Bunch07, Bunch08, Koenig11]. These additional outstanding characteristics give suspended graphene devices a high potential for high sensitivity sensors [Hill11, Chaste12]. Further studies examined the mechanical properties, *e.g.* of graphene balloons (see figure 1.2g and h) [Georgiou11] and the mechanical response of suspended membranes to a point pressure load (see figure 1.2i) [Lee08]. In addition, Newton rings have been observed on graphene balloons (see figure 1.2g) and suggest that, even if only 0.335 nm thin [Ni07], graphene is not fully transparent and optical interferences play an important role in suspended graphene.

All the works cited above, and thousands (!) of others, show that the electrical, optical and mechanical properties are well studied and understood. Hence, one can use these well defined properties and their modifications (due to external perturbations) in order to probe the intrinsic state of graphene and its interaction with the environment. For this purpose, an appropriate tool is Raman spectroscopy, which probes the electron-phonon coupling [Raman28, Ferrari06]. The latter is indeed sensitive to the charge carrier density [Pisana07, Stampfer07, Yan07, Berciaud09], mechanical strain [Mohiuddin09, Huang10, Lee12a], temperature [Calizo07, Chae09] and the crystalline quality [Lucchese10, Cancado11, Eckmann12] as well as to the number of layers [Ferrari07, Graf07, Malard09b, Ferrari13].

Notably, Raman spectroscopy allows for a fast and minimally invasive local *in situ* probing of doping and strain [Lee12a]. With changing number of charge carriers, the phonon energy and lifetime are renormalized due to electron-phonon interactions [Lazzeri06]. Mechanical strain changes the bond length in the crystal which impacts the phonon modes. This sensitivity is of great interest for characterization of suspended graphene membranes. This approach is in contrast to conventional measurement techniques such as AFM nano-indentation, which requires a more sophisticated experimental setup for *in situ* measurements of pressurized suspended graphene membranes.

Here comes into play the work of this thesis. The increasing interest of researchers in suspended graphene devices [Mizuno13, Reserbat-Plantey13, Castellanos-Gomez15, Sommer15] requires for a detailed understanding of both the strain and doping distribution in such devices. Suspended graphene membranes form a clean system, free from substrate influences, and both strain and doping might be finely tuned within a blister test and an electric field-effect geometry, respectively.

We show in this thesis that the blister test geometry allows for a controlled application of biaxial strain. A thorough Raman analysis of such graphene blisters permits to gain important information about the strain induced phonon mode shifts and the Grüneisen parameters, difficult to access in experiments on supported graphene. Furthermore, we take advantage of the device geometry, which acts as an optical cavity for Raman measurements, and interpret the interference induced modulation of the signal with varying pressure load. In that way, we show how one can deduce the membrane deflection and the Young's modulus of graphene in an elegant way.

Furthermore, we generalize this original method of the deflection determination and study in detail the electrostatically induced deflection of suspended graphene in a field-effect geometry. This issue is notably interesting because classical transport measurements does not allow for an *in situ* observation of the mechanical response [Bolotin08b], which might lead to an undesired collapse of the membrane. Within our work we highlight the great potential of Raman spectroscopy for such *in situ* studies, giving at the same time local information about both the gate-induced charge carrier densities and deflection-induced mechanical strain. In addition, we complete our consideration by providing a model which can serve as a guideline for improving the design of graphene-based resonators and can, in particular, estimate an unstable deflection regime in the vicinity of collapse.

Thus, our work contributes to a better understanding on the subtle interplay between doping and strain in suspended graphene devices. This issue is of notable importance, because strain in suspended graphene occurs not only when it is voluntarily induced by a pressure load application, but is present as *built-in* strain in as fabricated devices [Bao09, Metzger09, Chen09b]. The significance of this parameter will appear recurrently in the manuscript because it is found to influence

the mechanical response of the membranes, not only in static deflections, but also in graphene-based resonators, where pre-strain governs the resonance frequency [Bunch07, Chen09a].

Organisation of this work

This thesis manuscript is divided into eight chapters. Following the present introduction, in **chapter 2**, we introduce general properties of graphene, such as its atomic structure, its electronic bandstructure and phonon dispersion. A detailed knowledge of these properties is mandatory for a comprehension of the electron-phonon coupling in graphene, in particular for a correct interpretation of the observed Raman processes. We further highlight the interest in studying suspended graphene from the "transport point of view" and introduce a model based on the theory of elasticity, which describes the mechanical response of suspended graphene membranes to an external pressure load.

Chapter 3 presents Raman spectroscopy as a powerful tool to probe the electron-phonon coupling in graphene, which is sensitive to changes in the charge carrier density, the quality of the graphene and the strain. The strong electron-phonon coupling at certain points of the Brillouin zone is understood with the help of chapter 2.

In **chapter 4**, we shortly introduce the main sample fabrication techniques and present our confocal micro-Raman setup, allowing for measurements under ambient conditions, under vacuum and at cryogenic temperatures. We furthermore show how we acquire and process our data.

The core of this thesis is focused on suspended graphene membranes. In order to characterize suspended graphene devices in view of charge carrier densities and built-in strain, we take advantage of the knowledge on Raman spectroscopy, which we have laid as as a basis in the previous chapters. Hence, in **chapter 5**, we focus on a statistical analysis of spatially resolved Raman maps and deduce sample dependent average values of built-in strain. Furthermore, the results allow for a spatial resolution of strain down to the sub-micrometer scale within one suspended membrane.

In **chapter 6**, we take advantage of the extremely low doping level in suspended graphene (which we have demonstrated in chapter 5), and study the Raman spectra of a pressurized graphene blister, subjected to pure biaxial strain. A careful analysis of both the change in the intensities and the frequencies of the main Raman features allows for a deep insight in the mechanical response of graphene membranes to an external pressure load. Interestingly, we show that we are able to extract important mechanical parameters, such as the Grüneisen parameters and the Young's modulus of graphene by solely optical means.

In contrast to the previous chapter, where the graphene membranes have been pressurized by the application of a gas pressure difference, in **chapter 7** we apply a backgate voltage to suspended

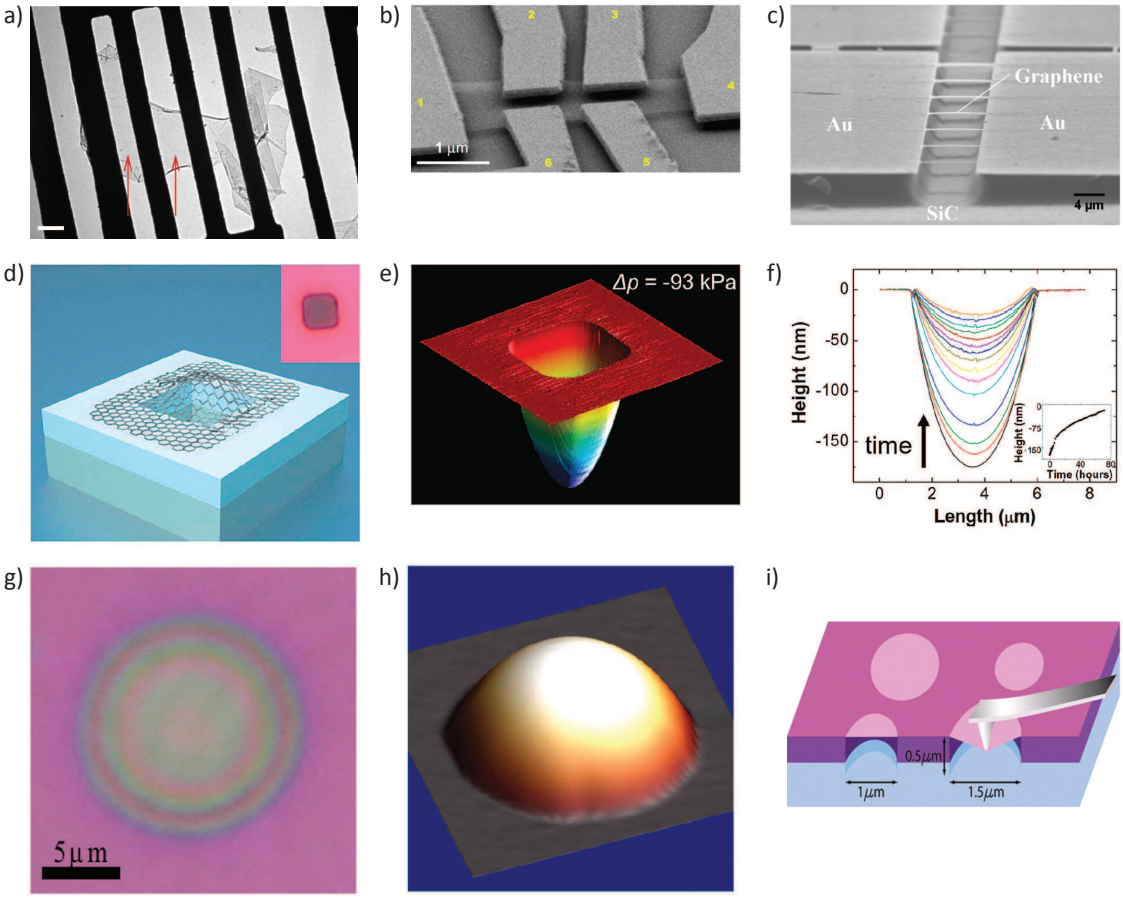

Figure 1.2: Overview of suspended graphene samples. **a)** Bright-field transmission electron microscope (TEM) image of a suspended graphene membrane. Its central part (homogeneous and featureless region indicated by arrows) is monolayer graphene. Such devices allowed for electron diffraction imaging showing single crystal without domains. The scale bar is 500 nm. Image taken from ref. [Meyer07]. **b)** Scanning electron microscope (SEM) image of a suspended graphene device with six metal contacts. The image is taken at 15° with respect to the sample plane. The sample underwent wet etching processes and were current annealed, before showing a strong increase of the electron mobility. Image taken from ref. [Bolotin08b]. **c)** SEM image of suspended epitaxial graphene, showing an array of doubly clamped (by gold pads) graphene beams of $8\,\mu$m length and widths ranging from 0.5 to $3.5\,\mu$m. Wet etching is involved in the fabrication process. Image taken from ref. [Shivaraman09]. **d)** Sketch of a mechanically exfoliated graphene sealed microchamber (*Inset:* optical image of a single atomic layer graphene drumhead on 440 nm of SiO_2). The dimensions of the microchamber are $4.75\,\mu\text{m}\times 4.75\,\mu\text{m}\times 380$ nm. **e)** AFM image of the graphene sealed microchamber of (d) with a pressure difference $\Delta p = -93$ kPa across it. The minimum dip in the z-direction is 175 nm. **f)** AFM line traces taken through the center of the graphene membrane of (d). The images were taken continuously over a time span lasting until relaxation (see inset), revealing the impermeability of graphene. (d)-(f) are taken from ref. [Bunch08]. **g)** Optical micrograph under white light of a graphene bubble deposited on silicon. Newton rings are visible. **h)** $3\,\mu\text{m}\times 3\,\mu$m topography AFM scan of a bubble. (g) and (i) are taken from ref. [Georgiou11]. **i)** Sketch of a nano-indentation measurement with an atomic force microscope (AFM) tip. Image taken from ref. [Lee08].

graphene membranes. This gating has two effects: Charge carriers are added to the membrane and the electrostatic pressure induces a deflection, which eventually leads to an unstable behavior of the membrane and makes it collapse. We present an advanced analysis of the deflection, based on a model of theory of elasticity, and finally analyze the regime of unstable deflections for a variety of device geometries.

In **chapter 8**, we conclude about our work and show that our findings will stimulate future work on graphene and other 2d material based micrometer-sized opto-mechanical systems.

The **Appendix** contains additional data, which are not shown in the main manuscript, but to which we refer.

2 General theoretical background on graphene

In this first chapter we introduce the basic characteristics of graphene. We outline its exceptional properties which are derived from the crystalline structure of graphene, such as its band structure and related high electron mobility. Furthermore, we focus on the vibrational properties, both in monolayer and few layer graphene. Finally, we account for studying suspended graphene, decoupled from the substrate, and include some aspects of theory of elasticity in order to know the mechanical response of these membranes when they are subjected to a pressure load.

2.1 Atomic structure

The name graphene was introduced by Boehm *et al.* in 1994 [Boehm62, Boehm94] to designate a single layer of carbon atoms tightly packed into a two-dimensional honeycomb crystal lattice. The designation *graphene* is a composition of *graph*-ite, whose building-block it is, and benz-*ene*, referring to the carbon rings found again in benzene molecules. From a crystallographic point of view, not all the carbon atoms are equivalent. Two types of atoms can be identified. As shown in figure 2.1a, the atoms labeled A (blue circle) have their nearest neighbors at $0°$, $120°$ and $240°$, which are labeled B (yellow circle), whereas the atoms B have their nearest neighbors (atoms A) at $60°$, $180°$ and $360°$. Thus, the graphene lattice can be seen as a triangular lattice with a basis of two atoms A and B.

The distance between two neighboring atoms A and B is $a = 1.42\,\text{Å}$, which corresponds roughly to the mean value of the simple ($a = 1.54\,\text{Å}$) and a double ($a = 1.34\,\text{Å}$) carbon-carbon bond length, as it is the case for benzene [Fox95]. The basis vectors of the elementary cell are $\boldsymbol{a}_1 = \frac{a}{2}(3, \sqrt{3})$ and $\boldsymbol{a}_2 = \frac{a}{2}(3, -\sqrt{3})$. The three vectors connecting an atom B to its nearest neighbors A are $\boldsymbol{\delta}_1 = \frac{a}{2}(1, \sqrt{3})$, $\boldsymbol{\delta}_2 = \frac{a}{2}(1, -\sqrt{3})$ and $\boldsymbol{\delta}_3 = -a(1, 0)$ (see figure 2.1a). The basis vectors of the reciprocal lattice in momentum space are $\boldsymbol{b}_1 = \frac{2\pi}{3a}(1, \sqrt{3})$ and $\boldsymbol{b}_2 = \frac{2\pi}{3a}(1, -\sqrt{3})$. The first Brillouin zone is characterized by four high symmetry points, indicated by black points

in figure 2.1b and labeled Γ, M, K and K'. We note that, in particular, the two points K and K' are not equivalent, which means that they cannot be connected one to another by a reciprocal lattice vector[1]. K and K' play an important role for the physics of graphene, for reasons pointed out later. Their positions in momentum space are given by the vectors $\boldsymbol{K} = \left(\frac{2\pi}{3a}, \frac{2\pi}{3a\sqrt{3}}\right)$ and $\boldsymbol{K'} = \left(\frac{2\pi}{3a}, -\frac{2\pi}{3a\sqrt{3}}\right)$ [Castro Neto09].

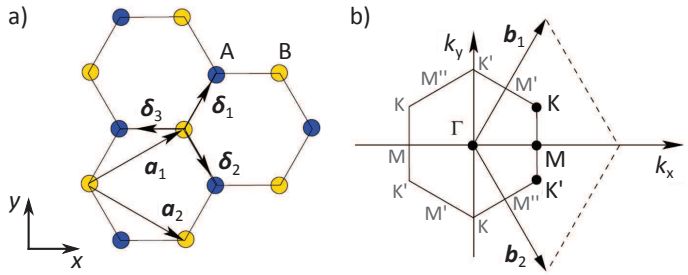

Figure 2.1: a) Honeycomb lattice structure of graphene, composed of a triangular lattice with a basis of two inequivalent carbon atoms, A and B. The basis vectors $\boldsymbol{a}_1$ and $\boldsymbol{a}_2$ span the unit cell and the vectors $\boldsymbol{\delta}_1$, $\boldsymbol{\delta}_2$ and $\boldsymbol{\delta}_3$ connect an atom B to its three nearest neighbors A. **b)** First Brillouion zone with the basis vectors $\boldsymbol{b}_1$ and $\boldsymbol{b}_2$ of the reciprocal space. High symmetry points are indicated with a black circle and labeled Γ, M, K and K'. Figure adapted from ref. [Castro Neto09].

2.2 Electronic properties

In its neutral state, each carbon atom possesses six electrons. Its electronic configuration is $1s^2 2s^2 1p^2$. The two 1s electron orbitals are located in the vicinity of the atomic nucleus and are not involved in chemical bonding or reactions. On the contrary, in graphene, the $2s^2 1p^2$ electron orbitals hybridize, *i.e.* the 2s, $2p_x$ and $2p_y$ mix and form three hybrid orbitals labeled sp2, which are separated by an angle of $120°$ in the *xy*-plane. The orbital $2p_z$ is perpendicular to that plane. The interaction (of the atomic orbitals) with the neighboring carbon atoms gives rise to molecular orbitals, which are denoted σ and σ^* in the *xy*-plane and π and π^* perpendicular to that plane. These orbitals are called bonding and anti-bonding, respectively. The bonding orbitals are energetically more favorable and are thus occupied by the eight electrons of the two carbon atoms in the elementary cell. In consequence, the π^* and σ^* orbitals are empty.

Going from the picture of individual carbon atoms to the whole graphene lattice, the molecular orbitals become bands. Energetically, the π (and π^*) bands are situated close to the Fermi level whereas the σ (and σ^*) bands are further away and well separated by an energy of more

[1] In fact, all corners of the Brillouin zone and the points in the middle of the line connecting these corners are high symmetry points. In particular, the intersections of $\boldsymbol{b}_1$ and $\boldsymbol{b}_2$ with the Brillouin zone border, labeled M' and M'', are not equivalent to M. However, a reciprocal vector can be found to connect the remaining four corners of the Brillouin zone, so that only K and K' are not equivalent at the corners [Fuchs08].

than 10 eV [Thomsen04]. Thus, in experiments below this energy range, it is sufficient to consider only electrons in the π (and π^*) bands.

2.2.1 Band structure

Since the structure of the electronic bands determines the electrical and optical properties of the material, it is important to have knowledge about it. The first calculation of the π and π^* bands in graphite materials has been performed by Wallace in 1947 by using a tight binding model [Wallace47]. In 2002, Reich *et al.* conducted refined calculations using the same model for graphene and carbon nanotubes [Reich02]. In this model, the electrons can hop from one atom to its three nearest neighbors (non equivalent atoms) with an energy cost τ of ≈ 2.7 eV and to its six next nearest neighbors (equivalent atoms) with an energy cost τ', where $0.02\tau \lesssim \tau' \lesssim 0.2\tau$ [Reich02, Deacon07, Castro Neto09]. The tight binding Hamiltonian taking into account nearest neighbor and next nearest neighbor hopping writes as

$$\mathcal{H} = -\tau \sum_{\langle i,j\rangle,s} \left(a^\dagger_{s,i} b_{s,j} + \text{h.c.}\right) - \tau' \sum_{\langle\langle i,j\rangle\rangle,s} \left(a^\dagger_{s,i} a_{s,j} + b^\dagger_{s,i} b_{s,j} + \text{h.c.}\right) \tag{2.1}$$

where $a_{i,s}$ ($a^\dagger_{i,s}$) annihilates (creates) an electron with spin s ($s = \uparrow, \downarrow$) on the site $\boldsymbol{R}_i$ on the sublattice A [an equivalent definition is used for sublattice B with $b_{i,s}$ ($b^\dagger_{i,s}$)].

The energy bands derived from this Hamiltonian are [Wallace47]

$$E_\pm(\boldsymbol{k}) = \pm\tau\sqrt{3 + f(\boldsymbol{k})} - \tau' f(\boldsymbol{k}), \tag{2.2}$$

with

$$f(\boldsymbol{k}) = 2\cos\left(\sqrt{3}k_\text{y}a\right) + 4\cos\left(\frac{\sqrt{3}}{2}k_\text{y}a\right)\cos\left(\frac{3}{2}k_\text{x}a\right), \tag{2.3}$$

where $\boldsymbol{k}$ is the wave vector of an electron and the plus (minus) sign applies to the upper π^* (lower π) band. Since equation (2.3) contains only cosine-terms, it is mirror symmetric with respect to the k_x-k_y-plane at $E = 0$, if one sets $\tau' = 0$. Taking into account the next nearest neighbor hopping ($\tau' \neq 0$), the corresponding electronic dispersion is shown in figure 2.2a.

In this figure, one distinguishes well the π and π^* bands. Since each carbon atom contributes with one π electron and each electron may occupy either a spin-up or a spin-down state, the lower π band is completely filled (valence band) and the upper π^* is completely empty (conduction band) [Fuchs08]. Thus, the Fermi level is situated at the points where the π and π^* bands touch,

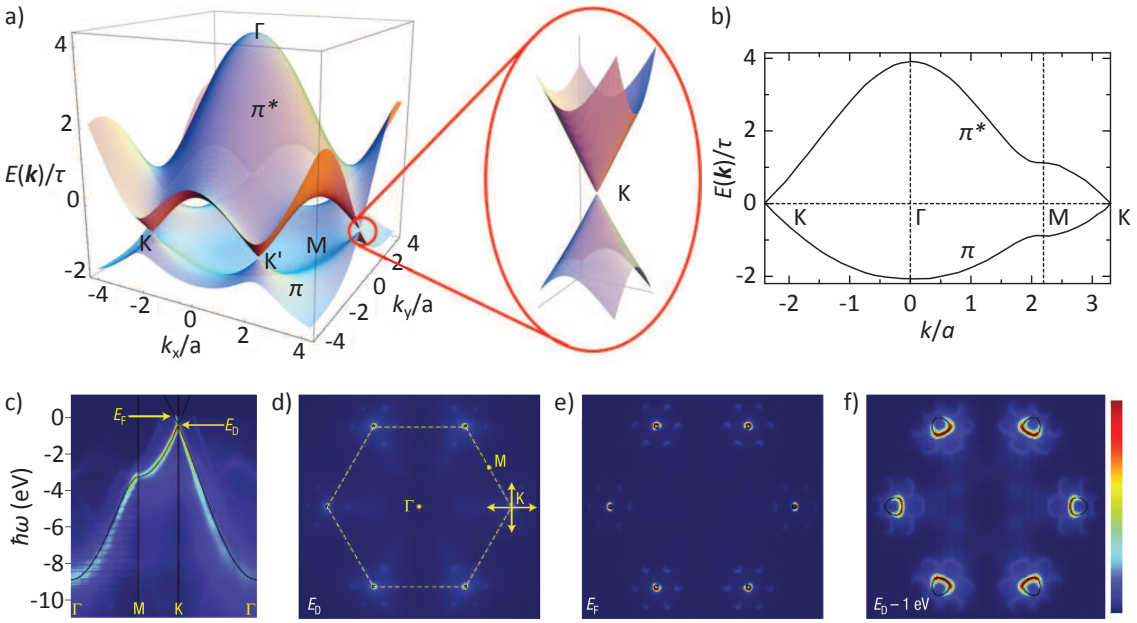

Figure 2.2: a) Energy dispersion of electrons in graphene obtained within the tight-binding model, for $\tau = 2.7$ eV and $\tau' = -0.2\tau$. The energy dispersion is plotted in units of τ as a function of the wave-vector components k_x and k_y in units of a. The valence (π) and conduction (π^*) bands are well separated. The Fermi level is situated at the points where the π and π^* bands touch. A zoom of the energy dispersion near to the K point is shown on the right. Figure adapted from ref. [Castro Neto09]. **b)** Cut through the energy dispersion along characteric lines, connecting the points K $\rightarrow \Gamma \rightarrow$ M $\rightarrow$ K. Figure adapted from ref. [Fuchs08]. **c)** Experimental energy distribution of states as a function of momentum along the principle directions $\Gamma \rightarrow$ M $\rightarrow$ K $\rightarrow \Gamma$. **d)**, **e)** and **f)** Constant energy maps of the electronic states for $E = 0$, $E = -0.45$ eV and $E = -1.45$ eV, respectively, with respect to neutral graphene. In the figures, the data were obtained on initially electron-doped graphene on SiC, a common feature for this substrate [Varchon07], and are represented with respect to this initial doping (with a Fermi level at ≈ 0.45 eV within the π^* band). Figures adapted from ref. [Bostwick07].

i.e. at[2] $E = 0$. These points correspond to the K and K' points introduced previously[3]. In the vicinity of these points, the energy dispersion has a cone shape, which is represented in the zoom of figure 2.2a. This feature will be discussed in detail in the following subsection. Nevertheless, we note already that the fact that next nearest neighbor hopping is taken into account cancels the electron hole symmetry when higher energies are involved. Furthermore, the cone in the zoom will be deformed by the saddle points at M, this feature is called trigonal warping. In figure 2.2b cuts along characteristic lines are shown, connecting the points K $\rightarrow \Gamma \rightarrow$ M $\rightarrow$ K. One sees that next to the Fermi level, only the K (K') points are contributing to the electron (or hole) conduction. In particular, in the case of neutral graphene, no conduction electrons are available, because the π bands are filled and the π^* bands are empty. Hence, graphene is a semi-metal, or a semiconductor with zero band gap.

Experimentally, the dispersion relation of graphene can be determined by angle resolved photo-emission spectroscopy (ARPES). In such a measurement, one takes advantage of the energy and momentum conservation in an electron-photon scattering process. The measurement consists of the detection of the direction and energy of a photo-emitted electron, which previously has been excited by a photon of well defined energy and momentum. The angle dependence of the photo-emitted electron yields precisely the momentum dependence of the energy and thus the dispersion relation, as we show in figures 2.2c-f in the case of epitaxially grown graphene. Here, Bostwick *et al.* measured the energy distribution as a function of momentum along the characteristic lines $\Gamma \rightarrow$ M $\rightarrow$ K $\rightarrow \Gamma$ and plotted color maps of the states at different energies [Bostwick07]. Figure 2.2d shows a color map for neutral graphene, indicating the confinement of the electronic states near the K and K' points, whereas in figures 2.2e and f, energies of -0.45 and -1.45 eV are scanned, indicating the cone like character of the energy dispersion and the effect of trigonal warping for higher energies, respectively.

2.2.2 Band structure in the vicinity of the Dirac point

In the range of low energy, *i.e.* energies smaller than τ ($= 2.7$ eV), only the electronic states with wave vectors $\boldsymbol{k}$ next to the K and K' points are allowed. Mathematically, this conditions writes as $\boldsymbol{k} = \boldsymbol{K}^{(\prime)} + \boldsymbol{q}$ with $|\boldsymbol{q}| \ll |\boldsymbol{K}^{(\prime)}|$, or, as $|\boldsymbol{K}^{(\prime)}|$ is proportional to $1/a$, one can write $|\boldsymbol{q}|a \ll 1$.

[2] We note that this is an arbitrary choice, the energies are always defined with respect to a constant. We note also, that this simplified picture is only valid at $T = 0$ (without thermal energy broadening).

[3] We note that there is a conceptual difference between the K and K' points which one could define as the points where the π and π^* touch and the K and K' points defined by the pure crystallographic considerations. The touching points can, in principle, move away from the K and K' points, if τ is anisotropic [Hasegawa06, Dietl08]. However, in natural graphene, these touching points are situated at the Brillouin zone corners and the notation K and K' points can be used for the touching bands [Fuchs08].

Electronic dispersion relation

Let us first set $\tau' = 0$. Corrections taking into account $\tau' \neq 0$ will be discussed later. Under these conditions, the cosines in equation (2.3) can be rewritten according to the relation $\cos(a+b) = \cos(a)\cos(b) - \sin(a)\sin(b)$ and then series expanded up to orders of $|\boldsymbol{q}|^2 a^2$ (the linear terms cancel out). With equation (2.2), the approximated energy dispersion then writes as

$$E_{\pm}(\boldsymbol{q}) = \pm\frac{3}{2}\tau|\boldsymbol{q}|a. \tag{2.4}$$

This equation strongly reminds the energy-momentum relation $E = \hbar|\boldsymbol{k}|c_0$ of photons, *i.e.* particles without mass. Defining v_F as $v_\mathsf{F} = 3\tau a/(2\hbar)$, equation (2.4) takes the form

$$E_{\pm}(\boldsymbol{q}) = \pm\hbar|\boldsymbol{q}|v_\mathsf{F}. \tag{2.5}$$

Here, v_F takes the role of a velocity (Fermi velocity) and is approximately equal to 1×10^6 m/s. If one considers the general relativistic energy dispersion, $E(|\boldsymbol{q}|) = \pm\sqrt{\hbar^2|\boldsymbol{q}|^2c^{*2} + m^{*2}c^{*4}}$, an effective mass of $m^* = 0$ can be attributed to the electrons, which results in an effective speed of light, c^*, which here is equal to the Fermi velocity v_F. We note that, however, the electrons in graphene are not relativistic in the sense that their velocity is approximately 300 times smaller than that of light, but they are nevertheless often called *massless Dirac fermions* because they obey the Dirac equation [Castro Neto09].

Taking into account a finite value of τ', the energy dispersion is affected by some corrections (again up to the second order of $|\boldsymbol{q}|a$) and writes as

$$E_{\pm}(\boldsymbol{q}) = \pm\hbar|\boldsymbol{q}|v_\mathsf{F} + 3\tau' - \left[\frac{9\tau' a^2}{4} \pm \frac{3\tau a^2}{8}\sin\left(3\theta_{\boldsymbol{q}}\right)\right]|\boldsymbol{q}|^2 \tag{2.6}$$

with $\theta_{\boldsymbol{q}} = \arctan(\mathsf{q_x}/\mathsf{q_y})$. Hence, the presence of τ' shifts the position of the Dirac point and breaks the electron-hole symmetry [Castro Neto09] (see also figure 2.2). Furthermore, for higher energies, the dispersion dependence on the direction in momentum space plays an increasing role. This threefold symmetry is called, as already mentioned above, trigonal warping [Ando98, Dresselhaus02] and can be identified in the ARPES measurements shown in figure 2.2f.

Density of states

Both with finite and zero τ', the density of states shows semi-metallic behavior [Wallace47, Bena05]. In order to describe phenomena occurring in relation with the electron (or hole) density, the density of states per surface area, $g(E)$, has to be known. Hobson and Nierenberg derived an analytical expression for the case $\tau' = 0$ [Hobson53]. In the vicinity of the Dirac point ($|\boldsymbol{q}|a \ll 1$), the density of states can be approximated by

$$g(E) = \frac{2E}{\pi(\hbar v_F)^2}. \tag{2.7}$$

Here is taken into account the spin degeneracy and the so called valley degeneracy (which is nothing else than the fact that an electron can occupy two distinct states in momentum space, namely $\boldsymbol{K}$ and $\boldsymbol{K'}$, at the Fermi level). Considering a finite τ' leads to corrections, which are presented in figure 2.3. The density of states $g(E)$ is plotted as a function of E/τ for the case of $\tau' = 0.2\tau$ (a and b) and $\tau' = 0$ (c and d). In particular, one can see that $g(E)$ scales linear with E next to the Dirac point, and that the density of states vanishes at one point. One can also see that, due to the next nearest neighbor hopping, this linearity is slightly different for electron and hole doping. The canceling of electron-hole symmetry is more striking at higher energies, where van Hove singularities dominate the density of states.

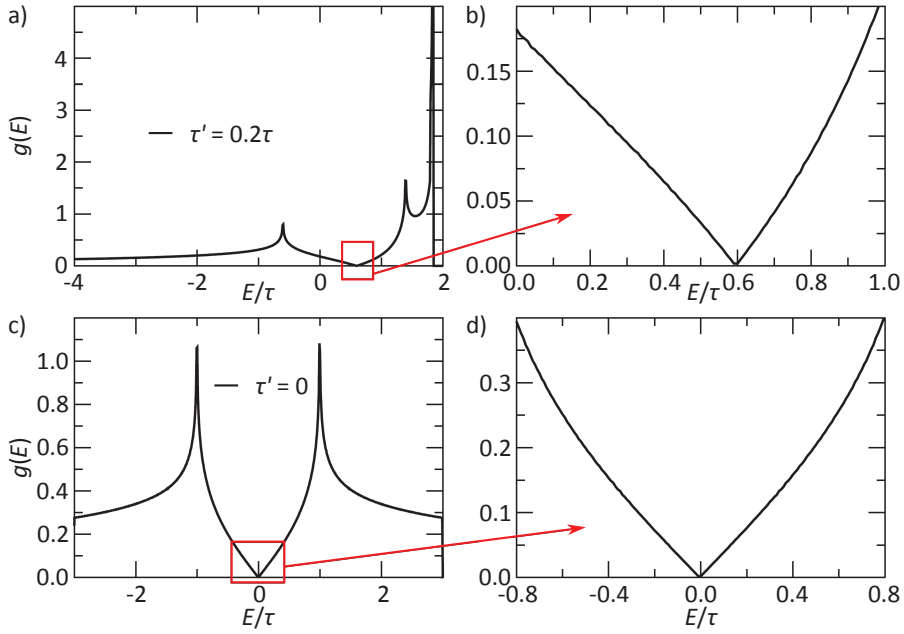

Figure 2.3: a) and **b)** Density of states computed from the energy dispersion in equation (2.2), for the case of $\tau' = 0.2\tau$. (b) is a zoom in of figure (a), close to the neutrality point. **c)** and **d)** Density states for the case of $\tau' = 0$. Figure adapted from ref. [Castro Neto09].

The fact that the density of states vanishes linearly at the Dirac points is a direct consequence of the linearity of the energy dispersion in the vicinity of the Dirac points. This particular characteristic is in contrast to the conventional case of a two dimensional (2d) electron gas in metals or semiconductors, where $E \propto k^2$ and $g^{2d}(E) = \text{const}$. In table 2.1, we compare the density of states as a function of the energy for different dimensionalities and dispersion relations, in particular for a linear (*e.g.* graphene) and a parabolic (*e.g.* free electron gas) dispersion relation.

	1d	2d	3d
linear disp. rel. ($E \propto k$)	$g^{1d}(E) = \text{const.}$	$g^{2d}(E) \propto E$	$g^{3d}(E) \propto E^2$
parabolic disp. rel. ($E \propto k^2$)	$g^{1d}(E) \propto 1/\sqrt{E}$	$g^{2d}(E) = \text{const.}$	$g^{3d}(E) \propto \sqrt{E}$

Table 2.1: Relation between the dimensionality d of the system, the dispersion relating the momentum with wavevector k to the energy E and the density of states $g(E)$.

In this context, let us mention two carbon based systems closely related to graphene, but showing different density of states. First, in bilayer graphene, the energy dispersion is parabolic which leads to a constant density of states of this 2d material. Second, in metallic single walled carbon nanotubes, which is quasi 1d, the energy dispersion is also constant [Thomsen04]. This fact underlines the interest in studying monolayer graphene with its unique linear dispersion relation.

2.2.3 Tuning of the electronic properties by field effect

Due to the zero density of states at the Dirac points, the electronic conductivity of neutral graphene is quite low. However, the conductivity can be changed by tuning the Fermi level, *i.e.* by adding or removing electrons from the neutral graphene. The first is electron doping whereas the latter, due to the absence of electrons, is called hole doping. Doping allows then for potentially better electrical conductivity than, *e.g.*, copper at room temperature.

The charge carrier density is calculated by integrating the product of the density of available states per surface in the conduction band, $g(E)$, and of the Fermi-Dirac probability function, $f(E) = \left[e^{(E-E_F)/k_B T} + 1\right]^{-1}$ [Ashcroft75]:

$$n_e = \int_0^{+\infty} g(E)\, f(E)\, \mathrm{d}E \qquad \text{and} \qquad n_h = \int_0^{+\infty} g(E)\, [1 - f(E)]\, \mathrm{d}E \tag{2.8}$$

for electrons and holes, respectively. At $T = 0$, the Fermi-Dirac probability function is 1 in every energy slice $\mathrm{d}E$ and one can directly see that in the case of graphene, $n \propto E^2$, in contrast to the conventional case of 2d electron gases in metals or semiconductors, where $n \propto E$.

In practice, charge carriers are usually added to graphene within a field effect geometry, *i.e.* an external electric field is applied by means of a potential difference between the graphene and a gate electrode, separated by a dielectric non-conducting layer. In that case, the charge carrier density n is proportional to the applied potential difference, *i.e.* a gate voltage V_g and depends on the geometrical capacitance (per surface) of the separating layer, c. n then write as $n = cV_g$. A common practice is the use of highly doped silicon with a silicon oxide layer as dielectric spacer, because of its abundance and good conductivity properties as well as of its relatively cheap, easy and well established production process. Furthermore, the use of Si/SiO_2 substrates offers an

easy identification of graphene monolayers by means of optical microscopy and has still other advantages, as will be discussed in detail in section 3.5. In figure 2.4a we show a sketch of such a measurement geometry.

The electric field effect has first been observed on few layer graphene in 2004 by Novoselov *et al.* and soon later on one layer graphene [Novoselov04, Novoselov05a, Zhang05]. Figure 2.4b shows the electric field effect on the source drain resistivity (see also figure 2.4a), measured on a monolayer graphene on a Si/SiO_2 substrate. Positive (negative) V_g induces electrons (holes) with a charge carrier concentration proportional to V_g. Thus, the decreasing resistivity ρ indicates a strong mobility μ of the charge carriers, because it is connected via $\mu = (ne\rho)^{-1}$ to the resistivity. Here, a value of $\mu \approx 5000\,\mathrm{cm^2V^{-1}s^{-1}}$ is attained, which is commonly the case for graphene deposited on Si/SiO_2 [Geim07, Bolotin08b].

We note that other techniques exist to change the Fermi level in graphene, *e.g.* by introducing charge carriers by adding impurities (chemical doping) [Liu11], or by an electric field effect created by an ion gel deposited directly on the graphene, called electrochemical top-gating (in contrast to silicon bottom-gating) capable to dope graphene in a more efficient way [Lu04, Das08, Wang10b, Froehlicher15a].

Furthermore, even if charge carriers can be added efficiently to graphene, a non-negligible disadvantage compared to silicon based transistors persists: the difference between the states of conductivity, called on/off ratio, is not very high, which acts on the energy consumption and the reliability of such electronic devices. In particular, even in ultraclean devices, the current cannot be turned off completely, because even in the limit of vanishing n, a minimum conductivity persists. This conductivity is an intrinsic property of the 2d Dirac electrons and its value is $\sigma_\mathrm{min} = e^2/(4\hbar)$ [Ando02, Peres06, Mak08, Tombros11, Mak12]. In experiments, this value is not observed because charged impurity scattering and residual charge density induced by the inhomogeneous charge distribution in the samples limit the conductivity [Tan07].

However, reducing the lateral size of graphene to a few nanometers leads to a band gap opening at the Dirac point, allowing for a higher on/off ratio, suitable for electronic devices [Han07, Wang08b].

Nevertheless, due to its extraordinary optical and mechanical properties, graphene remains an interesting candidate for, *e.g.*, flexible and transparent electrodes, as will be exposed later in the manuscript.

2.2.4 Substrate influences and the interest of suspended graphene

Factors limiting the detailed study of graphene in the vicinity of the Dirac points, and, for applications, limiting the charge carrier mobility are the quality of the graphene and, in particular, the interaction of graphene with the underlying substrate, *e.g.* Si/SiO_2. Actually, the initial dop-

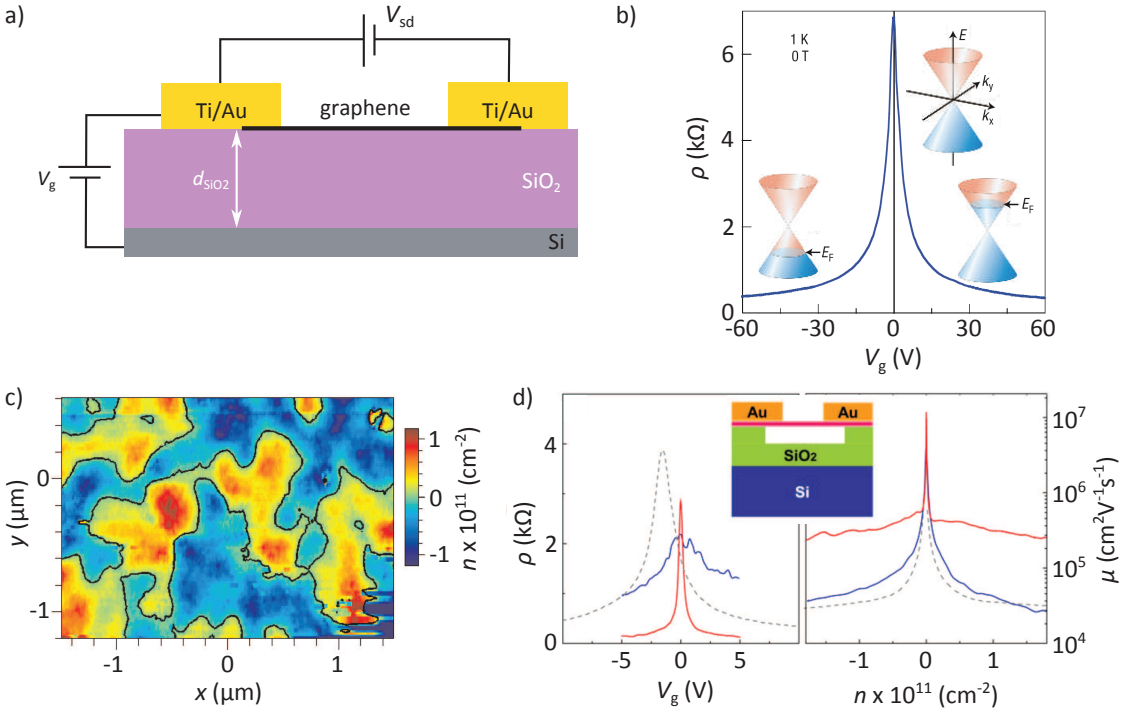

Figure 2.4: a) Scheme of graphene in a typical field effect geometry. The gate voltage V_g permits to tune the charge carrier density n in the graphene, which is contacted by titanium and gold. Additionally, a source-drain voltage, V_{sd}, can be applied to the graphene in order to measure its resistivity. The underlying SiO_2 layer serves as dielectric spacer layer. **b)** Electric field effect in graphene at $T = 1$ K. The insets show the conical low energy dispersion with changing V_g. Positive (negative) V_g induces electrons (holes) with a charge carrier concentrations $n = cV_g$ where $c \approx 7.2 \times 10^{10}\,\mathrm{cm^{-2}V^{-1}}$ for field effect devices with $d_{SiO_2} = 300$ nm. The rapid decrease in resistivity ρ indicates their high mobility and does not notably change with temperatures up to 300 K. Figure adapted from ref. [Geim07]. **c)** Spatial charge density fluctuations showing electron/hole puddles on a graphene flake deposited on Si/SiO_2. The data in the color map has been extracted from surface potential measurements by STM. The black contour marks the zero density contour. Figure adapted from ref. [Martin08]. **d)** Measured resistivity ρ (in a four probe geometry) as a function of gate voltage V_g for a suspended graphene device before (blue) and after (red) current annealing; data from a high-mobility device on the Si/SiO_2 substrate (grey dashed line) is shown for comparison. The gate voltage is limited to ± 5 V range to avoid mechanical collapse. $T = 5$ K. The inset shows the device geometry of the suspended sample. Figure adapted from ref. [Bolotin08b].

ing level in deposited graphene depends strongly on the substrate [Wang08d, Shi09, Lafkioti10, Goncher13] and is known to be generally hole-doped on SiO_2 [Ryu10]. In addition, the charge is not homogeneously distributed over the surface but forms kind of puddles on the sub-micrometer scale, as can be seen on the scanning tunneling microscopy (STM) image in figure 2.4c [Martin08, Martin15]. Charge puddles varying from -1×10^{12} to $+1 \times 10^{12}\,\mathrm{cm}^{-2}$ have been observed [Xue11]. The exact charge distribution on supported graphene depends strongly on the fabrication method, but clean and intrinsic graphene is only obtained when it is decoupled from the substrate either by adding an inert atomically flat layer [like boron nitride (BN)] [Dean10, Xue11, Forster13] or by suspending it [Meyer07, Frank07, Bolotin08b, Berciaud09, Ni09].

In figure 2.4d we show a comparison of resistivity measurements on supported graphene (grey dashed line) and on suspended graphene before (blue line) and after (red line) current-induced heating. The latter has been applied in order to clean the graphene, which has been in contact with resist and organic solvents. Thus, clean suspended graphene directly results in a significant improvement of the electrical transport properties. Bolotin *et al.* achieved charge carrier mobilities of more than $200\,000\,\mathrm{cm}^2\mathrm{V}^{-1}\mathrm{s}^{-1}$ at $4\,\mathrm{K}$, which is an improvement by a factor 10 compared to typical values measured on graphene deposited on Si/SiO_2. A study of the temperature dependence on the mobility reveals that charge density inhomogeneity and flexural phonons limit the mobility [Bolotin08a, Castro10].

2.3 Optical properties

Apart from its exceptional conductivity properties, graphene possesses interesting optical properties, which are also closely related to the Dirac-like character of the electrons. In order to get an understanding of how light interacts with graphene, we first have to make clear which processes might occur. When light impinges a material, part of it is either reflected ($\mathcal{R}$), absorbed ($\mathcal{A}$) or transmitted ($\mathcal{T}$). Energy conservation requires $\mathcal{R} + \mathcal{A} + \mathcal{T} = 1$. In graphene, $\mathcal{R}$ is smaller than $0.1\,\%$ and can be neglected in comparison to $\mathcal{A}$ and $\mathcal{T}$ [Bonaccorso10]. The absorption coefficient $\alpha_{\mathrm{abs}}(\omega)$, which depends on the photon energy, relates the initial intensity of the light, I_0, to the transmitted intensity after a certain distance z, $I(z)$, via an exponential decay [Lambert60]:

$$I(z) = I_0 e^{-\alpha_{\mathrm{abs}}(\omega) z}. \tag{2.9}$$

The absorption coefficient is, in turn, related to imaginary part of the refractive index of the material. If one writes the refractive index as $\tilde{n}(\omega) = n(\omega) + i\kappa(\omega)$, it is

$$\alpha_{\mathrm{abs}}(\omega) = \frac{2\omega\kappa(\omega)}{c_0}. \tag{2.10}$$

Thus, to get an expression of $\mathcal{A}$, it is sufficient to determine $\kappa(\omega)$.

On the other hand, the square of the complex refractive index is nothing else but the the dielectric constant $\varepsilon(\omega)$ [Dresselhaus, accessed on 12th of November 2015]. In turn, the dielectric constant determines the optical properties of a solid by means of the conductivity $\sigma(\omega)$ of the material [Ashcroft75, Appendix K, page 776]:

$$\varepsilon(\omega) = n^2(\omega) = \varepsilon^0(\omega) + \frac{4\pi i\sigma(\omega)}{\omega}. \tag{2.11}$$

In general, one is free to redefine the arbitrary function of frequency $\varepsilon^0(\omega)$ [Ashcroft75], and following Ziegler *et al.*, we put it to 1 [Ziegler14, page 11]. In solids, one has to consider contributions from intraband and interband processes to the optical properties. The first are processes which correspond to the electronic conduction by free charge carriers, thus, this is the governing process in metals. These intraband processes can be understood in their simplest terms by the classical Drude theory [Dresselhaus], giving rise to the complex Drude conductivity σ_{D}. In addition to this free carrier processes, there are interband processes which correspond to the absorption of electromagnetic radiation by an electron in an occupied state below the Fermi level, thereby inducing a transition to an unoccupied state in a higher band (see the scheme in figure 2.5). This interband process is intrinsically a quantum mechanical process and has to be described in terms of quantum mechanical concepts. Usually, the presence of an energy gap between the bands requires a threshold energy, but this energy is not necessary in graphene since the bands touch an the K points. The transitions then depend on the coupling between the valence (π) and conduction (π^*) bands, and the magnitude of these transitions is determined by the momentum matrix elements coupling the π states to the π^* state [Dresselhaus].

Let us consider an incident photon with energy $\hbar\omega$ as a perturbation. The corresponding interaction Hamiltonian connecting the initial state in the π band and the final state in the π^* band can be inserted in Fermi's Golden rule in order to obtain the interband current density [Dresselhaus, Nair08a]. The result of this calculation is a value of $\sigma_{\mathsf{i}} = e^2/(4\hbar)$ [Kuzmenko08, Mak08, Nair08a], which corresponds to the minimum conduction value mentioned in subsection 2.2.4. Interestingly, this value does not depend on the photon energy, because within the factors in the product of Fermi's Golden rule, the ω-dependence cancels out (the matrix element is $\propto \omega^{-2}$, the density of states $\propto \omega$ and the energy of the incident photon $\propto \omega$). Or, in other words, the graphene Hamiltonian describing the linear bands has no intrinsic energy scale with which the photon energy can be compared.

Summing both intra- and interband contributions, the square of the refractive index writes as

$$n^2(\omega) = 1 + \frac{4\pi i}{\omega}\left[\sigma_{\mathsf{D}}(\omega) + \sigma_{\mathsf{i}}(\omega)\right]. \tag{2.12}$$

The relative importance of both contributions basically depends on the considered spectral light range. Whereas the Drude conductivity plays a role in the infrared range (photon energy

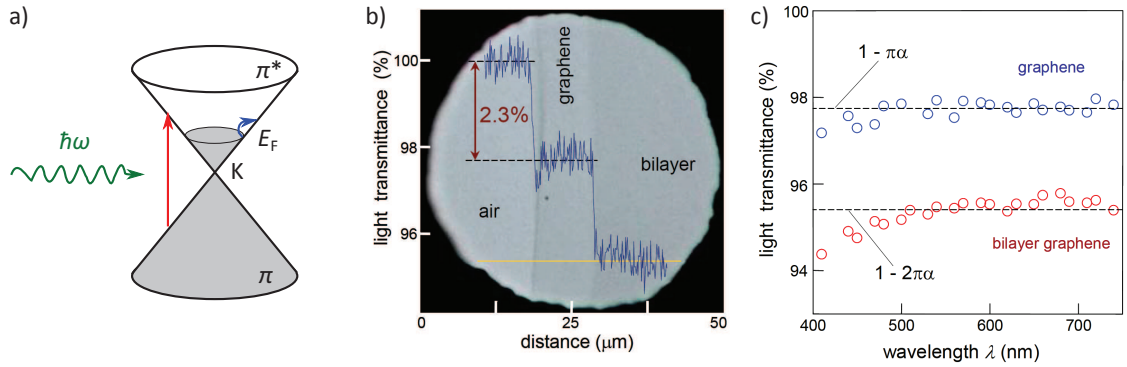

Figure 2.5: a) Schematic of intra- (red arrow) and interband (blue arrow) processes in graphene, resulting from the absorption of a photon with energy $\hbar\omega$ (green arrow). The grey areas represent occupied states. Due to the Pauli principle, an interband transition occurs from an occupied state below the Fermi level to an unoccupied state above the Fermi level. **b)** Optical image of 1L and 2L graphene exfoliated over transparent holes. The line scan profile shows the intensity of transmitted white light along the yellow line. Increasing the number of graphene layers leads to a drop of $2.3\,\%$ of the intensity of the transmitted light. **c)** Transmittance of 1L and 2L graphene regions of the sample shown in (b), as a function of the light wavelength. The transmittance is measured by analyzing images taken in an optical microscope when the membrane is illuminated through narrow-band filters. (b) and (c) are taken from ref. [Nair08a].

$\leq 50\,$meV), the interband transitions are dominant in the range between ultra-violet and mid infra-red (photon energy between $50\,$meV and $4\,$meV). Since in this work we will deal only with visible light, we neglect the intraband processes and can write n as $n = \sqrt{1 + 4\pi i\sigma_\mathrm{i}/\omega}$. Since $4\pi\sigma_\mathrm{i}/\omega \ll 1$, a series expansion of the square root yields directly the imaginary part of n. Hence, one can write

$$\alpha_\mathrm{abs} = \frac{2\omega\kappa}{c_0} \approx \frac{4\pi\sigma_\mathrm{i}}{c_0} \tag{2.13}$$

With $\sigma_\mathrm{i} = e^2/(4\hbar)$, $\alpha_\mathrm{abs} \approx \pi\alpha$, where α is the fine structure constant. Thus, the energy fraction absorbed by a single graphene layer is $\mathcal{A} \approx 1 - e^{-\pi\alpha} \approx \pi\alpha \approx 2.3\,\%$.

Actually, the fine structure constant describes the coupling strength between relativistic electrons and photons and is used in quantum electrodynamics. The interaction between photons and electrons is described by the fine structure constant. This is a direct consequence of the fact that the charge carriers in graphene can be seen as Dirac like particles [Nair08b]. Nair *et al.* measured the absorbed part of the light for graphene (monolayer and few layer), as shown in figure 2.5b, and find the value of $2.3\,\%$ per graphene layer. The absorption coefficient is constant over the spectral range of visible light for one layer graphene, which is due to the linear bands (see figure 2.5c, we note that this approximation becomes invalid for higher photon energies above approximately $2.5\,$eV), and is simply multiplied by the number of layers for few layer graphene.

Let us note that, even if light absorption is efficient in graphene, in particular taking into account its thickness, graphene is a quasi-zero light emitter because the absence of a band gap causes non-radiative charge carrier relaxation [Park07, Lui10, Mak12]. The type of light emission from graphene the most widely investigated is the inelastic scattering associated with optical phonon emission (and absorption) [Ferrari06, Ferrari07, Pimenta07, Malard09b]. This process called Raman process plays an important role for the study of phonons in graphene and, because of electronic resonances, also for probing important aspects of the electronic structure, which is directly related to the number of charge carriers [Das08, Berciaud09], mechanical strain [Mohiuddin09, Zabel11, Lee12a], defect density [Cancado11, Eckmann12] and the number of graphene layers [Graf07, Malard09b].

In our experimental work, Raman scattering spectroscopy will be the key measurement technique. Since the Raman process involves the interaction of light with charge carriers and phonons, the knowledge about phonons in graphene is of great importance. For this reason, the following section is entirely dedicated to phonons in mono- and few layer graphene.

2.4 Phonons in graphene layers

In this section we will address the possible phonon modes in a graphene monolayer, discuss the phonon dispersion and how this dispersion can be determined. In a second part, we consider additional phonon modes arising from interlayer coupling in few layer graphene and graphite.

2.4.1 Atomic displacement

Since monolayer graphene consists of two atoms per unit cell, it shows six vibration modes, three acoustic (A) and three optical (O). Two of them are longitudinal (L) in the plane (iLA and iLO), two are transversal (T) in the plane (iTA and iTO) and two are transversal out of plane (oTA and oTO). The atomic displacement corresponding to these phonons at the Γ point is sketched in figure 2.6 (column for one layer graphene). From a crystallographic point of view, graphene belongs to the point group D_{6h} (Schönflies notation) [Malard09a, Loudon64]. The irreducible representation within this point group corresponding to the phonon modes described above, are E_{2g}, B_{2g}, A_{2u} and E_{1u} (see annotations in figure 2.6) [Nemanich77, Ferrari13]. Graphite belongs to the same point group, but has a different unit cell, consisting of four atoms. Indeed, considering an AB stacking order, the two atoms of the unit cell in each layer are now inequivalent. This doubles the number of optical modes, they become Davydov-doublets [Davydov69, Ferrari13]. The corresponding irreducible representations are annotated in the right columns of figure 2.6 for graphite. We can distinguish in plane and out of plane atomic displacements, rigid layer displacements and acoustic modes. For completeness, Raman active modes are marked with a blue rectangle (straight line).

The corresponding modes will be discussed in chapter 3. Note that monolayer graphene has no infrared active modes, observable in infrared absorption spectroscopy (blue rectangle with dashed line), but that the Davydov splitting between in-phase and out-of-phase modes is the origin of the infrared activity of graphite [Nemanich77].

However, N layer graphene with N $\neq 1$ has a different point group than graphite, because the translation invariance of the four atom unit cell does not hold anymore [Yan09]. The point group is D_{3d} and D_{3h} for N even and N odd, respectively [Malard09a]. Pictorially, the main symmetry operation distinguishing between even and odd layers are the horizontal mirror plane, which is absent for even N, and the inversion, which is absent for odd N [Malard09a]. It is important to mention the difference in the point groups with respect to graphite, because it is the physical origin for the fact that certain modes, which are optically inactive in graphite, are active in N layer graphene. This is, *e.g.* the case for the layer breathing-like B_{2g} mode in graphite, which is Raman active in few layer graphene (see chapter [**?**]) [Lui14].

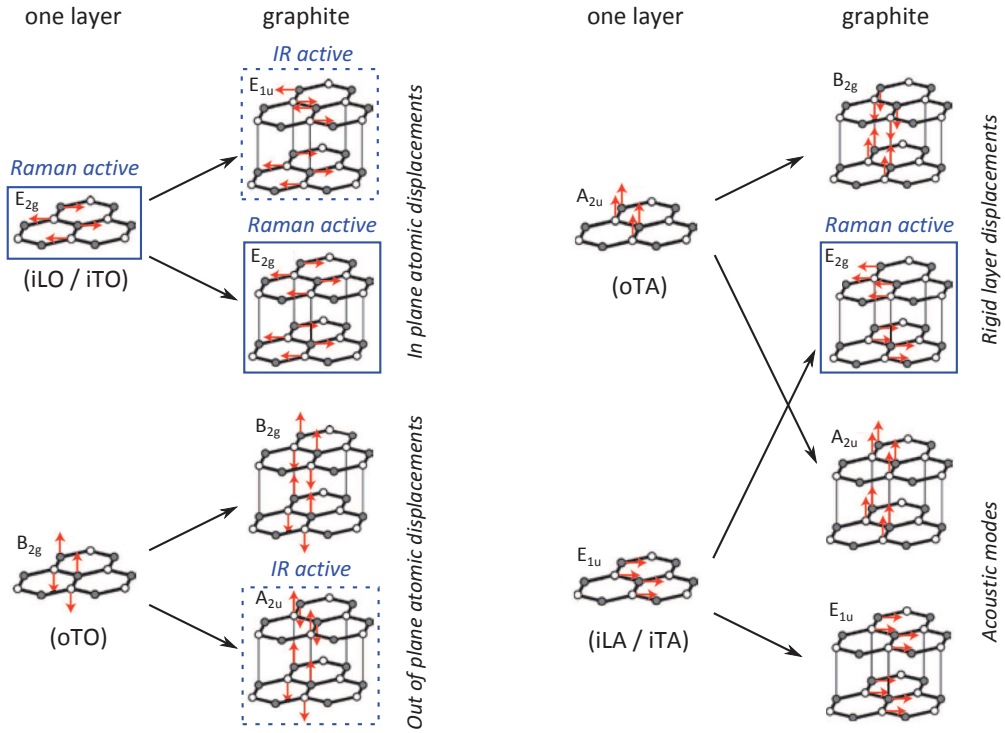

Figure 2.6: Correlation of the zone center vibrational modes (at the Γ point) of monolayer graphene (left columns) and graphite (right columns). The Raman and infrared active phonons are marked with a blue rectangle (straight and dashed line, respectively). Empty and filled circles represent inequivalent carbon atoms (see section 2.1). The red arrows show the atom displacements. The black arrows show how each phonon mode in graphene monolayer gives rise to two phonon modes in graphite. Figure inspired adapted from references [Nemanich77] and [Ferrari13].

Adding more layers in AB stacking order increases the number of atoms in the unit cell (2N for N layer graphene). The symmetry group is not the same as for monolayer graphene. However, the symmetry groups for N layer graphene, with N even or odd (from now on, N $\neq$ 1) are the same as for 2L and 3L graphene, respectively. It turns out that for these groups, a representation can be found in which the Raman active phonon modes are maintained in N layer graphene; detailed considerations on the involved symmetry groups can be found in references [Saha08], [Malard09a] and the PhD thesis of J. Yan [Yan09].

2.4.2 Phonon dispersion

From a theoretical point of view, the phonon dispersion (of graphite) has been determined using empirical force-constant calculations [Nicklow72, Al-Jishi82, Mohr07]. This approach assumes three constants for the interaction of an atom with its nearest neighbor. The fifth nearest neighbor is taken into account in these calculations in order to account for an accurate description [Mohr07].

To resolve the full range of lattice vibrations along the high symmetry lines $\Gamma \rightarrow$ M $\rightarrow$ K $\rightarrow \Gamma$ experimentally, inelastic neutron [Nicklow72] or X-ray scattering [Maultzsch04b, Mohr07, Grüneis09] as well as electron energy loss spectroscopy (EELS) [Oshima88, Siebentritt97, Yanagisawa05] can be employed. Due to the lack of quality and the required size for the above mentioned measurement techniques, the full range of the phonon dispersion in monolayer graphene has not been recorded yet, the available data are obtained from graphite or few layer graphene sources. In figure 2.7, we show experimental data obtained by X-ray scattering. Of course, one might interject that Raman spectroscopy itself could be used to determine the phonon dispersion, however, since the interaction is closely related to the electron dispersion, only a small part of the reciprocal space is accessible (near Γ and K).

A very successful tool in theoretical physics is the calculation of functionals depending on the electron density in solid states (density functional theory, DFT). Applied to graphene, the phonon dispersion has been modeled in good agreement with experimental data [Dubay03, Wirtz04, Maultzsch04b, Piscanec04, Mounet05, Bonini07, Yan08b]. However, in the common approach of DFT, the long-range character of the electron-electron interaction is neglected. These effects are taken into account by the so called GW method, which considers a screened electron-electron interaction[4]. This method is considered as the most precise approach to determine electronic bands, and, in particular, phonon dispersions [Lazzeri08]. Since electron-phonon coupling is expected to take place in the vicinity of the Γ and K points, a precise knowledge of the phonon dispersion is mandatory. It turns out that the GW method accounts for a notable correction of

[4] Considering an electron in its environment, which it is screening, is summarized in the so called self energy, which itself is calculated by means of a Green's function G and the corresponding interaction W: $\Sigma \approx iGW$ is then the GW approximation.

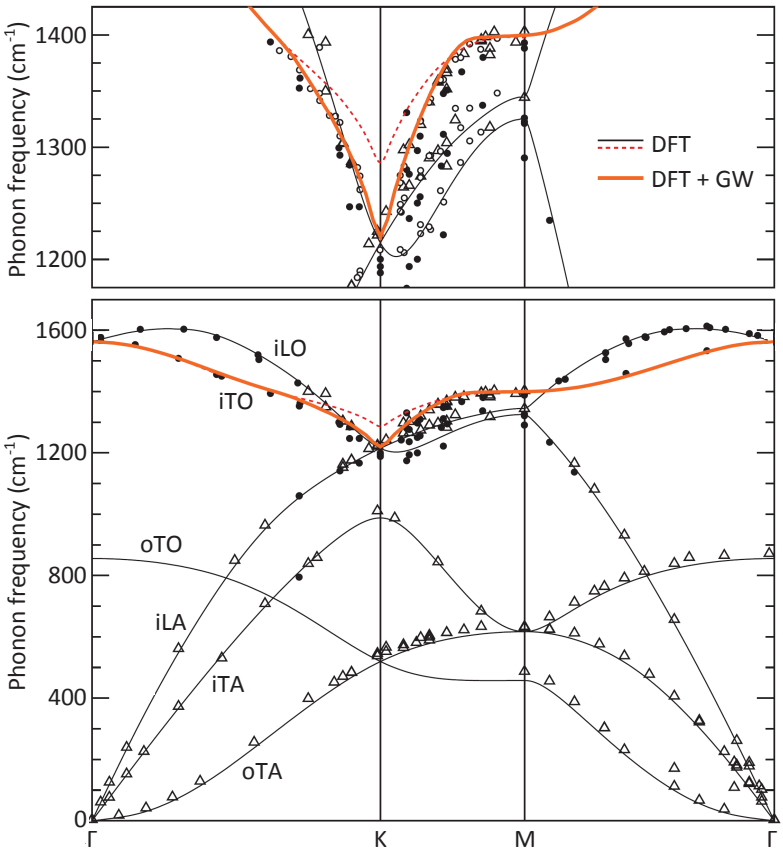

Figure 2.7: Phonon dispersion of graphite/graphene. **Experimental data** are obtained from X-ray scattering measurements, including data from references [Maultzsch04b] (filled dots), [Mohr07] (open triangles) and [Grüneis09] (open dots). **Theoretical data** are DFT calculations (black straight and red dashed lines) and GW corrections (orange straight line) from references [Lazzeri08] and [Grüneis09]. Figure adapted from ref. [Venezuela11].

the standard DFT calculations, in particular at the K point [Lazzeri08, Grüneis09, Venezuela11]. We show the theoretical DFT calculations including the GW correction in figure 2.7.

A zoom in the range of the optical phonons in the vicinity of the K point (upper part of figure 2.7) displays an interesting feature: The phonon frequency varies abruptly with momentum near K. Such a phenomenon is rather uncommon in other materials; its occurance is strongly related to the electronic dispersion of graphene. Kohn stated in 1959, if there are two electronic states with wave vectors $\boldsymbol{k}_1$ and $\boldsymbol{k}_2 = \boldsymbol{k}_1 + \boldsymbol{q}$, both on the Fermi surface, it is $|\nabla_{\boldsymbol{q}}\, \omega(\boldsymbol{q})| = \infty$ [Kohn59]. This so called *Kohn anomaly* occurs at the Γ point ($\boldsymbol{q} \approx 0$, on the iLO branch) and the K point ($\boldsymbol{q} \approx \boldsymbol{K}$, on the iTO branch) of graphene [Piscanec04, Maultzsch04b].

Finally, we stress that the phonon dispersion shown in figure 2.7 is the one of monolayer graphene. As discussed in the previous chapter, the addition of layers leads to a Davydov splitting of the modes [Froehlicher15b]. In particular, the layer breathing mode of the oTA phonon splitting has a finite frequency at Γ, which is $\approx 120\,\mathrm{cm}^{-1}$ [Karssemeijer11, Tan12, Lui13]. A zoom in to even lower phonon frequencies reveals the splitting of the iLA and iTA modes (at $\approx 40\,\mathrm{cm}^{-1}$) [Tan12]. The corresponding zoom in of the phonon dispersion can be consulted *e.g.* in ref. [Tan12].

For completeness, let us note that part of the acoustic branches has been studied at ultra-low frequencies by means of Brillouin scattering, allowing for the extraction of the sound velocity in graphene [Wang08e].

2.5 Suspended graphene as a two dimensional membrane

There is an extended interest in studying suspended graphene, which is decoupled from any substrate influences, particularly true in terms of substrate induced doping and charge puddles [Bolotin08b, Martin08, Berciaud09, Chen09b, Xue11], as already indicated in subsection 2.2.4. This interest is not only nurtured by improved transport properties, but also by the challenge of using a membrane within its ultimate thickness limit. Three particular features facilitate studies on suspended graphene membranes:

First, graphene adheres strongly to the commonly used Si/SiO_2 substrate [Koenig11, Gao14]. Deposited over apertures of various shapes and subjected to a pressure difference, the strong adhesion ensures the lack of slipping and allows for the examination of the mechanical response to a pressure difference. Here, we refer to the work of Bunch *et al.* and Georgiou *et al.*, which we have presented in an exemplary manner in chapter 1 (see figure 1.2) [Bunch07, Bunch08, Georgiou11]. Of course, at a certain pressure difference the adhesion energy is overcome and delamination occurs. Such a pressure dependent delamination test is shown schematically in figure 2.8a and b. The corresponding membrane deformation using AFM is plotted in figures 2.8c. For an approximately $4\,\mu$m diameter aperture delamination starts with a pressure difference in the MPa range [Koenig11].

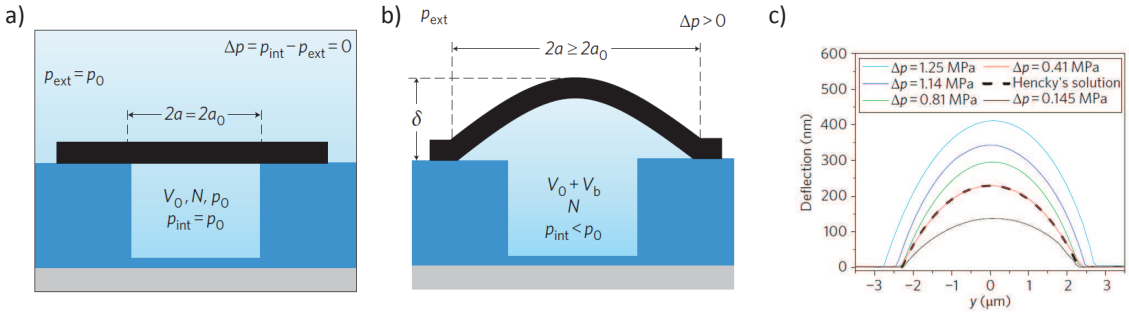

Figure 2.8: a) Schematic of a graphene-sealed microcavity before it is placed in the pressure chamber. The pressure inside the microcavity, p_{int}, is equal to the external pressure p_{ext}, so the membrane is flat. After four to six days inside the pressure chamber, p_{int} increases to p_0. **b)** When the microcavity is removed from the pressure chamber, the pressure difference across the membrane causes it to bulge upward and eventually delaminate from the substrate, causing the radius a to increase. **c)** Deflection *vs.* position for five different values of Δp between 0.145 MPa (black) and 1.25 MPa (cyan). The dashed black line is obtained from Hencky's solution for $\Delta p = 0.41$ MPa [Hencky15]. The deflection is measured by AFM along a line that passes through the centre of the membrane. Figures are taken from ref. [Koenig11].

However, in general, every suspended graphene membrane is somehow attached to a substrate at its extremities, either by simple van der Waals interaction [Koenig11, Yoon12, Gao14, Jung14] or by clamping it with metal contacts [Bunch07, Du08, Bolotin08b].

Second, the images shown in chapter 1, in particular the data in figure 1.2c, reveal that graphene is impermeable to standard gases [Bunch08]. Indeed, it takes several days for a pressurized membrane to come back to its initial state, and even it is questionable whether the relaxation is not due to a gas diffusion through the underlying Si/SiO_2.

Third, the highly charge conducting graphene is composed of light carbon atoms, which forms the perfect platform for inducing a deflection either by an electrostatic pressure load [Bolotin08b] or by the application of an AC back gate voltage [Bunch07, Chen09a], leading to a high frequency deflection modulation.

In any case, it is crucial to know the mechanical response of the graphene membrane due to an external pressure load, be it by a gas pressure difference or by means of electric pressure.

Supported graphene can be considered as flat and in equilibrium with its environment, even when a pressure load normal to its surface is applied [Meyer07, Martin08]. In contrast, the observed deflection of suspended graphene is the result of an equilibrium state minimizing the contribution of bending and stretching for a given external pressure load. We note that in the geometries considered here, the gravitational force is negligible[5]. In particular, its value is unimportant when an air pressure difference or an electrostatic pressure is applied. The force acting on the membrane leads consequently to a deformation of the graphene sheet. The issue is now

[5]The weight of a monolayer of graphene is 7.57×10^{-7} kg/m^2. The gravitational force F_g acting on a suspended device with typical dimensions of *e.g.* $20 \times 5\,\mu\text{m}^2 = 10^{-10}$ m^2 is $F_g = mg \approx 10^{-15}$ N.

to determine the displacement response of the sheet due to an external force. In other words, in thermodynamics the total free energy $\mathcal{F}$ has to be minimized in order to find the equilibrium deflection.

In particular, in thin plates or membranes, the bending and stretching energy contribute to $\mathcal{F}$, apart from the external pressure load P. In the following, we will first introduce the definitions of strain and stress tensors and then utilize the definitions to determine the bending and stretching contributions to the free energy of thin plates. As the graphene is an ultra-thin membrane, we will further focus on the limit of vanishing thickness and bending stiffness. In particular, we will see that the result strongly influences the relationship between P and the maximal deflection ξ_{max}.

Fundamental definitions

The following considerations mainly follow Landau's book *Theory of elasticity* [Landau70].

Let an arbitrary body have to points separated by a distance $\mathrm{d}l$. In a three-dimensional Cartesian coordinate system $\mathrm{d}l^2$ is $\mathrm{d}x_1^2 + \mathrm{d}x_2^2 + \mathrm{d}x_3^2$. Under the action of applied forces, the body changes its shape and volume, *i.e.* the distance between these two points changes to $\mathrm{d}l'$, where $\mathrm{d}l'^2 = \mathrm{d}x_1'^2 + \mathrm{d}x_2'^2 + \mathrm{d}x_3'^2$. Let us define the displacement vector $\boldsymbol{u}$ with the components $u_{\mathsf{i}} = x_{\mathsf{i}}' - x_{\mathsf{i}}$. Using the Einstein summation rule and substituting $\mathrm{d}u_{\mathsf{i}} = (\partial u_{\mathsf{i}}/\partial x_{\mathsf{k}})\mathrm{d}x_{\mathsf{l}}$, one can write

$$\mathrm{d}l'^2 = \mathrm{d}l^2 + 2\,\frac{\partial u_{\mathsf{i}}}{\partial x_{\mathsf{k}}}\,\mathrm{d}x_{\mathsf{i}}\mathrm{d}x_{\mathsf{k}} + \frac{\partial u_{\mathsf{i}}}{\partial x_{\mathsf{k}}}\frac{\partial u_{\mathsf{i}}}{\partial x_{\mathsf{l}}}\,\mathrm{d}x_{\mathsf{k}}\mathrm{d}x_{\mathsf{l}} = \mathrm{d}l^2 + 2u_{\mathsf{ik}}\,\mathrm{d}x_{\mathsf{i}}\mathrm{d}x_{\mathsf{k}}. \tag{2.14}$$

Here, the **strain tensor** u_{ik} has been defined as

$$u_{\mathsf{ik}} = \frac{1}{2}\left(\frac{\partial u_{\mathsf{i}}}{\partial x_{\mathsf{k}}} + \frac{\partial u_{\mathsf{k}}}{\partial x_{\mathsf{i}}} + \frac{\partial u_{\mathsf{l}}}{\partial x_{\mathsf{i}}}\frac{\partial u_{\mathsf{l}}}{\partial x_{\mathsf{k}}}\right) \tag{2.15}$$

and gives the change in an element of length when the body is deformed. For small deformations, u_{i} is small, thus one can neglect the last summand in equation (2.15), which is of second order.

When the body is deformed, internal forces called stresses arise in order to return the body to equilibrium. For a given portion of the body, the total force per unit volume, $\boldsymbol{F}$, is given by the volume integral over all small volume elements $\mathrm{d}V$ in that portion, *i.e.* $\int \boldsymbol{F}\mathrm{d}V$. Various parts of that portion might act on one another, but the total resultant force is zero due to Newton's third law. Thus, the total force can be regarded as the sum of the forces exerted on the given portion by the surrounding portions. That means that the forces act on the surface of that portion. Hence, the resultant force can be represented as an integral over the surface, and this for every component $\int F_{\mathsf{i}}\,\mathrm{d}V$. In vector analysis, integrating a scalar over a volume integral can be transformed into an integral over a surface element if the scalar is the divergence of a vector. In our case, we

have the integral of a vector (F_i) over a volume, which implies that F_i must be the divergence of a tensor of rank two, *i.e.* be of the form

$$F_\mathsf{i} = \frac{\partial \sigma_{\mathsf{ik}}}{\partial x_\mathsf{k}}, \tag{2.16}$$

where σ_{ik} is called the **stress tensor**. The component σ_{ik} is the i-th component of the force per unit area acting perpendicular to the x_k-axis. In other words, by taking elements of area in the planes of xy, yz and zx, the force per unit area parallel to the x-axis is σ_{xx} whereas σ_{yx} and σ_{zx} are tangential forces along the y and z-axis, respectively.

The stress tensor can be expressed in terms of the strain tensor using the Poisson ratio[6] ν and the Young's modulus E in the following way:

$$\sigma_{\mathsf{ik}} = \frac{E}{1+\nu}\left(u_{\mathsf{ik}} + \frac{\nu}{1-2\nu}\, u_{\mathsf{ll}}\delta_{\mathsf{ik}}\right), \tag{2.18}$$

where, again, the Einstein summation is used and δ_{ik} is the Kronecker delta. We note that here, the strain tensor is a linear function of the stress tensor, *i.e.* the deformation is proportional to the applied forces. Equation (2.18) is valid for small deformations and can be seen as Hooke's law.

In order to access the final equilibrium state of the deformed body, we have to know the **total free energy** $\mathcal{F}$, which is supposed to be a function of the strain tensor. For small deformations, $\mathcal{F}$ can be expanded in terms u_{ik}. Note that the term of lowest order is of order two because on the undeformed body no external forces act, *i.e.* $\sigma_{\mathsf{ik}} = 0$. This implies that $\partial\mathcal{F}/\partial u_{\mathsf{ik}} = 0$ because in thermodynamics, the components of the stress tensor can be obtained by differentiating the free energy with respect to the components of the strain tensor. Hence, one can write the total free energy as

$$\mathcal{F} = \mathcal{F}_0 + \frac{1}{2}\lambda u_{\mathsf{ii}}^2 + \mu u_{\mathsf{ik}}^2 \tag{2.19}$$

with λ and μ the Lamé coefficients. Using the definition of these coefficients, $\mathcal{F}$ can be expressed in terms of the Poisson ratio ν and the Young's modulus E:

$$\mathcal{F} = \frac{E}{2(1+\nu)}\left(u_{\mathsf{ik}}^2 + \frac{\nu}{1-2\nu}\, u_{\mathsf{ii}}^2\right). \tag{2.20}$$

[6] The Poisson ratio ν is a measure of the strain response transverse to the axis on which the strain is applied. It is defined as

$$\nu = -\frac{\mathsf{d}\epsilon_{\mathsf{trans}}}{\mathsf{d}\epsilon_{\mathsf{axial}}}, \tag{2.17}$$

and can also be expressed in terms of volume changes. Indeed, when a material is compressed in one direction, it usually tends to expand in the other two directions perpendicular to the direction of compression.

According to Euler's homogeneous function theorem, here applicable for a function of degree 2, one can write $u_{ik}\partial\mathcal{F}/\partial u_{ik} = 2\mathcal{F}$ [Forster76], and with $\partial\mathcal{F}/\partial u_{ik} = \sigma_{ik}$ one gets another useful form of the expression for the free energy:

$$\mathcal{F} = \frac{1}{2}\,\sigma_{ik}u_{ik}. \tag{2.21}$$

Bending energy of thin plates

Using the notation above, we might now determine the free energy of a bent plate. To do so, we consider a thin plate, *i.e.* its thickness t is small compared to the other two dimensions. Furthermore, the deformations are supposed to be small compared to the plate dimensions. As sketched in figure 2.9, bending a plate of thickness t results in compressing (expanding) the lower (upper) part.

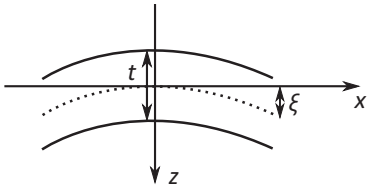

Figure 2.9: Schematic of a bent plate of thickness t. For small deflections, the displacement ξ is only along the z-axis.

The displacement of the neutral line (dotted in figure 2.9 and in the following denoted with the index (0)) along the z-axis is called ξ. For small deformations, the displacement in x (and y) direction can be neglected and the displacement vector is

$$u_x^{(0)} = u_y^{(0)} = 0, \qquad u_z^{(0)} = \xi(x,y). \tag{2.22}$$

Now we will analyze the components of the stress tensor which will give some conditions to determine the strain tensor. Namely, comparatively small forces on the surface of the plate are needed to bend it. These forces are considerably smaller than the internal stresses due to the compression and expansion. Thus, on *both surfaces* of the plate, one can put $\sigma_{xz} = \sigma_{yz} = \sigma_{zz} = 0$. In the plate, we further suppose that these quantities are small, since they are zero at the surface and the plate is thin. Thus, for these quantities, equation (2.18) writes as

$$\begin{aligned} \sigma_{zx} &= \frac{E}{1+\nu}\,u_{zx}, \qquad \sigma_{zy} = \frac{E}{1+\nu}\,u_{zy} \qquad \text{and} \\ \sigma_{zz} &= \frac{E}{(1+\nu)(1-2\nu)}\,\left[(1-\nu)u_{zz} + \nu(u_{xx}+u_{yy})\right]. \end{aligned} \tag{2.23}$$

These equations are then set to zero. With the definition of the strain tensor (equation (2.15)), one obtains

$$\frac{\partial u_{\mathrm{x}}}{\partial z} = -\frac{\partial \xi}{\partial x}, \qquad \frac{\partial u_{\mathrm{y}}}{\partial z} = -\frac{\partial \xi}{\partial y} \qquad \text{and} \qquad u_{\mathrm{zz}} = -\frac{\nu}{1-\nu}(u_{\mathrm{xx}} + u_{\mathrm{yy}}). \tag{2.24}$$

Here, u_{z} has directly been replaced by ξ. Integrating the first two equations with respect to z and putting the constants of integration to zero in order to ensure the initial condition $u_{\mathrm{x}} = u_{\mathrm{y}} = 0$ for $z = 0$, we get

$$u_{\mathrm{x}} = -z\,\frac{\partial \xi}{\partial x} \qquad \text{and} \qquad u_{\mathrm{y}} = -z\,\frac{\partial \xi}{\partial y}. \tag{2.25}$$

Finally, all the components of the strain tensor are known, *i.e.*

$$\begin{aligned} u_{\mathrm{xx}} &= -z\,\frac{\partial^2 \xi}{\partial x^2}, \qquad u_{\mathrm{yy}} = -z\,\frac{\partial^2 \xi}{\partial y^2}, \qquad u_{\mathrm{xy}} = -z\,\frac{\partial^2 \xi}{\partial x \partial y}, \\ u_{\mathrm{xz}} &= u_{\mathrm{yz}} = 0 \qquad \text{and} \qquad u_{\mathrm{zz}} = \frac{\nu}{1-\nu}\,z\left(\frac{\partial^2 \xi}{\partial x^2} + \frac{\partial^2 \xi}{\partial y^2}\right). \end{aligned} \tag{2.26}$$

Using equation (2.20), we can write down the free energy per unit volume of the plate:

$$\mathcal{F} = z^2\,\frac{E}{1+\nu}\left\{\frac{1}{2(1-\nu)}\left(\frac{\partial^2 \xi}{\partial x^2} + \frac{\partial^2 \xi}{\partial y^2}\right)^2 + \left[\left(\frac{\partial^2 \xi}{\partial x \partial y}\right)^2 - \frac{\partial^2 \xi}{\partial x^2}\,\frac{\partial^2 \xi}{\partial y^2}\right]\right\}. \tag{2.27}$$

The total free energy of the plate is obtained by integrating over the volume. The integration over z can be easily performed from $-t/2$ to $+t/2$. Thus, only the integration over the surface remains. The total free energy due to the bending of a thin plate is

$$\begin{aligned} \mathcal{F}_{\mathrm{b}}(\xi) = \frac{D}{2} &\iint \left(\frac{\partial^2 \xi}{\partial x^2} + \frac{\partial^2 \xi}{\partial y^2}\right)^2 \mathrm{d}x\mathrm{d}y \\ &+ \iint (1-\nu^2)\left[\left(\frac{\partial^2 \xi}{\partial x \partial y}\right)^2 - \frac{\partial^2 \xi}{\partial x^2}\,\frac{\partial^2 \xi}{\partial y^2}\right] \mathrm{d}x\mathrm{d}y. \end{aligned} \tag{2.28}$$

Here, D is the bending rigidity, defined as $D = Et^3/[12(1-\nu^2)]$. To obtain the equation of equilibrium, $\mathcal{F}_{\mathrm{b}}$ has to be minimized. Performing the variation is a calculation over several pages and can be looked up in ref. [Landau70]. We content ourselves with giving the result of this calculation:

$$D \triangle^2 \xi - P = 0. \tag{2.29}$$

In this equation, $\triangle$ is the Laplace operator, $\triangle = \partial^2/\partial x^2 + \partial^2/\partial y^2 + \partial^2/\partial z^2$, and P is an external force per unit area acting on the plate and normal to the surface.

A simple dimension analysis of equation (2.29) reveals how the deflection at the center of a plate (with dimension a) evolves with P. It is

$$P \propto \frac{D}{a^4}\,\xi_{\mathsf{max}}. \tag{2.30}$$

We emphasize the fact that P is directly proportional to ξ_{max}.

Large deflections and stretching energy of thin plates

In the previous subsection we studied small deformations of a thin plate, resulting in only expansion and compression of the upper and the lower part of the plate, respectively. If, however, the thin plate is clamped and the deflections become larger, it is evident that additional longitudinal forces act on the plate, which is due to a stretching. The strain tensor (over the whole plate) is then only a function of x and y, *i.e.* $\sigma_{\mathsf{xz}} = \sigma_{\mathsf{yz}} = \sigma_{\mathsf{zz}} = 0$. Injecting these conditions into equation (2.18), one gets the relations

$$u_{\mathsf{zz}} = -\frac{\nu}{1-\nu}\,(u_{\mathsf{xx}} + u_{\mathsf{yy}}) \qquad \text{and} \qquad u_{\mathsf{xz}} = u_{\mathsf{yz}} = 0. \tag{2.31}$$

Again by means of equation (2.18), we get the non-zero components of the stress tensor:

$$\begin{aligned} \sigma_{\mathsf{xx}} &= \frac{E}{1-\nu^2}\,(u_{\mathsf{xx}} + \nu u_{\mathsf{yy}}), \\ \sigma_{\mathsf{yy}} &= \frac{E}{1-\nu^2}\,(u_{\mathsf{yy}} + \nu u_{\mathsf{xx}}), \\ \sigma_{\mathsf{xy}} &= \frac{E}{1+\nu}\,u_{\mathsf{xy}}. \end{aligned} \tag{2.32}$$

In the following, we put α and β as suffixes, which can take the two values x and y, still keeping the Einstein sum convention. The strain tensor, which we have defined in equation (2.15), then writes as

$$u_{\alpha\beta} = \frac{1}{2}\left(\frac{\partial u_\alpha}{\partial x_\beta} + \frac{\partial u_\beta}{\partial x_\alpha}\right) + \frac{1}{2}\,\frac{\partial \xi}{\partial x_\alpha}\,\frac{\partial \xi}{\partial x_\beta}. \tag{2.33}$$

The stretching energy per unit surface area of the plate is, according to equation (2.21), $\mathcal{F}_{\mathsf{s}}(u_{\alpha\beta}) = \frac{1}{2} t u_{\alpha\beta}\sigma_{\alpha\beta}$. This term can be added to equation (2.28) in order to get the total free energy of the plate, consisting of the pure bending energy and the stretching energy. The result of the variation of the (free) bending energy has been presented previously and can be performed independently because the energies build a simple sum. The variation of the stretching energy is again a lengthy

calculation (see ref. [Landau70] for details), thus we give directly the final result of the equations of equilibrium:

$$\begin{aligned} D\Delta^2\xi - \frac{\partial}{\partial x_\beta}\left(t\sigma_{\alpha\beta}\frac{\partial\xi}{\partial x_\alpha}\right) &= P \\ \frac{\partial\sigma_{\alpha\beta}}{\partial x_\beta} &= 0. \end{aligned} \tag{2.34}$$

These equations form a system of equations for large deflections of thin plates and are called Föppl-von Kármán equations [Föppl07, Kármán10]. They cannot be solved exactly, even in very simple cases [Landau70]. Nevertheless, let us have a closer look on it. Although bending and stretching energy (and their equilibrium states, corresponding to the first and second summand, respectively) are presented as competing energies, the different powers of the plate thickness t in the summands allows for considering, *e.g.*, the particular case of a very thin plate, *i.e.* a membrane. We will discuss this case in the following subsection.

Discussion: the case of membranes

Since the bending part in equation (2.34) is of order 3 (we remind that $D \propto t^3$), it is negligible compared to the stretching part when we consider the case of membranes. Nonetheless, both equations in equation (2.34) have to be fulfilled. These equations have three unknowns, $\xi(x,y)$ and the two components u_{x} and u_{y} of the displacement vector, which are contained in the stress tensor. This fact can be overcome by introducing the so called stress function χ, defined by $\sigma_{\mathrm{xx}} = \partial^2\chi/\partial y^2$, $\sigma_{\mathrm{xy}} = \partial^2\chi/\partial x\partial y$ and $\sigma_{\mathrm{yy}} = \partial^2\chi/\partial x^2$. With these definitions, equations (2.34) rewrite after a short calculation (see ref. [Landau70] for details) as

$$D\,\triangle^2\,\xi - t\left(\frac{\partial^2\chi}{\partial y^2}\frac{\partial^2\xi}{\partial x^2} + \frac{\partial^2\chi}{\partial x^2}\frac{\partial^2\xi}{\partial y^2} - 2\,\frac{\partial^2\chi}{\partial x\partial y}\frac{\partial^2\xi}{\partial x\partial y}\right) = P, \tag{2.35}$$

$$\triangle^2\,\chi + E\left[\frac{\partial^2\xi}{\partial x^2}\frac{\partial^2\xi}{\partial y^2} - \left(\frac{\partial^2\xi}{\partial x\partial y}\right)^2\right] = 0. \tag{2.36}$$

This is another representation of the Föppl-von Kármán equations. It allows us to estimate how the deflection at the center ξ_{max} of a (quadratic) membrane evolves with P by doing a dimension analysis. Equation (2.36) shows that $\chi \propto E\xi^2$. As stated above, we neglect the first term in equation (2.35). Then, it is

$$P \propto \frac{Et}{a^4}\,\xi_{\mathrm{max}}^3, \tag{2.37}$$

where a is the lateral dimension of the membrane[7].

We would like to stress the importance of this result, because it is in stark contrast with the result of the dimension analysis of a plate with finite bending stiffness. More precisely, the pressure load scales linearly with the deflection if the bending energy is the governing energy in the plate, whereas it scales with the third power of the deflection if the bending energy is negligible.

We note that there is a wide range of literature dealing with the mechanics of thin films subjected either to point or pressure loads (*e.g.* references [Timoshenko59, Tsakalakos81, Vlassak92, Karimi97, Poilane00, Wan03]). Depending on the thickness, the elastic properties, *e.g.* the bending stiffness, and prestrain (or built-in strain) thin films are either treated as plates or membranes. To clarify how a thin plate should be considered, Komaragiri *et al.* treats both extreme cases (plate and membrane) as well as the transition between the plate and membrane regime. Furthermore, they elaborate for which case an analytical solution exists. In particular, their study justifies the treatment of graphene as a membrane [Komaragiri05, Yue12].

Furthermore, several authors examined the influence of prestrain (or built-in strain) on the relationship between P and ξ_{max}. Different geometries were studied, in particular the case of a circular [Vlassak92, Beams95, Williams97] and rectangular [Medvedyeva11] membranes. These investigations suggest unanimously that a term proportional to ξ_{max} should to be added to the relationship $P \propto \xi_{\text{max}}^3$. Thus, in accordance with equation (2.37) and taking into account a built-in strain T_0, one can write

$$P = K_1 T_0 \xi_{\text{max}} + K_2 E t \xi_{\text{max}}^3, \tag{2.39}$$

where K_1 and K_2 are geometry dependent constants. The prestrain contribution scales linearly with P, as it is the case for thin plates with finite bending stiffness. Hence, a certain amount of built-in strain can be regarded as an effective bending stiffness moderating the deflection of the membrane with increasing P. For larger deflections, the ξ_{max}^3-term governs the equation.

2.6 Conclusion

In this chapter, we have a basis in order to understand the response of graphene to external perturbations, both at the atomic level (phonons) and at the microscopic level (membrane deflec-

[7] We note that another approach exists: Additional longitudinal stresses caused by the bending are ignored, thus the components of the tensor $\sigma_{\alpha\beta}$ are simply equal to the constant external stretching forces. In other words, $t\sigma_{\alpha\beta}$ can be replaced by $T\delta_{\alpha\beta}$, where T is the absolute magnitude of the stretching force per unit length [Landau70]. Thus, equation (2.34) rewrites as

$$T \triangle \xi + P = 0. \tag{2.38}$$

A dimension analysis reveals that $P \propto T\xi_{\text{max}}/a^2$. At first sight one could think that P scales linearly with ξ_{max}. However, T is unknown and usually connected to the relative elongation of the membrane, which, in turn, determines ξ. This crucial point will in particular be discussed in chapter 7.

tions). In addition, we have pointed out the unique electronic and optical properties of graphene closely related to its electronic dispersion, and we have discussed the interest of using suspended graphene, which forms the ideal platform for both fundamental physics studies in the vicinity of the Dirac point and studies for applications. The latter can be grossly summarized with the two terms *sensing* and *tuning*: The shrinking of the device dimensionality increases the sensitivity of the mechanical response to external perturbations, which makes graphene a promising candidate for *e.g.* mass sensing [Singh10, Hill11, Chaste12]. The precise control of the deflection of suspended graphene by an AC back-gate voltage might also be used to finely tune near-field coupling, as recently shown by Reserbat-Plantey *et al.* [Reserbat-Plantey15].

3 Raman scattering spectroscopy of graphene

As it will be exposed thoroughly in this chapter, vibrational Raman spectroscopy probes the coupling of photo-excited electron-hole pairs with crystal lattice vibrations. Consequently, this measurement technique is expected to be sensitive to external perturbations which influence the electron and phonon dispersion, *e.g.* the number of graphene layers, the amount of charge carriers, temperature, or mechanical strain. In other words, Raman spectroscopy is a fast, contactless and minimally invasive tool to probe the features we have introduced in the previous chapter.

First, tuning the charge carrier density within a FET geometry will impact the phonon modes due to the accompanied lattice parameter change and the interaction between charge carriers and phonons. In addition, a different charge carrier lifetime influences the phonon modes.

Second, mechanical strain effects directly the lattice parameter and hence the energy of the phonons. In particular, Raman spectroscopy helps to identify tensile and compressive, biaxial and uniaxial strain. The latter, for instance, is distinguished because of the degeneracy breaking of certain phonon modes.

Third, the number of layers can be probed by identifying additional phonons in the Raman spectra, arising from the Davydov splitting. Furthermore, some Raman modes are strongly sensitive to the electronic dispersion, which changes from monolayer to few layer graphene.

Finally, even in the case of suspended membranes, graphene is on top of a multilayered structure, *e.g.* Si, SiO_2, air or vacuum. The change of the thickness of one of these layers gives rise to optical interferences which affect the intensity of the observed Raman signal. This feature will be discussed at the very end of this chapter.

3.1 The Raman process

In section 2.3 we introduced a simplified model of light interaction with graphene, consisting of reflection, absorption and transmittance, and omitted luminescence and every kind of light scattering. This approximation is justified by the fact that the latter are negligible when graphene is seen by the naked eye. As already mentioned, light emission due to photo-luminesence, in particular fluorescence, is suppressed due to the absence of a band gap, which quickly brings the energy of highly excited electron hole pairs down to lower energies [Sun08][1].

The processes involving light scattering have to be classified into elastic and inelastic processes, *i.e.* in processes where the incoming and outgoing photon has the same energy and where part of the photon energy is transferred to the crystal, respectively. The first process is called *Rayleigh scattering* [Strutt99, Hecht02, page 86] (see also figure 3.1)[2]. Inelastic light scattering involves the interaction with one or more elementary excitations. If these excitations are acoustic phonons, one talks about *Brillouin scattering*, which involves phonons with very low frequencies and therefore is a phenomenon on a large scale within the probed crystal. In higher frequency range, one talks about *Raman scattering* (named after C. V. Raman [Smekal23, Raman28]), where one has to distinguish between Raman scattering from (purely) electronic excitations (so called *electronic* Raman scattering) [Koningstein73, Kashuba09][3] and Raman scattering from phonons. The latter process involves the creation of an electron-hole pair which emits one (or several) phonons and then recombines, this process is called electro-vibrational or *vibrational* Raman scattering. Usually, this process is associated with optical phonons, however, in certain cases, combinations of optical and acoustic phonons can give rise to Raman modes [Sato11, Lui12].

In this thesis we probe graphene exclusively by vibrational Raman scattering spectroscopy, which is meant when we speak abbreviatorily about Raman spectroscopy in the following.

In the Raman process, the coupling between electrons and phonons plays an important role. In general, the main coupling mechanisms are the coupling to phonons inducing a potential deformation in the vicinity of the (moving) atoms and the one to phonons inducing a polarization in the material [Ziman60, chapter 5], the so called Fröhlich coupling [Fröhlich54]. The latter is par-

[1] We note that this is the case for neutral graphene at equilibrium. Heating up graphene, either by intense ultrafast laser pulses [Lui10, Wang10a, Shang11] or by applying a strong electric field [Berciaud10, Freitag10], allows for the detection of hot carrier caused photo-luminescence and the measurement of their relaxation time. This effect is particularly enhanced on biased suspended graphene, where heat transport to the underlying substrate is reduced [Kim15b].

[2] Although observed and used to identify monolayer graphene [Casiraghi07a, Blake07], elastic light scattering only plays a minor role in graphene science because it does not reveal any structural or electronic information.

[3] Note that electronic Raman scattering in graphene is challenging, because there are no distinct electronic levels (see section 2.2.1). However, the application of a magnetic field causes the charge carriers to circulate in cyclotron orbits with quantized energies called Landau levels [Miller09, Song10]. Electronic Raman scattering on these artificially induced distinct electronic levels is called *magneto*-Raman scattering, which has been applied to monolayer and few layer graphene recently [Faugeras11, Berciaud14, Neumann15b, Neumann15a].

ticularly important in materials consisting of different atoms, which is expected to induce a dipole moment, but is, however, absent in graphene because it consists of the same kind of atoms.

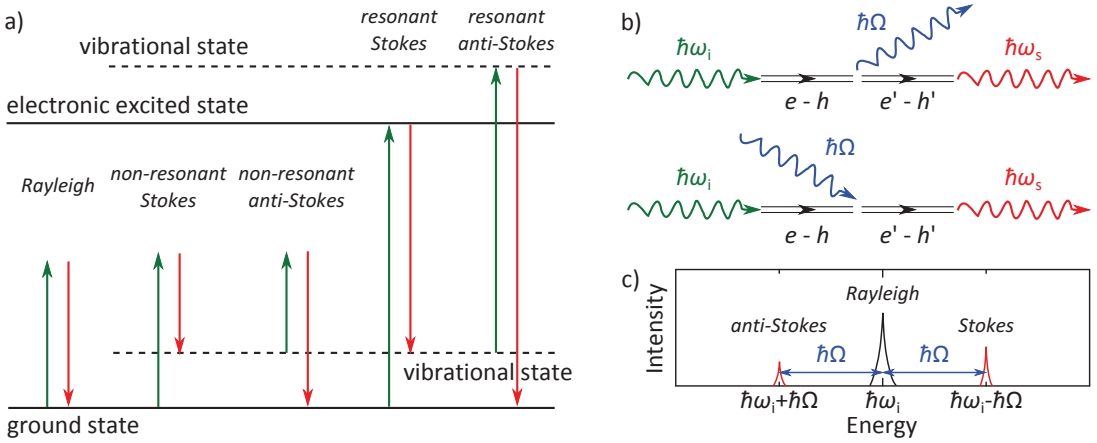

Figure 3.1: a) Rayleigh and Raman scattering processes in resonant and non resonant conditions. **b)** Upper part: Sketch of the Stokes process where an incoming photon with energy $\hbar\omega_i$ excites an electron-hole pair e-h. The pair decays into a phonon with energy $\hbar\Omega$ and another electron-hole pair e'-h'. The latter recombines by emitting a photon with energy $\hbar\omega_s$. Lower part: Corresponding Anti-Stokes process where the phonon is absorbed by the e-h pair. (a) and (b) are adapted from the Supplementary Information of ref. [Ferrari13]. **c)** Schematic representation of a Raman spectrum, showing the energy of Rayleigh, Raman Stokes and anti-Stokes lines with respect to the initial photon energy $\hbar\omega_i$. Note that the energy scale is increasing from the right to the left. In Raman spectroscopy, the scale is usually expressed in wavenumbers with respect to $\hbar\omega_i$ (see main text).

During the Raman scattering process, a photon with frequency ω_i and wavevector $\boldsymbol{k}_i$ perturbs the system of the crystal lattice. This perturbation increases the total energy of the system by the quantity $\hbar\omega_i$ and creates an electron-hole pair (see figure 3.1). In general, the energy of the electron does not correspond to a stationary state of the system, *i.e.* the electron is in a virtual state and the scattering process is non-resonant. On the contrary, if the electron energy corresponds to a well defined energy level of the system, the scattering process is resonant and thus more efficient. In any case of the inelastic scattering process, the system tends to decrease its energy and emits a photon with frequency ω_s and wavevector $\boldsymbol{k}_s$. The energy $\hbar\omega_s$ of the emitted photon can be lower or higher than the energy of the incident photon. In the first case, the Raman process is called Stokes, and in the latter case anti-Stokes. The energy loss or gain is due to the interaction with a lattice vibration, a phonon, with frequency Ω and wavevector $\boldsymbol{q}$. Energy and momentum conservation imply the following relationships:

$$\hbar\omega_i = \hbar\omega_s \pm \hbar\Omega \qquad \text{and} \qquad \boldsymbol{k}_i = \boldsymbol{k}_s \pm \boldsymbol{q}. \tag{3.1}$$

Here, the $+$ $(-)$ corresponds to the Stokes (anti-Stokes) process. Figure 3.1b resumes equation whereas figure 3.1a highlights the different resonant and non-resonant processes. Note that the case $\omega_\mathrm{i} = \omega_\mathrm{s}$ corresponds to Rayleigh scattering.

In experiments, a laser source is used in order to generate a monochromatic photon flux on the sample, and the scattered photons are dispersed and recorded, which gives rise to distinct peaks corresponding to photons having lost (Stokes) or gained (anti-Stokes) the energy of the vibrational states ($\hbar\Omega$) (see figure 3.1c, and see chapter 4 for details concerning the experimental Raman setup). The Stokes peak corresponds to a process where the system is initially in its fundamental ground state, whereas the anti-Stokes peak requires already a system with excited states. This is the reason why the anti-Stokes peak has, in general, a lower intensity[4]. Therefore, in standard Raman spectroscopy only the Stokes peaks are recorded.

Let us finally introduce a commonly used convention in spectroscopy, *i.e.* the expression of the spectral position of the recorded Raman peaks in cm^{-1}. Actually, the spectral position of the Raman peaks with respect to the incident photon is independent of the latter. Thus, it is more convenient to represent Raman spectra not in terms of energy (frequency or wavelength), but in terms of the so called *Raman shift*, according to the following equation:

$$\text{Raman shift}\,(\mathrm{cm}^{-1}) = \left(\frac{1}{\lambda_\mathrm{i}(\mathrm{nm})} - \frac{1}{\lambda_\mathrm{s}(\mathrm{nm})}\right) \times 10^7, \tag{3.2}$$

where λ_i is the wavelength of the incident photon and λ_s the wavelength of the scattered photon, corresponding to the Raman peak.

3.2 Raman modes of graphene and few layer graphene

The first Raman spectrum of graphite has been measured in 1970 [Tuinstra70] and theoretically investigated in 2004 [Reich04]. The first measurement on exfoliated isolated monolayer graphene has been performed by Ferrari *et al.* in 2006 [Ferrari06]. Since then, Raman spectroscopy has become an invaluable tool to investigate the coupling of optically created electron-hole pairs with phonons.

In order to attribute the observed peaks in the spectra to the corresponding phonon modes, let us first refer to the possible phonon modes in monolayer graphene and graphite at the Γ point, which we have identified in section 2.4. Whether a phonon mode is Raman active or not depends strongly of the symmetry of this mode. The symmetry determines if the matrix element contain-

[4] It is quite obvious that the intensity of the anti-Stokes peak decreases for increasing phonon energy, because the higher the phonon energy, the more energy the system must have. Or, more mathematically, phonons follow the Bose-Einstein distribution, *i.e.* the probability for a Stokes process scales as $1+[\exp(\hbar\Omega/k_\mathrm{B}T)-1]^{-1}$, whereas for the anti-Stokes process it scales as $[\exp(\hbar\Omega/k_\mathrm{B}T)-1]^{-1}$. Hence, the intensity ratio of the anti-Stokes and Stokes peaks is proportional to $\exp(-\hbar\Omega/k_\mathrm{B}T)$. Thus, increasing the temperature would be a way to increase the anti-Stokes/Stokes ratio. In fact, this ratio might be used to measure the temperature in, *e.g.*, graphene [Chae09, Berciaud10].

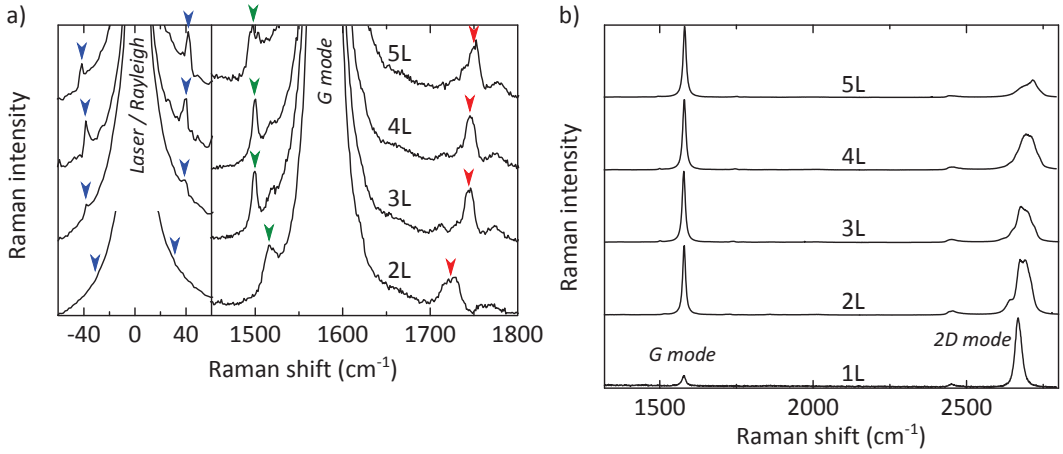

Figure 3.2: Raman spectra of mono- and few layer suspended graphene highlighting Raman features at the Γ point, recorded with a laser energy of 2.33 eV. **a)** *Left part:* Low energy Raman bands (blue arrows) corresponding to the rigid layer shear-like displacement. The measurement of these peaks at the flanks of the Rayleigh scattered light is challenging and needs a combination of several high performance optical filters (type BragGrate). The shear mode of 2L graphene could not be resolved in our measurements but its theoretical position is indicated (see ref. [Tan12]). *Right part:* The combination of the degenerate iLO/iTO modes and the rigid layer breathing-like displacement gives rise to modes in the vicinity of the pure in plane atomic displacement LO/TO mode (G mode). Part of rigid plane modes are (anti-)Stokes scattered, marked with (green) red arrows. **b)** Spectra in the range between 1300 and $2800\,\mathrm{cm}^{-1}$, showing the first order G mode feature and the second order resonant 2D mode feature (see main text for details).

ing the Raman interaction Hamiltonian vanishes or not. A detailed analysis of symmetry considerations can be found in ref. [Dresselhaus, chapter 8] and in particular in references [Saha08] and [Loudon64]. It turns out that only the E_{2g} symmetry is Raman active at the Γ point (see figure 2.6).

With increasing phonon energy, one first observes a peak at approximately $40\,\mathrm{cm}^{-1}$ on few layer graphene, also symmetry allowed in graphite (see left part of figure 3.2a, blue arrows). This peak is due to a rigid layer displacement and attributed to the so called shear mode [Tan12, Wu14]. Because of its low energy, its anti-Stokes counterpart is also recorded. We note that for its experimental observation, high performance optical filters are necessary in order to block the laser and Rayleigh lines [Tan12]. Naturally, this peak is not observed in monolayer graphene. We further note that in polar 2d materials, the shear mode is much easier to observe [Froehlicher15b].

At higher phonon energies, a strong peak at $\approx 1581\,\mathrm{cm}^{-1}$ appears, irrespective of the number of layers (see figure 3.2b). This peak called G peak, or **G mode**, is always present in sp^2 carbons [Malard09b, Ferrari13] and is attributed to the degenerate iLO/iTO branch occurring within one layer (see also the phonon dispersion in figure 2.7).

In the range between 1400 and $1800\,\mathrm{cm}^{-1}$, several other peaks occur, only present in few layer graphene (see figure 3.2a, green and red arrows), arising from the difference in point groups

between graphene/graphite and few layer graphene (see section 2.4.1). We note that in the phonon dispersion for graphene/graphite, these peaks do not correspond to any zone-center phonon mode. They are attributed to a second order[5] scattering process combining the iLO/iTO modes with the rigid layer breathing-like modes (in literature often called ZO' modes) [Sato11, Herziger12, Lui12]. Thus, these rigid layer compression and dilation modes, which are not Raman active in graphite, are here probed with a combination of the iLO/iTO modes in the case of few layer graphene. We note that the pure Raman active (few layer!) rigid layer breathing-like modes at lower energy have recently been measured, but need a thermal activation to be observed [Lui14]. They are not observed in our spectra due to their very low intensities. Note that these modes are Raman and infrared inactive in the bulk graphite.

Since the energy of both rigid layer displacement modes depend on the number of layers, the detection of these modes allow for an unambiguous determination of the number of graphene layers, up to approximately 8 layers.

In the Raman spectra of figure 3.2b, apart from the G mode, another feature at $\approx 2670\,\mathrm{cm}^{-1}$ is observed, which corresponds to a process of higher order, because the energy loss of the incident photon is too high to be attributed to a first order single phonon process. In fact, this mode is called **2D mode** and attributed to a resonant process involving two phonons with finite and opposite momentum, where $|\boldsymbol{q}| \approx \boldsymbol{K'} - \boldsymbol{K} = \boldsymbol{K}$. The fact that this mode is resonant makes it particularly sensitive to the electron and phonon dispersion. Additional graphene layers change significantly the electronic structure due to the layer coupling, notably in the case of 2L graphene [Aoki07, Zhang08, Castro Neto09]. Hence, a more complex electronic structure results in a 2D mode consisting of several sub-features [Graf07, Herziger14]. The evolution of the 2D peak with increasing number of layers has been studied experimentally [Graf07, Malard09b] and the distinctive shapes help to determine the exact number of layers (see figure 3.2b). Note that the spectra are recorded on suspended graphene, where the Raman signal is subjected to interference effects; the difference in the intensity ratio of the 2D and G mode feature is irrelevant (see section 3.5).

A further mode, which is not seen in the spectra in figure 3.2b, has to be mentioned in the context of the 2D mode. That is the defect related D mode, which occurs at approximately half of the energy of the 2D mode [Pimenta07, Lucchese10]. Since this mode corresponds to the measurement of one phonon with $|\boldsymbol{q}| \approx \boldsymbol{K}$, momentum conservation requires that the missing momentum is taken by a defect in the crystal lattice [Cancado11, Eckmann12]. Our graphene crystals are of high quality and thus do only show a negligible intensity of this mode.

[5] We note that second order is meant in the sense of a Raman process involving two phonons (in contrast to first order, a process involving one phonon, *e.g.* the G mode). However, in terms of perturbation theory, the first order is a third order process!

Other modes, which are closely related to the basic idea of the double resonant process of the 2D mode, can be observed, but are of minor interest for this thesis. Ref. [Ferrari13] gives a summary of all double resonant processes which might occur. Let us note that processes involving four or more phonons can also be observed [Tan98, Wang07, Basko08, Rao11, Gupta15].

In this thesis, we basically deal only with the G and 2D mode features. Thus, in the following, we restrict ourselves to these two and go more into the details of their physical origin. Henceforth, we will not use the term *peak* but rather the term *mode* for the Raman features because the first solely describes the observation of a higher intensity in a certain spectral range whereas the latter reflects the physical interpretation of the appearance of the peak, *i.e.* due to a vibrational *mode*.

3.2.1 G mode

As already introduced above, the G mode is associated with the doubly degenerate phonon modes iTO and iLO (see the phonon dispersion in figure 2.7). The representation of these vibrational modes in the real space is shown in figure 3.3, where one can see that the iTO and iLO modes correspond to the displacement of the sublattices A and B with respect to each other. This displacement is in phase opposition and generates no net phonon momentum, thus it is $\boldsymbol{q} \approx 0$ (the wavevectors of incident and scattered photons are negligibly small compared to the phonon energies), or, in other words, the G mode is associated to the optical phonons at the Brillouin zone center, *i.e.* at the Γ point. Indeed, the measured Raman shift of the G mode agrees with the phonon frequency in figure 2.7 at Γ. Note that in case of mechanical deformation of the graphene lattice, the degeneracy of the two modes is broken, which results in the observation of two peaks, recorded on uniaxially stretched graphene [Mohiuddin09, Huang09, Mohr09, Polyzos15] or in carbon nanotubes [Jorio02, Dresselhaus05, Piscanec07].

This phenomenological explanation in real space is insufficient to understand a bunch of experimental observations, in particular the change of the fwhm Γ_G, the spectral position ω_G, or even the integrated intensity I_G as a function of external influences, *e.g.* doping [Das08, Kalbac10].

For an ideal case of a dispersionless and undamped phonon, the corresponding Raman peak would be a Dirac distribution[6] with zero width, infinite height but well defined area. In reality, phonons decay, *e.g.* into other phonons due to anharmonicity [Bonini07], or into electron-hole pairs due to electron-phonon coupling, which broadens the Dirac distribution into a Lorentzian profile [Basko09b], so that one can describe the shape of the peak corresponding to the G mode as

$$I(\omega) = \frac{2I_\mathsf{G}}{\pi} \frac{\Gamma_\mathsf{G}}{4(\omega - \omega_\mathsf{G})^2 + \Gamma_\mathsf{G}^2}. \tag{3.3}$$

[6] Note that there is no link between the *Dirac* δ-distribution $\propto \delta(\omega - \omega_{\text{phonon}})$ and the *Dirac* point, cone or particle.

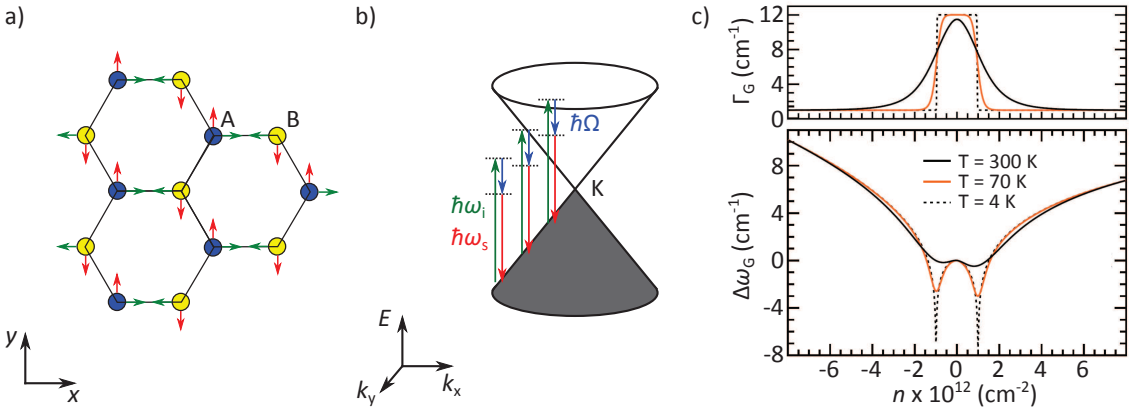

Figure 3.3: a) Atomic displacements of the degenerate iLO and iTO modes (green and red arrows) at the Γ point. For each mode, the sublattices of atoms A and B vibrate with phase opposition. **b)** Representation of Dirac cone for neutral graphene (the gray area are filled states) and processes contributing to the G mode. The dotted lines are virtual states. **c)** Γ_G and $\Delta\omega_G$ as a function of the charge density n, for different temperatures, obtained from DFT calculations taking into account adiabatic and non-adiabatic contributions of the phonon frequency shift (see main text for details). Figure (c) is adapted from ref. [Lazzeri06].

Here, I_G is the integrated intensity of the G mode feature, Γ_G is its full width at half maximum of the peak and ω_G is the peak frequency.

Let us consider the case of neutral graphene, *i.e.* the Fermi energy is situated at the K point, as schematically indicated in figure 3.3b. To get an idea of I_G, we have to know which electronic states are involved in the creation of a quasi-zero momentum phonon and thus contribute to I_G. Basko carried out important calculations and established expressions for the transition matrix elements describing all contributions to the charge-quasi-zero momentum phonon coupling [Basko08, Basko09a]. In fact, usually the G mode process is only presented schematically, as in figure 3.3b, masking possible pathways like the emission of a phonon by the electron, by the hole, at the vertex of the electron-hole creation or recombination etc. (see ref. [Basko09a] for details). The calculation of the overall matrix element taking into account all contributions (which partly cancel out because of quantum interference effects [Kalbac10, Chen11]), unveils that mostly the electronic states in the energy range of the incident photon contribute to I_G, *i.e.* states with an energy $E_{\boldsymbol{k}}$ in the range $0 \lesssim E_{\boldsymbol{k}} \lesssim \hbar\omega_i$ (see the arrows in figure 3.3b). This fact implies that the creation of an electron-hole pair is not bounded to a fixed (real) state, but to *virtual* states. That is the reason why the G mode is considered as a non-resonant Raman process (see also figure 3.1a).

3.2.2 2D mode

The physical origin of the 2D mode feature, giving rise to the peak observed at approximately $2670\,\mathrm{cm}^{-1}$, underwent a long period of discussion since the first Raman spectra [Tuinstra70] had been observed [Vidano78, Nemanich79, Vidano81, Al-Jishi82, Pócsik98]. Even if proposed earlier

[Baranov87], the paper of Thomsen and Reich explaining a doubly resonant mechanism involving two phonons is recognized as the first theoretical description of the 2D mode [Thomsen00]. Indeed, their publication treated a double resonant process involving the electron scattering with one phonon and a defect, giving rise to the above mentioned D mode, only visible in defected graphene (see figure 3.4).

Since both resonant D and 2D modes are of the same physical origin, one can discuss them within the same picture. In figure 3.4 we compare a Raman spectrum of defect-free graphene (lower part) with damaged graphene[7]. The interest in showing the spectrum of damaged graphene is because first, the spectral position of some peaks helps to elucidate the mechanisms giving rise to the 2D peak, and second, the comparison between the two spectra leads to a valuable discrimination of the quality of our graphene samples.

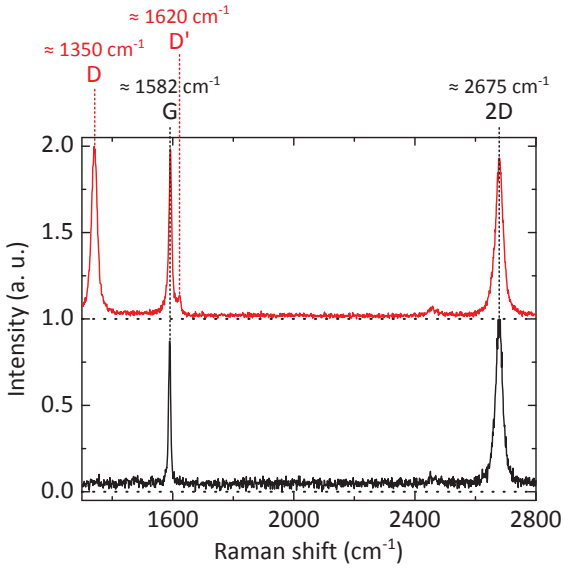

Figure 3.4: Typical Raman spectrum of defect free (black line) and defected (red line) graphene. Both spectra are obtained from exfoliated graphene on a Si/SiO_2 substrate. The defects in the upper spectrum are introduced by excessive charge carrier adding by means of top-gating with an ion gel. These data are provided by G. Froehlicher. The Raman spectra has been recorded using a laser wavelength of 532 nm (see chapter 4 for details on the experimental setup).

The basic idea is that the incident photon creates an electron-hole pair which scatters with a phonon of momentum with wavevector $\boldsymbol{q} \approx \boldsymbol{K'} - \boldsymbol{K} = \boldsymbol{K}$. Momentum conservation requires that one of the charge carriers undergoes a further scattering event with momentum $-\boldsymbol{q}$, either elastically or inelastically. The first event implies no energy loss of the charge carrier and takes place in the presence of defects (D mode), whereas the latter implies the scattering with another

[7]The graphene here has been damaged by an electrochemical reaction [Froehlicher15a].

phonon (2D mode). A sketch of one possible process for the 2D mode (inelastic scattering) is shown in figure 3.5a. Here, the electron scatters with a phonon and the hole with another phonon.

If either the electron or the hole scatters elastically with a defect, one momentum transfer vector in the sketch would not be tilted but strictly horizontal, *i.e.* $\hbar\Omega$ would be zero. In contrast to the 2D mode process, which is fully resonant, the D mode process requires an intermediate virtual state and is partly resonant. All possible processes are presented as Goldstone diagrams in figure 3.5b, where we distinguish between processes involving only one charge carrier (which scatters twice, white background) and two charge carriers (gray background).

Thus, in the Raman spectra in figure 3.4, the 2D mode is attributed to the doubly resonant mechanism involving two phonons with opposite momenta $+\boldsymbol{q}$ and $-\boldsymbol{q}$, and the D mode, visible in the spectrum of defected graphene, is attributed to the mechanism involving one phonon and a defect scattering event. Accordingly, the D mode is not present in the spectrum of defect-free graphene, and the energy loss of the electron-hole pair giving rise to the 2D mode is approximately twice the energy loss in the D mode event. Experimentally it has furthermore been shown that the I_{D} increases with increasing amount of defects and that I_{2D} is maximum for pristine graphene and decreases with increasing disorder [Ferrari07, Pimenta07, Martins Ferreira10, Lucchese10].

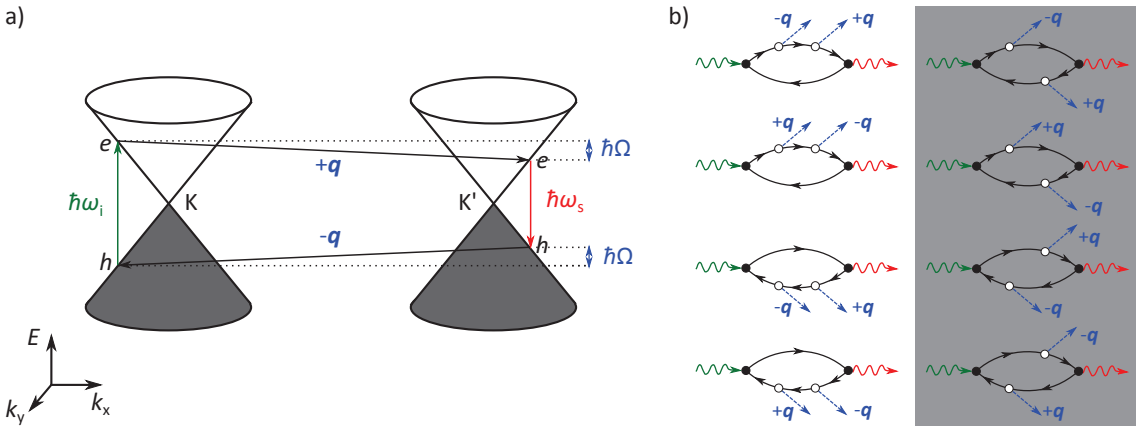

Figure 3.5: a) Schematic representation of a typical process contributing to the 2D mode phonon. An incoming photon with energy $\hbar\omega_{\mathrm{i}}$ creates an electron-hole pair and the electron scatters with a phonon with wavevector $+\boldsymbol{q}$ and energy $\hbar\Omega$. The energy of the phonon is determined by the phonon dispersion (see figure 2.7) at K. To fulfill momentum conservation, the hole scatters with a phonon with wavevector $-\boldsymbol{q}$. **b)** Goldstone diagrams of all processes susceptible to contribute to the 2D phonon process. The process represented in (a), *e.g.*, is the second process in the right column. Processes where the electron (or the hole) scatters twice are also possible (left column). (b) is adapted from ref. [Venezuela11].

Let us finally note the presence of a peak labeled D' at approximately $1620\,\mathrm{cm}^{-1}$. This peak is also only present in defected graphene and mostly attributed to the *intra*-valley version of the D mode process (in contrast to the *inter*-valley process of the D mode, see ref. [Ferrari13] for more details).

Even if the picture described above is convincingly simple and often employed to grossly describe the mechanism giving rise to the 2D peak, recent studies suggested that the analysis of the 2D mode should be refined [Maultzsch04a, Venezuela11, Berciaud13]. To get the full picture of the processes giving rise to the 2D peak, one has to consider the transition matrix element for each intermediate state involved in the process, *i.e.* use Fermi's Golden rule to the fourth order. Furthermore, one has to be aware of influences from trigonal warping, which is responsible for the observation of two sub-features in undoped clean graphene [Berciaud13], attributed to the so called *inner* and *outer* process. We will discuss this observation in detail later. At high energies of the incident photons, trigonal warping leads to a partly vanishing 2D mode [Tyborski15]. In experiments on supported graphene in the with excitation in the visible light range, influences on the shape due to trigonal warping are usually smeared out and clean graphene is required to have a deeper insight in the 2D mode mechanism [Berciaud13].

In the following, we will briefly discuss the matrix elements contributing to the 2D mode intensity. In addition, we will focus on the line shape of the 2D mode and address corrections in the symmetry of the peak due to trigonal warping.

The Raman intensity for a given $\boldsymbol{q}$ results from a sum over $\boldsymbol{k}$ of all scattering amplitudes, which are complex numbers. Following the work of Venezuela *et al.*, the real and imaginary part of the scattering amplitudes are of the same order of magnitude. As a consequence, the sum of these complex numbers can interfere constructively and destructively. Their calculations reveal that for the processes presented with a gray background in figure 3.5b, the interference is constructive. Thus, the processes where each charge carrier of the electron-hole pair scatters with a phonon, respectively, are dominant, and this to equal parts, giving rise to the 2D mode intensity [Venezuela11]. The authors stress that the relatively high intensity (the 2D process is a fourth order process!) originates from quantum interference effects and that the classical argument of being a fully resonant process does not account for the intensity [Maultzsch04a, Basko07].

Maultzsch *et al.* pointed out that quantum interferences strongly affect the line shape of the processes involving phonons with wavevector $\boldsymbol{q} \approx \boldsymbol{K}$ [Maultzsch04a]. Indeed, Basko proposed a modified Lorentzian line shape:

$$\frac{\mathrm{d}I_{\mathrm{2D}}(\omega)}{\mathrm{d}\omega} \propto \left[(\omega - \omega_{\mathrm{2D}})^2 + \frac{\Gamma_{\mathrm{2D}}^2}{4(2^{2/3}-1)}\right]^{-3/2}, \tag{3.4}$$

where Γ_{2D} and ω_{2D} are the full width at half of the maximum value of the peak (fwhm) and the peak frequency, respectively, of the 2D mode feature [Basko07, Basko08]. This equation can be integrated and normalized to 1 so that one can extract its integrated intensity I_{2D}, convenient for experimental data analysis:

$$I_{\mathrm{2D}}(\omega) = I_{\mathrm{2D}}\Gamma_{\mathrm{2D}}^2 \left\{ 8(2^{2/3}-1)\left[(\omega-\omega_{\mathrm{2D}})^2 + \frac{\Gamma_{\mathrm{2D}}^2}{4(2^{2/3}-1)}\right]^{3/2}\right\}^{-1}. \tag{3.5}$$

We note that in the work of this thesis we use the line shape proposed by Basko in a pure *phenomenological* manner. We have stated that this shape adjusts well the experimental data of the 2D mode feature, in particular better than a pure Lorentzian profile, but not necessarily better than a Voigt profile. However, the latter requires more fitting parameters, whereas the Basko profile comes along solely with the peak position and its linewidth.

The inverse lifetime of the electrons (holes), 2γ, is related to the fwhm, Γ_{2D}, according to

$$\Gamma_{\mathrm{2D}} = 8\gamma\frac{v_{\mathrm{TO}}}{v_{\mathrm{F}}}\sqrt{2^{2/3}-1}. \tag{3.6}$$

v_{TO} and v_{F} are the phonon and Fermi velocities, respectively. Equation (3.5) takes into account only the broadening due to the charge carriers and neglects the one of the phonon states as well as the anisotropy of the phonon dispersion (trigonal warping) [Basko08], which means that the experimentally measured line shape is always broader than equation (3.6). One measures usually $\Gamma_{\mathrm{2D}} \approx 30\,\mathrm{cm}^{-1}$ [Berciaud09], which hence corresponds to an unrealistically large value of $2\gamma \approx 200\,\mathrm{meV}$.

The broad width of the 2D mode feature is an indication that other mechanisms have to be taken into account. In addition, an asymmetric line shape is often observed on ultra-clean graphene samples [Berciaud09, Luo12, Lee12b].

In order to account for these observations, we have a look on the electron iso-energy contours in the vicinity of the high symmetry line $\Gamma \rightarrow \mathrm{K} \rightarrow \mathrm{M} \rightarrow \mathrm{K'} \rightarrow \Gamma$ (see figure 3.6a). Cuts near E_{F} are white and have circular shape whereas cuts further away from E_{F} display a trigonal shape. Thus, phonons with slightly different wavevectors contribute to the Raman 2D process, in particular, phonons with wavevector $\boldsymbol{q}_{\mathrm{outer}} > \boldsymbol{K}$ ($\boldsymbol{q}_{\mathrm{inner}} < \boldsymbol{K}$) corresponding to a vector connecting the *outer*most (*inner*most) part of the contours. A schematic representation of these two processes is shown in figure 3.6b.

A closer look to the electronic dispersion reveals that $\boldsymbol{K} - \boldsymbol{q}_{\mathrm{inner}} \neq \boldsymbol{q}_{\mathrm{outer}} - \boldsymbol{K}$. This can be easily seen by a pure geometrical analysis: The distance between K and the energy contour line when going in the Γ-direction is shorter than when going in the M-direction (see straight and dashed blue arrows, respectively, in figure 3.6a and b). The same argument holds for the K' point. Different phonon momenta should provide different phonon energies, in particular in the case of a symmetric phonon dispersion around K. However, DFT calculations with GW corrections show that trigonal warping effects slightly steepen the phonon dispersion in the M-direction and flatten it in the Γ-direction [Lazzeri08] (see figure 3.6c). The momentum magnitudes are such as the

trigonal warping effect of the electron and momentum dispersions mainly cancel out [Grüneis09, Venezuela11], at least in the range of exicitations with visible light.

Thus, experimentally, the distinction between inner and outer loop is challenging [Berciaud13]. Within the past decade, the dominant contribution to the intensity of the 2D mode feature has been first attributed to the outer loop [Thomsen00, Kürti02, Ferrari06, Graf07], before a possible explanation by a dominant inner loop came up [Huang10, Mohr10, Frank11, Mafra11, Yoon11b]. In particular, Venezuela *et al.* performed a detailed calculation of the sub-processes contributing to the 2D mode, not only taking into account $\boldsymbol{q}_{\text{inner}}$ and $\boldsymbol{q}_{\text{outer}}$ but all possible wavevectors $\boldsymbol{q}_{\text{n}}$. These can be determined geometrically by shifting the energy contour at K to K' and identifying the nesting contours, as sketched in figure 3.6d and e. The ensemble of all possible wavevectors is then presented in figure 3.6f as dashed white line and superimposed with the calculated Raman 2D mode intensity, decomposed in components associated to phonons with a given wavevector $\boldsymbol{q}_{\text{n}}$, for an incident photon energy of 2.4 eV. To complete, we show the phonon iso-energy contours in figure 3.6g. Note that the pictorial (one dimensional) argumentation about the trigonal warping effect on the cancellation of the 2D mode phonon splitting does also hold for wavevectors away from the high symmetry line, because the trigonal warping corrections of electron and phonon iso-energy contours in figures 3.6d and g are opposite (triangles pointing to M *vs.* pointing away from M).

The comparison of the 2D mode measured on suspended and supported graphene in a range of excitation energies range from 1.5 to 2.7 eV, which is shown in figures 3.6h and i, reveals an unambiguous asymmetric lineshape on ultra-clean suspended graphene, and on supported graphene the asymmetry is smeared out due to unintentional charge transfer from the underlying SiO_2 substrate [Berciaud09, Berciaud13]. The experimental observation of the asymmetry on suspended graphene samples is an indication for an imperfect cancellation of the electron and phonon trigonal warping effects, even if the Raman shift between the two sub-features is small ($\approx 12\,\text{cm}^{-1}$). Furthermore, the authors observed a broadening of the two 2D sub-features with decreasing photon energy, which is in contradiction with equation (3.6). Thus, it seems as if Γ_{2D} is not simply proportional to the electron/hole lifetime but that other contributions from a broader range of phonon energies have to be taken into account.

We note that photon excitations in the UV range lead to a significant broadening and splitting of the 2D mode feature. This is because the cancellation of the trigonal warping effects is canceled [Venezuela11]. At even higher excitations approaching the M point (≈ 5 eV) (see figures 2.2a and b), the inner process becomes suppressed, as shown recently on graphite [Tyborski15].

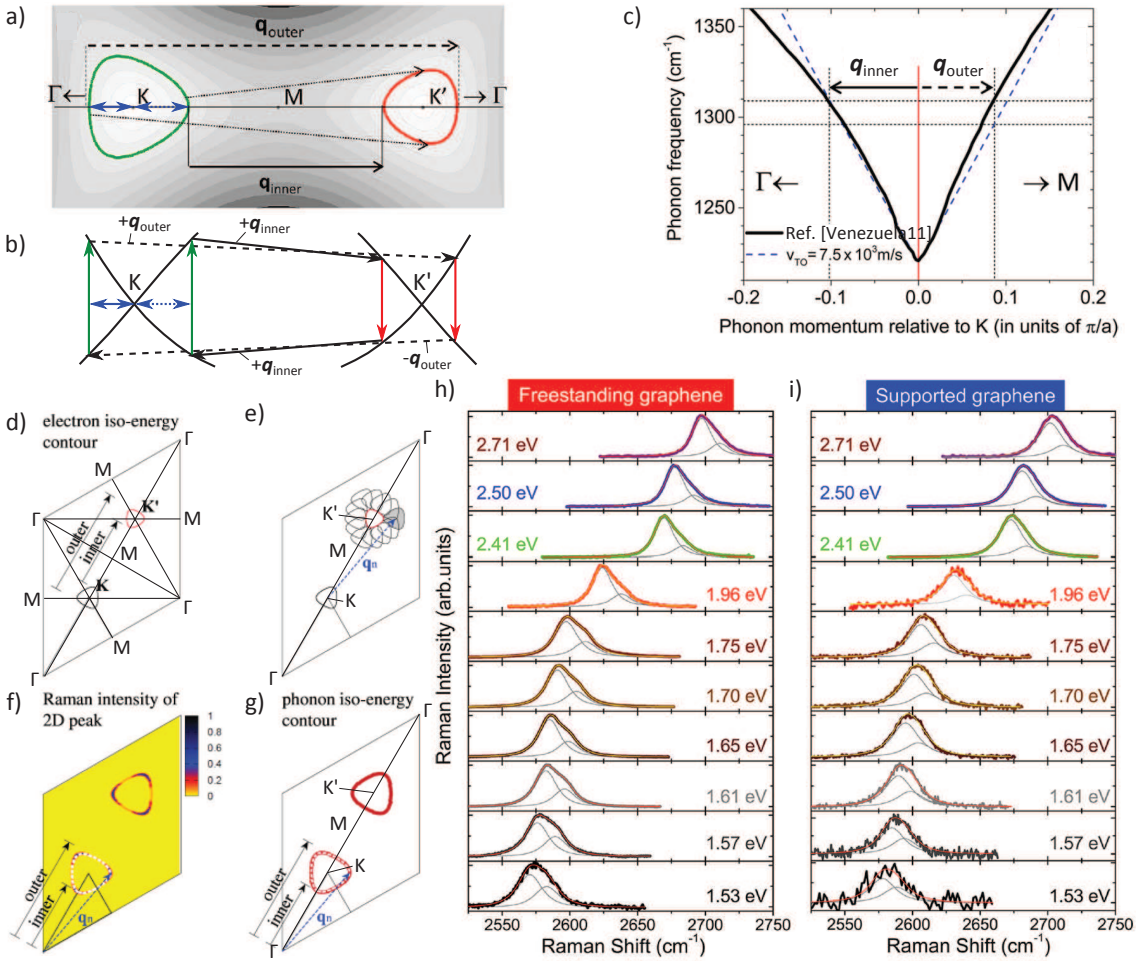

Figure 3.6: a) Schematic representation of the 2D mode process in the two-dimensional Brillouin zone of graphene. The trigonal warping of the electronic dispersion, computed using a tight binding model [Castro Neto09], is clearly visible. The green (red) lines represent the iso-energy contours at the incoming and outgoing photon energies. The solid (dashed) arrow corresponds to the inner (outer) loop. The dotted arrows illustrate contributions from optical phonons away from the high symmetry lines. The blue arrows highlight the different distances of the iso-energy contour in Γ and M direction. **b)** 1d fully resonant representation of the inner (black straight arrows) and outer (black dashed arrows) loops in the momentum-energy space, along $\Gamma \rightarrow$ K $\rightarrow$ M $\rightarrow$ K' $\rightarrow \Gamma$. The underlying process is the same as represented in figure 3.5. **c)** Theoretical dispersion of the TO phonon branch (black solid line, extracted from Venezuela *et al.* (see also figure 2.7) [Venezuela11] in the vicinity of the K point along the $\Gamma \rightarrow$ M $\rightarrow$ K line. The dashed blue line represents an isotropic phonon dispersion. The solid (dashed) horizontal arrow represents the inner (outer) phonon momentum (relative to the K point) calculated for a laser energy of 1.5 eV, using the fully resonant 1d models in (b). (a), (b) and (c) are adapted from ref. [Berciaud13]. **d)** The triangularly distorted contour around K for a laser excitation energy of 2.4 eV. The energy of the contour around K' is reduced by half of the energy of the corresponding 2D mode phonon (corresponds to an energy of 2.06 V). **e)** q_n is one of the vectors such that the contour near K translated by q_n is tangent to (nesting) the contour near K'. **f)** Raman intensity distribution in the reciprocal space for the 2D mode, as calculated by Venezuela *et al.* [Venezuela11]. The dashed closed line is defined by the ensemble of the q_n vectors. **g)** Phonon iso-energy contours. As discussed in the main text, the trigonal warping of these contours is opposite to the one of the electron iso-energy contours. (d)-(g) are adapted from ref. [Venezuela11]. **h)** and **i)** show Raman measurements of the 2D mode feature at different excitation energies, on suspended and supported graphene, respectively. An asymmetry is clearly visible on the former, whereas this asymmetry is smeared out on the latter. The figure is adapted from ref. [Berciaud13].

3.3 Sensitivity to external perturbations

3.3.1 Influence of doping

Adding charges to neutral graphene has an impact on both the G and 2D mode phonons, and that both on the energy, *i.e.* the spectral position of the corresponding peak, and the lifetime, which is proportional to the inverse of the linewidth of the peak.

The G mode process is non-resonant and of first order, whereas the 2D mode process is non-resonant and of fourth order. Hence, this distinction leads to a different response upon a change in the Fermi energy. In the following, we will first discuss the influence of doping on the G mode and then on the 2D mode.

Experimentally, a shift of ω_{G} is observed with changing doping level [Yan07, Pisana07, Das08, Yan08a, Araujo12, Froehlicher15a]. The reported stiffening of ω_{G}, irrespective of the sign of the charge carriers, is a consequence of the fact that the energy of the electronic states are in the same range as the phonon energies. This observation has been published by Yan *et al.*, and nearly at the same time by Pisana *et al.* under the title *Breakdown of the adiabatic Born-Oppenheimer approximation*. This approximation assumes that the lighter electrons adjust adiabatically to the motion of the heavier nuclei, remaining at any time in their instantaneous ground state [Pisana07]. However, in graphene, the electrons do not have enough time to adjust their momenta to reach the instantaneous adiabatic ground state, because of collisions with phonons [Shafraniuk15]. This is also a direct consequence of the lack of an energy gap. Thus, due to the interaction of the electrons and the phonons, the phonon energy has to be renormalized. The shift due to this renormalization with respect to ω_{G}^0, the phonon frequency of neutral graphene, is obtained by time-dependent perturbation theory and writes as [Ando06, Pisana07]:

$$\Delta\omega_{\mathsf{G}}^{\mathsf{NA}} = \frac{\lambda_\Gamma}{2\pi\hbar} \fint_{-\infty}^{\infty} \frac{[f(E-E_{\mathsf{F}}) - f(E)]\, E^2\, \mathsf{sgn}(E)}{E^2 - (\hbar\omega_{\mathsf{G}}^0)^2/4}\, \mathsf{d}E, \tag{3.7}$$

where $\fint$ denotes the Cauchy principal value and f the Fermi-Dirac distribution at a given temperature T. λ_Γ is a dimensionless coefficient corresponding to the electron-phonon coupling strength at the Γ point[8]. The superscript index NA refers to the fact that the renormalization is non-adiabatic.

De facto, an adiabatic contribution to the shift of ω_{G} has to be taken into account, because the doping also induces a change of the lattice parameters, *i.e.* a change of the carbon-carbon bond strength [Pietronero81]. In contrast to the non-adiabatic contribution, the adiabatic is not symmetric with respect to electron and hole doping. Negative doping adds electrons to the anti-bonding orbitals (see also 2.2) which leads to a phonon softening, whereas removing electrons

[8] Here, the definition of the coupling strength coefficient is defined as in ref. [Basko08]. The coefficient α' used in references [Pisana07] and [Lazzeri06] is $\alpha' = \lambda_\Gamma/(2\pi)$.

leads to a phonon hardening [Lazzeri06, Kalbac10]. Here, the adiabatic Born-Oppenheimer approximation can be used and results in an analytic expression obtained by varying the lattice spacing constant within DFT calculations [Lazzeri06]:

$$\frac{\Delta\omega_{\mathsf{G}}^{\mathsf{A}}}{2\pi c_0} = -2.13n - 0.0360n^2 - 0.00329n^3 - 0.226|n|^{3/2}, \tag{3.8}$$

which is, as expected, not symmetric in n, the charge carrier density. The Fermi energy at a given n is $E_{\mathsf{F}} = \mathrm{sgn}(n)\hbar v_{\mathsf{F}}\sqrt{\pi|n|}$, where v_{F} is the, in a first approximation, constant Fermi velocity[9]. Thus, the overall doping induced change in the frequency of the G mode phonon can be written as

$$\Delta\omega_{\mathsf{G}}^{\mathsf{D}} = \omega_{\mathsf{G}}^{\mathsf{D}} - \omega_{\mathsf{G}}^{0} = \Delta\omega_{\mathsf{G}}^{\mathsf{NA}} + \Delta\omega_{\mathsf{G}}^{\mathsf{A}}, \tag{3.9}$$

where ω_{G}^{0} is the frequency of the G mode phonon for undoped graphene. In figure 3.3c we show the corresponding result of the calculations performed by Lazzeri *et al.* for different temperatures [Lazzeri06]. As already reported by Ando in 2006, the frequency shift exhibits a logarithmic singularity when the Fermi energy is half of the energy of the optical phonon [Ando06]. Due to the thermal broadening, the singularity is smeared out with increasing temperature. Thus, in order to observe this particular phonon behavior, low temperatures and clean graphene samples with vanishing charge inhomogeneity are required, a reason why suspended graphene samples build the ideal platform to do so. We note that the phonon stiffening at higher n has been observed in several experiments [Pisana07, Das08, Kalbac10, Chen11, Froehlicher15a] and that the phonon renormalization in 2L graphene has been sudied in detail, which is experimentally less challenging because the E_{F} scales linearly with n in 2L graphene whereas it scales with the square root of n in 1L graphene [Yan07, Yan08a]. Thus, tuning n results rapidly in a high E_{F} compared to 2L graphene, making an exact screening of the phonon anomaly challenging.

We now consider the change in Γ_{G} with doping. The phonon linewidth is directly related to its lifetime. A short lifetime displays the presence of many available decay channels which results in a broadening of the energy. In fact, in undoped samples the phonon can decay by creating an electron-hole pair [Lazzeri06, Piscanec07]. If the Fermi energy is higher (lower) than half of the phonon energy, this process is suppressed because the final states are occupied by electrons (empty). The phonon lifetime is longer which results in a narrow G mode [Yan07]. This evolution is also a further result of the calculations of Lazzeri *et al.* [Lazzeri06]:

$$\Delta\Gamma_{\mathsf{G}} = \Gamma_{\mathsf{G}} - \Gamma_0 = \frac{\lambda_\Gamma}{4}\,\omega_{\mathsf{G}}^{0}\left[f\left(-\frac{\hbar\omega_{\mathsf{G}}^{0}}{2} - E_{\mathsf{F}}\right) - f\left(\frac{\hbar\omega_{\mathsf{G}}^{0}}{2} - E_{\mathsf{F}}\right)\right]. \tag{3.10}$$

[9] Some authors report a Fermi velocity which depends on n [Hwang12, Siegel13, Faugeras15], in particular, an increase of v_{F} has been observed for low doping levels in very clean graphene [Elias11].

Here, Γ_0 takes into account sources of broadening that are independent on the charge carrier density, *e.g.* anharmonic coupling (to other phonons) [Bonini07] or the instrument response function (see chapter 4 for more details on the experimental setup).

A plot of equation (3.10) is shown in the upper part of figure 3.3c, for different temperatures. The limits of the Pauli blocked phonon decay are sharp at $T = 4$ K and are smeared out at higher temperatures. However, a significantly higher linewidth can still be observed for undoped graphene at room temperature [Yan07, Das08, Froehlicher15a]. We note that Γ_0 in experiments is rather 5 to $8\,\mathrm{cm}^{-1}$ (due to the response of the spectrometer and anharmonic effects such as electron-electron or phonon-phonon coupling [Berciaud09]), which consequently leads to a higher value of Γ_G at $n = 0$ than shown in figure 3.3c, typically 14 to $16\,\mathrm{cm}^{-1}$.

Since a multitude of possible quantum pathways are probed in the G mode Raman process, the change in the Fermi energy might contribute to an enhancement or a reduction of I_G due to quantum interference effects [Basko09b, Kalbac10, Chen11]. In experiments, I_G has been observed to be nearly constant, at least for doping levels with $E_\mathsf{F} < \hbar\omega_\mathsf{i}$. At higher doping levels ($2E_\mathsf{F} \approx \hbar\omega_\mathsf{i}$), Chen *et al.* and Kalbac *et al.* observed constructive quantum interferences responsible for a strong increase of I_G [Kalbac10, Chen11].

We now briefly comment on the effect of doping on the 2D mode feature. First, it has been observed that the asymmetry in the line shape vanishes when charge carriers are added on suspended graphene [Berciaud13]. This observation is in agreement with the symmetric line shape on supported graphene on SiO_2 (see, *e.g.*, figure 3.6i), where graphene is known to be unintentionally doped [Martin08, Xue11]. Thus, to first approximation, the 2D mode of supported graphene can be regarded as a broadened copy of the intrinsic 2D mode feature observed on clean suspended graphene.

When the charge carrier density is further increased, one observes only slight changes in both ω_2D and Γ_2D (see experiments on supported back-gated [Yan07, Das08] and top-gated graphene [Froehlicher15a]). ω_2D varies little at moderate doping ($|E_\mathsf{F}| \lesssim 200\,\mathrm{meV}$), but tends to stiffen (soften) significantly for stronger hole (electron) doping. This evolution of ω_2D can be qualitatively understood as the sum of a dominant adiabatic contribution and a weaker non-adiabatic contribution. The latter is reduced as compared to the case of the G mode feature, because the 2D mode feature involves phonons that are significantly away from the edges of the Brillouin zone [Das08, Froehlicher15a].

Finally, we address the dependence of I_2D on doping. In contrast to I_G (in the limit of $|E_\mathsf{F}| \leq \hbar\omega_\mathsf{i}/2$) [Basko09a, Kalbac10, Chen11], I_2D is significantly affected by doping [Das08, Basko09b, Das09]. Under full resonance, the photon-generated electron-hole pairs can scatter not only with phonons but also with doping-induced electrons or holes. This additional scattering mechanism is responsible for a decrease in I_2D, which is, again, much stronger than for I_G [Chen11]. Indeed, following Basko [Basko08, Basko09b], I_2D is proportional to $(\gamma_\mathsf{K}/(\gamma_\Gamma + \gamma_\mathsf{K} + \gamma_\mathsf{ee}))^2$, where $\gamma_{\Gamma,\mathsf{K}}$

are the phonon scattering rates at the Γ and K point, respectively, and γ_{ee} is the electron-electron scattering rate, which scales linearly with E_F [Basko09b]. This linear dependence has been shown for $|E_F| \gtrsim 200$ meV, within a range between -100 and $+100$ meV, I_{2D} can be regarded as constant [Froehlicher15a].

3.3.2 Influence of strain

With reference to the adiabatic contribution of the charge carriers to the phonon frequency, we already mentioned that the change in the lattice constant leads to a change in the Raman frequencies. Of course, this change can be achieved in a more trivial manner, *i.e.* by applying mechanical strain. This strain can be uniaxial, biaxial or a mixture of both, and either compressive or tensile (dilative). Uniaxial strain breaks the degeneracy of the iLO/iTO phonon branches giving rise to the G mode, which splits into two phonons labeled G^- and G^+, corresponding to a phonon of lower ($-$) and higher frequency ($+$) (see figure 3.7a and b) [Huang09, Mohiuddin09, Mohr09]. According to ref. [Mohiuddin09], the strain induced frequency shift of ω_G is

$$\Delta\omega^S_{G\pm} = -\omega^0_G\,\gamma_G\,(\epsilon_l + \epsilon_t) \pm \frac{1}{2}\,\beta_G\,\omega^0_G\,(\epsilon_l - \epsilon_t). \tag{3.11}$$

Here, ϵ_l and ϵ_t are the longitudinal and transverse component of the strain, γ_G is the Grüneisen parameter and β_G the shear deformation potential. Thus, in practice, an increasing component of uniaxial strain, first broadens the G mode feature and then evolves into two distinct peaks [Huang09, Mohiuddin09, Metzger09]. Note that, in the case of biaxial strain, equation (3.11) reduces to a simple shift of ω_G according to $\Delta\omega^S_G = -2\,\omega_G\gamma_G\,\epsilon$.

Note that, under uniaxial strain, the intensity of the G mode sub-feature strongly depends on the laser polarization and that it can be used to determine the orientation of the graphene flake [Huang09, Mohiuddin09].

The latter equation for biaxial strain holds also for the change in ω_{2D}, by replacing the indices G by 2D. In particular, the Grüneisen parameter γ_{2D} is different for the 2D mode phonon. In figure 3.7c we compare spectra of supported graphene and of the center of a graphene bubble, which shows a consequent shift of the Raman peaks due to biaxial strain. In addition, figures 3.7d and e display the spatial distribution of ω_G and ω_{2D}, revealing that the biaxial strain is strongest at the center of the bubble [Zabel11].

The degeneracy breaking under uniaxial strain shifts the position of the Dirac cones with respect to their initial positions at K and K' in the reciprocal space [Huang10]. When large strain is applied along high-symmetry directions (zig-zag or armchair), the Dirac cones at the K points shift opposite to those at the K' points. As discussed previously, the 2D mode process involves phonons with momentum transfer between neighboring Dirac cones. Therefore, the 2D mode process under uniaxial strain involves phonons with different momenta and different energies, which is ex-

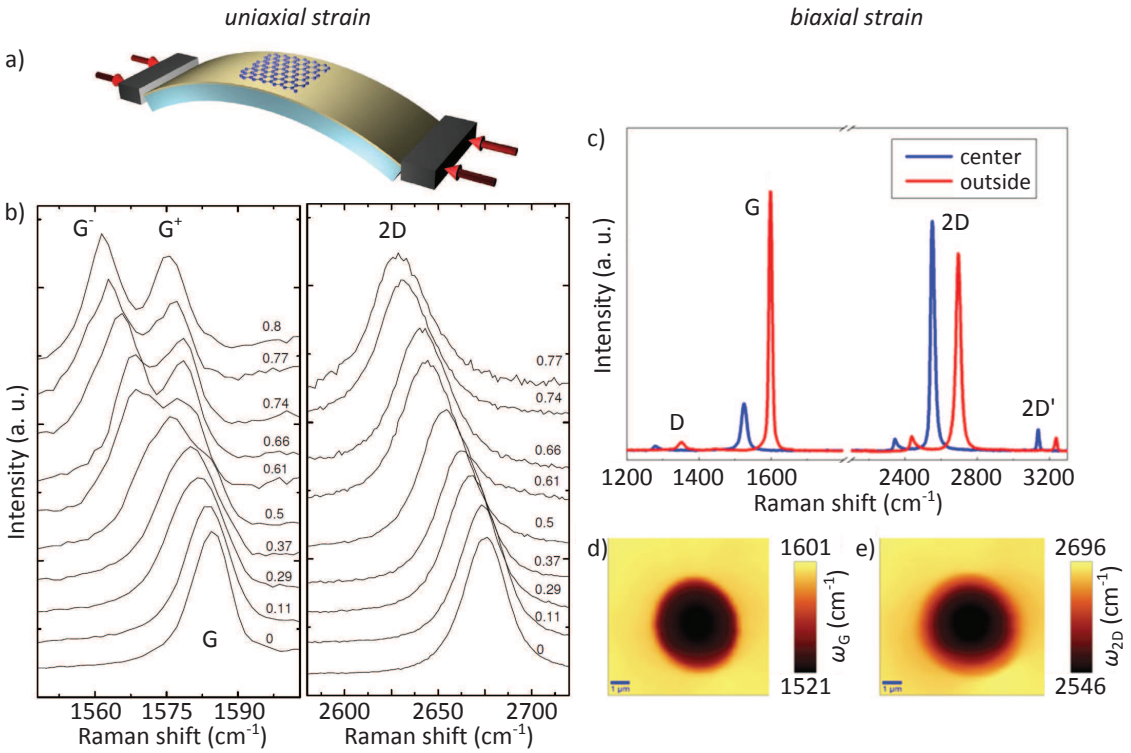

Figure 3.7: Influence of uni- (left) and biaxial (right) strain on the Raman G and 2D modes. **a)** Scheme of uniaxially applied strain by bending a graphene sheet exfoliated on a flexible SU8 substrate. **b)** Raman spectra measured on a device as in (a), showing a shift of the G and 2D modes and a splitting of the first into two subfeatures G^- and G^+. A broadening of the 2D mode feature is observed, but no splitting, because the strain axis did not correspond to a high-symmetry direction ($\lambda_{\text{laser}} = 514\,\text{nm}$). (a) and (b) are taken from ref. [Mohiuddin09]. **c)** Raman spectra measured at the center of a graphene bubble (blue line) and on flat graphene supported by the substrate (red line) ($\lambda_{\text{laser}} = 488\,\text{nm}$). Tensile biaxial strain at the center of the bubble leads to a downshift of the Raman modes. **d)** and **e)** Smoothed Raman maps of the G and 2D peak position on the bubble, respectively. ω_G and ω_{2D} strongly decrease when going from the substrate to the center of the bubble. (c)-(e) are taken from ref. [Zabel11].

pressed as a splitting of the 2D mode feature in the Raman spectra [Huang10, Frank11, Yoon11b, Popov13, Polyzos15]. Note that this splitting is only observed when the strain axis is along a high-symmetry direction. Within intermediate directions, the Raman spectra show a strain-induced broadening [Huang10].

To conclude this section, we finally give an overview of the main characteristics one expects from a Raman measurement on a clean unperturbed (undoped and unstrained) graphene membrane ($\lambda_{\text{laser}} = 532\,\text{nm}$):

- absence of the D and D' mode features at approximately $1350\,\text{cm}^{-1}$ and $1620\,\text{cm}^{-1}$,
- ω_{G} at $1581 \pm 1\,\text{cm}^{-1}$,
- Γ_{G} of $14 \pm 1\,\text{cm}^{-1}$,
- asymmetric line shape of the 2D mode feature. [Berciaud13]

3.4 Correlation of the Raman frequencies

In the previous section we have seen that both doping and strain affect both the G and 2D mode. Some features directly give an information about the doping level, such as Γ_{G} (see equation (3.10) and figure 3.3c), or the kind of strain (splitting of the modes). However, these characteristics are limited when the issue is the exact determination of the strain and doping level. Hence, considering ω_{G} and ω_{2D} is appropriate since both shift with strain and doping, but with different shift rates $\partial\omega_{\text{2D}}/\partial\omega_{\text{G}}$. Lee *et al.* studied in detail the shift rates of supported graphene, where thermal annealing introduced charge carriers and strain at the same time [Lee12a]. Then, the authors analyzed the frequency shifts upon doping and strain by correlating them.

This *optical separation of mechanical strain from charge doping* is based on a vector decomposition model in the ω_{G}-ω_{2D}-plane, reliably up to certain limiting conditions, which will be discussed hereafter. Before introducing the basic principle of Lee's proposition, we have to address an intriguing question, which is one of the limiting factors, or let us say difficulties, for a reliable application of the vector decomposition model. This is the question of the reference point (ω^0_{G}, ω^0_{2D}) of undoped and unstrained graphene.

One might suppose that ω^0_{G} corresponds to the value usually measured on graphite, which is $1581 \pm 1\,\text{cm}^{-1}$ and has been confirmed on several measurements on clean graphene samples [Berciaud09, Ni09]. However, for ω^0_{2D}, the situation is more complicated. ω_{2D} and hence ω^0_{2D} depends on the energy of the incoming photon [Pócsik98, Ferrari13], thus every given reference point is not universal but has to be considered with respect to the laser wavelength. Furthermore, ω_{2D} depends on the phonon (v_{TO}) and the Fermi velocity (v_{F}). These quantities might be different on suspended and supported graphene. Here, we should already anticipate that in the vicinity of

the reference point, the correlations are not very well defined, in particular because ω_G and ω_{2D} vary little at low deoping levels. We will come back to the limits of the model later. Let us now outline Lee's vector decomposition model, supposing that one is able to define a reference point $(\omega_G^0, \omega_{2D}^0)$.

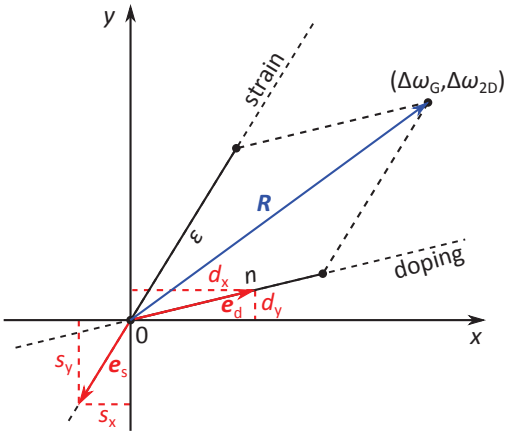

Figure 3.8: Schematic of the vector decomposition of the strain and doping component in the ω_G-ω_{2D}-plane. The point $(\Delta\omega_G, \Delta\omega_{2D})$ defines a vector $\boldsymbol{R}$ which can be projected on the vectors $\boldsymbol{e}_s$ and $\boldsymbol{e}_d$ which form the coordinate system of strain and doping.

The aim is to be able to attribute every measured pair of ω_G and ω_{2D} to a value of strain ϵ and charge density n. Let $\boldsymbol{R}$ be a a vector of Raman shifts $(\Delta\omega_G, \Delta\omega_{2D})$ in the x-y-plane (ω_G-ω_{2D}-plane) (see blue vector in figure 3.8). $\boldsymbol{R}$ can be expressed in a coordinate system with $\boldsymbol{e}_s$ and $\boldsymbol{e}_d$ as basis vectors, where $\boldsymbol{e}_s$ is a vector along the strain shift rate:

$$\boldsymbol{e}_s = \begin{bmatrix} s_x \\ s_y \end{bmatrix}, \qquad \left.\frac{\partial\omega_{2D}}{\partial\omega_G}\right|_{\text{strain}} = \frac{s_y}{s_x} \tag{3.12}$$

and $\boldsymbol{e}_d$ is a vector along the doping shift rate:

$$\boldsymbol{e}_d = \begin{bmatrix} d_x \\ d_y \end{bmatrix}, \qquad \left.\frac{\partial\omega_{2D}}{\partial\omega_G}\right|_{\text{doping}} = \frac{d_y}{d_x}. \tag{3.13}$$

$\boldsymbol{R}$ in the new coordinate system is then

$$\boldsymbol{R} = n \begin{bmatrix} d_x \\ d_y \end{bmatrix} + \epsilon \begin{bmatrix} s_x \\ s_y \end{bmatrix} = \begin{bmatrix} n \\ \epsilon \end{bmatrix}, \tag{3.14}$$

where n and ϵ are the projections on the doping and the strain axis in the new coordinate system. Solving equation (3.14) with respect to n and ϵ gives the result

Ref.	Method	$\partial\omega_{2D}/\partial\omega_G\vert_h$	$\partial\omega_{2D}/\partial\omega_G\vert_e$	Samples
[Das08]	exf., bg, SiO_2	0.65	0.2	1
[Das09]	exf., bg, SiO_2	0.75	0.2	1
[Tiberj13]	exf., bg, hydr.phil. SiO_2	0.6	-0.2	1
	exf., bg, hydr.phob. SiO_2	-	0.17	1
[Fromm13]	epit., tg, SiO_2	0.38 ± 0.02	-0.10 ± 0.03	2
[Froehlicher15a]	exf., tg, SiO_2	0.55 ± 0.20	0.2 ± 0.13	30

Table 3.1: Overview of the doping induced shift rates available in literature. All samples are exfoliated (exf.) on Si/SiO_2 substrates, the gating is done either by back-gating (bg) or top-gating (tg) using an ion gel. Fromm *et al.* used transferred epitaxial (epit.) graphene. The given errors are the standard deviation for the referenced using more than one sample.

$$\begin{aligned} n &= M_d \frac{\Delta\omega_G s_y - \Delta\omega_{2D} s_x}{s_y d_x - s_x d_y} \\ \epsilon &= M_s \frac{\Delta\omega_{2D} d_x - \Delta\omega_G d_y}{s_y d_x - s_x d_y}. \end{aligned} \tag{3.15}$$

The length of the unity vectors $\boldsymbol{e}_s$ and $\boldsymbol{e}_d$ is 1, s_x, s_y, d_x and d_y can be expressed in terms of the corresponding slopes:

$$\begin{aligned} s_x &= \cos\left[\arctan\left(\left.\frac{\partial\omega_{2D}}{\partial\omega_G}\right|_{strain}\right)\right] \\ s_y &= \sin\left[\arctan\left(\left.\frac{\partial\omega_{2D}}{\partial\omega_G}\right|_{strain}\right)\right] \\ d_x &= \cos\left[\arctan\left(\left.\frac{\partial\omega_{2D}}{\partial\omega_G}\right|_{doping}\right)\right] \\ d_y &= \sin\left[\arctan\left(\left.\frac{\partial\omega_{2D}}{\partial\omega_G}\right|_{doping}\right)\right]. \end{aligned} \tag{3.16}$$

In order to define a scale in the strain and doping direction, we have multiplied the equations (3.15) with scaling factors M_d and M_s, respectively. These factors have to be determined by looking at the Raman shifts caused by a known amount of charge in unstrained graphene and of strain in undoped graphene.

Several authors have analyzed the shift rates $\partial\omega_{2D}/\partial\omega_G$ upon doping [Das08, Das09, Fromm13, Tiberj13, Froehlicher15a] and have found out that the shift rates are different for electron and hole doping. A summary of the shift rate values, the used methods and the number of studied samples is reported to table 3.1.

The reported values of $\partial\omega_{2D}/\partial\omega_G$ vary slightly from sample to sample. We point out that the doping shift rate found recently by Froehlicher et al. is in good agreement with the average values found in literature (see table 3.1). Furthermore, their study covered the statistical analysis of 30 samples, which justifies the choice to use their calibration to determine the scaling factors $M_{d,e}$ and $M_{d,h}$.

In figure 3.9a, we show the frequency correlation of five ion gel top gated samples in FET geometry, on which the frequency shifts are either electron (e) or hole (h) doping induced. In addition, figure 3.9b displays the charge density n as a function of the quantity $[(\Delta\omega_G)^2+(\Delta\omega_{2D})^2]^{1/2}$, which corresponds to the length of the projection on the doping component. Thus, this quantity can directly be used to determine M_d, which corresponds to the slope. It is (for a laser wavelength of 532 nm):

$$\begin{aligned} M_{d,\text{electrons}} &= 4.4 \times 10^{11}\ \text{cm}^{-1} \\ M_{d,\text{holes}} &= -3.6 \times 10^{11}\ \text{cm}^{-1}. \end{aligned} \tag{3.17}$$

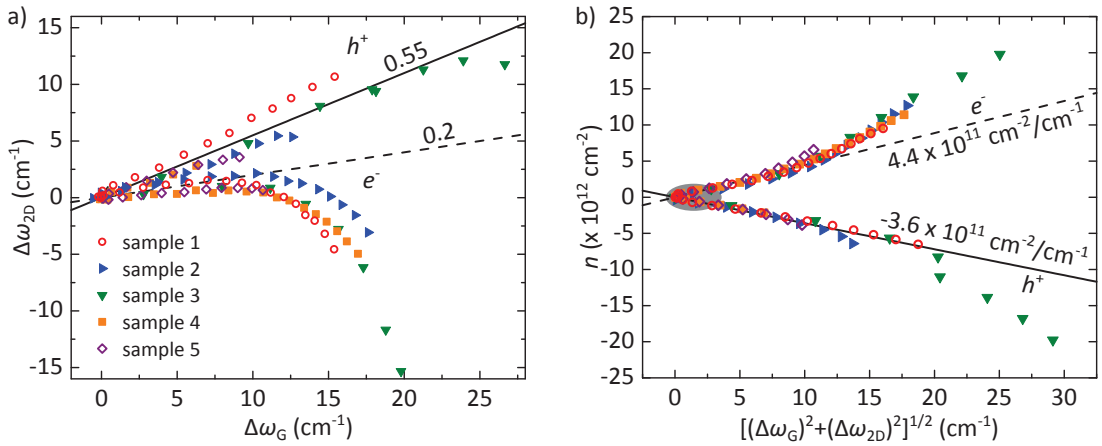

Figure 3.9: a) Correlation of ω_G and ω_{2D} upon hole and electron doping, for five different top-gated samples in FET geometry. The data are presented with the relative Raman shifts $\Delta\omega_G = \omega_G - \omega_G^0$ and $\Delta\omega_G = \omega_{2D} - \omega_{2D}^0$, where ω_G^0 and ω_{2D}^0 might be slightly different due to initial strain induced Raman shifts. The slopes are indicated along the linear fits. **b)** Charge carrier density n as a function of the shift $[(\Delta\omega_G)^2 + (\Delta\omega_{2D})^2]^{1/2}$ from the reference point corresponding to undoped graphene, allowing for a direct determination of the scaling factor M_d. Data are shown for the five samples in (a). The continuous and dashed lines are global linear fits, performed in the low doping regime on the electron and hole branches, respectively. The data in (a) and (b) are taken from ref. [Froehlicher15a].

Importantly, the measurement results of Froehlicher *et al.* provide an indication of the validity range of the vector decomposition model. At charge carrier densities lower than $\approx 1\times10^{12}$ cm^{-2}, in particular for devices exhibiting a low charge inhomogeneity, the renormalization of the G mode due to the electron-phonon interaction [Piscanec04, Lazzeri06, Das08] has to be taken into ac-

count. For higher charge densities the data suggest that the model is valid up to charge densities of $\approx 1 \times 10^{13}\,\mathrm{cm}^{-2}$.

The definition of the shift rates upon uniaxial strain has to be refined because of the peak splitting. However, the 2D mode splitting is only observed under certain conditions (see subsection 3.3.2), and shift rates for the G^+ ($\partial\omega_{2D}/\partial\omega_{G^+}$) and G^- mode ($\partial\omega_{2D}/\partial\omega_{G^-}$) can be determined independently.

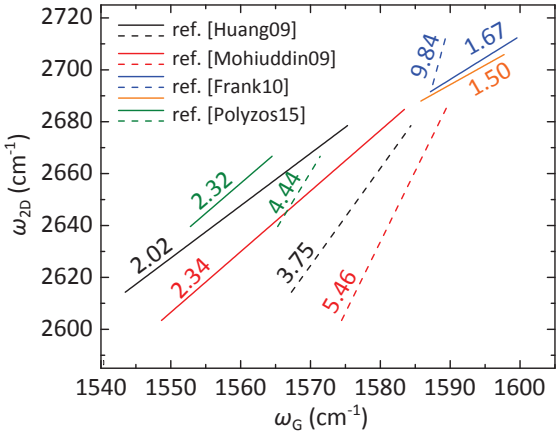

Figure 3.10: Correlation of ω_{G^-} (straight lines) and ω_{G^+} (dashed lines) with ω_{2D} in the case of uniaxial strain, for data available in literature. The experimental data points are not shown for clarity, only the linear fits are presented in the range of the experimental data. Data from ref. [Mohiuddin09] are taken on a flexible device with SU8 as substrate, using a laser wavelength of 514 nm (see figure 3.7a and b). Data from ref. [Huang09] are taken on graphene exfoliated on a flexible PDMS film, using a laser wavelength of 532 nm. The stretching in ref. [Frank10] is performed using a multilayer of several flexible polymers, using a laser wavelength of 785 nm. In contrast to the other works, compressive strain is applied and buckling of the graphene is the limiting factor for larger strain values. The authors of ref. [Polyzos15] clamp the graphene between two PMMA layers and define an opening by electron-beam lithography, which induces an intrinsic strain in the membrane.

Figure 3.10 gives an overview of the shift rates in the literature (see caption of the figure for more details). The available data cover a strain range of 0 to 3.1 % [Huang09], 0 to 1.3 % [Mohiuddin09], -0.1 to -0.65 % [Frank10] and 0.42 to 0.75 % [Polyzos15] for the G^+ subfeature whereas they cover a range of 0.5 to 3.1 % [Huang09], 0.2 to 1.3 % [Mohiuddin09], 0 to -0.65 % [Frank10] and 0.42 to 0.75 % [Polyzos15] for the G^- subfeature[10].

The application of biaxial strain to graphene has been an experimental challenge [Ding10], until pressurized suspended graphene started to be investigated [Bunch07, Bunch08, Chen09a, Koenig11]. The advancements in suspended graphene engineering stimulated Raman experiments on graphene blisters, which allowed for accessing biaxial strain in an elegant way without Piezo-electrically driven substrates [Zabel11, Lee12b, Kitt13]. Metzger *et al.* performed the

[10] In order to add the data of ref. [Polyzos15], we used the dominating ω_{2D1} sub-feature in the plot in figure 3.10c.

first Raman study on biaxial strained graphene exfoliated over swallow depressions [Metzger09]. For the shift rate, a value of $\partial\omega_{2D}/\partial\omega_G = 13\,\text{cm}^{-1}/6\,\text{cm}^{-1} \approx 2.17$ can be extracted. Georgiou *et al.* discovered bubbles on large ($\approx 100\,\mu$m) as exfoliated graphene flakes on flat substrates [Georgiou11]. These bubbles attain impressive diameters of $\approx 20\,\mu$m and heights up to $1\,\mu$m, which give rise to Newton rings under white light[11] (see figure 1.2 in chapter 1). On this kind of bubbles, Zabel *et al.* performed Raman measurements and observed strong downshifts of $73\,\text{cm}^{-1}$ and $143\,\text{cm}^{-1}$ for the G and 2D mode, respectively. Attributed to biaxial strain, a shift rate of $\partial\omega_{2D}/\partial\omega_G = 2.46$ is obtained.

Furthermore, the Raman measurements of Lee *et al.* on pressurized graphene flakes exfoliated over pits with varying diameter reveal a shift rate of $\partial\omega_{2D}/\partial\omega_G = 2.35$ [Lee12b]. Another interesting study from Kitt *et al.* exists, where the authors put graphene microchambers under high pressure up to 0.8 MPa, which results in a deflection of ≈ 700 nm for pits of $8\,\mu$m of diameter [Kitt13]. The downshift of the G mode feature is $58\,\text{cm}^{-1}$, however, the authors do not report on the 2D mode.

Thus, the strain induces shift rates are much higher than the ones induced by doping. All reported values on biaxial strain are in good accordance with the value of 2.2 reported by Lee *et al.* [Lee12a][12].

However, the knowledge of the shift rates $\partial\omega_{2D}/\partial\omega_G$ tells us only that there is strain but not how much. A difficult issue is to correctly calibrate the amount of strain in the graphene. The flakes could slide and sudden release of built-in strain could falsify the estimation of strain [Kitt13]. The strain calibration leads to the determination of the Grüneisen parameters γ_G and γ_{2D}, since they involve the quantity $\partial\omega/\partial\epsilon$. This experimental challenge is responsible for a certain dispersion of the Grüneisen parameters [Metzger09, Ding10, Zabel11, Kitt13]. Nonetheless, in accordance with theoretical first principle calculations [Thomsen02, Mohiuddin09, Cheng11] and high pressure measurements on graphite and carbon nanotubes [Hanfland89, Sandler03] as well as on graphene [Proctor09] (and also anticipating our results on pressurized graphene blisters presented in chapter 6), we can use values of $\gamma_G = 1.8$ and $\gamma_{2D} = 2.4$, which correspond to $\partial\omega_G/\partial\epsilon = -57\,\text{cm}^{-1}/\%$ and $\partial\omega_G/\partial\epsilon = -128\,\text{cm}^{-1}/\%$. Hence, we can determine the scaling factor M_s for biaxial strain as:

$$M_s = \left[(-57\,\text{cm}^{-1}/\%)^2 + (-128\,\text{cm}^{-1}/\%)^2\right]^{-1/2} = 7.14 \times 10^{-3}\,\%/\text{cm}^{-1}. \tag{3.18}$$

Note that a detailed summarizing table of the shift rates and Grüneisen parameters is reported to chapter 6, where we compare with our results (see table 6.2 and figure 6.16).

[11] Although we also obtained large flakes of up to $400 \times 150\,\mu\text{m}^2$ with our exfoliation technique, we never observed this kind of bubbles.

[12] Note that the work of references [Lee12a] and [Lee12b] are from two different research groups.

We finally stress that the approach of pressurized graphene blisters to apply strain is particularly interesting and convincingly elegant: Due to the strong adhesion to the substrate [Koenig11, Gao14] and the impermeability to standard gases [Bunch08], a simple air pressure difference between both sides of the graphene is sufficient to strain the membrane.

3.5 Optical interference effects in graphene multilayered systems

The substrate on which graphene is often exfoliated or transferred can be considered as a multilayered system, *e.g.* [Si - SiO_2 - graphene] for supported graphene [Blake07, Yoon09], [Si - air/vacuum - graphene] for suspended graphene without oxide, [Si - SiO_2 - air/vacuum - graphene] for suspended graphene with residual oxide, or [quartz - graphene - MgO] with MgO as an insulating spacing layer [Federspiel15]. Since the involved layer thicknesses are of the same order of magnitude as the wavelength of the light, interference effects come into play. These effects depend on the layers and their thicknesses and have two major consequences.

The first is of great practical use, because for the system [Si - SiO_2 - graphene] the choice of the oxide thickness determines the visibility of graphene by means of a simple optical microscope [Blake07]. The flagrant difference between a substrate of 200 nm and 300 nm oxide thickness is shown in figures 3.11a(1) and a(3), both showing a device with graphene and FLG, illuminated by white light. The surrounding optical images are taken with narrow band width filters of different wavelengths and highlight the fact that the optical contrast of graphene strongly depends on the oxide thickness and the wavelength of the illuminating light. Figure 3.11b sketches the expected contrast as a function of the oxide thickness and the wavelength. It turns out that Si/SiO_2 substrates with oxide thickness of 90 nm, 285 nm and 500 nm are the most suitable for identifying graphene by optical means (and for Raman studies with $\lambda_{\text{laser}} = 532$ nm).

The second consequence comes into play when Raman measurements are performed on multilayered systems [Yoon09, Reserbat-Plantey13, Li12]. To understand the subtle interplay between the different layer thicknesses, the laser wavelength and the wavelength of the scattered Raman photons a detailed comprehension of the interference effects is mandatory because it turns out that they strongly influence the intensity of the Raman modes. Thus, on supported samples, one should choose an adapted layer geometry to get Raman spectra of good quality and to avoid long experimental acquisition times. Furthermore, it should be stressed that comparing the intensity ratios of different Raman modes strongly depends on the underlying multilayered systems, as it has been pointed out by Yoon *et al.* for the case of [Si - SiO_2 - graphene].

Finally, before coming to the calculation of interference induced enhancement factors, it should be mentioned that the intensity of the Raman modes can change within one sample. This is the case when the deflection of suspended graphene membranes is tuned by an external pressure, because the air/vacuum thickness changes.

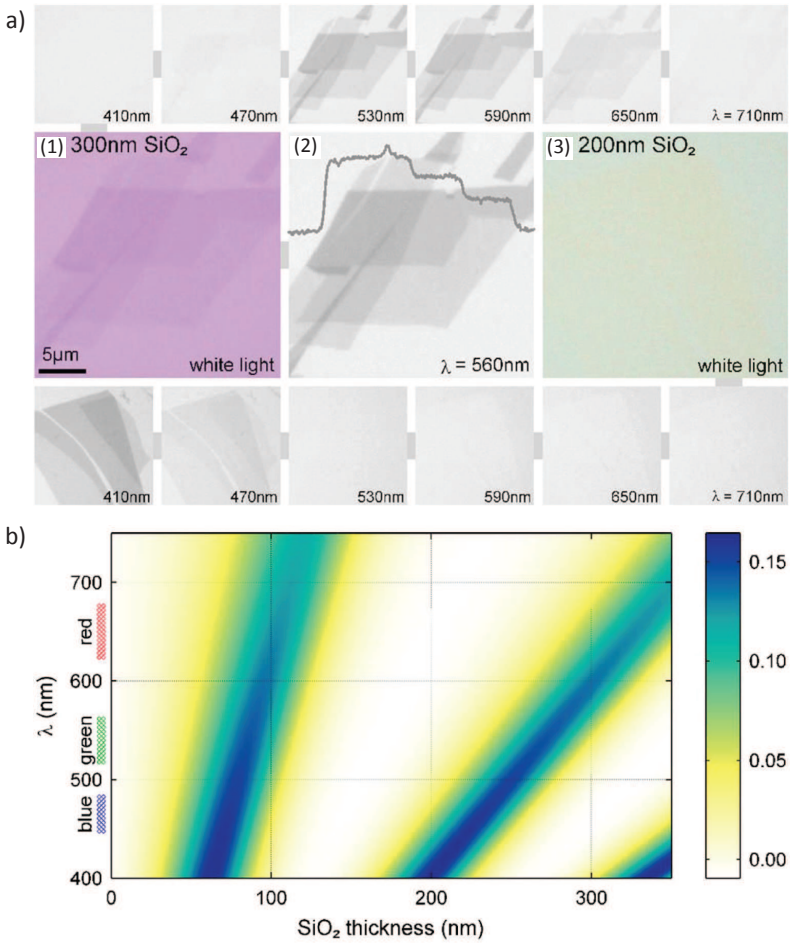

Figure 3.11: a) Optical images of graphene mono- and few layer samples illuminated by white light [(1) and (3)] and filtered by various narrow bandwidth filters [(2) and surrounding images]. The graphene layers are visible in (1) whereas the optical contrast vanishes in (3). The fact that the contrast is highly dependent on the illuminating wavelength is supported by the surrounding images, for both samples. **b)** Color plot of the contrast as a function of wavelength and oxide thickness. Figures are taken from ref. [Blake07].

In the following subsections, the one layer interference of a Fabry-Pérot is deduced which is then used recursively for a multilayered structure. In the case of Raman measurements, the graphene layer has to be considered separately because the Raman interaction takes place within the layer, which changes the interference term of that layer. Then, the calculation results of the interference induced Raman enhancement factors are presented.

3.5.1 One layer interferences: Fabry-Pérot

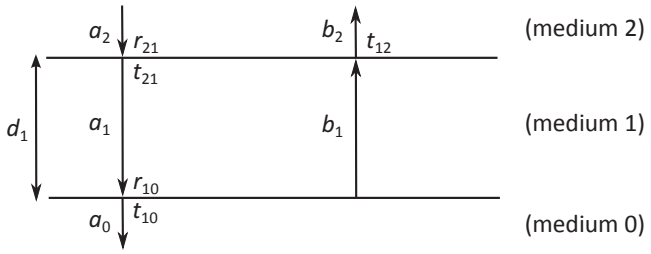

Figure 3.12: Schematic one layer Fabry-Pérot. The electric fields for incoming and outgoing light can be calculated in each layer 0, 1 and 2 by taking into account the reflection and transmission coefficients and the phase induced by the distance d_1.

Let us suppose that one layer of a medium 1 with refractive index $\tilde{n}_1$ is encapsulated between two media (0 and 2) with refractive indexes $\tilde{n}_0$ and $\tilde{n}_2$ ($\tilde{n}$ is the complex refractive index). Let a_1 (a_2) be the incoming and b_1 (b_2) the reflected electric field of the light in medium 1 (2) (see figure 3.12). We further suppose that no electric field is coming from the bottom, which is the case for Raman measurements in reflection geometry. Thus, in medium 0 the total electric field is a_0. The relationships between the components of the electric field write as

$$\begin{aligned} a_1 &= t_{21}a_2e^{i\phi_1} + r_{12}b_1e^{2i\phi_1} \\ b_1 &= r_{10}a_1 \\ b_2 &= r_{21}a_2 + t_{12}b_1e^{i\phi_1}, \end{aligned} \tag{3.19}$$

where r_{ij} and t_{ij} are the reflection and transmission coefficients at the interface ij for normal incidence, defined as

$$\begin{aligned} r_{ij} &= \frac{\tilde{n}_i - \tilde{n}_j}{\tilde{n}_i + \tilde{n}_j} \\ t_{ij} &= \frac{2\tilde{n}_i}{\tilde{n}_i + \tilde{n}_j} \end{aligned} \tag{3.20}$$

and ϕ_i is the phase in medium i. The phase is defined as $\phi_i = 2\pi\tilde{n}_i d_i/\lambda$ with λ the wavelength. b_2 can be expressed as a function of a_2, thus the ratio of the incoming and reflected electric

field in medium 2, A_{21}, can be expressed in terms of the phases, the reflection and transmission coefficients:

$$A_{21} = \frac{b_2}{a_2} = \frac{r_{21} - r_{10}r_{12}r_{21}e^{2i\phi_1} + r_{10}t_{12}t_{21}e^{2i\phi_1}}{1 - r_{10}r_{12}e^{2i\phi_1}}. \tag{3.21}$$

Using the relationships $r_{ij} = -r_{ji}$ and $r_{ij}r_{ji} - t_{ij}t_{ji} = -1$, A_{21} can be rewritten as

$$A_{21} = \frac{r_{21} + r_{10}e^{2i\phi_1}}{1 + r_{10}r_{21}e^{2i\phi_1}}, \tag{3.22}$$

which is the general Fabry-Pérot formula.

3.5.2 Multilayer interferences

For a multilayered structure, r_{10} in equation (3.22) can be considered as an effective refractive index taking into account the reflected electric field of the underlying multilayered structure. Thus, one can write recursively for every jth layer:

$$A_{j+1,j} = \frac{r_{j+1,j} + A_{j,j-1}e^{2i\phi_j}}{1 + r_{j+1,j}A_{j,j-1}e^{2i\phi_j}}. \tag{3.23}$$

3.5.3 Interference of the Raman interaction within a graphene layer

The layer where the Raman interaction takes place has to be considered separately. Let us take a layer l (which is the graphene) of thickness d_l, sandwiched between two media k and m (see figure 3.13). The Raman interaction takes place at a distance $x < d_l$. In order to know how the Raman signal is enhanced or suppressed due to interference effects, one has to calculate the electric field of the incoming laser light at the position x, E_x, and the electric field of the emitted Raman signal coming out of the layered system, E_{out}.

The incoming laser light with an electric field E_0 in medium m is first transmitted from medium m to medium l and undergoes multiple reflections within medium l, crossing the position x after each reflection, as it is sketched with black points in figure 3.13a. Note that the incidence is normal to the surface, but the incoming laser beam has been drawn with an angle for a better illustration. E_x can be written as

$$\begin{aligned} E_x = E_0\, t_{ml}\, (&\underbrace{e^{i\phi_x}}_{①} + \underbrace{r_{lk}\, e^{i(\phi_{2d_l} - \phi_x)}}_{②} + \underbrace{r_{lk}r_{lm}\, e^{i(\phi_{2d_l} + \phi_x)}}_{③} + \underbrace{r_{lk}^2 r_{lm}\, e^{i(\phi_{4d_l} - \phi_x)}}_{④} \\ &+ \underbrace{r_{lk}^2 r_{lm}^2\, e^{i(\phi_{4d_l} + \phi_x)}}_{⑤} + \underbrace{r_{lk}^3 r_{lm}^2\, e^{i(\phi_{6d_l} - \phi_x)}}_{⑥} + \dots) \end{aligned} \tag{3.24}$$

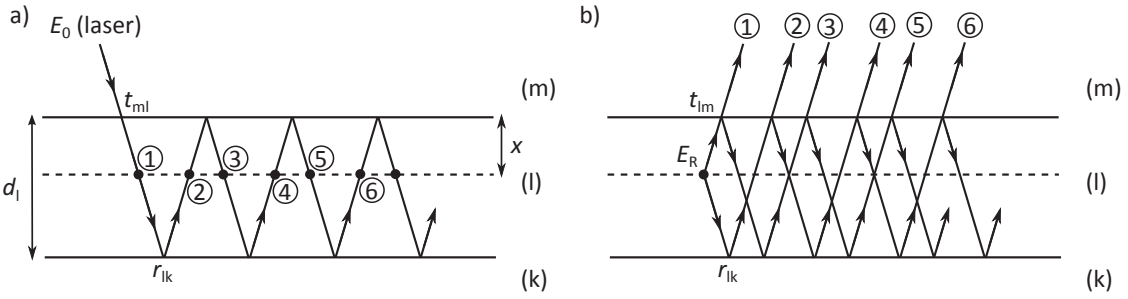

Figure 3.13: Schematic representation of the interference processes within a graphene layer (medium l), sandwiched between two media k and m. The light incidence is perpendicular to the plane; for a better illustration the incidence is drawn under an angle. **a)** The incident light undergoes multiple reflections and interacts several times (①, ②, ...) with the graphene lattice at the position x. The effective interacting electric field is the sum of these terms. **b)** The Raman scattered signal undergoes multiple reflections, the outcoming electric field is the sum of the contributions ①, ②, *etc.*

Let us group the even and the odd terms and use the relationship $1+w+w^2+w^3+...+w^n = (1-w^{n+1})/(1-w)$ which is valid for every complex number w. We can write

$$\begin{aligned} E_x = E_0 t_{ml} \{ & e^{i\phi_x} \left[\frac{1-(r_{lk}r_{lm}\, e^{i\phi_{2d_l}})^{n+1}}{1-r_{lk}r_{lm}\, e^{i\phi_{2d_l}}} \right] \\ & + r_{lk}\, e^{i(\phi_{2d_l}-\phi_x)} \left[\frac{1-(r_{lk}r_{lm}\, e^{i\phi_{2d_l}})^{n+1}}{1-r_{lk}r_{lm}\, e^{i\phi_{2d_l}}} \right] \}. \end{aligned} \tag{3.25}$$

For $n \to \infty$ the term $|r_{lk}r_{lm}\, e^{i\phi_{2d_l}}|^{n+1} \to 0$, so that one can simplify the expression to

$$E_x = E_0 t_{ml}\, \frac{e^{i\phi_x} + r_{lk}\, e^{i(\phi_{2d_l}-\phi_x)}}{1-r_{lk}r_{lm}\, e^{i\phi_{2d_l}}}. \tag{3.26}$$

The Raman interaction at the position x creates an electric field E_R which also undergoes multiple reflections in medium l before leaving it (see figure 3.13b). Thus, E_{out} and E_R are connected by

$$\begin{aligned} E_{\text{out}} = E_R t_{lm} (& \underbrace{e^{i\phi_x}}_{①} + \underbrace{r_{lk}\, e^{i(\phi_{2d_l}-\phi_x)}}_{②} + \underbrace{r_{lk}r_{lm}\, e^{i(\phi_{2d_l}+\phi_x)}}_{③} + \underbrace{r_{lk}^2 r_{lm}\, e^{i(\phi_{4d_l}-\phi_x)}}_{④} \\ & + \underbrace{r_{lk}^2 r_{lm}^2\, e^{i(\phi_{4d_l}+\phi_x)}}_{⑤} + \underbrace{r_{lk}^3 r_{lm}^2\, e^{i(\phi_{6d_l}-\phi_x)}}_{⑥} + ...), \end{aligned} \tag{3.27}$$

where the sum in brackets turns out to be the same as in equation (3.24), so that one can write

$$E_{\text{out}} = E_R t_{lm} \frac{e^{i\phi_x} + r_{lk} e^{i(\phi_{2d_l} - \phi_x)}}{1 - r_{lk} r_{lm} e^{i\phi_{2d_l}}}. \tag{3.28}$$

Here again, for E_x and E_{out}, r_{lk} can be considered as an effective reflection coefficient, in particular it can be replaced by the expression in equation (3.23) if the medium k is a multilayered structure.

The ratios E_x/E_0 and E_{out}/E_R can be considered as net absorption and scattering terms, respectively, and be used to calculate an overall enhancement factor EF for the intensity of the measured Raman signal. With an integration over the thickness of medium l, EF is then

$$\text{EF} = \int_0^{d_l} \left| \frac{E_x}{E_0} \times \frac{E_{\text{out}}}{E_R} \right|^2 \, \mathrm{d}x. \tag{3.29}$$

Let us note here, that the fact that the Raman interaction takes place within the graphene layer leads to an important modulation of the Raman signal. In particular, when one calculates the reflection coefficient of, *e.g.*, the system [Si - SiO_2 - graphene] with varying oxide thickness, the intensity (of the reflected laser beam) is only weakly modulated. This makes the use of the Raman signal for interference modulated intensity measurements particularly interesting, because of its higher sensitivity.

3.5.4 Refractive indices

To accurately calculate interference dependent enhancement factors, an exact knowledge of the involved complex refractive indexes $\tilde{n} = n + i\kappa$ is mandatory. For SiO_2 the real part n is obtained by means of the following equation, established by Malitson in the seventies [Malitson65]:

$$n^2 - 1 = \frac{0.6961663\lambda^2}{\lambda^2 - 0.0684043^2} + \frac{0.4079426\lambda^2}{\lambda^2 - 0.1162414^2} + \frac{0.8974794\lambda^2}{\lambda^2 - 9.896161^2} \tag{3.30}$$

Here, the wavelength λ is expressed in μm. The imaginary part κ is zero in the visible range.

In the first years of the rise of graphene, its optical properties were difficult to accesss. Classical optical measurement techniques failed because of graphene's sub-nanometer thickness, its dielectric anisotropy and the small sample size obtained by mechanical exfoliation [Wang08a]. With different techniques, some data points were obtained for n and κ, and DFT calculations confirmed these values, as it can be seen in figure 3.14 [Ni07, Blake07, Bruna09, Klintenberg09, Cheon14]. In 2010, Weber *et al.* succeeded in measuring the refractive index by spectroscopic ellipsometry on a sufficiently large flake ($150 \times 380\,\mu\text{m}^2$) [Weber10]. We use this data in the following calculations because it is in good agreement with the other available measurements and permits to calculate interference effects over the whole range of visible light.

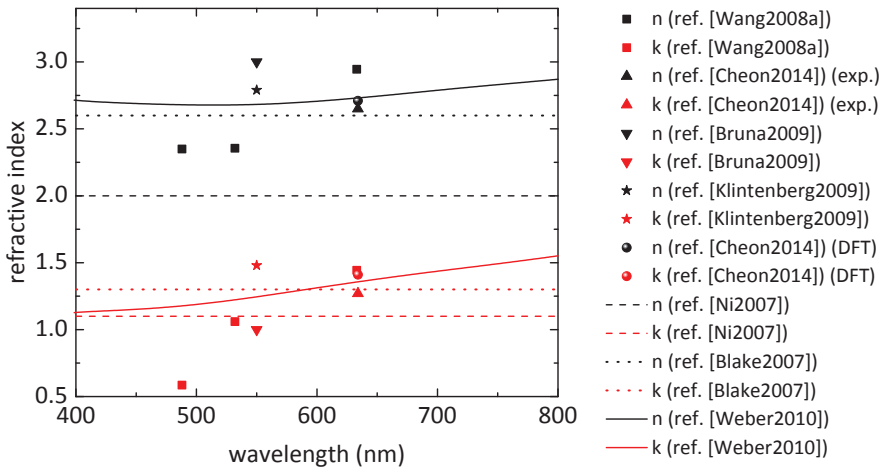

Figure 3.14: Synthesis of refractive indexes of graphene available in literature. Experimental data are obtained by wavelength dependent contrast imaging (exfoliated graphene) [Ni07, Blake07], spinning-disc picometrology (exfoliated graphene) [Wang08a], surface plasmon resonance (CVD graphene) [Cheon14], reflectance and transmission measurements using graphite and graphene [Bruna09] and spectroscopic ellipsometry (exfoliated graphene) [Weber10]. The presented theoretical data are obtained by DTF calculations [Cheon14, Klintenberg09].

Finally, for silicon we use the tabulated values from ref. [Vuye93].

3.5.5 Theoretical prediction for suspended graphene systems

After these more theoretical considerations, we now come back to the initial question, *i.e.* how does interference affect the intensity of the Raman modes. In other words, a measured intensity of a Raman mode x (*e.g.* G or 2D) is the interference-free intensity $(I_x)_{\text{int.}-\text{free}}$ (which might depend on the experimental setup, doping, etc.) modulated by the enhancement factor EF_x[13]:

$$(I_x)_{\text{mes}} = EF_x \times (I_x)_{\text{int.}-\text{free}} \,, \tag{3.31}$$

and the task is to find the theoretical values of EF_x.

As elaborated at the beginning of this section, silicon substrates with oxide thickness 285 nm and 500 nm are commonly used in order to easily localize graphene monolayers, as we do.

Depending on the etching process (see section 4.1.2) and the employed substrate, suspended graphene devices with three different types of multilayered systems can be fabricated (with the corresponding thicknesses in round brackets, see also the schemes in figure 3.15a, b and c):

[13] Note that $(I_x)_{\text{int.}-\text{free}}$ cannot be obtained by a single measurement. A series of measurements with varying thickness of one layer in the multilayered system is necessary. Furthermore, the theoretical value of EF_x has to be renormalized for every measurement series, which is possible when the measurement series of I_x covers a minimum and a maximum value.

1. [Si - air/vacuum (h_{air}) - graphene]

2. [Si - SiO_2 ($d_{SiO_2} = 285\,\text{nm} - d_{\text{air}}$) - air/vacuum ($d_{\text{air}} < 285\,\text{nm}$) - graphene]

3. [Si - SiO_2 ($d_{SiO_2} = 500\,\text{nm} - d_{\text{air}}$) - air/vacuum ($d_{\text{air}} < 500\,\text{nm}$) - graphene]

System 1 represents the case of no oxide layer between the silicon and the graphene membrane, which can be achieved by choosing long etching times to take away all the oxide. Consequently, h_{air} is higher than the oxide thickness of the chosen substrate.

System 2 starts with an oxide thickness of 285 nm, of which a certain thickness d_{air} is replaced by air/vacuum. Of course, d_{air} and d_{SiO_2} depend on each other. The same holds for system 3 where the initial oxide thickness is 500 nm.

In figure 3.15, a, b and c can be considered as heads of three columns, because the three graphs in each column represent colorplots of the enhancement factors for the G mode, 2D mode and their intensity ratios for each system, respectively. The enhancement factors have been calculated by means of a homemade Matlab script, using equation (3.29) and the refractive indexes of subsection 3.5.4.

Figure 3.15d shows a colorplot of the theoretical enhancement factor for the G mode as a function of h_{air} and the incident laser wavelength λ_{laser} for system 1. The scale is set from 0 to 1 and is the reference scale for figures 3.15e-i. The EF pattern is characterized by stripes of strong enhancement in the h_{air}-λ_{laser}-plane. The same holds for the 2D mode (figure 3.15g). In contrast, the pattern is quiet different for system 2 and 3 (see figures 3.15e, f, h and i), in particular there is a large area of suppressed Raman signal in the d_{air}-λ_{laser}-plane for system 2. That means, in practice, a Raman signal measured with a laser wavelength between 600 and 700 nm is always suppressed, no matter how much SiO_2 is etched away.

This example shows that, to measure a reasonable Raman intensity, the proper depth d_{air} and laser wavelength have to be chosen carefully, because the Raman intensity strongly depends on the underlying system and the chosen thicknesses. Furthermore, measurements on pressurized suspended graphene with varying air/vacuum thickness are expected to be strongly modulated by interference effects.

Figures 3.15j-l represent the ratio of the normalized enhancement factors of the 2D and the G mode, $(EF_{2D}/EF_G)_{\text{norm}}$. Since the wavelength of the Raman scattered G and 2D photons is different, this ratio is also a strong function of the chosen thicknesses and λ_{laser}.

Frequently used laser wavelengths are 532 and 633 nm. In order to highlight the strong dependence on λ_{laser}, we plot in figure 3.16 cuts extracted from figure 3.15 for these wavelengths.

Note that it is important to consider the different wavelengths of the laser and the Raman signal. This difference is responsible for the beating which is observed for larger thicknesses. The beating gets more important when the laser wavelength is decreased. In former analyses, this

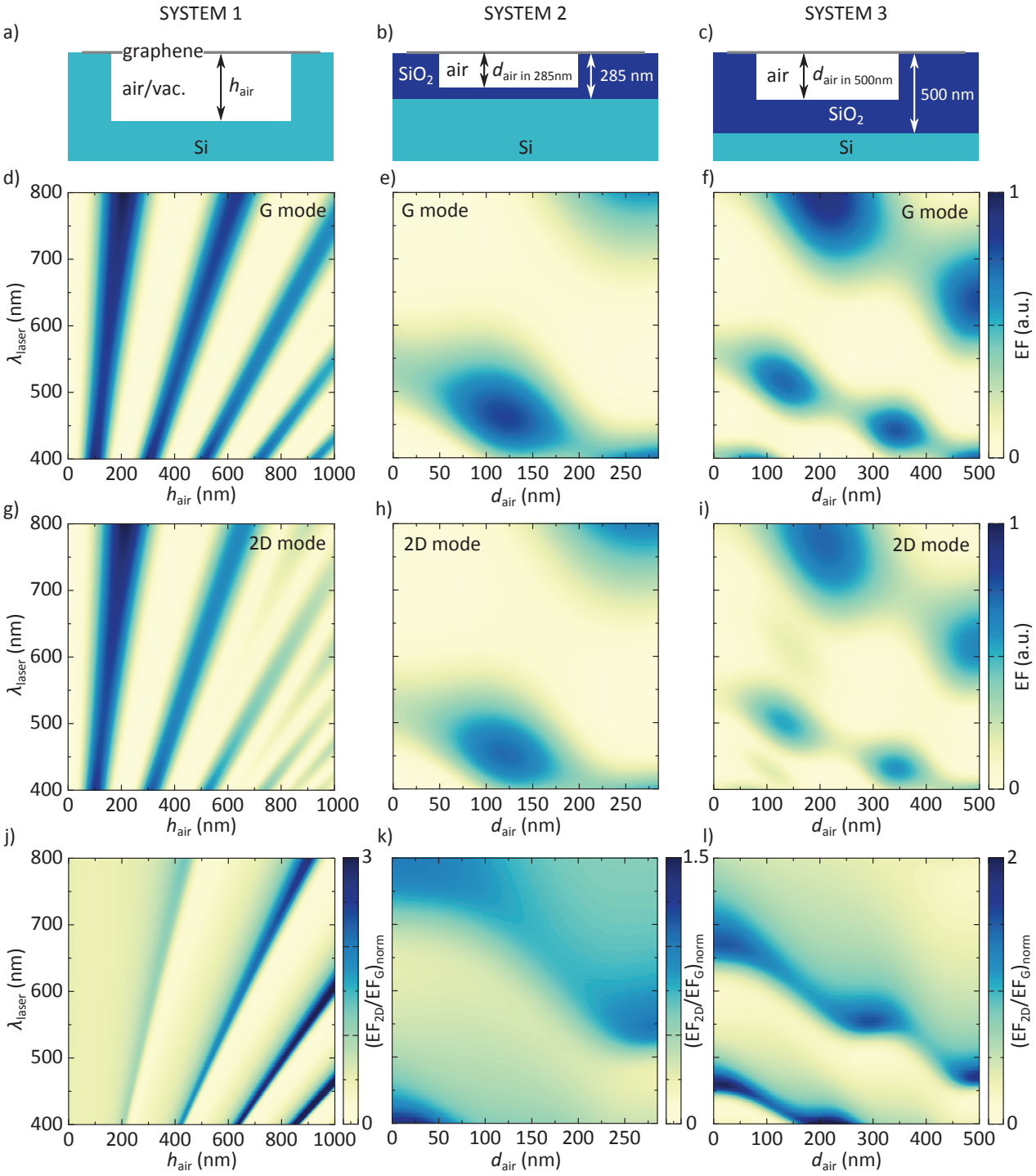

Figure 3.15: a), **b)** and **c)**, showing a sketch of the device geometries of system 1, 2 and 3 (see main text), can be considered as heads of the three columns. **d)**, **e)** and **f)** [**g)**, **h)** and **i)**] show color plots of the theoretical enhancement factor EF as a function of the laser wavelength and the air thickness in the oxide for the G [2D] mode. **j)**, **k)** and **l)** represent the ratio I_{2D}/I_G. The z-scale is chosen in the following way: The maximum and minimum EF in (d) are set to 0 and 1, respectively, and EF in (e)-(i) are scaled with respect to that scale. The ratio EF_{2D}/EF_G in (j)-(l) is the ratio calculated using these normalized values.

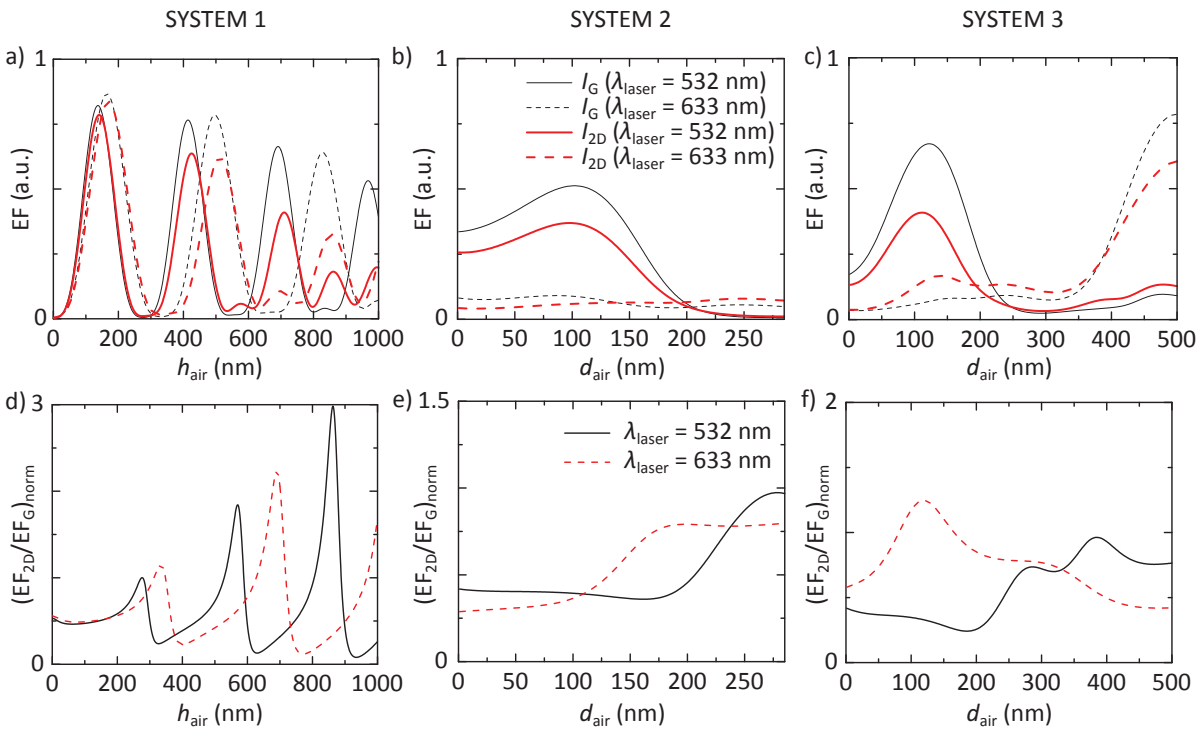

Figure 3.16: Cuts of the color plots at $\lambda_{laser} = 532$ nm and 633 nm. **a)** Calculated enhancement factors for the G (black) and 2D (red) mode for a laser wavelength of 532 nm (straight line) and 633 nm (dashed line), as a function of h_{air} (system 1). The corresponding ratios of the intensities are plotted in **(d)**. The same quantities are presented in **(b)** and **(e)** as well es in **(c)** and **(f)** for the systems 2 and 3, respectively.

effect has been neglected and the Raman signal has been treated with the same wavelength as the laser [Nemanich80, Ager90, Wang08c].

3.6 Conclusion

In this chapter we have shown that vibrational Raman spectroscopy is a suitable tool for probing external perturbations in graphene such as doping and mechanical strain. Furthermore, it is sensitive to the number of layers and to the crystalline quality of graphene. Additionally, we have calculated an expression for an optical interference induced enhancement factor for the Raman signal, which takes into account the fact that graphene is often deposited on a multilayered structure.

To conclude, we have seen that the spectral positions, the widths and the intensities of the Raman modes are extremely sensitive to a bunch of external perturbations, which makes a thorough data analysis indispensable. Hence, a lot of information can be extracted by even a single Raman measurement series, as will be seen in the following chapters.

4 Device fabrication and experimental set-up

In the first part of this chapter, the required fabrication steps to arrive from a virgin silicon wafer to a measurable suspended graphene device with source, drain and backgate contacts are outlined. The second part of this chapter is dedicated to the experimental micro-Raman setup, allowing for Raman measurements under ambient conditions as well as under vacuum and at cryogenic temperatures. This setup includes an optical and electrical access.

4.1 Device fabrication and fabrication techniques

A bare Si wafer covered by a thermal SiO_2 layer of thickness 285 nm or 500 nm (suitable for optical microscope identification of graphene monolayers, see section 3.5) is cut into pieces of adequate size for further fabrication processing.

4.1.1 Optical lithography

These pieces are spin-coated by a thin flat layer of photo-sensitive resist in order to undergo a step of optical lithography. This technique for patterning micrometer-sized structures is a powerful tool because it permits to transfer rapidly a geometric pattern from a photo-mask to the photo-sensitive resist on the Si/SiO_2 substrate. Optical lithography is limited by light diffraction. To achieve highest possible resolution, ultra-violet (UV) light is used allowing for item patterning of $\approx 4\,\mu$m.

The spin-coated resist is sensitive to UV light exposure. The resist is used as positive tone resist, *i.e.* the molecules of the exposed area are modified in order to be soluble in a chemical developer in which they are washed away (see figure 4.2a and b). However, the non-exposed area stays unaffected by the developer and thus covered. The resist acts then like a mask for following fabrication steps.

4.1.2 Wet and dry etching

For the purpose of having trenches or pits in the SiO_2 layer, an etching process taking away the oxide is necessary. To do so, a wet etching process with a buffered HF solution[1] can be used. HF removes only the oxide and has no effect on the pure silicon under the oxide. Another way to remove the uncovered SiO_2 is to shoot reactive ions on the sample. This dry etching process is called Reactive Ion Etching (RIE)[2]. The advantage of this technique is that the combination of chemical reaction and the momentum transfer results in sharp edges, in contrast to other etching processes [Heinecke76]. Unlike HF etching, RIE physically etches all materials and therefore also attacks silicon. We note that the resist mask ensures that the etching acts only at the predefined positions (see figure 4.2c).

4.1.3 Mechanical exfoliation and determination of number of layers

Once the etching process is finished, the resist is washed away with acetone in an ultrasonic bath and cleaned with ethanol and isopropyl alcohol. In this thesis, we use exclusively graphene from a natural graphite source, which still have the best prerequisites. In order to deposit monolayer graphene on the cleaned samples, we use the scotch-tape method of mechanical exfoliation established by Geim and Novoselov in 2004 [Novoselov04, Novoselov05b].

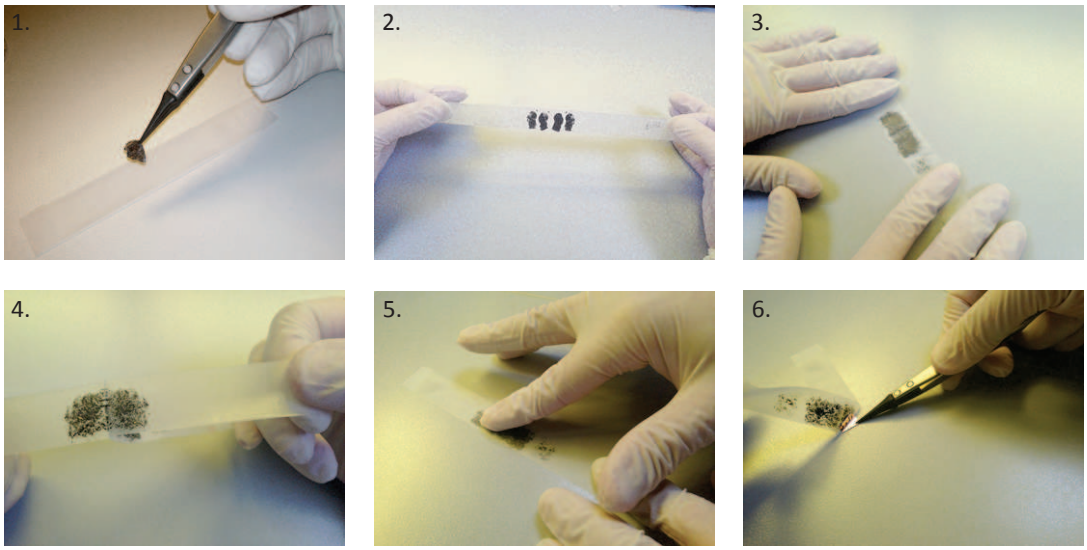

Figure 4.1: Photos of the six exfoliation steps described in the main text.

Before exfoliation, the substrates are surface-activated by a 10 min lasting oxygen plasma, which provides for a better adhesion of the graphene on the substrate (see figure 4.2d and e).

[1] BHF, ammonium fluorid (NH_3F) and $H_2O_{50}HF_{50}$ with ratio 6:1
[2] We use CH_4 as active gas.

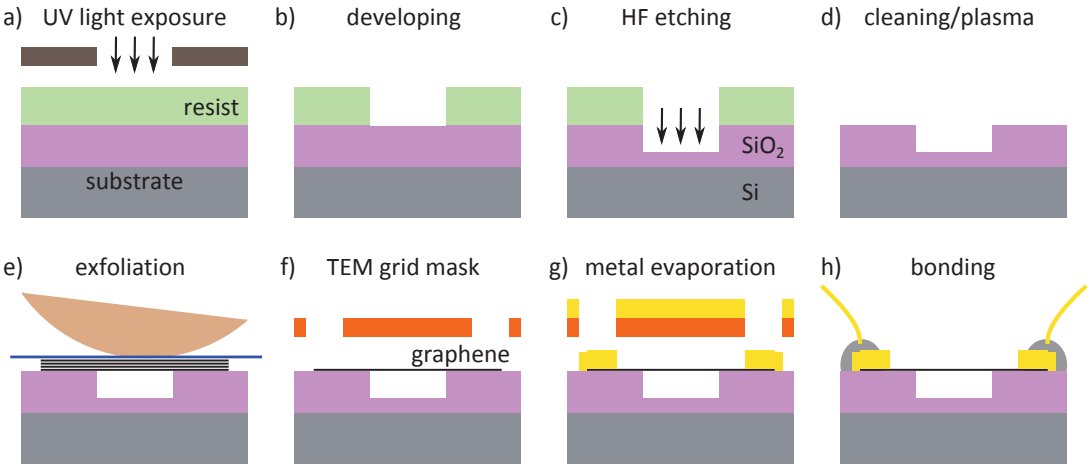

Figure 4.2: Schematic summary of the fabrication steps. **a)** The sample is spin-coated by a photo-sensitive resist and exposed to UV light through a pre-patterned mask, changing the chemical properties of the resist at the exposed area. **b)** The chemically modified resist is washed away by a developer, uncovering the bare SiO_2. **c)** The uncovered surface is attacked by HF or RIE etching, removing a certain thickness of SiO_2, depending on the exposition time. **d)** The sample is cleaned in acetone/ethanol/isopropanol and surface-activated by oxygen plasma etching. **e)** Graphene is exfoliated on the sample as described in the main text (see also figure 4.1). **f)** After localizing suspended graphene membranes by optical microscopy, a TEM grid is aligned and fixed on the sample. **g)** This TEM grid serves as mask for the metal evaporation process [Ti (3 nm) and Au (47 nm)], covering the suspended part of the graphene and thus protecting it from metal deposition. **h)** Finally, the Ti/Au contacts are connected to a chip carrier by means of thin gold wires. The latter are glued with conductive silver epoxy both on the sample and the chip carrier.

The exfoliation process, which is done rapidly after oxygen plasma, can be summarized in the following steps:

1. put a graphite piece on scotch tape
2. fold the scotch tape and open it delicately to increase the surface
3. stick another scotch tape to the first scotch tape and press delicately on it
4. take off slowly the two scotch tapes and keep the first, repeat steps 2 and 3 with that scotch tape until transparent zones appear
5. stick the scotch tape with thin transparent graphite on a substrate and massage with a finger by applying moderate pressure, for some minutes
6. take off slowly the scotch tape from the substrate

Photos illustrating each of the exfoliation steps are shown in figure 4.1. Graphite pieces, few layer graphene and graphene monolayers are present on the sample and can be detected by their

optical contrast difference under an optical microscope. This detection is possible because one layer graphene absorbs ≈ 2.3 % of the incident light, and this absorption is, as an approximation, proportional to the number of layers, and so is the contrast (see section 2.3). In addition, the use of optimized substrates with the suitable oxide thickness facilities the detection (see section 3.5). The position of monolayer graphene is then located with respect to optical markers (numbers) (see figures 4.3a and b). The number of layers is further confirmed by Raman spectroscopy (see section 4.2).

4.1.4 Contacting: Metal deposition and bonding

Since for the work of this thesis, ultra-clean graphene is required, any contact with resist or organic solvents has to be avoided. Thus, the standard lithography procedure for evaporating metal contacts should be excluded, and that is the reason why we align adapted transmission electron microscopy (TEM) grids as shadow mask above the sample. We achieve an alignment precision of roughly $1\ \mu$m, sufficient for our device geometry. Thin metal films can then be deposited with a controlled thickness in the nanometer range by heating and evaporating solid metal under high vacuum ($\approx 10^{-7}$ bar). Different metals can be evaporated successively within one machine, the metal sources being placed in hollows in a revolving disc. An electron beam heats the metal source to create an evaporation cone containing metal atoms which then deposit above the metal source. The sample to be covered is upside down within that cone, and the thickness is controlled by shutters and a quartz crystal micro-balance in a very accurate way. The result of such an evaporation is shown in figures 4.3b and c, at different scales.

After metal evaporation, the sample is cut in order to fit in a chip carrier dedicated for measurements within a cryostat. The metal contacts on the sample are connected to the chip carrier by a manual bonding procedure. For this purpose, conductive silver paste is used to glue the sample at the bottom of the chip carrier. Then, conductive epoxy is dropped on the sample and the chip carrier. Before drying, these drops are connected by a thin gold wire.

Finally we note that figure 4.2 summarizes well the here described fabrication steps in a schematic way.

4.2 Experimental setup

4.2.1 Confocal micro-Raman setup

For Raman measurements, a home-built confocal microscope setup in backscattering geometry is used. The setup allows for spatially resolved micro-Raman measurements under ambient conditions or at cryogenic temperatures and/or under vacuum.

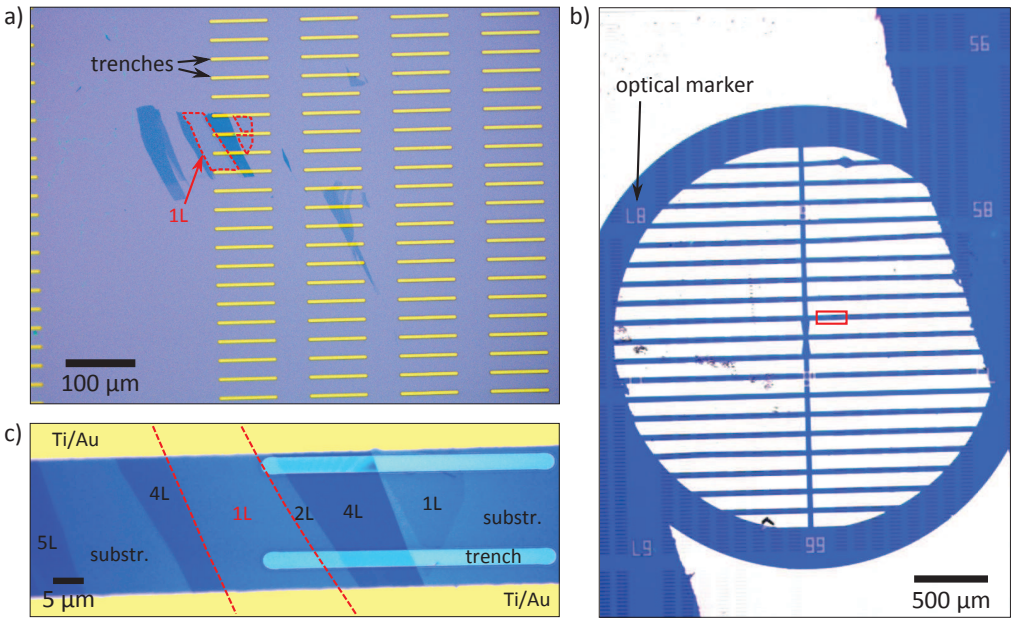

Figure 4.3: a) Optical image of a device pre-patterned with $80\ \mu$m long and $5\ \mu$m wide trenches. The image has been taken after exfoliation of natural graphite, resulting in the presence of few layer (dark violet, strong optical contrast) and monolayer (light violet, marked with a red dashed line) graphene. **b)** Optical image of the same sample as in (a), after metal contact evaporation by means of a TEM grid as shadow mask. The numbers are optical markers to facilitate the location of suspended graphene. **c)** Zoom in of (b) (red rectangle), showing two Ti/Au (3 nm/47 nm) contacts in the vicinity of a suspended monolayer graphene (marked with a red dashed line).

Let us evoke the basic measurement principle with the help of the sketch in figure 4.4a. In this simplified sketch, the sample and the spectrometer are located at the extremities of the main optical axis. A previously enlarged and cleaned laser beam of wavelength 532 nm (exclusively used in this thesis, green line in figure 4.4a) is directed towards the sample by means of a dichroic mirror, which is transmissive for wavelengths $\gtrsim 535$ nm. The laser beam is focused on the sample via an objective[3] which is mounted on a *xyz*-Piezo element allowing for a precise positioning of the laser spot on the sample. The range of the Piezo is $100\ \mu$m in x- and y-direction and $20\ \mu$m in z-direction.

The backscattered light (orange line in figure 4.4a) is collected by the same objective and passes through the dichroic mirror, which allows for a first spectral separation of the Rayleigh and Raman scattered light. The subsequent beam is spatially filtered with the help of two lenses (L1 and L2) and a pinhole (P) of diameter $50\ \mu$m. The lens L1 permits to focus the incident beam at the center of the hole and the lens L2 to parallelize the outgoing beam. The pinhole is spatially conjugated with the laser spot on the sample, which ensures that the recorded signal originates from a well defined spot on the sample and furthermore improves the signal to noise ratio. A spectral notch filter (F) further blocks the reflected laser and Rayleigh signal, so that the Raman signal can enter the detection system. This system consists of a dispersive element (a grating with 900 lines/μm) and a CCD camera (1340×100 pixel), which is cooled with liquid nitrogen. Nobel gas lamps are used for calibration prior to the measurement runs. The Piezo element and the CCD camera are controlled by a Labview interface, allowing for a spatial scanning of the sample and recording Raman spectra at each point.

For localization of the graphene, white light (yellow line in figure 4.4a) can be focused on the sample by means of a tiltable beam-splitter, and the optical image can then be detected by a tiltable mirror and a camera.

4.2.2 Measurements at room and cryogenic temperatures

With the help of the setup described above, quick Raman measurements under ambient conditions can be performed, simply by mounting the sample on a sample holder (with adjustable angle) connected to a *xyz*-stage, allowing for a coarse position adjustments (see photo in figure

[3] We mainly use two objectives:

- $\times 20$ with a numerical aperture (NA) of 0.45
- $\times 50$ with NA $= 0.65$.

The calibration of the resultant laser spot sizes is reported to the Appendix, see figure A.1. We note that the values of the NA are low, which justifies the approximation of the normal incidence in section 3.5. We would like to draw the reader's attention to the Supplementary Information of ref. [Yoon09], where the Raman enhancement factors for the system [Si - SiO_2 - graphene] has been calculated as a function of the NA.

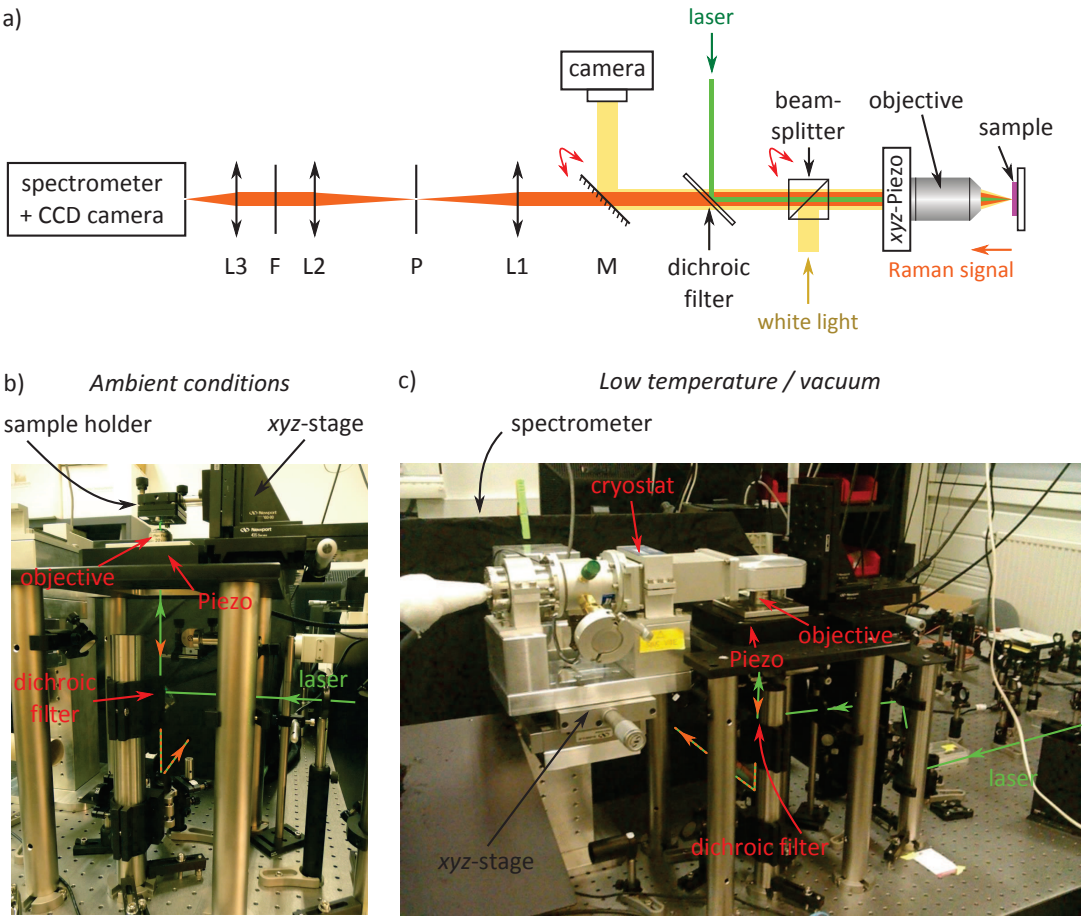

Figure 4.4: a) Sketch of a confocal micro-Raman setup in backscattering geometry. See main text for details. L1, L2 and L3 are confocal lenses, F is a notch filter, P is a pinhole and M is a plan mirror. The mirror and the beam-splitter for white light injection are tiltable (red arrows). The objective is mounted on a Piezo translation element. **b)** Photo of the home-built Raman setup for measurements under ambient conditions. The sample is mounted on a sample holder connected to a *xyz*-stage, allowing for coarse angle and position adjustments. **c)** Photo of the same measurement setup, but in low temperature / vacuum measurement conditions. The sample is in the cryostat with optical and electrical access. The cryostat is mounted on a coarse *xyz*-stage. The laser beam is highlighted with a green line. The dotted orange line indicates the backscattered light.

4.4b). The Piezo element with the objective ensures fine positioning. The measurements we will present in chapter 5 are performed within this setup configuration.

For measurements under vacuum, we make use of a pumped out cryostat, which acts as a vacuum chamber (see photo in figure 4.4c). The cryostat is equipped with a $1\ \mathrm{cm}^2$ circular quartz window, allowing for an optical access to the inserted sample. The cryostat itself is mounted on a coarse *xyz*-stage. The measurements of chapter 6 are performed within this setup configuration, with a variable pressure between vacuum and atmospheric pressure in the cryostat.

Finally, the inserted sample is in contact with a cold finger, which can be thermally connected to a ^{4}He flow. Within this configuration, we can achieve temperatures down to $4\,\mathrm{K}$, which are measured in the vicinity of the sample with the help of a temperature detector. Importantly, the bonded sample sitting in the chip carrier is electrically connected to a matrix box, which itself is connected to a two channel sourcemeter (Keithley 2612A). This sourcemeter can be used to apply a source-drain bias and a gate voltage, and to measure the source-drain and gate currents. In chapter 7 we will present low temperature measurements on gated graphene which have been performed within this setup configuration.

4.3 Data acquisition and treatment

As mentioned previously, the Raman signal is dispersed on a 1340×100 pixel nitrogen-cooled CCD camera. The camera is connected to a computer and can be controlled by a software called WinSpec. We use this software for recording single spectra. If the issue is to acquire several Raman spectra over a larger area, we use a LabView interface which controls at the same time the camera and the Piezo element. In order to extract the spectral position, width and intensity on selected Raman peaks (G mode, D mode and 2D mode), we make use of the matrix treatment program MatLab. The corresponding MatLab scripts have been written by F. Federspiel and further adjusted. *E.g.*, the Raman data published in references [Godel13] and [Mahmood15] have been analyzed in that way.

For gate dependent measurements, we have furthermore developed a Labview interface with the help of M. Romeo, allowing for a controllable gate voltage application in the presence of a bias voltage (if required). In particular, this program permits a smooth gate voltage ramping with an adjustable delay time before starting the Raman measurement.

MatLab scripts for optical interference calculations (see section 3.5), modeling of gate induced deflection (see section 7.3), and various fitting procedures have been written by myself.

4.4 Conclusion

In this chapter we have shown that we are able to fabricate suspended graphene devices without exposing the graphene sheets to any resist. In this way we preserve their cleanness and can study the intrinsic properties of graphene. Furthermore, we have developed and mounted a confocal micro-Raman setup allowing for a fast Raman characterization and electrical measurements under vacuum and cryogenic temperatures.

We note that the design and installation of the experimental setup as well as the sample fabrication have been part of the work for this thesis.

5 Built-in strain in suspended graphene

Depositing graphene on a pre-patterned target substrate (*e.g.* with holes, pits or trenches) results in suspending part of the graphene, *i.e.* direct contact with the substrate is avoided. Once the graphene is deposited, the strong adhesion of graphene to the substrate makes the suspension of the flake possible and it does not collapse [Koenig11, Yoon12, Gao14, Kim15a], if it is not already broken by an unintentional manipulation during exfoliation or transfer.

The graphene flake is not fully deconnected from the substrate, even though large suspended areas up to several $10\,\mu\text{m}^2$ can be achieved [Bunch07, Bolotin08b, Berciaud09, Bao10]. It is coupled to the substrate via van der Waals interaction, which is responsible both for maintaining the residual tension in the fabrication process and for self-tensioning of the graphene when the flake adheres to the walls of the trench or hole [Liao15]. Previous works revealed initial tensions between 2.2×10^{-3} and $0.66\,\%$, measured with different experimental techniques [Bunch07, Bunch08, Lee08, Barton11, Chen09a, Huang11, Wang12]. Bunch *et al.* and Chen *et al.* found values from 2.2×10^{-3} to $0.26\,\%$ using graphene resonators [Bunch07, Bunch08, Chen09a]. In addition, Lee *et al.* measured built-in strain values of suspended graphene flakes by nanoindentation in an atomic force microscope, which range from 0.02 to $0.2\,\%$ [Lee08]. Huang *et al.* obtained initial built-in strain ranging from 0.02 to $0.66\,\%$ for ten high-quality samples, using the same method [Huang11][1].

However, for the measurements mentioned above, either nanoindentation (*e.g.* with an AFM tip) is necessary [Lee08, Huang11, Zandiatashbar14] or the electrically induced vibration frequency of a graphene membrane has to be scanned [Bunch07, Bunch08, Chen09a]. Built-in (or pre-)strain

[1] These strain values, denoted ϵ, can be converted into a tension T (in N/m) using the Young's modulus $E = 1.05\,\text{TPa}$ [Lee12b], the thickness of graphene $t = 0.335\,\text{nm}$ [Ni07] and the Poisson ratio $\nu = 0.16$ of graphite in the basal plane [Blakslee70], according to the equation [Medvedyeva11]

$$T = \frac{Et}{1-\nu^2}\,\epsilon \approx 360\,\text{N/m}\,\epsilon. \tag{5.1}$$

Thus, the observed built-in tension values can reach $2.4\,\text{N/m}$, which is well below the breaking strength of graphene ($42\,\text{N/m}$) [Lee08]. Note that the built-in tensions are much higher than the breaking strengths of conventional materials, *e.g.* steel would break at $0.8\,\text{N/m}$ using a comparable thickness [Cardarelli08]. Note also, that even defective graphene membranes with a high amount of sp^3 defects show similar strengths [Zandiatashbar14].

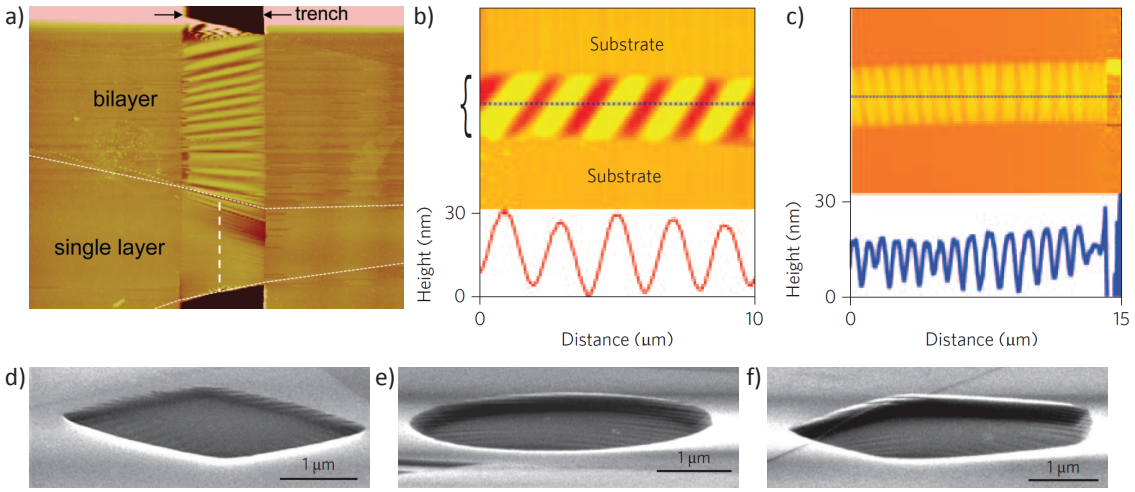

Figure 5.1: a) AFM image of a mechanically exfoliated 1L and 2LG device, suspended over a $3\,\mu$m wide trench, showing strain and ripple formation (Image taken from [Chen09b]). **b)** and **c)** AFM iamges of two suspended 1LG showing ripple formation with different periodicity, indicating built-in strain. **d)**, **e)** and **f)** SEM images of graphene membranes suspended over holes of various shapes. In particular at the borders of the mebrane, ripples are visible (Images (b) to (f) are taken from [Bao09].

plays an important role in changing the extent of tunability of the resonators and their resonance frequency, that are critical parameters for various applications, *e.g.* mass sensing [Sakhaee-Pour08, Singh10, Hill11, Chaste12]. In addition, often built-in strain is not homogeneously distributed over the membrane, as can be seen in figure 5.1a, where Chen *et al.* suspended a 1L and 2LG over a $3\,\mu$m wide trench, thermally annealed it and performed AFM measurements on it [Chen09b]. The membrane is not completely flat but strained. Another example is the so called ripple formation which has been observed by Bao *et al.* [Bao09]. Here, ripples of different periodicity have been investigated after different annealing procedures (see figures 5.1b and c). These ripples are not only observed on graphene exfoliated over trenches but also identified at the borders of membranes suspended over openings of various shapes (see figures 5.1d-f).

In this chapter we will show that Raman spectroscopy, as a non-invasive measurement technique, is capable to probe even small strain in as exfoliated suspended graphene membranes. Minor levels of isotropic and/or anisotropic built-in strain, which may not be resolved by polarized Raman spectroscopy because no splitting of the G and 2D mode occurs (in the case of uniaxial strain), *i.e.* below $\approx 0.6\,\%$, can be probed [Mohiuddin09, Mohr10, Yoon11b, Popov13, Polyzos15].

5.1 Raman spectra and hyperspectral mapping

We consider a couple of suspended graphene devices [four exfoliated over trenches (T1 to T4) and four over holes (H1 to H4) with widths of $\approx 5\,\mu$m and radii of $\approx 4\,\mu$m, respectively]. In figures

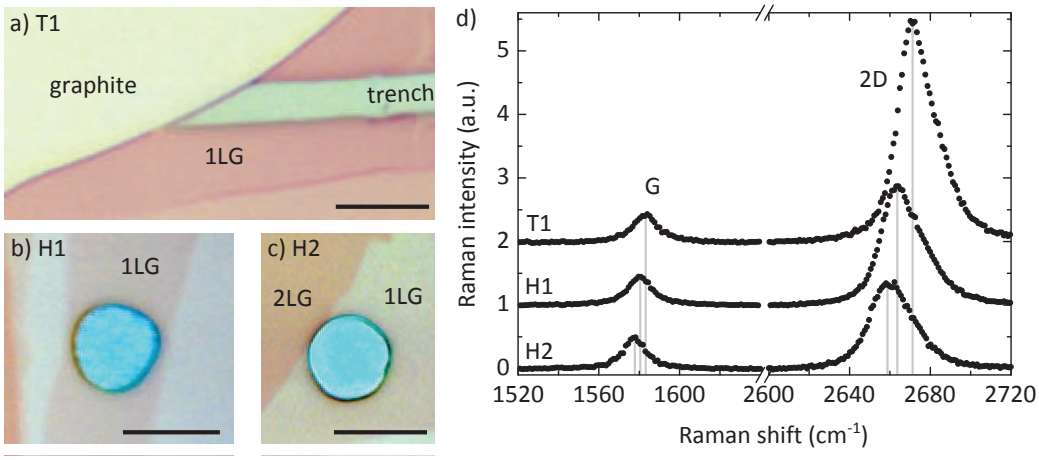

Figure 5.2: a), **b)** and **c)** Optical micrographs of three different suspended graphene devices, obtained by mechanical exfoliation. The first is suspended over a trench (T1), the second and the third (H1 and H2) suspended over holes. The images show clear optical contrast between the graphene monolayer and the neighboring bulk graphite (T1), the substrate (H1) or a graphene bilayer (H2). The scale bars are 10 μm. **d)** Raman spectra recorded at the center of the three suspended devices under ambient conditions, showing the G and 2D mode features. The spectra are offset for clarity and normalized to the integrated intensity of the G mode. The grey lines highlight the fact that the spectral position of the peaks is different for the three spectra.

5.2a, b and c are shown three typical devices, the first one suspended over a trench (T1) and the second and third ones suspended over holes. The optical contrast is clear between the 1LG and the neighboring bulk graphite, substrate and 2LG. The difference in color between the trench (yellow-greenish) and the holes (turquoise) is due to the different depth. All the three substrates are covered with 285 nm, but underwent different sample preparations. T1 has been prepared by using wet HF etching where a residual oxide layer is still present in the trench ($\approx$ 110 nm), whereas H1 and H2 has been etched by RIE which has attacked the underlying oxide (see chapter 4).

In an exemplary manner, we show three Raman spectra which has been recorded at the center of the trench (T1) and holes (H1 and H2) using a laser wavelength of 532 nm, under ambient conditions (see figure 5.2d). The Raman spectra exhibit a broad G mode (full width at half maximum (fwhm) of 14 ± 1 cm^{-1}) and an asymmetric 2D mode. Both observations are fingerprints of a quasi-undoped sample, with a residual charge carrier density of at most a few 10^{11} cm^{-2} (see section 3.3 in chapter 3) [Berciaud09, Berciaud13]. The spectra are normalized with respect to the integrated intensity of the G mode. The measured intensity of the 2D mode on T1 is larger than on H1 and H2, this discrepancy is a direct consequence of the different underlying multilayered system and the accompanied interference effects (see section 3.5).

Interestingly, although the spectra are qualitatively very similar, clear shifts of the Raman G and 2D modes, by as much as $6\,\mathrm{cm}^{-1}$ ($13\,\mathrm{cm}^{-1}$) for the G (2D) mode can be observed when going from sample T1 to sample H2. In order to unravel the origin of these shifts, we performed spatially resolved Raman measurements on all the eight suspended samples, which all displayed signatures of very low residual doping (see also the list in subsection 3.3.2).

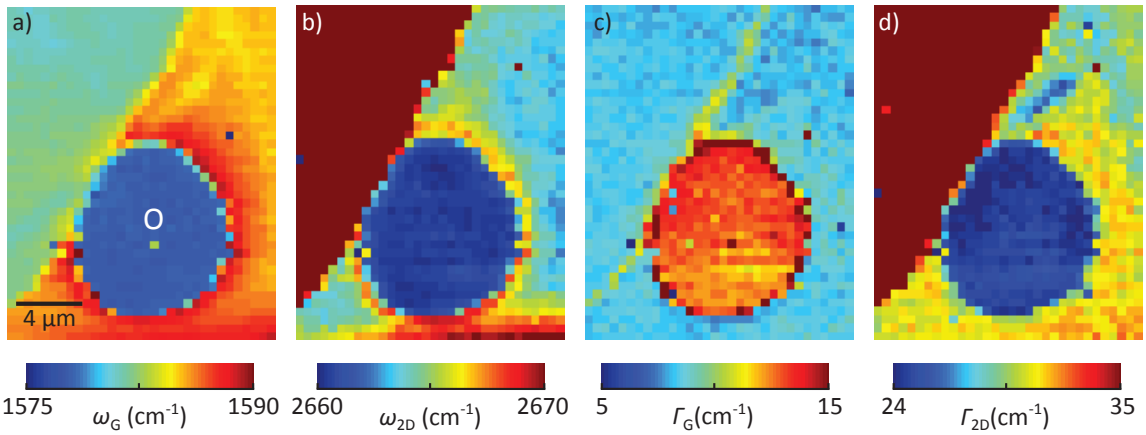

Figure 5.3: Hyperspectral Raman maps recorded on sample H2 (see figure 5.2c), measured with a laser wavelength of 532 nm, with a step size of 500 nm. The maps show the frequency distribution of the Raman G and 2D mode features, in **(a)** and **(b)**, respectively, as well as their fwhm, in **(c)** and **(d)**, respectively. The spectrum of H2 shown in figure 5.2d has been taken at the position of the white circle. The scales are chosen to highlight the 1LG features.

As an example, we show hyperspectral Raman maps of the peak frequencies, ω_G and ω_{2D}, (see figures 5.3a and b) as well as the corresponding fwhm Γ_G and Γ_{2D} (see figures 5.3c and d), recorded on sample H2 (see figure 5.2c). For the G mode, ω_G and Γ_G were extracted from single Lorentzian fits. The 2D mode is slightly asymmetric on the suspended part, and symmetric on the supported part. In order to qualitatively compare spectra recorded on the suspended and supported part, ω_{2D} and Γ_{2D} were extracted from a modified single Lorentzian fits at the power $3/2$, as introduced by Basko in ref. [Basko08] (see subsection 3.2.2). Even if the underlying mechanisms of the 2D mode process are neglected (distinction of the inner and outer process leading to an asymmetric lineshape, see subsection 3.2.2 in chapter 3) [Maultzsch04a, Basko08, Narula14], this choice is justified because we checked on selected spectra that a more refined analysis similar to that of ref. [Berciaud13], using two 2D subfeatures (each described by the modified Lorentzian profile introduced by Basko) had no impact whatsoever on the physics discussed thereafter.

In the Raman maps, the freestanding portion of sample H2 appears with a stark contrast relative to the neighboring supported part on all four maps. The G and 2D modes are softer on suspended graphene than on the neighboring supported region. The G mode width is broader ($\Gamma_G \approx 13\,\mathrm{cm}^{-1}$ on sample H2) on the suspended region. This is due to resonant coupling of G mode phonons to low-energy electron hole pairs in undoped graphene [Yan07, Pisana07, Berciaud09].

Consequently, the narrower G mode features observed on supported graphene ($\Gamma_G \approx 8\,\mathrm{cm}^{-1}$ on sample H2) suggest a doping level larger than $10^{12}\,\mathrm{cm}^{-2}$ [Yan07, Pisana07, Das08]. Finally, the 2D mode is narrower on suspended graphene than on supported graphene, as discussed in ref. [Berciaud13]. Very similar results are observed on all suspended samples. In particular, we systematically find values of Γ_G near $14 \pm 1\,\mathrm{cm}^{-1}$ (see figure 5.4a).

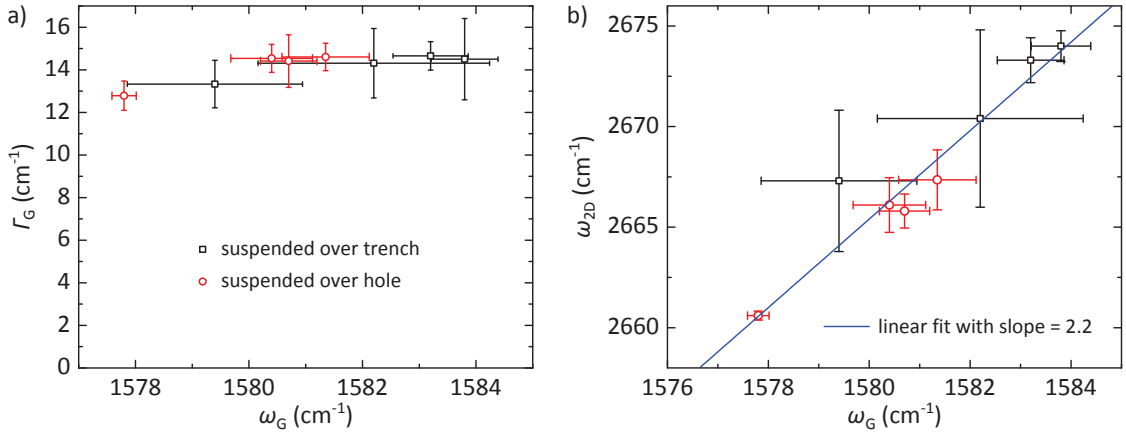

Figure 5.4: a) Spatially averaged correlation between $\langle\Gamma_G\rangle$ and $\langle\omega_G\rangle$ on suspended graphene devices (over holes: open circle, over trenches: filled square). $\langle\Gamma_G\rangle$ is constantly $\approx 14\,\mathrm{cm}^{-1}$, indicating a low doping level $< 3\times10^{11}\,\mathrm{cm}^{-2}$, whereas $\langle\omega_G\rangle$ varies from sample to sample. The error bars are the standard deviations. **b)** Spatially averaged values of ω_G and ω_{2D} for the same suspended samples as in (a) are shown. The red solid line is a linear fit to the data revealing a slope of 2.2 ± 0.1. All measurements were made using a laser wavelength of 532 nm.

5.2 Estimating built-in strain in suspended graphene devices

From all eight Raman maps we calculated the spatially averaged values of ω_G, ω_{2D}, and Γ_G on the suspended and supported part. We carefully excluded Raman spectra at the limits between suspended and supported area in order to avoid artefacts in the peak positions and width which might come from the finite laser spot size. We denote the corresponding data $\langle\omega_G\rangle$, $\langle\omega_{2D}\rangle$ and $\langle\Gamma_G\rangle$. The standard deviation is also calculated and represented as error bars in figures 5.4a and b.

The systematically broad G mode indicates a low doping level, but the spectral position of the peaks on the suspended area varies significantly from sample to sample. In figure 5.4b we show the correlation between $\langle\omega_G\rangle_{susp}$ and $\langle\omega_{2D}\rangle_{susp}$ of the eight devices with the corresponding standard deviations and a linear fit of these data. The slope of the linear fit is 2.2 ± 0.1; a strong indication that strain is the origin of the different sample dependent Raman frequencies. This assumption is in agreement with previous studies on biaxially strained graphene devices (see also section 3.4) [Metzger09, Ding10, Zabel11, Lee12b, Lee12a].

Furthermore, we can exclude a doping induced shift, because at room temperature, where phonon anomalies [Yan08a] are smeared out, ω_G shows a quasi-symmetrical upshift upon doping, irrespective of the sign of the added carriers up to charge densities of $\approx 10^{13}\,\mathrm{cm}^{-2}$. In addition, the 2D mode feature stiffens (softens) upon hole (electron) doping [Das08]. Nevertheless, it is well established that graphene layers on SiO_2 undergo hole doping [Ryu08, Ryu10]. Thus, the downshifts up to $1577.8\,\mathrm{cm}^{-1}$ for the G mode and $2660.6\,\mathrm{cm}^{-1}$ for the 2D mode cannot be explained by doping.

Using the vector decomposition model which has been proposed by Lee *et al.* and detailed in section 3.4, we can now determine the amount of strain in the suspended graphene membranes. To do so, we use equations (3.15) and (3.16) as well as the scaling factor $M_s = 7.14 \times 10^{-3}\,\%/\mathrm{cm}^{-1}$. But as the relative Raman shifts $\Delta\omega_G$ and $\Delta\omega_{2D}$ are involved in the calculation, critical parameters are the values of the unstrained and undoped graphene, which define the reference point (ω_G^0, ω_{2D}^0).

In figure 5.4b, we observe several points with a G mode frequency near $1581\,\mathrm{cm}^{-1}$, which correspond to the value commonly measured on bulk graphite. Also, the mean G mode frequency measured on our samples is $1581 \pm 2\,\mathrm{cm}^{-1}$. Hence, we estimate that $\omega_G^0 \approx 1581\,\mathrm{cm}^{-1}$. At this frequency, we measured $\omega_{2D}^0 = 2667 \pm 1\,\mathrm{cm}^{-1}$.

With this reference point (for suspended graphene and a laser wavelength of $532\,\mathrm{nm}$) we determine the averaged strain values on the eight suspended devices which are summarized in the first column of table 5.1. We see that both compressive (negative sign) and tensile (positive sign) built-in strain are present in the suspended samples. The strain is marked with an error which is directly the standard deviation of ω_G and ω_{2D} within the suspended area.

Some suspended samples exhibit a very narrow frequency distribution whereas others spread more. In order to understand why this distribution is so different from one sample to another, we forbear with the averaged values and come back to the raw frequency data of the suspended part. In figure 5.5a we plot the correlation of ω_G and ω_{2D} for each Raman spectrum recorded by hyperspectral mapping on our samples, or, in other words, each data point corresponds to a spatially different pixel on the maps (see also the map of sample H2 in figure 5.3 and sample T2 in figure 5.6).

As examples representing the variety of frequency distribution within one sample, let us discuss samples H1, H2, T1 and T2. H2 shows a very small frequency distribution whereas the data of H1 is more extended in all directions in the ω_G-ω_{2D}-plane. Hence, H1 is more affected by both strain *and* doping. Interestingly, the data from the suspended part of T1 and T2 are well aligned on a slope of 2.2. This observation implies that the variation of the charge concentration is mini-

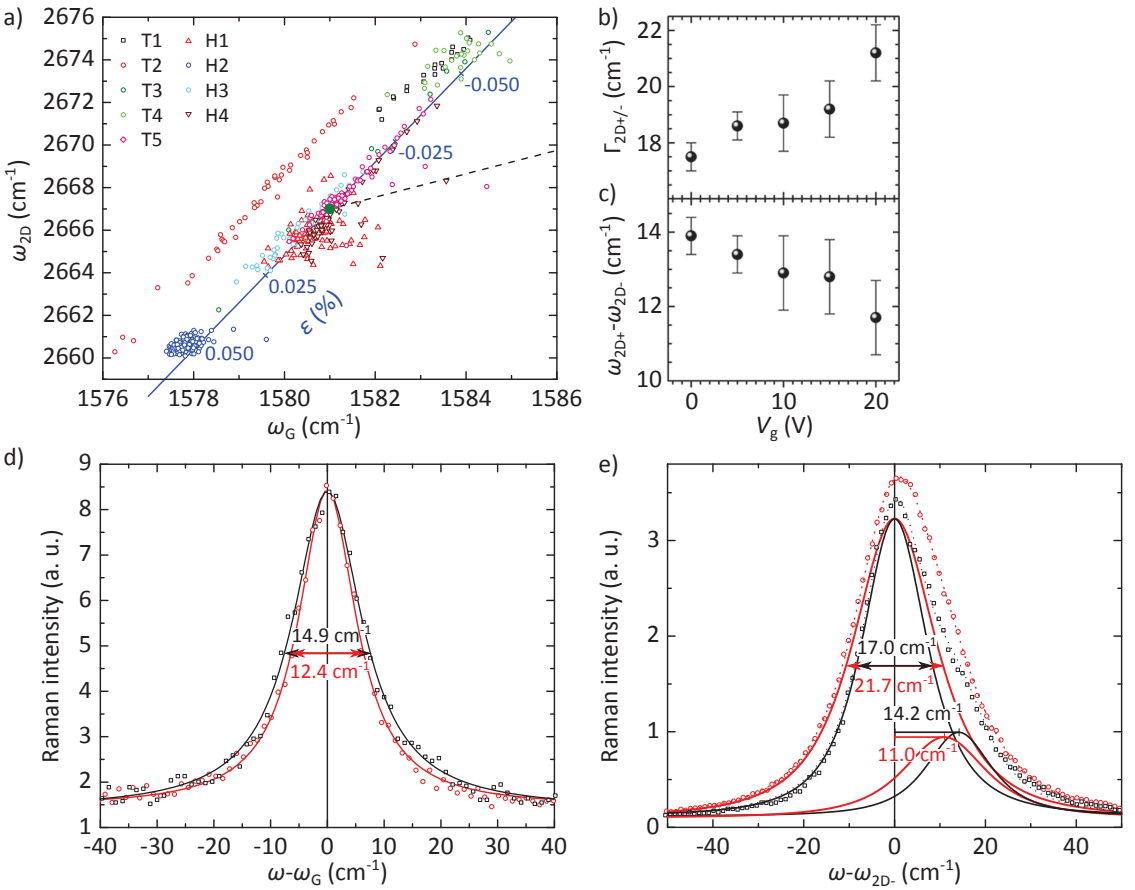

Figure 5.5: a) Correlation of ω_G and ω_{2D} (fitted with a single modified Lorentzian lineshape) for the suspended part of several samples, showing different extents of frequency distribution. The most striking difference is observed between samples H2 and T2, showing a confined distribution ($\epsilon \approx +0.05\,\%$) and a large spread along the slope 2.2 (ϵ ranging from -0.05 to $+0.04$), respectively. **b)** and **c)** Evolution of $\Gamma_{2D^+/-}$ (b) and $\omega_{2D^+} - \omega_{2D^-}$ (c) as a function of an applied back gate voltage V_g on a suspended graphene device. The data are adapted from ref. [Berciaud13] and illustrate the transition from clean undoped graphene to slightly doped graphene. The peak broadening and decreasing $\omega_{2D^+} - \omega_{2D^-}$ with increasing V_g point the way to a broad and symmetric 2D mode feature, often observed on supported graphene. **d)** and **e)** Raman data recorded on the suspended part of sample T2 (red) and T3 (black). (d) shows the raw data of the G mode and the corresponding Lorentzian line shape fit. The line width of T2 is slightly smaller than that of T3. (e) shows a detailed analysis of the 2D mode feature of sample T2 and T3. The spectra are normalized with respect to the amplitude of the $2D^-$ sub-feature, for a better comparison. Compared to sample T3, the 2D mode sub-features of T2 are broadened and $\omega_{2D^+} - \omega_{2D^-}$ is reduced. For both fits it is $\Gamma_{2D^+} = \Gamma_{2D^-}$.

mal, but the strain can vary locally within the suspended part (within this analysis from -0.06 to -0.04 % for T1 and from -0.05 to $+0.04$ % for T2[2]).

However, sample T2 is slightly different from the other samples, because the data in figure 5.5a are shifted to higher values of ω_{2D}, which is, at first sight, surprising because strong doping induced Raman shifts would follow the dashed line in figure 5.5a and low doping levels are expected to have only a minor influence on ω_{2D} [Das08, Froehlicher15a]. To understand this different behavior we have to remind the limits of the vector decomposition model and the way how we have proceeded in the analysis of the raw Raman spectra. Indeed, even if slightly asymmetric, we have fitted the 2D mode feature by a symmetric quasi-Lorentzian line shape. This choice is justified by the fact that for all suspended samples, the spectral difference between the $2D^-$ and $2D^+$ sub-mode features is constant ($\omega_{2D^+} - \omega_{2D^-} \approx 14\,\mathrm{cm}^{-1}$) as well as their integrated intensity ratio ($I_{2D^-}/I_{2D^+} \approx 3.5$) and a constant width ($\Gamma_{2D^-} = \Gamma_{2D^+} \approx 17\,\mathrm{cm}^{-1}$). These values are in clear agreement with the 2D mode characteristics observed in ref. [Berciaud13] for undoped graphene. Furthermore, Berciaud *et al.* probed the transition from an undoped suspended graphene device, exhibiting an asymmetric lineshape, to a doped device showing a symmetric line shape, by applying a back gate voltage. This transition is marked by a decrease of the spectral difference of the sub-mode features and by a broadening (see figure 5.5b and c).

On sample T2, we observe all fingerprints of a slight doping. The G mode fwhm is slightly lower ($\Gamma_G \approx 12.8 \pm 0.8\,\mathrm{cm}^{-1}$), the spectral difference of the 2D sub-mode features is smaller ($\omega_{2D^+} - \omega_{2D^-} = 11.0 \pm 0.8\,\mathrm{cm}^{-1}$) and their width is increased ($\Gamma_{2D^-} = \Gamma_{2D^+} = 21.6 \pm 0.6\,\mathrm{cm}^{-1}$). In figures 5.5d and e we compare the G and 2D mode features on selected spectra recorded on sample T2 (slightly doped, red) and T3 (undoped, black). In particular, by comparing $\Gamma_{2D^{+/-}}$ and $\omega_{2D^+} - \omega_{2D^-}$ with the data obtained on a gated graphene membrane (see figures 5.5b and c), sample T2 exhibits clearly features of a slightly doped graphene.

The fact that ω_{2D} is hardened on this slightly doped samples is not an artifact of the fitting procedure due to a different shape of the peak. Fitting an asymmetric line shape as in figure 5.5e with decreasing asymmetry with a symmetric line would not lead to higher values of ω_{2D}. Hence, our results suggest that the reference point (ω_G^0, ω_{2D}^0) of doped graphene is slightly different compared to undoped graphene. Indeed, we should be aware of the fact that the 2D mode process strongly depends on the exact evolution of the electron and phonon dispersion (see section 3.2.2). In particular, a different local dielectric environment, *e.g.* by some surface contaminations, might impact the Fermi velocity, the phonon velocity and the electron-hole lifetime, all three involved in the width of the 2D mode feature [Elias11, Hwang12, Faugeras15]. In fact, according to equation (3.6), Γ_{2D} is proportional to $\gamma v_{TO}/v_F$. Thus, a broader 2D mode feature might accompany a

[2] In general, a slight trend of tensile strain in suspended graphene exfoliated over trenches and of compressive strain over holes as well as a larger strain range over trenches could be identified. However, to confirm this trend, a larger statistic would be preferable.

renormalization of the mode, which is, in our sample (and at a laser energy of 2.33 eV) a slight upshift of the 2D mode[3].

We take advantage of this rather meticulous analysis in order to point out the limits of the vector decomposition model. For a correct determination of the strain, the knowledge of the reference point (ω_{G}^0, ω_{2D}^0) is crucial. For undoped graphene, we estimated ($\omega_{\mathsf{G}}^0 = 1581\,\mathrm{cm}^{-1}$, $\omega_{\mathsf{2D}}^0 = 2667\,\mathrm{cm}^{-1}$), where ω_{2D}^0 is here the spectral position extracted from a single quasi-Lorentzian profile. Slight doping seems to shift the reference point, as discussed above. This observation is, in particular, a hint that the reference point is different on supported graphene, since the dielectric screening of the electrons and phonons is different. It is important to keep this conclusion in mind, in particular for the analysis in section 5.3, where we compare doping and strain in suspended and supported graphene devices.

Let us note that, even if the reference point for slightly doped graphene might be different, the main conclusion which is extracted from figure 5.5a still holds. Samples H1 and T2 exhibit a comparable average strain, but the spatial spreading of the Raman frequencies reveals a non-trivial built-in strain distribution. This remark underlines the fact that Raman spectroscopy is indeed a highly precise tool for local strain probing in graphene. That means, in particular, that strain can be spatially resolved within the limit of diffraction. As sample T2 displays an large strain distribution, we take this sample in an exemplary manner and illustrate the spatial strain mapping in figure 5.6, by keeping the reference point in figure 5.5a (green point). We show in figure 5.6a an optical micrograph of the sample T2, and in b and c hyperspectral Raman maps of ω_{G} and ω_{2D}, respectively. The phonon softening of both G and 2D modes in the lower right part of the trench is then, by applying equations (3.15) and (3.16), translated in a strain varying in a range of $\Delta\epsilon = \pm 0.06\,\%$. Here $\Delta\epsilon = \epsilon - \epsilon_0$, where ϵ_0 depends on the definition of the reference point. The lack of knowledge about the exact reference point prevents us here of giving an absolute value of strain. Hence, we show within the map in figure 5.6d only relative values. However, on the upper (lower) part of the trench, the phonons stiffen (soften) and the graphene membrane might be under compressive (tensile) strain. Note that the choice of a different reference point for supported graphene would also change the absolute value of the strain, but not its distribution. Furthermore, it seems as if the strain propagates on the supported part of the graphene flake and that, for this sample, the trench appears as a disturbance.

These observations further stress the importance of local Raman mapping in order to characterize each sample correctly.

[3] In fact, the issue is rather complicated, because in very clean and neutral graphene, v_{F} is higher [Elias11], but the Kohn anomaly is also more pronounced (v_{TO} higher). That means in practice that one is not able to decouple these two effects, which seem to cancel a pronounced influence on Γ_{2D}. Nonetheless, the effects we talk about here are in a very narrow frequency range (approximately $1\,\mathrm{cm}^{-1}$).

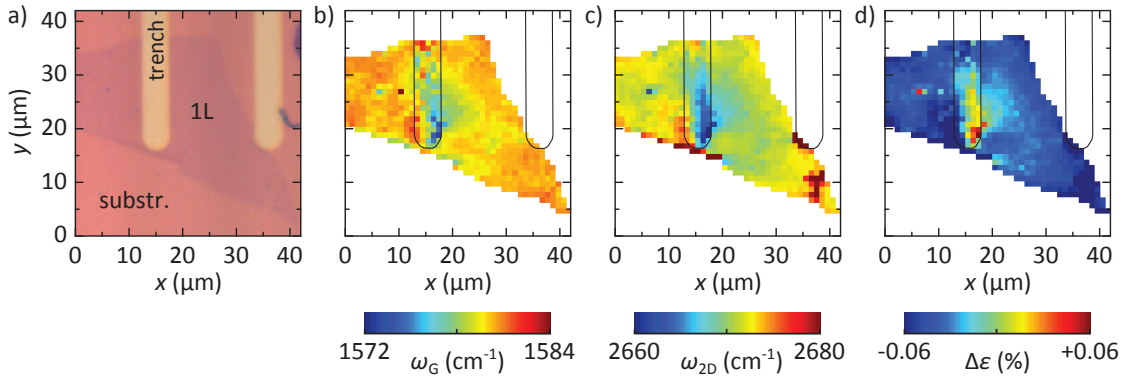

Figure 5.6: Example of hyperspectral Raman mapping for strain determination. **a)** Optical micrograph of sample T2, a graphene flake exfoliated over an $\approx 5\,\mu$m wide trench. **b)** and **c)** Spatially resolved Raman maps of the sample shown in (a), displaying ω_G and ω_{2D}, respectively. The spectra are recorded with a $\times 20$ objective (NA $= 0.45$) at a laser wavelength of 532 nm. The step size $1\,\mu$m and the acquisition time 2 s. This time is a compromise between a long acquisition time which would lead to a higher accuracy, in particular in Γ_G, but also lead to defocusing, and a short acquisition time sufficient to extract the Raman frequencies. Note that the data in figures 5.5a, d and e are extracted from a different map with an acquisition time > 1 min. **d)** Spatial distribution of the strain ϵ in %, extracted from the correlation of ω_G and ω_{2D} shown in (b) and (c), using equations (3.15) and (3.16) and a reference point of ($\omega_G^0 = 1581\,\text{cm}^{-1}$, $\omega_{2D}^0 = 2667\,\text{cm}^{-1}$).

5.3 Comparing doping and strain in suspended and supported graphene

Up to now, we omitted the data of the supported part. In figure 5.7a and b we additionally plot the frequency clouds of the supported part of samples T1, H1 and H2 and the corresponding mean values with their standard deviation, respectively.

Interestingly, the data follow a general trend, *i.e.* they are shifted along a line with a slope of 0.55 with respect to the values recorded on the suspended part. The upshift of ω_G is at least $\approx 5\,\text{cm}^{-1}$, which is an indication that charge carrier densities of at least $1 \times 10^{12}\,\text{cm}^{-2}$ are achieved [Lazzeri08, Lee12a]. Thus, we are entering the regime, where a linear dependence of ω_{2D} *vs.* ω_G is expected ($\gtrsim 6 \times 10^{11}\,\text{cm}^{-2}$) [Lee12a, Froehlicher15a], which is the precondition for the application of the vector decomposition model for doping. If we assume that the reference point is the same on the suspended and supported part, *i.e.* ($\omega_G^0 = 1581\,\text{cm}^{-1}$, $\omega_{2D}^0 = 2667\,\text{cm}^{-1}$), we should be aware of a small systematic error in the determination of the strain and doping, which is estimated to be in the range of 0.05 % and $1 \times 10^{12}\,\text{cm}^{-2}$ for the absolute values, but lower for relative values within one sample in the case of strain. However, the measurement of the reference point on supported graphene is quite challenging because the graphene is always influenced by doping, strain and screening effects.

However, one can fully benefit from the vector decomposition model when higher values of doping and strain are present. This is the case for supported graphene, in particular for the dop-

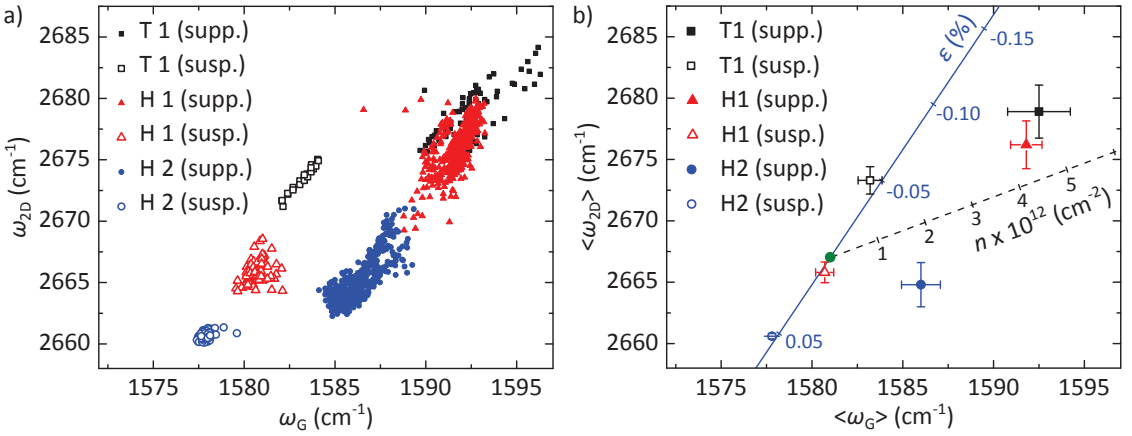

Figure 5.7: a) Correlation of ω_G and ω_{2D} from spectra measured on samples T1 (squares), H1 (triangles) and H2 (circles), extracted from Raman maps. The data recorded on the suspended (supported) part is represented with open (filled) symbols. The data of the suspended and supported graphene are well distinguishable for regarding each sample, but also from sample to sampe. **b)** Correlation of the spatially averaged frequency values represented in (a). The chosen reference point for neutral and unstrained graphene ($\omega_G^0 = 1581\,\text{cm}^{-1}, \omega_{2D}^0 = 2667\,\text{cm}^{-1}$) for a laser wavelength of 532 nm is added as dark green circle and defines the crossing point for the lines with slopes 2.2 for strain (blue straight) and 0.55 for hole doping (black dashed). The scaling obtained from equations (3.17) and (3.18) is added. The data of the suspended part are less spread and align on the strain line whereas the data of the supported part are more spread and shifted along the hole doping line.

ing component. Thus, we calculate the average strain $\langle\epsilon\rangle_{\text{supp}}$ and doping $\langle n\rangle_{\text{supp}}$ using the vector decomposition model (with $\partial\omega_{2D}/\partial\omega_G|_h = 0.55$, $M_{\text{d,holes}} = -3.6 \times 10^{11}\,\text{cm}^{-1}$ [Froehlicher15a] for hole doping and the reference point of suspended graphene). The obtained values are represented in table 5.1. $\langle\epsilon\rangle_{\text{supp}}$ is of comparable magnitude compared to $\langle\epsilon\rangle_{\text{susp}}$. In contrast, $\langle n\rangle_{\text{supp}}$ is at least one order of magnitude higher than $\langle n\rangle_{\text{susp}}$, which is estimated to be smaller than a few $10^{11}\,\text{cm}^{-2}$, by analyzing Γ_G and the asymmetry of the 2D mode line shape. Only an upper bound can be given, because at doping levels below $\approx 6 \times 10^{11}\,\text{cm}^{-2}$ (*i.e.* ≈ 100 meV), the frequency of the G mode does not scale linearly [Froehlicher15a]. On the supported part, values of $\approx 3 \times 10^{12}\,\text{cm}^{-2}$ are generally obtained.

This observation is coherent with former results reporting about doping in graphene deposited on Si/SiO_2 substrates[Martin08, Berciaud09, Ni10, Ryu10, Lee12a]. The large standard deviation of $\langle n\rangle_{\text{supp}}$, which is at least twice as large as the absolute values of $\langle n\rangle_{\text{susp}}$, is a fingerprint of the large charge inhomogeneity on the supported part.

5.4 Conclusion

In this chapter we have statistically evaluated eight suspended graphene devices by carefully analyzing hyperspectral Raman maps with respect to the linewidths and spectral position of the G

	$\langle\epsilon\rangle_{\text{susp}}$ (%)	$\langle\epsilon\rangle_{\text{supp}}$ (%)	$\langle n\rangle_{\text{supp}}$ ($\times 10^{12}$ cm^{-2})
T1	-0.05 ± 0.01	-0.06 ± 0.02	$+3.3 \pm 1.1$
T2	-0.01 ± 0.04	-0.03 ± 0.03	-0.5 ± 1.0
T3	-0.03 ± 0.05	-0.07 ± 0.04	$+3.5 \pm 1.4$
T4	-0.06 ± 0.01	-0.09 ± 0.02	-0.5 ± 0.7
H1	$+0.01 \pm 0.01$	-0.03 ± 0.02	$+3.6 \pm 0.7$
H2	$+0.05 \pm 0.00$	$+0.05 \pm 0.02$	$+3.3 \pm 0.7$
H3	$+0.01 \pm 0.01$	$+0.01 \pm 0.06$	$+3.0 \pm 2.0$
H4	$+0.00 \pm 0.02$	-0.01 ± 0.04	$+1.8 \pm 1.6$

Table 5.1: Spatially averaged strain and doping values with standard deviation for eight different samples. The values are obtained from Raman maps and subsequent vector projection, as discussed in the main text. Note that $\langle n\rangle_{\text{susp}}$ can only be estimated as being below a few 10^{11} cm^{2}.

and 2D modes. We find that suspended graphene is subjected to either compressive or tensile built-in strain. The sample dependent absolute average values can reach ≈ 0.1 %, and the strain range within one sample might be up to ≈ 0.1 %. Supported graphene undergoes comparable strain levels.

Furthermore, we find that suspended graphene exhibits a low doping level of $\approx 3\times10^{11}$ cm^{-2}, in contrast to a doping level of one order of magnitude higher on supported graphene. The charge inhomogeneity on the latter exceeds twice the estimate of residual doping on suspended graphene.

Our results are in agreement with previous studies about built-in strain in as exfoliated graphene [Bunch07, Bunch08, Lee08, Barton11, Chen09a, Huang11, Wang12]. In particular, our values of built-in strain are comparable with the gate-induced strain estimated by Bolotin *et al.* who measured a remarkably high electron mobility in their suspended graphene devices, in spite of strain [Bolotin08b].

We highlight that our measurement technique is contactless and offers a spatial resolution of locally varying strain down to the laser spot size ($\approx 1\ \mu$m^2) [Neumann15b]. We conclude that our suspended graphene devices build an ideal platform to access the vicinity of the Dirac point. In addition, our results may serve as a guide for advanced characterization of freestanding graphene-based devices, such as frequency-driven cavities [Chen09a, Engel12, Reserbat-Plantey13, Singh14]. Notably, it will turn out in the subsequent chapters that pre-strain in suspended graphene membranes has a non-negligible influence of the deflection properties.

Related publications

Paper:

- Dominik Metten, François Federspiel, Michelangelo Romeo, and Stéphane Berciaud, *Probing built-in strain in freestanding graphene monolayers by Raman spectroscopy*, Physica Status Solidi B **250**, 2681–2686 (2013) / DOI: 10.1002/pssb.201300220, ref. [Metten13].

Poster:

- Dominik Metten, François Federspiel, Michelangelo Romeo, and Stéphane Berciaud, *Probing residual doping and built-in strain in freestanding graphene monolayers by Raman spectroscopy*
  presented at
  - ▷ *Journées Néel*, Institut de Physique et de Chimie des Matérieux de Strasbourg, 3rd to 4th of September 2013, Strasbourg (France)
  - ▷ Winter school *Surface-Confined Synthesis of Nanostructures*, Collège doctoral franco-allemand (Karlsruher Institut für Technologie and Université de Strasbourg), 17th to 20th of February 2014, Baden-Baden (Germany)

6 All optical blister test of suspended graphene

In this chapter we present a detailed Raman study of pressurized graphene membranes covering circular pits. Due to the strong adhesion of graphene to the SiO_2 substrate [Koenig11, Yoon12, Boddeti13, Gao14] and its impermeability to standard gases [Bunch08, Berry13], the pressure difference induced bulging of the membrane can be considered as a so called *constant N blister test* where N refers to the number of molecules trapped inside the microchamber. The pressure difference is applied by putting the device into a vacuum chamber. Then, *in situ* spatially resolved Raman maps and line scans are recorded in dependence of the applied pressure difference.

The content of this chapter will be focused on the detailed analysis of the two prominent Raman G and 2D mode features with varying pressure difference. Two main observations will be evaluated:

- the **change in the integrated intensity** of the G and 2D modes by more than one order of magnitude
- the **change of the spectral position** of these modes up to several $10\,\mathrm{cm}^{-1}$.

The former might be attributed to interference effects, because the distance between the bottom of the pit and the membrane changes. For the analysis, the model developed in chapter 3 will be used. The latter will give important information about the strain induced phonon softening in the membrane. Merging these investigations will lead to

- the validation of the fact that **biaxial strain induced phonon softening obeys the ratio** $\partial\omega_{2D}/\partial\omega_{G} = 2.2$,
- the determination of the **intrinsic value of the** I_{2D}/I_{G} **ratio**,
- the determination of the **Grüneisen parameters** of the G and 2D modes,

- the validation of the $P \propto \xi_{\mathsf{max}}^3$**-dependence** for the membrane limit of the Föppl-von Kármán equations and
- the determination of the **Young's modulus** of graphene by using Hencky's solution for circular membranes.

Even though, in the research community, the exact value of the Young's modulus of graphene seems to converge to ≈ 1 TPa [Lee08, Jiang09, Lee12b, Annamalai12, Tan13] and Hencky's solution has already been applied successfully to graphene blisters [Hencky15, Koenig11, Yue12, Boddeti13, Lee14, Liao15], there is still a discussion remaining about the Grüneisen parameters, in particular. Also, often the shape of the bulged graphene membrane is examined by means of AFM, suspicious to introduce artefacts [Lu10, Bunch12], or by estimating the height by means of SEM imaging [Lee12b].

Here, the approach by Raman spectroscopy will allow us to determine the mechanical properties of graphene *in situ* by pure optical means. The bulging of the membrane, which can be considered as sealing a microchamber, is induced by a pressure difference Δp between the pressure inside the chamber, called p_{int}, and the pressure outside, called p_{ext}, thus, it is $\Delta p = p_{\mathsf{int}} - p_{\mathsf{ext}}$. In our measurement runs, which are performed within the cryostat presented in chapter 4 serving as vacuum chamber with optical access (at ambient temperature), p_{ext} is smoothly varied from approximately 10^{-2} Pa to atmospheric pressure, (100 ± 2) kPa.

Our results are based on the analysis of three suspended graphene membrane devices, labeled A, B and C, with comparable blister radius a ($\approx 4\,\mu$m) and slightly different pit depth d_{air} (ranging from (395 ± 10) nm for sample A to (340 ± 10) nm for sample B and C). In figure 6.1a we show the optical micrograph images of the three samples. The pit of sample A is neighbored by a bilayer graphene, whereas B and C are neighbored by multilayer graphene and graphite, respectively. Samples B and C have been left under vacuum for several hours prior to the measurement runs, so that they could undergo a significant leakage of the trapped air molecules, leading to a deflation and consequently to a negative Δp once the external pressure returns to atmospheric pressure. Hence, an inward bulging of the membrane is expected, as schematically sketched in figure 6.1b. This leakage is probably related to gas diffusion through the silicon oxide and favored for samples B and C because the distance from the pit to the uncovered substrate is shorter than for sample A [Bunch08, Koenig11].

In order to verify whether the leak rate has to be considered, Raman measurements are performed on the suspended graphene membranes at $p_{\mathsf{ext}} = p_{\mathsf{int}} = 100$ kPa before pumping out the vacuum chamber and again at $p_{\mathsf{ext}} = 100$ kPa, after a measurement series as a function of p_{ext}, starting from $p_{\mathsf{ext}} \approx 10^{-2}$ Pa. No significant changer of the Raman frequencies or of the integrated intensities of the Raman features are observed, which demonstrates that the leak rate of our pressurized membrane could be neglected over the duration of a measurement run.

Even if the results of the samples, which underwent a leakage before the measurement run, *i.e.* samples B and C, are quantitatively comparable with those obtained on sample A, the pressure load calibration is afflicted with a larger systematic error (see section B in the Appendix for more details). Thus, if not stated differently, we will present the results obtained on sample A and report the corresponding data from samples B and C in the Appendix (see section D).

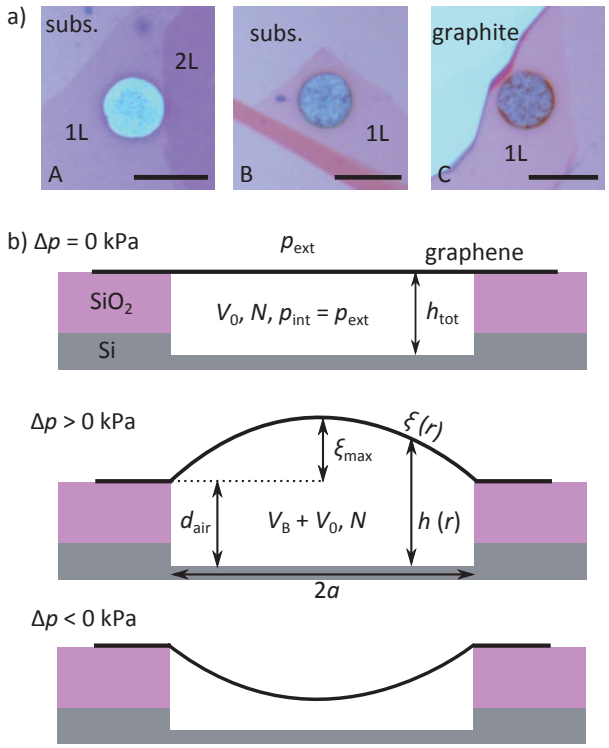

Figure 6.1: a) Optical micrograph images of sample A, B and C. The pit in the center of the images is covered by a single graphene sheet, indicated as 1L. The pit of sample A (B, C) is neighbored by a bilayer graphene (multilayer graphene, graphite). The scale bars are $10\,\mu$m. **b)** Schematic profile of the pit covered by a graphene membrane, subjected to a pressure difference $\Delta p = p_{\text{int}} - p_{\text{ext}}$. $\Delta p > 0$ kPa results in bulging up of the graphene, $\Delta p < 0$ kPa deflects the graphene membrane downwards. d_{air} denotes the depth of the pit. $\xi(r) = h(r) - d_{\text{air}}$ is changing with Δp, as do the corresponding distances at the center of the pit, $\xi_{\text{max}} = h_{\text{max}} - d_{\text{air}}$. Furthermore, V_0 denotes the volume of the cylindrical pit, V_{B} the volume of the blister and N the number of particles trapped under the membrane.

The values of Δp achieved in our measurement setup can be evaluated by applying the ideal gas law (see subsection B in the Appendix for details) and are fairly below 100 kPa (*e.g.* for sample A, Δp varies between (0 ± 2) and 74 ± 5 kPa), which is more than one order of magnitude below the threshold, at which delamination occurs [Koenig11]. Consequently, we can consider the blister radius as constant throughout our analysis.

6.1 Strain induced phonon softening

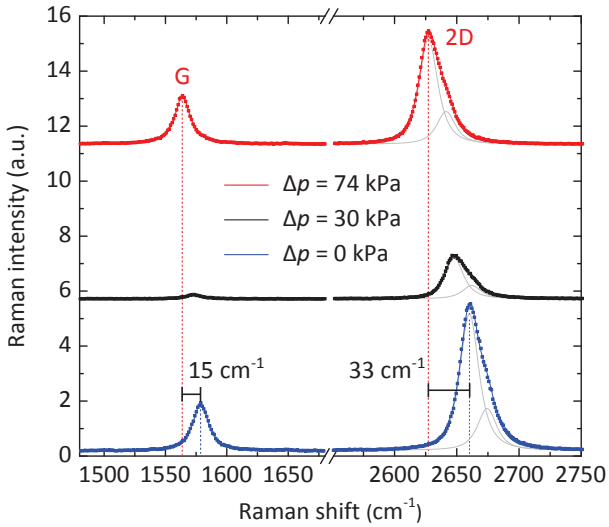

Figure 6.2: Raman spectra recorded at the center of the graphene membrane on sample A at different values of Δp. The spectra are offset for clarity. With increasing Δp, both G and 2D mode downshift and a change in the integrated intensity is observed. The G mode feature is fit to a single Lorentzian, whereas the 2D mode feature is fit to a modified double Lorentzian profile (light gray lines).

Raman spectra recorded at the center of the membrane for $\Delta p = 0, 30$ and 74 kPa are shown in figure 6.2. At pressure equilibrium, the Raman G mode feature (fit to a single Lorentzian) is centered at $\omega_G = 1578.8\,\mathrm{cm}^{-1}$, with a fwhm of $\Gamma_G = (15 \pm 1)\,\mathrm{cm}^{-1}$, characteristic of an undoped sample (see chapter 3) [Berciaud09]. We note that Γ_G remains at $(15 \pm 0.5)\,\mathrm{cm}^{-1}$ over the suspended membrane at each value of Δp, as can be seen in figure 6.3a, where the data pair ω_G, Γ_G is plotted for every Δp. In addition, we have added the expected evolution of Γ_G with ω_G according to the theory developed in chapter 2 for hole (straight red line) and electron doping (dashed blue line) to the graph. The evolution of the measured values confirm, in particular, that doping from the surrounding air molecules can be neglected and that our suspended graphene membranes allow investigations of strain without parasitic effects from unintentional doping.

The 2D-mode feature shows an asymmetric line shape, as typically observed on suspended graphene, and is fit to a modified double Lorentzian profile [Basko08], as in ref. [Berciaud13]. The lower energy feature has much higher integrated intensity and its peak frequency coincides with the peak frequency of the 2D mode feature. The spectral shift between the low- and the high-energy features (approximately $15\,\mathrm{cm}^{-1}$), as well as their integrated intensity ratio (approximately 3) is also constant over the suspended part, irrespective of Δp. Hence, we use the position of the low-energy 2D mode subfeature as the peak frequency, denoted ω_{2D}, and the sum of the integrated intensities of both subfeatures is referred to as I_{2D}. The values of $\omega_G = 1578.8\,\mathrm{cm}^{-1}$

	sample A	sample B	sample C
d_{air} (nm)	395 ± 10	340 ± 10	340 ± 10
a (nm)	4.1 ± 0.1	4.0 ± 0.1	4.0 ± 0.1
ω_G ($\Delta p = 0$) (cm^{-1})	1578.8 ± 1.0	1581.5 ± 1.0	1580.5 ± 1.0
ω_{2D} ($\Delta p = 0$) (cm^{-1})	2660.0 ± 1.0	2667.0 ± 1.0	2666.0 ± 1.0
ϵ (%)	0.05	0.00	0.01
Γ_G (cm^{-1})	15.0 ± 1.0	15.1 ± 1.0	14.8 ± 1.0

Table 6.1: Summary of the characteristics of the three graphene membrane devices used for blister tests.

and $\omega_{2D} = 2660.0\,\text{cm}^{-1}$ are slightly lower than expected for pristine graphene and might be attributed to an initial built-in strain of around 0.05 %, in accordance with our results in chapter 5. We note that very similar results to those described here are obtained on samples B and C, on which no significant built-in strain is observed (see also table 6.1). This similarity is an indication that low values of prestrain have a minor effect on bulging under uniform pressure load.

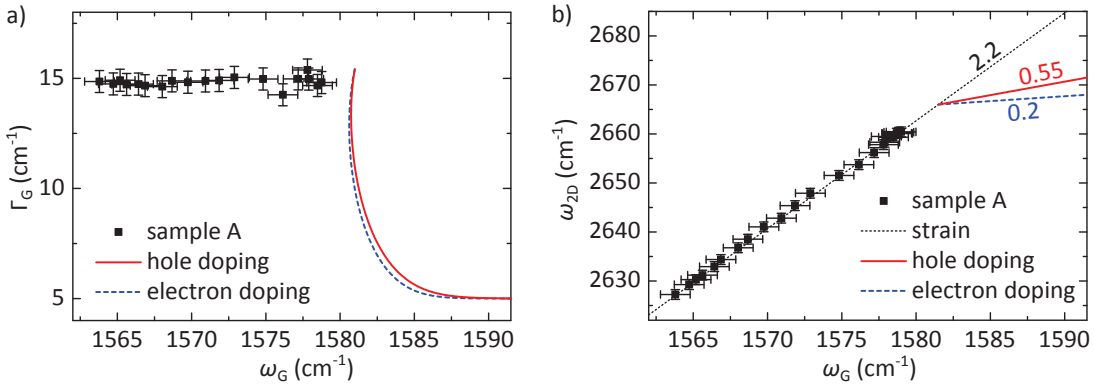

Figure 6.3: a) Γ_G vs. ω_G for different values of Δp (black squares), indicating a constant value of $\Gamma_G \approx 15\,\text{cm}^{-1}$ all over the measurement run on sample A. The theoretically expected evolution in the case of electron or hole doping is added as dashed blue and straight red line, respectively. **b)** Correlation of ω_G and ω_{2D} (black squares) and expected correlation extracted from ref. [Froehlicher15a].

When the sample is placed under high vacuum (see red curve in figure 6.2), both the G and 2D mode features soften (by $15\,\text{cm}^{-1}$ and $33\,\text{cm}^{-1}$ at the center of the membrane, respectively) but retain their peak shapes. At the center of the blister, the softening of the peaks is continuous with increasing Δp. The evolution of this softening is shown in figure 6.3b and, again, does not follow the expected evolution for electron and hole doping, as described in chapter 2 and in references [Das08, Froehlicher15a].

The spectra at $\Delta p = 0\,\text{kPa}$ and $\Delta p = 74\,\text{kPa}$ show comparable values of the integrated intensities, denoted I_G and I_{2D} for the G and 2D mode, respectively. A spectrum taken at an in-

termediate pressure difference, $\Delta p = 30$ kPa is also shown (black curve). Interestingly, it reveals a striking decrease of I_G, by one order of magnitude, and of I_{2D} by a factor of only approximately 4, compared to the measurement at $\Delta p = 0$ kPa. These important variations are due to interference effects caused by the change in distance between the bottom of the pit and the membrane and will be discussed later in section 6.2. Here, we concentrate on the Raman shifts and their dependence on Δp and on r, the radial distance from the center.

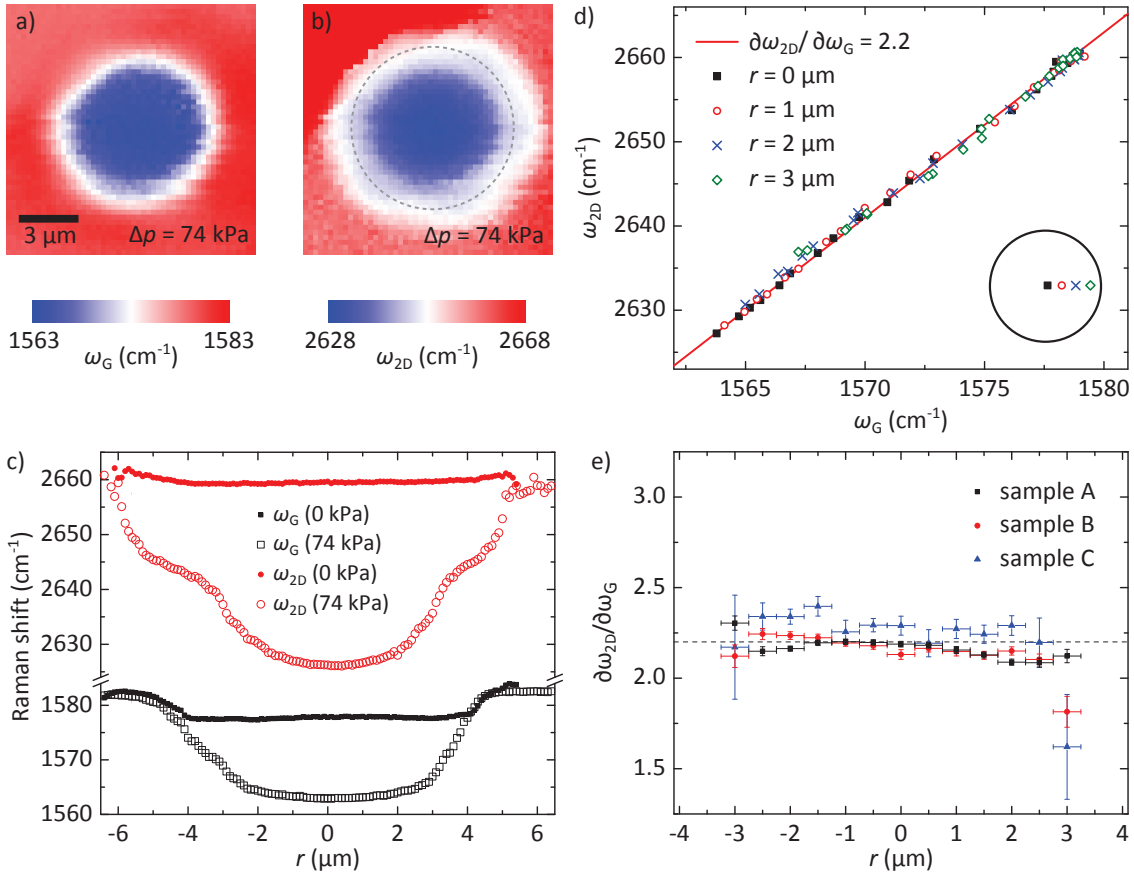

Figure 6.4: a) and **b)** Spatially resolved hyperspectral Raman maps of the G and 2D mode frequencies recorded on sample A, under a uniform pressure load of $\Delta p = 74$ kPa. The step size is 250 nm. The upper left part of the sample contains a supported bilayer region (see also figure 6.1a), where, as expected, ω_{2D} is significantly upshifted with respect to the monolayer 2D mode frequency. The border of the pit is represented by gray dashed circles. **c)** High-resolution radial line scans of ω_G (black squares) and ω_{2D} (red circles), recorded across the pit at $\Delta p = 0$ kPa (filled symbols) and $\Delta p = 74$ kPa (open symbols), with a step size of 100 nm. **d)** Correlation between ω_G and ω_{2D} plotted for each pressure difference at four different values of r, ranging from $r = 0\,\mu$m to $r = 3\,\mu$m. The solid line is a linear fit with a slope $\partial\omega_{2D}/\partial\omega_G = 2.2$. **e)** $\partial\omega_{2D}/\partial\omega_G$ as a function of r, the distance from the blister center, extracted from samples A, B and C. Within a radius of $|r| \leq 3\,\mu$m, $\partial\omega_{2D}/\partial\omega_G$ is 2.2 ± 0.1.

Figure 6.4 displays two-dimensional Raman maps, of ω_G (a) and ω_{2D} (b), recorded at $\Delta p = 74$ kPa on the sample A. The pressurized suspended region exhibits centrosymmetric distributions

of ω_G and ω_{2D} with minimum values much smaller than on the supported region. Indeed, a few microns away from the pit, the pressure-induced strain is relaxed, and homogeneous distributions of $\omega_G = (1581 \pm 1)\,\text{cm}^{-1}$, $\omega_{2D} = (2661 \pm 2)\,\text{cm}^{-1}$ and of $\Gamma_G = 9.5 \pm 1.0\,\text{cm}^{-1}$ are observed on supported graphene. The latter value suggests that this region is slightly doped, by approximately $2 \times 10^{12}\,\text{cm}^{-2}$, while the values of ω_G and ω_{2D} are consistent with a built-in tensile strain comparable to the one observed on the suspended region at $\Delta p = 0$ kPa [Berciaud09, Lee12a].

In figure 6.4c, we further compare the G and 2D mode frequencies at $\Delta p = 0$ kPa and $\Delta p = 74$ kPa along a radial line scan across the pit. For both data sets, the measured G mode frequencies converge very near the border of the pit (at approximately $r = 4\,\mu$m), whereas for ω_{2D} the convergence is observed at $r \approx 5.5\,\mu$m. This difference is attributed to the subtle interplay between the evolution of ω_G and ω_{2D}, due to strain relaxation at the edges of the pit, and the presence of residual doping on the supported part [Lee12a]. We note that in the Raman maps recorded by Zabel *et al.* on graphene bubbles, the same feature is observed [Zabel11]. For now, we neglect these features and concentrate on the range of $|r| \leq 3\,\mu$m where the Raman shifts are purely strain induced.

To further unveil phonon softening induced by tensile strain, we now investigate the correlation between ω_{2D} and ω_G as a function of Δp and the position on the graphene membrane. For this purpose, we record Raman line scans with a step size of 500 nm for 19 different values of Δp ranging from 74 down to 0 kPa. In figure 6.4d we show the correlation between ω_{2D} and ω_G recorded with varying Δp, at the center of the pressurized membrane ($r = 0\,\mu$m), and at $r = 1, 2$ and $3\,\mu$m from the center. At $\Delta p = 74$ kPa, ω_G (ω_{2D}) shifts down to $1563.8\,\text{cm}^{-1}$ ($2627.2\,\text{cm}^{-1}$) at the center, whereas ω_G (ω_{2D}) is $1567.7\,\text{cm}^{-1}$ ($2636.0\,\text{cm}^{-1}$) at $r = 3\,\mu$m. As shown in figure 6.4e, when varying Δp, the correlation between ω_{2D} and ω_G is linear, with a slope of $\frac{\partial \omega_{2D}}{\partial \omega_G} = 2.2 \pm 0.1$, irrespective of the position on the suspended graphene blister, for $|r| \leq 3\,\mu$m. Data extracted from samples B and C are added to this plot in order to point out that this correlation is systematically found in our graphene blisters.

Due to our membrane geometry, the pressure-induced stress and resulting tensile strain are essentially biaxial in the pressurized blister, in accordance with ref. [Zabel11]. Still, there may be a dominant radial, hence uniaxial, contribution when approaching the edges of the pit [Lee12b]. In our measurements, we observe a splitting of the G-mode feature below 500 nm from the border, which may arise from uniaxial strain [Huang09, Mohiuddin09]. However, the resulting G mode line shape is independent on the polarization of the incoming and scattered photons (see Appendix). Thus, the apparent bimodal G mode feature is attributed to a superposition of the Raman responses of the supported and suspended regions, due to the finite size of the laser spot, as it has been observed by Lee *et al.* [Lee12b]. This result suggests that contributions from uniaxial strain cannot be unambiguously resolved in the present study. Nevertheless, uniaxial or quasiuniaxial strain presumably results in the smaller phonon softening that is observed when approaching the

edges of the pressurized membrane, compared to the larger downshifts measured near the center, which arise from biaxial strain. The levels of strain achieved here are presumably too small to result in a sizable splitting of the Raman features near the edges of the graphene blister. We remind that the splitting occurs only at strain values larger than $0.6\,\%$ (see also chapter 3 and ref. [Mohiuddin09]).

6.2 Raman intensities and blister height

We now address the strong variations of the Raman scattering intensity observed when Δp is varied. As introduced in section 3.5 in chapter 3, any (semi-)transparent multilayered system underneath the graphene membrane gives rise to an interference based modulation of the Raman intensities. This modulation is slightly different for I_{G} and I_{2D} due to the different wavelength of the backscattered photons. Taking the notation of section 3.5, our blister geometry obeys system 1, *i.e.* the case of [Si - air/vacuum - graphene], where the distance $h(r)$ between the silicon and the graphene membrane changes with Δp. Indeed, interference rings appear clearly on the Raman maps of I_{G} and the ratio $I_{\mathrm{2D}}/I_{\mathrm{G}}$ recorded at $\Delta p = 74\,$kPa (see figures 6.5a and b). This result demonstrates that I_{G} and I_{2D} vary significantly over the pressurized membrane and not in the same manner. Conversely, as shown in the line scans of the Raman scattering intensities (see figure 6.5c), I_{G} and I_{2D} are nearly constant over the suspended area at $\Delta p = 0\,$kPa, which is consistent with a nearly flat suspended membrane at pressure equilibrium.

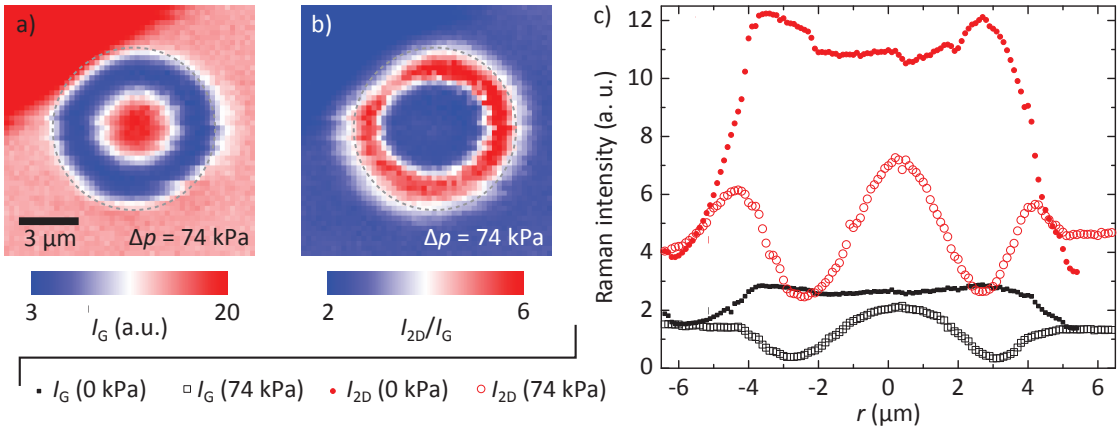

Figure 6.5: a) Hyperspectral Raman maps of the integrated intensity of the G mode feature, I_{G}, and **b)** of the ratio of the integrated intensities of the 2D and G mode features, $I_{\mathrm{2D}}/I_{\mathrm{G}}$, recorded on sample A, under a uniform pressure load of $\Delta p = 74\,$kPa. The step size is $250\,$nm. The border of the pit is represented by gray dashed circles. **c)** High-resolution radial line scans of I_{G} (black squares) and I_{2D} (red circles), recorded across the pit at $\Delta p = 0\,$kPa (filled symbols) and $\Delta p = 74\,$kPa (open symbols), with a step size of $100\,$nm. The corresponding legend is reported to the left, outside the graph in order to avoid overcharging of the figure.

6.2.1 Blister height and maximal deflection

As stated above, the varying distance between the bottom of the pit and the membrane leads to an interference induced modulation of the Raman intensities. This modulation is described by the enhancement factors EF which are defined in section 3.5 by equation (3.29). In order to directly compare our data of I_{G} and I_{2D} recorded on sample A with the theoretically predicted enhancement factors, we resume the cut of the enhancement factor color plots at $\lambda_{\mathsf{laser}} = 532\,\mathsf{nm}$ for the G and 2D mode (see figure 3.16a) and show it again in figure 6.6a.

The evolution of I_{G} and I_{2D} as a function of Δp at $r = 0\,\mu\mathsf{m}$ is then represented in figure 6.6b. The ratio between the maximal and minimal value of I_{G} (I_{2D}) reaches approximately 13 (approximately 6), and these two quantities are not proportional to each other. We note that we use a relatively low numerical aperture objective ($\mathsf{NA} = 0.45$), and can thus assume that the normal incidence approximation is valid in the vicinity of the graphene blister.

Let us now compare the data in figures 6.6a and b. The experimental evolution of I_{G} and I_{2D} as a function of Δp qualitatively resembles the calculated Raman enhancement factors. In particular, at $\Delta p = 0\,\mathsf{kPa}$, where $h_{\mathsf{max}} \approx d_{\mathsf{air}} = (395 \pm 10)\,\mathsf{nm}$, I_{G} and I_{2D} are close to their maximum values, which are reached at a finite $\Delta p \approx 1\,\mathsf{kPa}$. This evolution is very consistent with the calculated enhancement factors, which predict maxima at $h_{\mathsf{max}} = 416\,\mathsf{nm}$ and $h_{\mathsf{max}} = 426\,\mathsf{nm}$ for I_{G} and I_{2D}, respectively. Note the corresponding indication by a black star in the figure for I_{G}. Similarly, I_{G} and I_{2D} reach local minima at $\Delta p \approx 14\,\mathsf{kPa}$, corresponding to $h_{\mathsf{max}} \approx 550\,\mathsf{nm}$ and rise again towards another local maximum at higher Δp, which would correspond to $h_{\mathsf{max}} = 692\,\mathsf{nm}$ and $h_{\mathsf{max}} = 712\,\mathsf{nm}$ for I_{G} and I_{2D}, respectively. This result allows us to estimate that the maximum height $\xi_{\mathsf{max}} = h_{\mathsf{max}} - d_{\mathsf{air}}$ of the graphene blister, attained at $\Delta p = 74\,\mathsf{kPa}$, is close to $270\,\mathsf{nm}$.

Interestingly, the evolution of I_{2D} *vs.* Δp also reveals a slight bump in the range between $15\,\mathsf{kPa}$ and $45\,\mathsf{kPa}$, with a secondary maximum around $\Delta p \approx 30\,\mathsf{kPa}$. This feature also appears clearly in the theoretical calculation of the enhancement factor of the 2D mode near $h_{\mathsf{max}} \approx 580\,\mathsf{nm}$ (*i.e.*, $\xi_{\mathsf{max}} \approx 185\,\mathsf{nm}$). Note the corresponding indication by a red hash symbol in the figure. As discussed in section 3.5, this secondary maximum arises from the fact that the Raman enhancement factor is the product of an excitation term, with a quasiperiod of half the laser wavelength and a scattering term, with a larger quasiperiod of half the wavelength of the Raman scattered photons [Yoon09]. For Raman features at sufficiently large shifts (such as the 2D mode feature), this *beating* produces secondary maxima in the Raman enhancement factor. Conversely, a significant secondary maximum is neither expected nor observed for I_{G} in the height range investigated here. This observation further validates our experimental approach for the determination of the blister profile.

The identification of the corresponding maxima and minima is indispensable in order to correctly relate the intensities to h_{max}. The contrast between the maximal and minimal enhance-

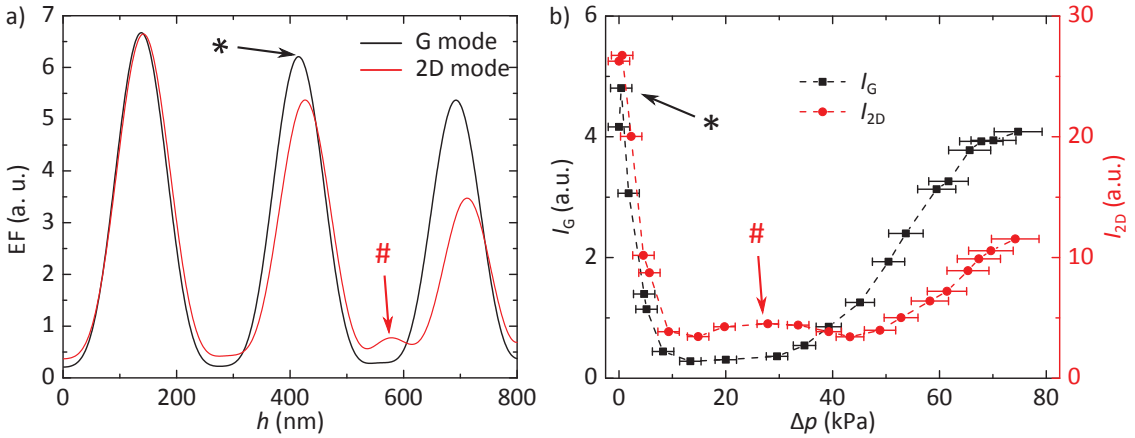

Figure 6.6: a) Calculated Raman enhancement factors EF of the G (black) and 2D (red) mode intensities, for a laser wavelength of 532 nm, according to equation (3.29). **b)** Evolution of the integrated intensities of the G (black squares) and 2D (red circles) mode features measured at the center of sample A, as a function of the pressure load Δp. The black star and the red hash symbol mark recognizable features, in order to identify the height regime (see main text for details). The dashed lines are a guides to the eye.

ment factors may be affected by experimental factors, such as local corrugation on the Si surface, as well as slight deviations from the normal incidence approximation, arising from the numerical aperture of the microscope objective or occurring near the edges of the pressurized membrane. Consequently, the calculated enhancement factors have to be renormalized with respect to the experimentally measured maxima and minima of I_{G} and I_{2D}.

We remind that samples B and C ($d_{\mathrm{air}} = 340 \pm 10$ nm) underwent a finite leakage before the pressure load dependent measurements which resulted in a negative pressure load after the measurement run. Thus, the values of h_{max} are below d_{air}. For these samples, h_{max} covers the range from 195 to 545 nm and from 217 to 612 nm, respectively. The corresponding data plots are reported to the Appendix (see figure D.4a and b).

6.2.2 Intrinsic value of $I_{\mathrm{2D}}/I_{\mathrm{G}}$

Interestingly, since both I_{G} and I_{2D} are interference modulated, so is their ratio $I_{\mathrm{2D}}/I_{\mathrm{G}}$ (see also figure 3.16a). In some scientific reports, this ratio has been used as criterion to identify monolayers and to estimate the doping level of a given sample [Ni09]. In this subsection we show an elegant approach to deconvolute the effect of interference effects on $I_{\mathrm{2D}}/I_{\mathrm{G}}$ in order to extract an intrinsic value of this ratio, which is, additionally, unaffected by any doping effects.

To do so, we come back to the raw spectra recorded on sample A and plot them in a way which highlights the important changes in $I_{\mathrm{2D}}/I_{\mathrm{G}}$. Hence, in figure 6.7a we show the evolution of the raw spectra with changing Δp, where again, the strain induced Raman shifts can be identified by the gray dashed line. We readily observe that the $I_{\mathrm{2D}}/I_{\mathrm{G}}$ ratio changes with varying Δp. In particular,

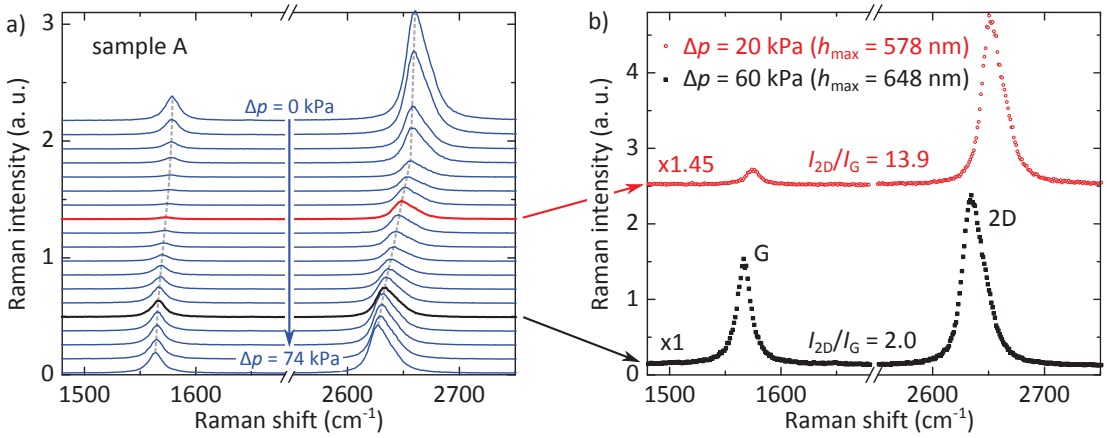

Figure 6.7: a) Series of Raman spectra recorded on sample A, with Δp ranging from 0 to 74 kPa (blue lines). The spectra are offset for clarity. The dashed gray lines connect the G and 2D peak position of subsequent spectra and are guides to the eye in order to outline the strain-induced Raman shifts. The two spectra in red and black, represented by thicker lines, correspond to the spectra in **(b)**, showing a change of I_{2D}/I_G by a factor of ≈ 7 as h_{max} varies only by 70 nm. The spectrum recorded at $\Delta p = 20$ kPa is offset and multiplied by a factor of 1.45 for clarity. Measurements are taken at $\lambda_{laser} = 532$ nm and with the $\times 20$ (NA $= 0.45$).

in the range of Δp with global low and intermediate Raman intensity, I_{2D}/I_G undergoes a drastic change by a factor of approximately 7. The corresponding spectra are accentuated by red and black lines in figure 6.7a and plotted in figure 6.7b, where they are normalized with respect to I_{2D} in order to better compare the intensity ratios. These spectra correspond to a h_{max} of 578 nm and 648 nm and show an I_{2D}/I_G of 13.9 and 2.0, respectively. For moderate strains (significantly below 1 %), I_{2D}/I_G is not expected to vary due to the deformation of the graphene lattice [Popov13]. Since our graphene blisters exhibit a very low doping level (below 3×10^{11} cm^{-2}), a doping induced change, as observed in the references [Das08], [Basko09b] and [Froehlicher15a], can be ruled out. Thus, this evolution is solely attributed to interference effects, which allows us to decouple the interference modulation from the intrinsic (*i.e.* doping and interference-free) value of I_{2D}/I_G, according to equation (3.31) written for the case of the intensity ratios:

$$\left(\frac{I_{2D}}{I_G}\right)_{mes}(h_{max}) = \frac{EF_{2D}}{EF_G}(h_{max}) \times \left(\frac{I_{2D}}{I_G}\right)_{intr}. \tag{6.1}$$

As exposed in the previous subsection, the measurements on sample A cover the range from $h_{max} = 395$ to 660 nm, whereas h_{max} varies from 195 to 545 nm and from 217 to 612 nm on sample B and C, respectively. Hence, due to the inward bulging of the latter, the evolution of I_{2D}/I_G is probed within a range of 465 nm. We plot the I_{2D}/I_G ratio (measured at $r = 0\,\mu$m) of samples A, B and C as a function of h_{max} in black, blue and red in figure 6.8a, b and c, respectively.

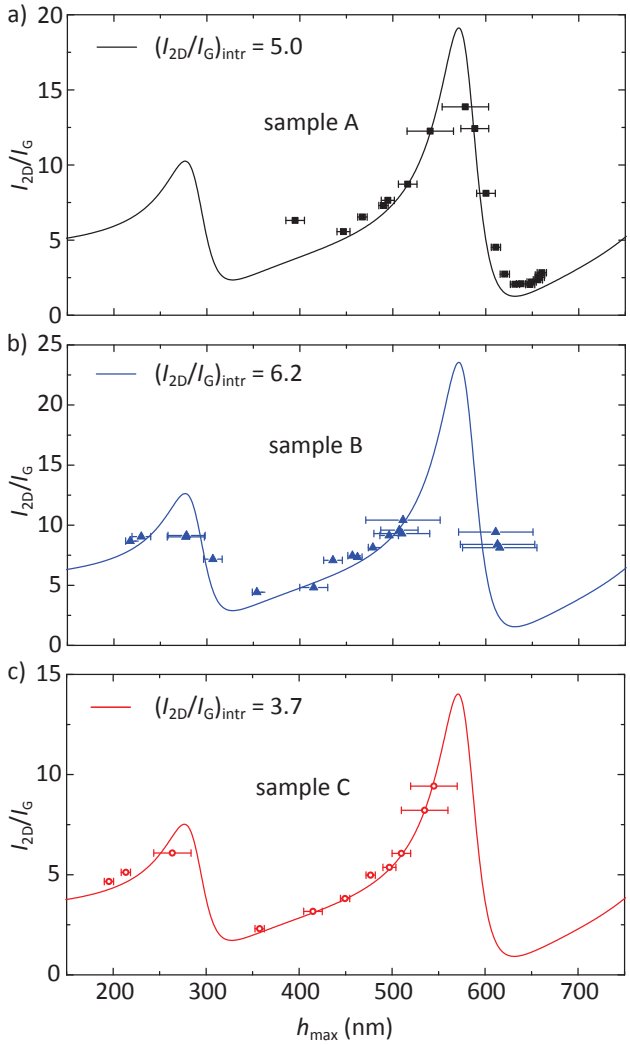

Figure 6.8: Evolution of the I_{2D}/I_G ratio between the integrated intensities of the 2D and G mode features for samples A, B, and C as a function of h_{max}. The symbols are our experimental measurements and the solid lines are fits based on equation (6.1). NA $= 0.45$.

On sample A, the measured ratio I_{2D}/I_G varies sharply from 2 (at $_{max} \approx 650$ nm) to 14 (at $_{max} \approx 580$ nm). This variation is slightly less pronounced on the data of samples B and C ($(I_{2D}/I_G)_{mes}$ ranges from ≈ 2.5 to ≈ 10). The data are fit to $EF_{2D}/EF_G(h_{max})$ according to equation (6.1), leaving $(I_{2D}/I_G)_{intr}$ as the only free fitting parameter. We find $(I_{2D}/I_G)_{intr} = 5.0 \pm 0.3$, 6.2 ± 0.6 and 3.7 ± 0.1 for samples A, B and C, respectively.

EF_{2D}/EF_G is characterized by sharp maxima at $h = 277$ and 571 nm. Around these values of h_{max}, I_G and I_{2D} reach their minimum values (see figure 6.6a) and precise experimental data are difficult to obtain. Based on the result of the fits, an average intrinsic value of $(I_{2D}/I_G)_{intr} = 5.0 \pm 1.5$ can be extracted. Note that this value is recorded at a laser wavelength of 532 nm, and that wavelength dependent Raman susceptibilities may strongly affect this ratio in the near ultraviolet or near infrared range [Basko08, Basko09b].

We note that the value $(I_{2D}/I_G)_{intr} = 5.0 \pm 1.5$ is in excellent agreement both with an estimate of 4.9 ± 0.7 obtained in electrochemically gated graphene transistors [Froehlicher15a] and with a statistical mean value of 4.6 with a standard deviation of 1.1 obtained by Federspiel *et al.* on graphene flakes exfoliated on quartz substrates (private communication), where interference effects are negligible. We are aware of artifacts from the numerical aperture (NA) in our measurements, but the low NA of the objective used here (NA $= 0.45$) suggests that one can neglect these effects here [Budde15].

6.2.3 Reconstruction of the blister profile

The determination of $(I_{2D}/I_G)_{intr}$ further validates the correctness of our analysis. Up to now, we only considered the the distance between the bottom of the pit and the membrane at the center of the blister. Of course, the translation of I_G and I_{2D} into a height is not only possible at the center to determine a value of h_{max}, but also over the whole blister profile, in order to determine $h(r)$. Thus, every line scan recording the integrated Raman intensities can directly be translated into a profile of the blister.

As an example, contour plots of I_G and of the subsequently translated blister height $\xi(r) = h(r) - d_{air}$ are presented as a function of Δp and r in figures 6.9a and b. Very similar data are obtained when $\xi(r)$ is deduced using I_{2D}, as shown in figure 6.9c and d. The gray area in the latter corresponds to values of low Raman intensity in figure 6.9c, and exact values of h (and thus ξ) are difficult to obtain, because the range of low Raman intensity is particularly large (between ≈ 520 and ≈ 620 nm). Also, at the borders of the blister (for values of $|r| > 3\,\mu$m), ξ has been extrapolated here to 0 nm at $|r| > 4\,\mu$m. Note that contour plots of sample B are available in the Appendix, nicely showing the evolution from an outward to an inward bulging (see figure D.5a to d).

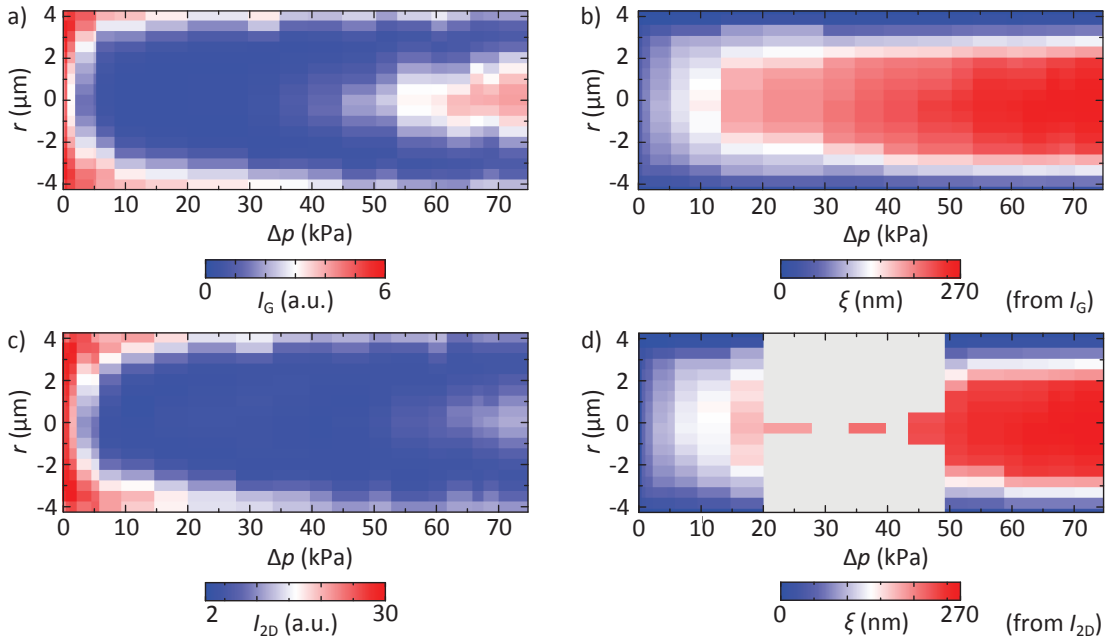

Figure 6.9: a) Intensity of the Raman G mode intensity I_{G} as a function of the pressure load Δp and the radial distance r. **b)** Membrane displacement ξ as a function of Δp and r, extracted from I_{G}. As described in the main text, the exact determination of the height is not possible (see also figure 6.10a), thus the data of ξ at $|r| > 3\,\mu$m are linearly extrapolated to $\xi = 0$ nm at $r = a = 4.1\,\mu$m. **c)** Intensity of the Raman G mode intensity I_{2D} as a function of Δp and r. Note that the small bump observed at the center between $\Delta p = 20$ and 35 kPa (marked with a hash symbol in figure 6.6b) is also visible in the contour plot. **d)** ξ as a function of Δp and r, extracted from I_{2D}. The result is very similar to (b). The gray area corresponds to values of low Raman intensity in (c), where the height cannot determined precisely.

We are now able to investigate the blister topography in more detail. The profiles for three different values of Δp are shown in figure 6.10a. Here, the error bars reflect directly the precision of the height determination governed by the broad valleys in the interference pattern. In a favorable case, *i.e.* in a range where the interference pattern shows a maximum or a steep slope, the precision is actually around 5 nm, which is in the range of the error in the pit depth. Furthermore, we would like to point out that a slight inward deflection of ≈ 20 nm is observed when the pressure load is tuned back to 0 kPa. This deflection either has been initially present in the device before the measurement run or is caused by a minimal air molecule loss during the measurements. Regardless of which reason, this deflection can be used to estimate an upper bound of the amount of air molecules which might have escaped during the measurement run. Supposing that the pressure difference is indeed zero, the volume is directly proportional to the number of particles. The tiny inwardly bulged volume is determined by integrating the profile in figure 6.10a over 2π and determined to 3.8×10^{-19} m^3, whereas the volume of the pit is directly given by $V_0 = \pi a^2 d_{SiO_2} = 2.09 \times 10^{-17}$ m^3. The ratio gives us the upper bound of the particle loss, which is 1.8 %. Thus, our study can indeed be considered as a *constant N blister test*.

Let us also note that the relative difference between the heights determined using I_G and I_{2D} is maximal 7 %. A graph showing this relative difference at the center of the blister is reported to the Appendix (see figure C.3b).

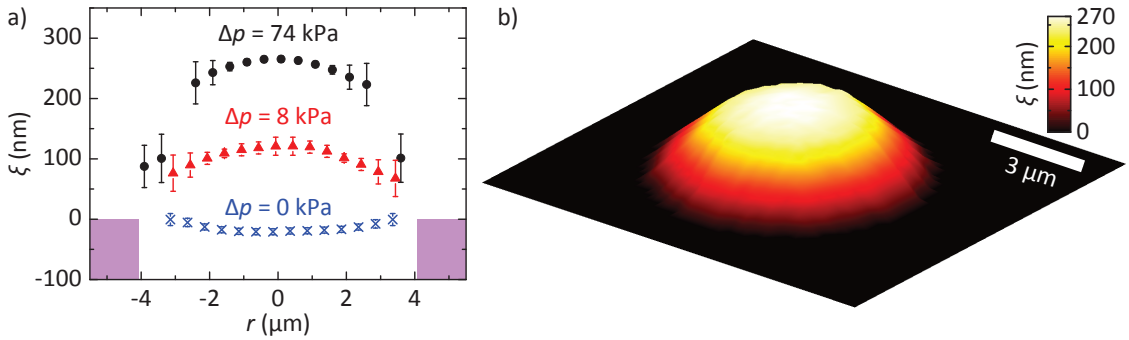

Figure 6.10: a) Blister height profile recorded at various values of Δp. The error bars in (b) take into account the fact that it is not possible to give an accurate value of the height when the Raman intensity is approaching a local minimum in the enhancement factor (see figure 6.6). **b)** Reconstruction of the three-dimensional blister topography at $\Delta p = 74$ kPa from the Raman intensity map of the G mode in figure 6.5a.

Having the above analysis in mind, as accurately as a Raman line scan can be translated into a blister profile, a Raman map contains all the information needed to reconstruct the three-dimensional blister topography. *E.g.*, let us take the Raman map of I_G, shown in figure 6.5a and translate every value of I_G into a value of ξ. The result is displayed in figure 6.10, where again,

every value of ξ at $3.0\,\mu$m $< r < 4.1\,\mu$m has been linearly extrapolated to 0 at the border of the blister in order to rule out influences on the Raman signal from the borders.

Let us emphasize that, in principle, a simple measurement of the back-reflected laser intensity could be employed to deduce $\xi(r)$ [Blake07, Reserbat-Plantey12]. However, due to the quasi-transparency of single-layer graphene, the maximum contrast expected in a reflectivity measurement is at most on the order of approximately $15\,\%$ for a graphene monolayer [Blake07], while we obtain a contrast of more than one order of magnitude on I_{G}. And, importantly, Raman measurements provide additional quantitative information on the strain in the graphene blister. This statement leads us straightforwardly to the next section, where the combination of the blister profiles and the strain induced Raman shifts permits the determination of the Grüneisen parameters of the G and 2D mode phonons.

6.3 Determination of the Grüneisen parameters

The investigation of the evolution of I_{G} and I_{2D} with varying Δp and the subsequent determination of the blister profiles allows us to estimate an average tensile strain ϵ_{p} induced by the uniform pressure load. It is

$$\epsilon_{\mathsf{p}} = \frac{L}{2a} - 1, \tag{6.2}$$

where L is the length of the cross section of the pressurized graphene blister (see figure 6.10a). We find that ϵ_{p} reaches values of up to $(0.33 \pm 0.07)\,\%$, well above the built-in strain of $0.05\,\%$ estimated in section 6.1.

We can now correlate ϵ_{p} to the Raman frequencies ω_{G} and ω_{2D} measured at the center of the blister (sample A), as shown in figure 6.11. Over the range $\epsilon_{\mathsf{p}} = 0\,\%$ to $0.33\,\%$, we observe roughly linear scalings with slopes $\partial\omega_{\mathsf{G}}/\partial\epsilon_{\mathsf{p}} = (-47 \pm 5)\,\mathrm{cm}^{-1}$/% strain and $\partial\omega_{\mathsf{2D}}/\partial\epsilon_{\mathsf{p}} = (-101 \pm 10)\,\mathrm{cm}^{-1}$/% strain, respectively. Nevertheless, in the limit of small deflections, a precise determination of ϵ_{p} remains challenging and the built-in strain (of $\approx 0.05\,\%$) is of competing magnitude. Therefore, in the following, we consider the range $\epsilon_{\mathsf{p}} = 0.1\,\%$ to $0.33\,\%$, for which ϵ_{p} can be estimated with sufficient accuracy. Within this range, we find slightly larger slopes of $\partial\omega_{\mathsf{G}}/\partial\epsilon_{\mathsf{p}} = (-57 \pm 5)\,\mathrm{cm}^{-1}$/% strain and $\partial\omega_{\mathsf{2D}}/\partial\epsilon_{\mathsf{p}} = (-128 \pm 10)\,\mathrm{cm}^{-1}$/% strain, respectively. Note that the ratio of these slopes, $[(-128)/(-57)]$, is 2.2, a direct consequence of the fact that ϵ_{p} determined both from the intensity of the G and 2D mode are very similar. This result is thus coherent with the slope of $\partial\omega_{\mathsf{2D}}/\partial\omega_{\mathsf{G}} = 2.2$ found in section 6.1.

Now, these slopes allow us to estimate the Grüneisen parameters of the G and 2D modes under biaxial strain, as

$$\gamma_G = \frac{1}{2\omega_G^0}\frac{\partial\omega_G}{\partial\epsilon_p} = 1.8 \pm 0.2 \qquad \text{and} \qquad \gamma_{2D} = \frac{1}{2\omega_{2D}^0}\frac{\partial\omega_{2D}}{\partial\epsilon_p} = 2.4 \pm 0.2, \tag{6.3}$$

respectively, where ω_G^0 and ω_{2D}^0 are the G and 2D mode frequencies of doping- and strain-free graphene.

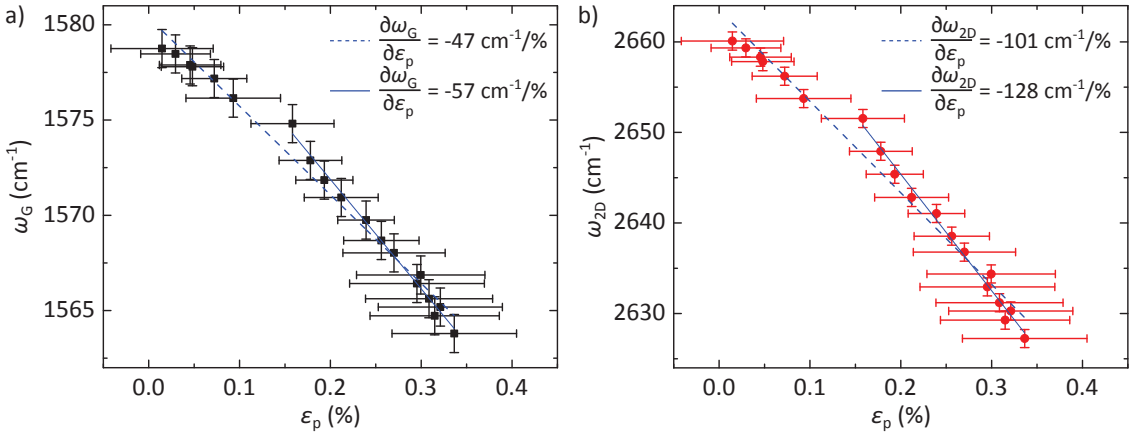

Figure 6.11: Evolution of the G **(a)** and 2D **(b)** mode frequencies measured at the center of sample A, as a function of the tensile strain ϵ_p induced by the uniform pressure load. The straight lines are linear fits. The error bars in ϵ_p arise from the uncertainty in a ($\Delta a = 0.1\ \mu$m), the uncertainty in the height determination and from the linear extrapolation to the border of the pit.

The Grüneisen parameters determined from samples B and C can be extracted in the same manner, as ω_G and ω_{2D} scale linearly with ϵ_p, both under outward and inward bulging of the blister. The slopes are comparable with those obtained from sample A, but slightly lower (see figure D.6 in the Appendix for more details).

6.4 Determination of the Young's modulus

We now consider the evolution of ξ_{max}, the deflection measured at the center of the blister, as a function of Δp. As shown in section 2.5 in chapter 2, the pressure load is proportional to the third power of the deflection, when the bending stiffness is negligible, *i.e.* in the case of a membrane. We remind equation (2.37):

$$\Delta p \propto \frac{Et}{a^4}\,\xi_{max}^3. \tag{6.4}$$

This result has been obtained from a simple dimension analysis of the Föppl-von Kármán equations (see equations (2.35) and (2.36)). Note that, in particular, it contains the known parameters of our graphene blister test, *i.e.* Δp and ξ_{max}. If, however, the proportionality constant, which we

will call K, the thickness of the membrane and its lateral dimensions are known, our data set can be used to determine the Young's (or elastic stretching) modulus of graphene.

6.4.1 Hencky's description of a membrane blister test

To resolve the Föppl-von Kármán equation in the case of a centrosymmetric pressurized membrane, Hencky proposed an analytical series solution of the profile already in 1915 [Hencky15, Wan95]. He found that $\xi(r)$ can be written as (in the case of zero pre-strain)

$$\xi(r) = \left(\frac{a^4 \Delta p}{Et}\right)^{1/3} \sum_{n=0}^{\infty} A_{2n} \left[1 - \left(\frac{r}{a}\right)^{2(n+1)}\right], \tag{6.5}$$

where the coefficients A_{2n} depend on a single parameter B_0 in the following way: $A_0 = 1/B_0$, $A_2 = 1/(2B_0^4)$, $A_4 = 5/(9B_0^7)$, $A_6 = 55/(72B_0^{10})$ and so on (see references [Hencky15] and [Wan95]). The parameter B_0 depends on the Poisson ratio ν. In the center of the blister, *i.e.* at $r = 0$, equation (6.5) rewrites as

$$\xi_{\mathsf{max}} = \left(\frac{a^4 \Delta p}{Et}\right)^{1/3} \sum_{n=0}^{\infty} A_{2n}. \tag{6.6}$$

Here, one can define $\left(\sum A_{2n}\right)^{-3} =: K$ where K is then the proportionality constant in equation (2.37):

$$\Delta p = \frac{KEt}{a^4}\, \xi_{\mathsf{max}}^3. \tag{6.7}$$

In addition to this result connecting the pressure load to the maximal deflection at the center, we can calculate the volume of the blister, V_{B}, by integrating Hencky's polynomial solution:

$$V_{\mathsf{B}} = \int_{r=0}^{a} r\, \mathsf{d}r \int_{\xi=0}^{\xi(r)} \mathsf{d}\xi \int_{\varphi=0}^{2\pi} \mathsf{d}\varphi = 2\pi a^2 \xi_{\mathsf{max}} \sqrt[3]{K} \sum_{n=0}^{\infty} \frac{n+1}{2n+4}\, A_{2n} = C\pi a^2 \xi_{\mathsf{max}}, \tag{6.8}$$

where C is another constant, directly related to K, and dependent on ν (as K), defined as $C = 2\sqrt[3]{K}\, \sum (n+1)/(2n+4)\, A_{2n}$.

In 1956, Campbell generalized equation (6.7) in order to account for residual pre-strain in the membrane. As mentioned in chapter 2, this contribution to the membrane deflection is expected to scale linearly with Δp. Thus, in the presence of a certain pre-strain T_0 (in N/m), one writes [Campbell56, Koenig13]:

$$\Delta p = \frac{4T_0}{a^2}\, \xi_{\mathsf{max}} + \frac{KEt}{a^4}\, \xi_{\mathsf{max}}^3. \tag{6.9}$$

6.4.2 Application of Hencky's solution to graphene blisters

Similarly to the determination of ϵ_p, we can estimate the blister volume V_B for each value of Δp (*i.e.* of ξ_{max}), and apply the result to equation (6.8) in order to deduce an average value for C. The corresponding plot is reported to the Appendix (see figure D.7). We deduce an average value of $C = 0.52 \pm 0.02$. This value is very close to those previously suggested for monolayer graphene by Boddeti *et al.* ($C(\nu = 0.16) = 0.524$) [Koenig11, Boddeti13]. In these conditions, one expects $K \approx 3$ (see figure D.8a and b in the Appendix for a graphical plot of the relationships between C, B_0 and K) [Hencky15, Wan95, Bunch08, Koenig11]. In particular, our results are in good agreement with a value of $K(\nu = 0.16) = 3.09$, proposed by Koenig *et al.*, which we will use in the following analysis.

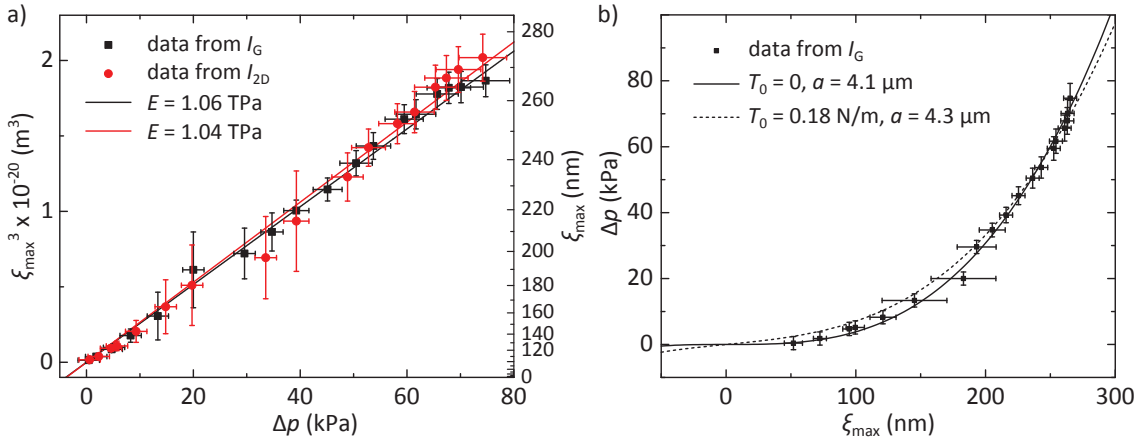

Figure 6.12: a) Third power of the height of the graphene blister on sample A, ξ_{max}, measured at its center, as a function of the pressure load Δp. Data obtained from the measurement of the G (2D) mode integrated intensity are shown with black squares (red circles). The black and red straight lines are linear fits to the data, respectively. The slope corresponds to the quantity $a^4/(KEt)$, which allows us to deduce an average value of $E = 1.05 \pm 0.1$ TPa. **b)** Comparison of fits on the Δp vs. ξ_{max} dependence. The straight line is equation (6.7) (without pre-strain), using $E = 1.05$ TPa and $a = 4.1$ μm. The dashed line is equation (6.9) (finite pre-strain), using $E = 1.05$ TPa and $T_0 = 0.18$ N/m (obtained from Raman frequency analysis). The value of $a = 4.3$ μm results from a fit on the data.

In figure 6.12, we show the relationship between ξ_{max}^3 and Δp for the data obtained from the measurement of the G and 2D mode integrated intensity, as black squares and red circles, respectively. Both data sets follow very similar linear scalings through the origin, in excellent agreement with equation (6.7). Using $K(\nu = 0.16) = 3.09$ [Bunch08, Koenig11] and $a = (4.1 \pm 0.1)$ μm, we deduce a value of $E = (1.06 \pm 0.1)$ TPa and $E = (1.04 \pm 0.1)$ TPa, for the Young's modulus, respectively.

By taking equation (6.7) for our analysis, we did not consider any pre-strain present in the membrane. At first sight, this choice might be justified by the perfect linear scaling when plotting

ξ^3_{max} *vs.* Δp. Nonetheless, a finite built-in strain of 0.05 % has been estimated by analyzing the Raman shifts of the unpressurized graphene membrane. Using the obtained result of the Young's modulus, the built-in strain can be expressed in units of N/m, which is then T_0 in equation (6.9). With the relationship $T_0 = \epsilon(1-\nu^2)/(Et)$ [Medvedyeva11], $\nu = 0.16$ and $Et = 351.75$ N/m one finds $T_0 \approx 0.18$ N/m. Is this finite built-in strain incompatible with the linear relationship in figure 6.12a? To answer this question, we plot the data obtained from I_{G} (Δp *vs.* ξ_{max}) together with equation (6.9) by setting $T_0 = 0$, $a = 4.1\,\mu$m and $E = 1.05$ TPa (straight line in figure 6.12b), which is just another way to represent the data in figure 6.12a. In addition, we plot equation (6.9) with a finite built-in strain of $T_0 = 0.18$ N/m (which corresponds to $\epsilon = 0.05$ %), and leave a as a free fitting parameter. A value of $a = 4.3\,\mu$m fits best the data. This value is just slightly above error bars which we estimated for a.

Actually, the blister radius is a critical parameter in equations (6.7) and (6.9), because is scales to the power of 4. Thus, the fact that we observe a finite built-in strain (determined by the Raman frequency analysis), is not completely in contradiction with a linear scaling of ξ^3_{max} *vs.* Δp, but reveals how sensitively the analysis depends on the blister parameters, in particular of its radius. We note that the exact determination of the blister radius is not only a question of measuring the pit radius but of knowing how the graphene membrane adheres to the borders of the pit [Lu10, Barton11].

Finally, in figure 6.13a and b, we compare the evolution of ξ_{max} as a function of the quantity $[a^4\Delta p/(KEt)]^{1/3}$ for samples A, B and C. Here, we also use $K = 3.09$, $t = 0.335$ nm and $E = 1.05$ TPa, as deduced from sample A. We use the measured value of $a = 4.1\,\mu$m for sample A and $4.0\,\mu$m for samples B and C. We note that here, the issue of built-in strain in samples B and C is voluntarily neglected since both samples displayed Raman frequencies of $\omega_{\text{G}} \approx 1581.5$ cm^{-1} and $\omega_{\text{2D}} \approx 2667$ cm^{-1}, a signature of built-in strain < 0.01 %. Within the representation in figure 6.13, the data for blisters with different radii can be compared directly to the slope of 1. In spite of the greater uncertainty in the determination of ξ_{max} and Δp for samples B and C, we find that the data measured on these samples is in good agreement with the data measured on sample A. We therefore come to the conclusion that a value of $E = 1.05 \pm 0.1$ can be determined for the Young's modulus of monolayer graphene from our three samples.

6.5 Pressurized 2L, 3L and 4L graphene

In this section we will briefly present some results obtained on pressurized 2L, 3L and 4L graphene devices and qualitatively compare the Δp-ξ_{max}-dependence with the one of 1L graphene. These multilayer graphene devices have been identified by means of optical microscopy on the same device as the 1L graphene of sample A, presented in the previous sections. The number of layers has been unambiguously determined by Raman spectroscopy, in particular by means of the shape

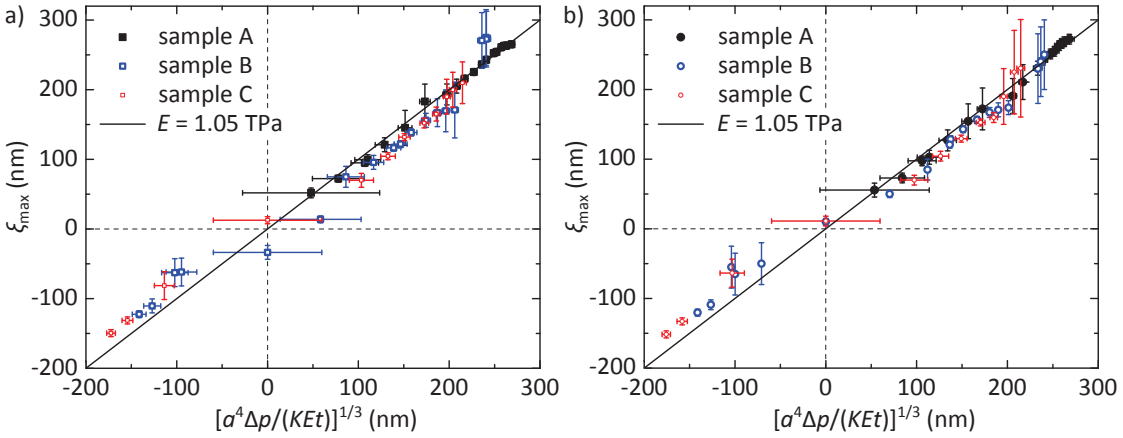

Figure 6.13: a) Height of the graphene blister center, ξ_{max}, for samples A, B and C, represented as a function of the quantity $[a^4\Delta p/(KEt)]^{1/3}$, where $E = 1.05\,\text{TPa}$, $K = 3.09$ and $t = 0.335\,\text{nm}$. a is sample dependent. The data is obtained from the measurement of the G mode integrated intensities. The straight line of slope 1 allows us to compare the data independently on a. **b)** The same data as in (a), obtained from the measurement of the 2D mode integrated intensities.

of 2D mode feature [Malard09b] and the spectral position of the N mode [Herziger12] and C mode [Tan12]. We note that the pit depth is the same as for sample A, *i.e.* $d_{\text{air}} = 395 \pm 10\,\text{nm}$.

As the strain at the center of the blister is biaxial and tensile, both G and 2D mode features soften with increasing Δp. In particular, in the case of a 2L graphene, they soften from 1582.6 to $1571.0\,\text{cm}^{-1}$ and 2692.0 to $2664.1\,\text{cm}^{-1}$, respectively. The correlation of these modes for different values of Δp permits to determine the value of $\partial\omega_{\text{2D}}/\partial\omega_{\text{G}}$ for 2L graphene, which we evaluated as 2.24 ± 0.12. The corresponding graph is reported to the Appendix (see figure E.9a and its caption for details). This value coincides perfectly with 2.22, which can be extracted from the data on 2L graphene bubbles of Zabel *et al.* [Zabel11]. Furthermore, $\partial\omega_{\text{2D}}/\partial\omega_{\text{G}}$ seems to be the same for 2L and 1L graphene.

To determine $h(r)$ and, in particular, h_{max} and ξ_{max}, we make use of the enhancement factors calculated from equation (3.29) for the case of few layer graphene in the configuration of system 1 (see section 3.5), by adjusting the membrane thickness as a multiple of the interlayer spacing of bulk graphite, $t_0 = 0.335\,\text{nm}$, to $2t_0$, $3t_0$ and $4t_0$, respectively. The corresponding EF as a function of h is plotted in figure 6.14a. By the way, due to the increasing number of layers, the transparency of graphene decreases and consequently the contrast in the interference modulation. Nevertheless, the difference in the position of the minima and maxima is negligible.

In figure 6.14b, the integrated intensity of the G mode feature, which has been obtained from a single Lorentzian fit, is plotted *vs.* the pressure load Δp. The latter has been accessed by using the ideal gas law and supposing that ω_{G} is proportional to Δp, *i.e.* in the same way as for 1L graphene (see Appendix for details). As in the case of 1L graphene, the intensity strikingly decreases

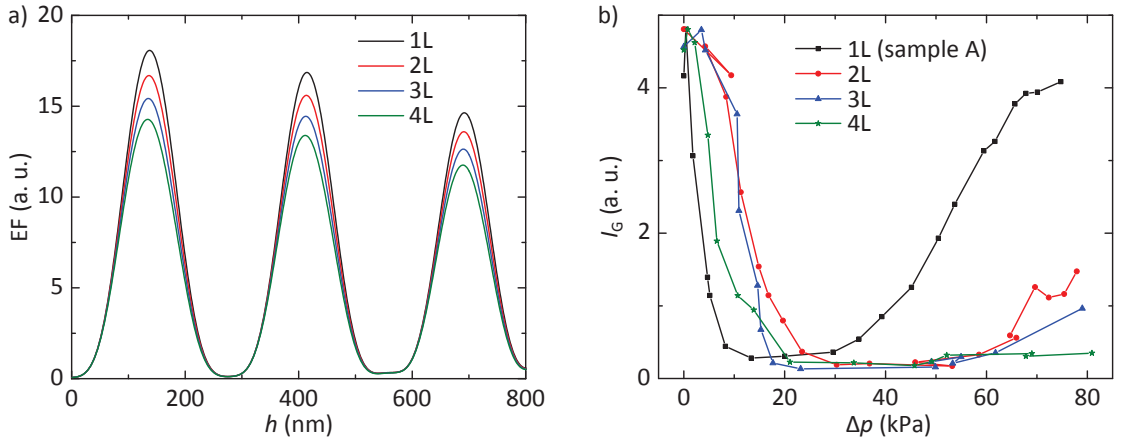

Figure 6.14: a) Calculated Raman enhancement factors EF of the G mode intensities, for 1L, 2L, 3L and 4L graphene, according to equation (3.29) ($\lambda_{\text{laser}} = 532$ nm). The contrast is decreasing with increasing number of layers. **b)** Evolution of the integrated intensities of the G mode feature measured at the center of the 1L (sample A), 2L, 3L and 4L graphene blister, as a function of the pressure load Δp. The solid lines are a guides to the eye. The data are rescaled in order to make coincide the maximum values of I_G at $\Delta p \approx 0$.

with increasing Δp. However, with further increasing Δp, I_G remains lower than for 1L graphene. The higher the number of layers, the stronger this effect is. *E.g.* in the case of 4L graphene, the low I_G persists up to $\Delta p \approx 80$ kPa. In view of the enhancement factors in figure 6.14a, this observation is interpreted as a lower blister height. Indeed, for the maximum pressure load[1], the following blister heights $\xi_{\text{max}} = h_{\text{max}} - d_{\text{air}}$ can be evaluated:

1L: 265 ± 5 nm

2L: 234 ± 5 nm

3L: 223 ± 10 nm

4L: 199 ± 20 nm

In accordance with the fact that I_G persists more at low I_G with increasing Δp and layer numbers, the error in ξ_{max} increases.

The translation of I_G in ξ_{max} for 1L, 2L, 3L and 4L graphene is shown in figure 6.15a, b, c and d, respectively, where Δp is plotted as a function of ξ_{max} (black squares). Black solid lines are added to the figures and correspond to equation (6.7), *i.e.* $\Delta p = KEt\xi_{\text{max}}^3/a^4$, where $K = 3.09$, $E = 1.05$ TPa and $a = 4.1\ \mu$m. t is the corresponding thickness of the number of layers and is the only changing parameter. The increasing thickness is responsible for a lower value of ξ_{max} for the

[1]Note that the maximal pressure load increases because the volume of the blister decreases with increasing number of layers. We remind that, in the case of $p_{\text{ext}} = 0$, the ideal gas law implies that $\Delta p = p_{\text{atm}} V_0/(V_0 + V_B)$.

same value of Δp. As mentioned earlier, the 1L graphene (sample A) is in perfect agreement with equation (6.7). However, 2L, 3L and 4L graphene exhibit slight deviations, even if the data are qualitatively in agreement with the expected ξ_{max}-Δp-dependence. In particular, the bulging of the 2L and 3L graphene devices is less pronounced as expected in the range of low pressure load (between $\Delta p = 0$ and 40 kPa, and $\Delta p = 0$ and 15 kPa, respectively). For all few layer samples, ξ_{max} reaches somewhat larger values as expected (of ≈ 30 nm) for pressure loads exceeding ≈ 50 kPa.

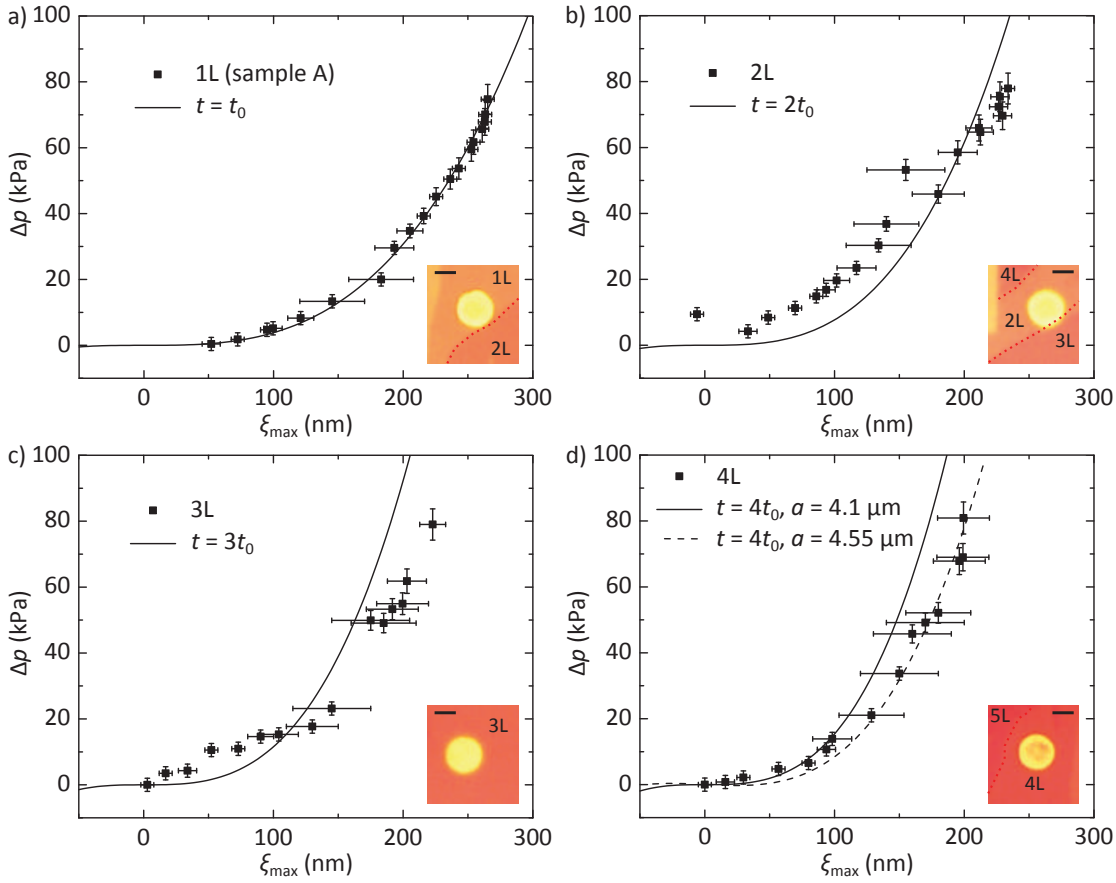

Figure 6.15: a) Δp *vs.* ξ_{max} for a 1L graphene blister (sample A), extracted from the Raman G mode feature. **b)**, **c)** and **d)** The same correlation for 2L, 3L and 4L graphene, respectively. The black solid lines represent $\Delta p = KEt\xi_{\text{max}}^3/a^4$ where $K = 3.09$, $E = 1.05$ TPa and $a = 4.1\,\mu$m. t is the corresponding thickness of the number of layers, taken as a multiple of the interlayer spacing of graphite, t_0. t and is the only changing parameter. **Insets:** Optical micrographs of the samples. The limits of neighboring few layer graphene with another number of layers as the considered one are marked with a red dashed line. The scale bars are $5\,\mu$m.

Several reasons might account for these slight deviations. First, the moderated bulging of the membrane in the case of 2L and 3L graphene is an indicator of an additional linear term in

equation (6.7). Equation (6.9) suggests that an eventual pre-strain in the membrane impacts the ξ_{max}-Δp-dependence, in particular in the regime of low deflections. A positive pre-strain ($T_0 > 0$) would account for a higher Δp needed to achieve a certain deflection ξ_{max}, as observed between 0 and 50 kPa for the 2L, and 0 and 20 kPa for the 3L graphene blister. However, there is disagreement with this assumption, because the measurement points at higher Δp (> 60 kPa) cannot be explained. Furthermore, the Raman frequencies of the G mode for the flat 2L, 3L and 4L graphene are $1582.2\,\text{cm}^{-1}$, $1581.6\,\text{cm}^{-1}$ and $1580.1\,\text{cm}^{-1}$, which indicates that pre-strain is negligible. One might also conceive of an increasing bending stiffness with increasing number of layers, which would lead to a linear ξ_{max}-Δp-dependence. However, the data of 4L graphene suggest that even here, the stretching contribution dominates, because the data follow nearly perfectly a third power dependence.

Secondly, it is not quite clear how graphene membranes adhere to the border of the pit, as discussed by Lu *et al.* [Lu10], and if slipping occurs. Furthermore, several authors report about an adhesion along the side walls of up to several nanometers [Lee08, Lee09, Barton11, Bunch12]. Experimentally, the exact transition from supported to suspended graphene and its spatial resolution is either contrast limited in SEM measurements or influenced by tip induced artifacts from AFM measurements. In particular, AFM measurements are not able to resolve the eventual adherence to the wall. Thus, if any adhesion to the walls is present in the case of 1L graphene, it might be possible that the radius of $a = 4.1 \pm 0.1\,\mu$m should be replaced by an effectively slightly larger radius in the case of few layer graphene. The portion of the membrane in actual contact with the substrate is reduced with respect to its thickness, leading to a weaker adhesion at the edges. *E.g.*, if one leaves the radius as only fitting parameter in equation (6.7), one would get $a = 4.55\,\mu$m, in the case of 4L graphene. This fit is added in figure 6.15d as a dashed line. This argument would furthermore be in agreement with a slightly larger blister radius ($a \approx 4.3\,\mu$m) deduced by the fit in figure 6.12b. However, a larger blister radius does not account for the strong deflection behavior at low Δp. Besides, we note that even for few layer graphene, the adhesion to the SiO_2 substrate is still almost as strong as for 1L graphene, so that we can conclude that the pressure loads applied here are at least of one order of magnitude lower than those necessary for delamination [Koenig11].

Thirdly, some authors report about a change in the Young's modulus with increasing layer number. The data available in literature are diverse and range from an important increase to more than 3 TPa for few layer graphene, measured by Annamalai *et al.* using the nano-indentation technique [Annamalai12], to ≈ 0.8 TPa for 2L graphene [Neek-Amal10, Annamalai13] or even 0.5 TPa [Frank07]. A recent work of the Bolotin group suggests that intrinsic crumpling effects the mechanics of suspended graphene and decreases its Young's modulus [Nicholl15]. However, we do not see any reason, why few layer graphene should be crumpled and not monolayer graphene, in particular when it is exfoliated at the same time from the same piece of graphite. In addition, the

measurements of Nicholl *et al.* are performed on devices which consist of CVD grown graphene and underwent thermal annealing, which induces further flexural phonons and static wrinkling (see also figure 5.1) [Bao09, Chen09b]. Other authors propose a constant (three dimensional) Young's modulus with increasing number of layers, both based on theoretical [Shi14, Xiang15] and experimental work [Bunch07, Koenig11]. If one supposes that the effective radius is the same for all few layer devices and the observed deviation is caused by a different Young's modulus, we would get 1.2 TPa for 2L, 0.8 TPa for 3L and 0.7 TPa for 4L graphene, by using E as only free fitting parameter.

Let us emphasize that this result is not that bad, in particular against the background of the fact that we are measuring in a regime of low pressure loads. We expect that higher pressure loads (in the range of MPa, but before delamination occurs) could allow for a more meaningful determination of E for few layer graphene.

After all, we cannot exclude that residues from the RIE fabrication process are present at the bottom of the pits. Since the common characterization techniques like profilometry and AFM are discarded because the few layer graphene covers the pit, we are restricted to an optical observation of the pit. Here, an optical contrast can be observed in the pit of the 4L graphene, which might be attributed to some contamination. This might have some influence on our measurements, since this effect is expected to have an influence only in the few nanometer range. We would like to mention that the presence of a 3L graphene in the neighborhood of the 2L graphene might influence the measurement results.

Finally, we would like to complete this section by referring to another interesting result, which is the determination of the intrinsic I_{2D}/I_G ratio of 2L graphene. Applying the same analysis as for 1L graphene (see subsection 6.2.2), a value of 1.3 ± 0.1 can be extracted from our data (see figure E.9b in the Appendix). In particular, we would like to stress that the ratio I_{2D}/I_G of a 2L graphene can be, under certain interference conditions, much larger than the ratio of 1L graphene (≈ 5 as maximum value for 2L graphene *vs.* ≈ 2 as minimum value for 1L graphene measured on our samples), thus this ratio is far from being an appropriate quantity to distinguish unambiguously 1L from 2L graphene.

6.6 Discussion

After this short excursion to few layer graphene, let us now come to the discussion of the results obtained on the three 1L graphene blisters. A summary of our experimental results and a selected survey of relevant literature values are presented in table 6.2. Let us first consider the slope $\partial\omega_{2D}/\partial\omega_G$. Our value of 2.2 ± 0.1 is in good agreement with recent studies by Zabel *et al.* on a graphene bubble and by Lee *et al.* on suspended graphene [Zabel11, Lee12b]. The latter exfoliated graphene flakes over pits with different diameters, ranging from 3.1 to $6.4\,\mu$m, and

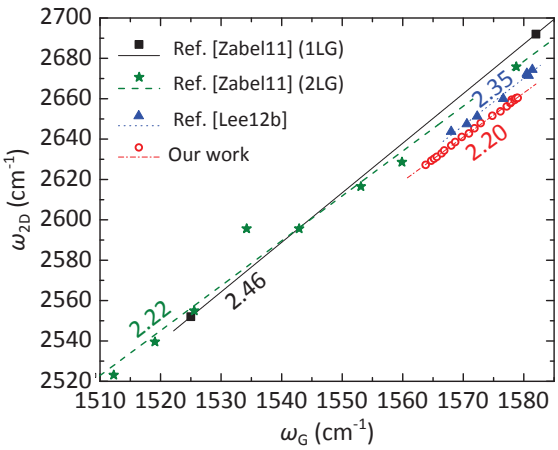

Figure 6.16: Correlation of ω_G and ω_{2D} extracted from references [Zabel11] ($\lambda_{laser} = 488$ nm) and [Lee12b] ($\lambda_{laser} = 514$ nm), compared to our findings ($\lambda_{laser} = 532$ nm). Zabel *et al.* measured on bubbles appearing on as exfoliated graphene and showing strong biaxial strain (1LG) and on pressurized 2LG. Lee *et al.* performed blister tests similar to ours, with constant pressure load and varying blister radius.

compared the Raman spectra under ambient conditions and under vacuum. The larger the diameter, the stronger the pressure difference and hence the Raman shift. The shift rate which can be extracted is $\partial\omega_{2D}/\partial\omega_G = 2.35$. In figure 6.16 we summarize graphically the available shift rates in literature and compare with our value. We have added measurements on 2L graphene by Zabel *et al.* However, Kitt *et al.* also studied pressurized graphene blisters, but only report on the G mode and not on the 2D mode values [Kitt13].

Interestingly, we demonstrate that the slope $\partial\omega_{2D}/\partial\omega_G$ is the same at the center of a pressurized blister, where strain is biaxial, and near its edges, where shear deformation (*i.e.* a uniaxial strain component) is present. We conclude that the value $\partial\omega_{2D}/\partial\omega_G = 2.2 \pm 0.1$, which also has been proposed by Lee *et al.* for thermally annealed, supported graphene [Lee12a], seems to be universal for graphene, in the limit of moderate strains below 1 % and of a uniaxial component as small as it does not lead to a broadening or splitting of the G mode feature. This splitting is observed for larger uniaxial strains inducing a shear deformation, hence the Raman signal strongly depends upon the polarization of the incoming and scattered phonons relative to the crystal orientation [Huang09, Mohiuddin09, Huang10, Frank11, Yoon11b, Kitt13]. These factors complicate the determination of $\partial\omega_{2D}/\partial\omega_G$ and consequently of the Grüneisen parameters.

Under biaxial strain, the Grüneisen parameters are determined more reliably, since these are simply proportional to $\partial\omega_{2D}/\partial\omega_G$. In general, the main challenge is to determine the amount of strain with accuracy. Our *all-optical* approach, based on the analysis of the interference modulated intensities of the Raman features and the subsequent blister profile determination, leads to values of ϵ_p, γ_G and γ_{2D}, which agree well with an estimation based on combined AFM and Raman measurements on a graphene bubble on a Si/SiO_2 substrate [Zabel11].

Ref.	Method	γ_G	γ_{2D}	$\partial\omega_{2D}/\partial\omega_G$	E (TPa)
Our work	Raman	1.8 ± 0.2	2.4 ± 0.2	2.2 ± 0.1	1.05 ± 0.1
[Lee08]	Nano-ind.	-	-	-	1.0 ± 0.1
[Metzger09]	Raman+AFM	2.4 ± 0.2	3.8 ± 0.3	2.17	-
[Ding10]	Raman*	-	2.98	2.8	-
[Zabel11]	Raman+AFM	1.8 ± 0.2	2.6 ± 0.1	2.46 ± 0.3	-
[Lee12b]	Raman+sim.	-	-	2.35 ± 0.2	2.4 ± 0.4
[Annamalai13]	Nano-ind.	-	-	-	1.12
[Kitt13]	Raman+AFM	1.89	-	-	-
[Thomsen02]	First princ.	2.0	-	-	-
[Jiang09]	Mol. dyn.	-	-	-	1.0 ± 0.1
[Mohiuddin09]	First princ.	1.8	2.7	-	-
[Cheng11]	First princ.	1.86	-	-	-
[Tan13]	Mol. dyn.	-	-	-	1.0 ± 0.1
[Nicholl15]	Interf.	-	-	-	0.06-0.3

Table 6.2: Overview of the Grüneisen parameters and shift rates for biaxial strain in graphene as well as values for the Young's modulus, obtained from experiments. Values obtained from first principle calculations and molecular dynamics studies are added to complete the table. Note that the last reference is in discrepancy with the former because it has been measured on crumpled suspended CVD graphene, thus it has not been fabricated the same way.

* Here, γ_G from ref. [Mohiuddin09] is used to calibrate the strain.

We find good agreement with theoretical predictions [Thomsen02, Mohiuddin09, Cheng11]. Interestingly, we demonstrate that a direct determination of ϵ_{p} from the integrated intensity of the Raman features can be performed *in situ*, as a function of Δp. Although the lateral resolution of our approach is set by the size of the laser spot (see figure A.1a in the Appendix) and limited by diffraction, the measured heights can be estimated with a precision up to about 5 nm. Our approach also has the major advantage of being contactless and minimally invasive, as opposed to scanning probe techniques, such as AFM, where sample-tip interaction is known to lead to artifacts when probing the topography of the suspended membrane [Bunch12]. In addition, our experimental setup is obviously easier and cheaper to implement than an *in situ* AFM setup, which would be an alternative way to probe the blister topography, as a function of a controllable pressure load with a better lateral resolution. In any event, we note that precise determinations of the Grüneisen parameters of graphene remain difficult, since these typically combine a local Raman measurement with an estimation of the amount of strain that is averaged over a much larger area. These experimental difficulties may, in part, explain the relatively large spread in the experimental values of γ_{G} and γ_{2D} reported in the literature (see table 6.2).

Finally, our measurement of the Young's modulus of graphene matches the value of bulk graphite and is in excellent agreement with values obtained by using scanning probe techniques, such as nano-indentation [Lee08, Annamalai12] and AFM [Koenig11], as well as with molecular dynamics simulations [Jiang09, Tan13]. Here, the Young's modulus is determined with accuracy using a simple, *all-optical* and minimally invasive approach. We note that Lee *et al.* have recently proposed a significantly larger value of E (see table 6.2 and ref. [Lee12b]). The latter estimate is obtained from a comparison of Raman scattering measurements with finite elements simulations. This discrepancy is probably due to the fact that ϵ_{p} has been qualitatively estimated using previously reported Raman measurements on uniaxially strained supported graphene [Yoon11b]. This difference further highlights the interest of our approach, which allows a combined study of the topography and of the vibrational properties of suspended graphene, from a consistent set of measurements.

6.7 Conclusion

Using micro-Raman scattering spectroscopy, we have performed blister tests on doping free suspended graphene membranes under a uniform pressure load. The data of three samples have been analyzed in view of the integrated intensities and the frequencies of the main Raman features of graphene. We find that the intensity of the Raman features of a suspended graphene membrane can vary by one order of magnitude for pressure load changes of only a few kPa. This interference induced modulation of the intensities is used to reconstruct the blister profile and further estimate the pressure induced strain in the membrane. Additionally, the interference

induced modulation is decoupled from the change in the I_{2D}/I_G **ratio** which allows the determination of its **intrinsic value** to 5 ± 1.

The analysis of the Raman frequency shifts reveals that they obey the correlation $\partial\omega_{2D}/\partial\omega_G = 2.2 \pm 0.1$ in the case of **biaxial strain**. Merging the strain induced shift rates of the G and 2D mode features with an average strain obtained from the blister profiles, the **Grüneisen parameters** are deduced to $\gamma_G = 1.8 \pm 0.2$ and $\gamma_{2D} = 2.4 \pm 0.2$.

For our graphene blisters, the pressure load is strictly proportional to the third power of the blister height, as expected, because graphene is the textbook example of an ultra-thin membrane. We use Hencky's solution of the Föppl-von Kármán equations and deduce a **Young's modulus** of 1.05 ± 0.10 **TPa**.

Thus, we have shown that an elegant all-optical and *in situ* extraction of important mechanical properties of graphene is possible by carefully analyzing the strain induced phonon softening and interference induced changes of the Raman mode intensities.

Finally, we emphasize the fact that the Raman intensity varies by one order of magnitude for pressure load changes of only a few kPa. This high sensitivity could be used for pressure detection applications. In particular, such a graphene-based barometer would be able to probe typical pressure variations in the atmosphere of the earth, since the variations are in the range of a few kPa between cyclones and anticyclones.

Related publications

Papers:

- Dominik Metten, François Federspiel, Michelangelo Romeo and Stéphane Berciaud, *An all-optical blister test on suspended graphene*, Physical Review Applied **2**, 054008 (2014) / DOI: 10.1103/PhysRevApplied.2.054008, ref. [Metten14].

- Dominik Metten, Guillaume Froehlicher, Stéphane Berciaud, *Doping- and interference-free measurement of I_{2D}/I_G in suspended monolayer graphene blisters*, Physica Status Solidi B **252**, 2390-2394 (2015) / DOI 10.1002/pssb.201552314, ref. [Metten15].

Poster:

- Dominik Metten, François Federspiel, Michelangelo Romeo, and Stéphane Berciaud, *An all-optical blister test on freestanding graphene*
  presented at
  - ▷ *Annual meeting of the GDRI Graphene Nanotubes*, 21th to 25th of February 2014, Strasbourg (France)

▷ *XXVIIIth International Winter School on Electronic Properties of Novel Materials*, 8th to 15th of March 2014, Kirchberg in Tirol (Austria)

Oral presentations:

- *Probing the vibrational and mechanical properties of freestanding graphene using Raman scattering spectroscopy*, Mid-term presentation, Scientific meeting at the Institut de Physique et de Chimie des Matériaux de Strasbourg, 10th of June 2014, Strasbourg (France)
- *All optical determination of the Young's modulus of graphene*, Condensed Matter in Paris (JMC14-CMD25), 24th to 29th of August 2014, Paris (France)

7 Suspended graphene under electrostatic pressure

In the previous chapter we have reported on an elegant way of introducing biaxial tensile strain to suspended graphene membranes in a blister test geometry. Since the observed membrane deflections are caused by the application of an air pressure difference, the frequency shifts in the Raman spectra can be attributed to pure strain, without any effect of doping.

In this chapter, we will consider the electrostatic gating approach which is widely used in the transport community in order to tune a source-drain current. In the case of micrometer-sized graphite derivatives, electrostatic gating is also employed to drive the motion and/or control the deflection, as for carbon nanotubes [Poncharal99] or suspended graphene membranes [Bunch07]. However, the electrostatically induced deflections may also be considered as an undesired side effect when examining the intrinsic transport properties. In particular, high back-gate voltages lead to large tensile strains and, ultimately, to an irreversible collapse of the device [Bunch07, Bolotin08b]. In the guideline of our results on the pressurized graphene blisters and motivated by recent studies on electrically gated suspended graphene [Chen09a, Barton11, Eichler11], combining optics and nano-mechanics [Reserbat-Plantey12, Lee12b, Reserbat-Plantey15], we performed a Raman scattering study on an electrostatically gated suspended graphene membrane. A schematic sketch of the device, which consists of an exfoliated graphene membrane suspended over a micrometer-sized trench, is shown in figure 7.1a, whereas figure 7.1b indicates the measurement principle.

In section 7.1 we will first focus on the integrated intensities of the Raman G and 2D mode features. As in our blister test study, the gate-induced variations of the distance between the bottom substrate and the graphene membrane lead to very large changes in the Raman intensities due to optical interference effects. Therefore, an analysis of the G and 2D mode intensities allows for an accurate, *in situ* measurement of the deflection up to the collapse of the membrane. This analysis further permits a validation of the intrinsic I_{2D}/I_G ratio found in chapter 6 (see section 6.2.2).

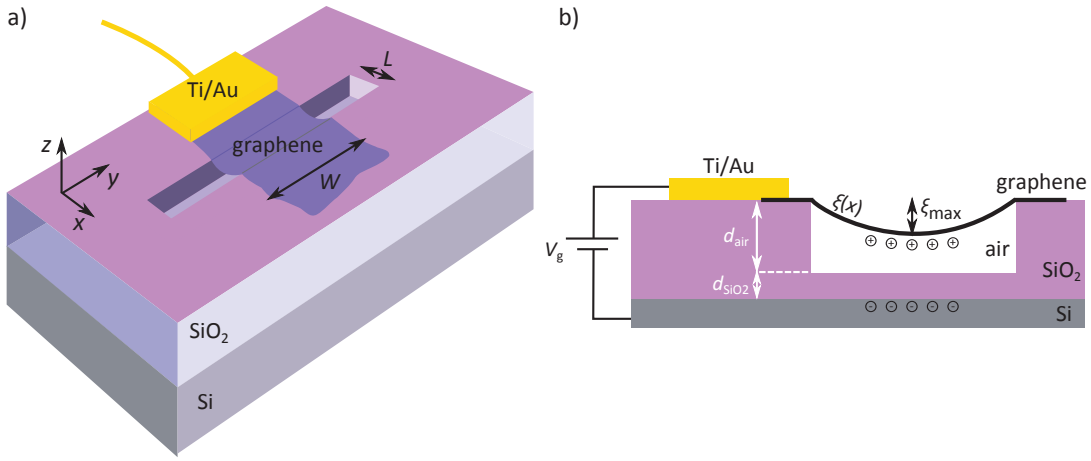

Figure 7.1: a) 3D scheme of a gated suspended graphene device with dimensions L and W in the x- and y-direction. The deflection induced by the electrostatic pressure is in the z-direction. **b)** Side view of the same device. The shape of the profile is described by $\xi(x)$ (supposing $W \ll L$) and depends on the applied gate voltage V_g. The maximal deflection at the center of the membrane is ξ_{max}.

Our observations will then be described by a mechanical model based on the Föppl-von Kármán equations, which we have introduced in section 2.5, including pre-strain in the membrane [Kármán10, Medvedyeva11]. The pressure load exerted on the suspended graphene is evaluated by examining the electrostatic attraction, either taking or not taking into account the gate-induced curvature of the membrane.

In addition, we will make use of our model and predict critical values of electrostatic pressure and deflection, at which the membrane collapses, for different device geometries. Furthermore, the corresponding charge carrier density is deduced, which is an important issue in transport measurements, in particular because its inhomogeneity increases with increasing deflections.

Finally, it will turn out of the analysis of the Raman frequencies that the obtained results form an important step towards a detailed understanding of the charge distribution and the observation of the phonon anomaly in clean suspended graphene devices [Das08, Lee12a].

7.1 Optical probing of the gate induced deflection

In this section we first briefly present a room temperature characterization of the device considered here, and then focus on the integrated intensities of the Raman G and 2D modes, acquired from a Raman measurement run at low temperature, by varying the back gate voltage.

Figure 7.2a shows an optical micrograph of the suspended 1L graphene, on which we performed the measurements, indicated by a red arrow. The 1L is neighbored by a 2L graphene. The substrate is a common Si/SiO_2 substrate with highly *p*-doped silicon covered by a silicon oxide layer of thickness $d_{SiO_2} = 500$ nm. The trench, fabricated by the HF etching method described in

$\langle\epsilon\rangle_{\text{susp}}$ (%)	$\langle n\rangle_{\text{susp}}$ ($\times 10^{11}$ cm^{-2})	$\langle\epsilon\rangle_{\text{supp}}$ (%)	$\langle n\rangle_{\text{supp}}$ ($\times 10^{12}$ cm^{-2})
$+0.06 \pm 0.01$	< 4	$+0.02 \pm 0.02$	$+2.5 \pm 0.7$

Table 7.1: Spatially averaged strain and doping values with standard deviations for the suspended graphene device shown in figure 7.2a. The values are obtained from the Raman maps (see figure 7.2b and c) and subsequent vector projection, as discussed in chapter 3.

chapter 4, has a width $L = 4.9\,\mu$m, measured by optical and scanning electron microscopy. Its depth is $d_{\text{air}} = (288 \pm 5)$ nm, measured by profilometry. Thus, the remaining oxide thickness is $d_{SiO_2} = (212 \pm 5)$ nm. A large area of the 1L graphene is supported and contacted with Ti (3 nm) and Au (47 nm) by means of the shadow mask technique (see chapter 4).

First, we focus on a Raman characterization of this device under ambient conditions in order to gain information about its built-in strain and initial doping level and, importantly, conclude that the graphene membrane is indeed suspended. Figures 7.2b and c represent Raman maps of the G mode frequency ω_G and its width Γ_G, respectively, under ambient conditions. ω_G ranges from 1584.5 to $1587.5\,\text{cm}^{-1}$ with a mean value of $1586.2\,\text{cm}^{-1}$ (standard deviation $1.0\,\text{cm}^{-1}$) on the supported part, which is delimited by a dashed black line in figure 7.2b. In contrast, ω_G ranges from 1576.0 to $1578.0\,\text{cm}^{-1}$ with a mean value of $1576.6\,\text{cm}^{-1}$ (standard deviation $0.5\,\text{cm}^{-1}$) on the suspended part (delimited by a dashed blue line). The careful observer might notice that this difference in ω_G is propagating on the 2LG but vanishes on the 4LG.

Γ_G is nearly homogeneously distributed on the supported part, with a mean value of $6.6\,\text{cm}^{-1}$, whereas it is $16.3\,\text{cm}^{-1}$ with a broader distribution on the suspended part. We note that the time to record the spectra has been 1 min and that the Raman intensity has been strongly reduced on the suspended part due to destructive optical interference. Hence, the width on the suspended part has a larger error than the one on the supported part.

The graphs in figures 7.2d and e correlate ω_G with ω_{2D} and Γ_G, respectively. The data are extracted from the delimited areas on the map in figure 7.2b and plotted as open blue squares for the suspended area and filled black squares for the supported area. For the former, in the frequency space (figure 7.2d), the data are concentrated with a small standard deviation and are downshifted along a slope of 2.2 with respect to neutral and unstrained graphene[1]. In contrast, the data of the supported area are aligned along a line with the same slope but shifted to higher ω_G. Following the vector decomposition model proposed by Lee *et al.* [Lee12a], refined in chapter 3 and applied to our suspended graphene samples in chapter 5, we might estimate average strain and doping levels on the suspended and supported part. The results are presented in table 7.1.

The suspended flake is subjected to a built-in strain of 0.06 ± 0.01 %. The spatial distribution of this strain is quasi homogeneous. The doping level (analyzed with respect to hole doping)

[1] Here we use the reference point ($\omega_G^0 = 1581\,\text{cm}^{-1}$, $\omega_{2D}^0 = 2667\,\text{cm}^{-1}$), as in chapter 5.

is in the range of a few 10^{11} cm^{-2}. However, the average strain on the supported part is less pronounced (0.02 %) but varies between -0.01 and 0.05 %. As a lot of samples deposited on SiO_2, the supported graphene exhibits a charge carrier density in the range of $\approx 3 \times 10^{12}$ cm^{-2}.

The data represented in figure 7.2e combine the two maps in figures 7.2b and c, and confirm the undoped character of the device by the two well distinguishable areas in the ω_G-Γ_G-plane.

Since the device is intrinsically undoped, it offers an ideal platform for sensing the change in the Raman spectra when charge carriers are added by applying a backgate voltage.

To do so, the sample is put under vacuum and thermally connected to a ^{4}Helium bath via a cold-finger, as specified in the experimental setup section (see section 4.2). A back gate voltage V_g is applied to the device. In our measurement run, V_g is swept down from 0 to -12 V and then up from -12 V to $+25$ V. At every 1 V step, the sweep is stopped and after a delay of 20 s, a Raman spectrum is recorded at the center of the suspended membrane, using a laser wavelength of 532 nm and a $\times 50$ objective. The laser power (before entering the objective) is kept below 0.4 mW in order to avoid laser induced heating and decomposition of the carbon lattice[2].

Figure 7.2g shows a cascade plot of the Raman G and 2D mode as a function of V_g, ranging from -11 to $+25$ V. Several interesting features can be observed. First, the intensity of the Raman modes increases strikingly with the increase of the absolute value of V_g up to $+19$ V. Second, a

[2]For measurements under vacuum, the thermal exchange with the environment is reduced. At a laser power of 0.7 mW, a burning of suspended graphene membranes on other devices has been observed when the laser spot remained focused with the $\times 50$ objective on the same point for longer than 10 min. Therefore, in addition to the low laser power, the laser light is blocked during the voltage sweep (between the records of the spectra) to avoid heat accumulation. We note that Kitt *et al.* report on this "laser induced dirt deposited at the center" [Kitt13].

Figure 7.2 ***(facing page)*****: a)** Optical micrograph of the suspended 1LG device. The red dashed line marks the limit of the 1L, which is neighbored by a 2L and 4L graphene. The scale bar is $5\,\mu$m. **b)** and **c)** Hyperspectral Raman maps of the device shown in (a), with a lateral resolution of $1\,\mu$m, showing the distribution of ω_G and Γ_G, respectively, using a laser power of 0.7 mW, under ambient conditions. The data taken into account for further analysis are delimited by a black (blue) dashed line in (b), for the supported (suspended) area. The suspended area is well distinguishable and characterized by a relatively low ω_G and high Γ_G. See main text for detailed discussion. **d)** Correlation of ω_G and ω_{2D} using the data extracted from the maps in (b) and (c). Data of the suspended (supported) area [see dashed lines in (b)] are shown as open blue (filled black) squares. A slope of $\partial\omega_{2D}/\partial\omega_G = 2.2$ for strain and 0.55 for hole doping are added as dashed black and straight red lines, respectively. **e)** Correlation of Γ_G and ω_G. **f)** Schematic side view sketch of the device. h_{max} denotes the distance between the 1LG and the bottom of the SiO_2 at its center. **g)** Cascade plot of Raman spectra recorded at the center of the suspended graphene membrane, as a function of V_g. Spectra are taken at 4 K with a max. laser power of 0.4 mW. The spectrum at $V_g = 0$ is drawn in red to highlight the symmetry of the Raman intensity with respect to the gate voltage. Spectra for $V_g > 19$ V showing very different characteristics are drawn in blue. The missing spectra at $+13$ and $+17$ V are strongly disturbed by cosmic rays and are therefore not shown. **h)** Selected Raman spectra for different V_g, multiplied by the factors indicated on the left in order to make appear the spectra with the same 2D mode intensity. With increasing V_g, I_{2D}/I_G decreases and for $+20$ V a sudden frequency shift of both modes is observed as well as a marked splitting of the G mode. The G (2D) mode peaks are fitted with a Lorentzian (double Baskonian) (red solid line). All spectra are taken using a laser wavelength of 532 nm.

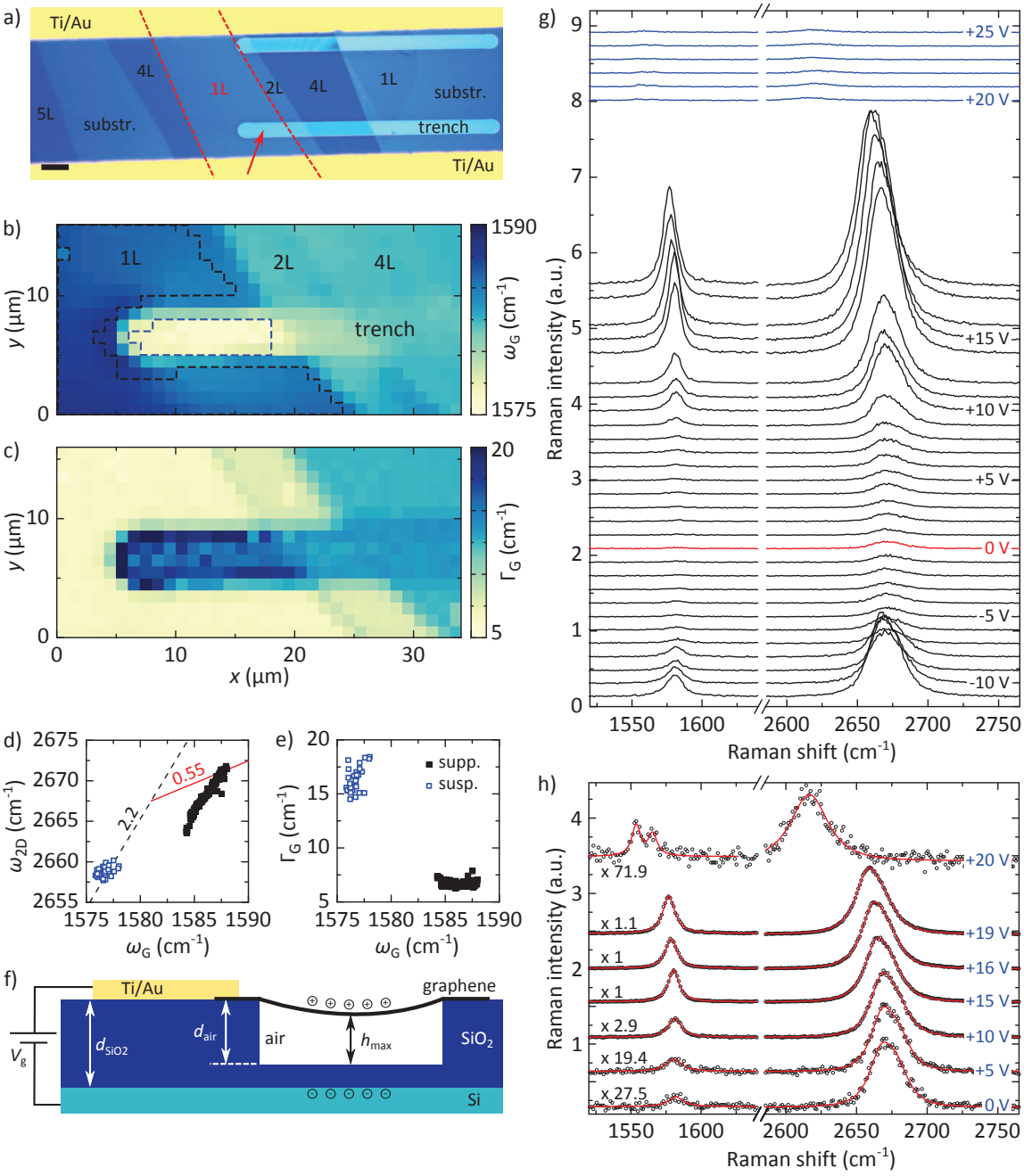
a)
Ti/Au
4L
1L
2L
4L
1L
substr.
5L
substr.
trench
Ti/Au
b)
1L
2L
4L
trench
y (μm)
10
0
1590
1575
ωG (cm-1)
c)
y (μm)
10
0
20
5
ΓG (cm-1)
0
10
20
30
x (μm)
d)
2675
2670
2665
2660
2655
ω2D (cm-1)
0.55
2.2
1575 1580 1585 1590
ωG (cm-1)
e)
20
15
10
5
ΓG (cm-1)
supp.
susp.
1575 1580 1585 1590
ωG (cm-1)
f)
Ti/Au
graphene
dSiO2
dair
air
hmax
SiO2
Vg
Si
g)
9
8
7
6
5
4
3
2
1
0
Raman intensity (a.u.)
+25 V
+20 V
+15 V
+10 V
+5 V
0 V
-5 V
-10 V
1550 1600 2600 2650 2700 2750
Raman shift (cm-1)
h)
4
3
2
1
Raman intensity (a.u.)
x 71.9
x 1.1
x 1
x 1
x 2.9
x 19.4
x 27.5
+20 V
+19 V
+16 V
+15 V
+10 V
+5 V
0 V
1550 1600 2600 2650 2700 2750
Raman shift (cm-1)

shift of the Raman modes to lower frequencies is observed at higher voltages. Third, as can be seen in figure 7.2h where the spectra are normalized with respect to the intensity of the 2D mode, the relative intensity of the 2D and G mode intensities, I_{2D}/I_G varies with V_g. For $V_g < 20$ V, these three characteristics remind the previous study of the pressurized graphene blister. In particular, they suggest that the change in intensity can be used to determine the distance h between the membrane and the silicon oxide (see sketch in figure 7.2f) at the center of the membrane.

Spectra recorded at $V_g > 19$ V (plotted in blue in figure 7.2g) further suggest that here, another regime is probed because the change in intensity is sudden and remarkable. In addition, when going from $+19$ to $+20$ V, the position and the shape of both the G and 2D mode change drastically (see the direct comparison of the spectra recorded at $+19$ and $+20$ V in figure 7.2h).

The aim of the next subsection is to deduce h_{max} at the center (and consecutively the deflection ξ_{max}) as a function of V_g, in order to understand the evolution of the deflection and, in particular, explain the drastic changes observed between $+19$ and $+20$ V. In one stroke, the intrinsic value of I_{2D}/I_G can be deduced, compared to the value deduced by the blister tests and thus checked for coherence.

The deflection data will be compared to a theoretical model in subsection 7.2.3 and the change in frequency of the Raman modes will be analyzed later in section 7.4.

7.1.1 Determination of the deflection

In order to establish the maximal deflection, I_G and I_{2D} are extracted from the spectra shown in figure 7.2g by taking the integrated intensities of Lorentzian and double modified Lorentzian fits, as presented in section 3.2, respectively. Fits of some selected spectra appear as red lines in figure 7.2h. We point out that the relative error in I_G and I_{2D} is much larger at low voltages and taken as 25 % for an absolute integrated intensity lower than 500 counts, whereas it is taken below 5 % for an integrated intensity higher than 4000 counts.

Figure 7.3a shows a semi-logarithmic plot of I_G and I_{2D} as a function of V_g. As mentioned earlier, I_G and I_{2D} increase with the absolute value of V_g, *i.e.* applying a negative or positive voltage has the same effect on the intensity. Furthermore, we observe that the change in intensity is reversible, because the data for negative V_g include a down- and an up-sweep. It is interesting to notice that I_{2D} (which has a minimum value at 0 V [red star in figure 7.3]) reaches a maximum at $+17$ V (red hash symbol) and decreases slightly up to $+19$ V. The fact that I_{2D} passes through a minimum and a maximum value offers the possibility to renormalize the theoretically calculated Raman enhancement factors with respect to the experimental data. Hence, it is possible to determine the distance h between the membrane and the bottom (and consecutively the deflection ξ_{max}) for all intermediate values of V_g.

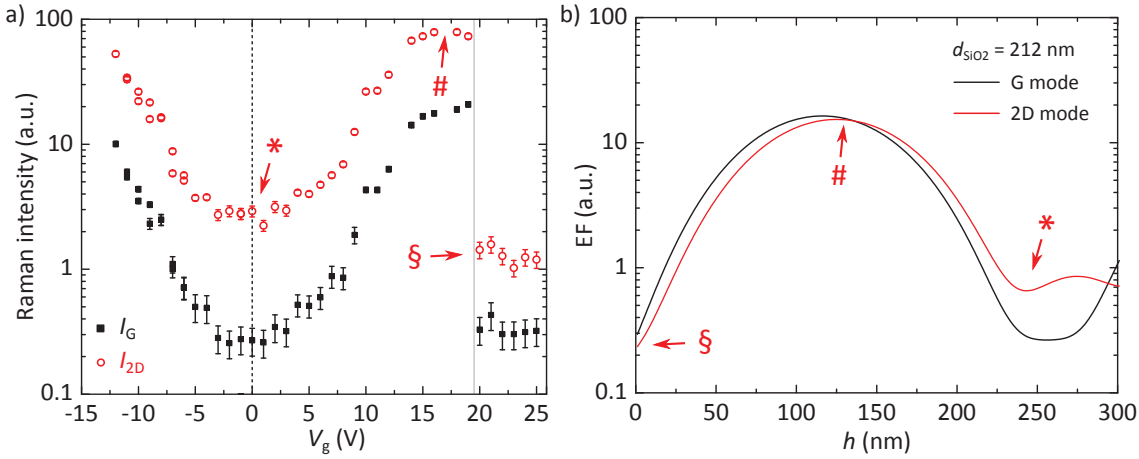

Figure 7.3: a) Semilogarithmic plot of I_G (black filled squares) and I_{2D} (red open circles) as a function of V_g. The evolution of the intensities is symmetric around $V_g = 0$ and undergoes a sudden change for $V_g > +19$ V which is attributed to a collapse of the graphene membrane, in accordance with the calculated Raman enhancement factors shown in **(b)** (see main text); these factors are calculated using the multilayer model developed in section 3.5, using $d_{SiO_2} = 212$ nm and $\lambda_{laser} = 532$ nm. h denotes the distance between the membrane and the bottom of the trench. Features discussed in the main text are marked with a star, hash symbol and paragraph sign.

Figure 7.3b is a plot of the theoretically calculated enhancement factors for the G and 2D mode, as a function of h, adapted for the system [Si - SiO_2 (of fixed thickness $d_{SiO_2} = 212$ nm) - air/vacuum (of varying thickness h) - graphene] (using a laser wavelength of 532 nm). In respect of the device geometry, the intensity values at 0 V can directly be attributed to the local minimum around 250 nm (red star for I_{2D}). Since the applied potential difference induces an attractive force between the bottom and the membrane, h decreases with V_g down to ≈ 120 nm, which corresponds a local maximum (red hash symbol for I_{2D}).

Now, the sudden change in intensity, which is observed when V_g goes from $+19$ to $+20$ V (indicated by a grey line in figure 7.3a) is necessarily attributed to a collapse of the graphene membrane. The intensity decreases drastically and the next local minimum for the enhancement factors is observed for $h = 0$ nm (red paragraph sign), which means that the graphene sheet is attached to the bottom of the trench. Two observations bolster this theory: First, regarding the intensities, I_G is at the same level at $V_g = 0$ and $V_g > +19$ V, whereas I_{2D} is lower at $V_g > +19$ V than at $V_g = 0$, which is also predicted by the enhancement factors (compare the values of EF at the position of the red star and the red paragraph sign in figure 7.3b). Second, regarding the actual shape and frequencies of the Raman modes, a strong downshift of both modes, a splitting of the G mode and a slight broadening of the 2D mode are observed. These features are a strong evidence of uniaxial strain greater than 0.6 % [Huang09, Mohiuddin09, Mohr10, Yoon11b,

Popov13, Polyzos15]. This strain is due to a large change in the length of the membrane, ΔL, because the sticked graphene is much more stretched than the suspended membrane.

A further gate sweep from $+25$ V to -25 V reveals no change in I_{G} and I_{2D}, hence the sticking of the membrane to the bottom of the trench is irreversible. A scanning electron microscope image taken one month after the electric measurements confirms the definite character of the collapse, and, in particular, the strong adhesion of the membrane to the bottom of the trench (see figure 7.4).

7.1.2 Intrinsic value of $I_{\mathsf{2D}}/I_{\mathsf{G}}$

Similar to the determination of the intrinsic value of the $I_{\mathsf{2D}}/I_{\mathsf{G}}$ ratio by analyzing the Raman intensities of the pressurized blister (see chapter 6), it is possible to fit the experimental data to the calculated ratio of the enhancement factors EF, according to

$$\left(\frac{I_{\mathsf{2D}}}{I_{\mathsf{G}}}(h)\right)_{\mathsf{mes}} = \left(\frac{I_{\mathsf{2D}}}{I_{\mathsf{G}}}\right)_{\mathsf{intr}} \times \frac{\mathsf{EF}_{\mathsf{2D}}}{\mathsf{EF}_{\mathsf{G}}}(h) \tag{7.1}$$

using $(I_{\mathsf{2D}}/I_{\mathsf{G}})_{\mathsf{intr}}$ as fitting parameter. But, in contrast to the blister test, care has to be taken, because in the suspended field effect geometry, the Fermi energy is tuned when h changes and thus $I_{\mathsf{2D}}/I_{\mathsf{G}}$ is not only a function of h but also of E_{F}. Basko *et al.* calculated that $\sqrt{I_{\mathsf{G}}/I_{\mathsf{2D}}}$ is proportional to the Fermi energy E_{F} [Basko09b]. However, the available experimental data in literature on supported graphene show no significant change (max. 10 %) of the intensity ratio within the range of $E_{\mathsf{F}} = -150$ meV and $+150$ meV [Das08, Froehlicher15a].

Figures 7.5a and b represent the $I_{\mathsf{2D}}/I_{\mathsf{G}}$ ratio as a function of h, where h has been extracted from the intensities of the G and 2D modes, respectively. The fact that the enhancement factors show a valley around 250 nm (see figure 7.3b) is responsible for large error bars in h whereas the (related) low Raman intensity around $V_{\mathsf{g}} = 0$ causes large error bars in $I_{\mathsf{2D}}/I_{\mathsf{G}}$. Consequently, the error bars are reduced between $h = 100$ nm and 200 nm, because of the relatively high intensities. The blue curves are fits based on equation (7.1) with the fitting parameters $(I_{\mathsf{2D}}/I_{\mathsf{G}})_{\mathsf{intr}} = 4.2$ and 4.5, which is in good accordance with our result on the three graphene blisters, presented in section 6.2.2.

We note that the intensity ratio measured on the collapsed graphene at $h = 0$ is also taken into account for the fit and nestle well against the blue curve. Furthermore we point out that the induced charges do not seem to influence $I_{\mathsf{2D}}/I_{\mathsf{G}}$ for this measurement run. We come back to this issue in section 7.4 where the analysis of the spectral position and width of the peaks will give more insight in the charge distribution.

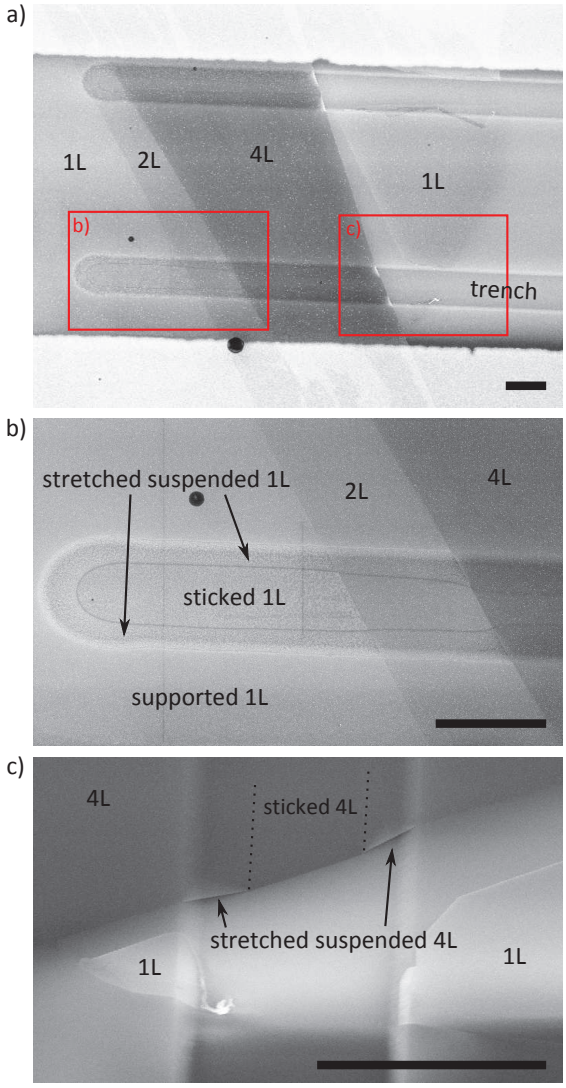

Figure 7.4: SEM images of the device after our gate-dependent Raman study, when the 1LG is sticked to the bottom of the trench. **a)** Overview of the device with red squares indicating the zoomed area in (b) and (c). **b)** The sticked area can be distinguished by a light grey line in the bottom. Also the neighboring 2LG and 4LG are sticked. The stretched suspended part at the borders of the trench is nicely seen in figure **(c)** for the 4LG, where the image is turned by 90° and tilted. The scale bar is $5\ \mu$m in all images.

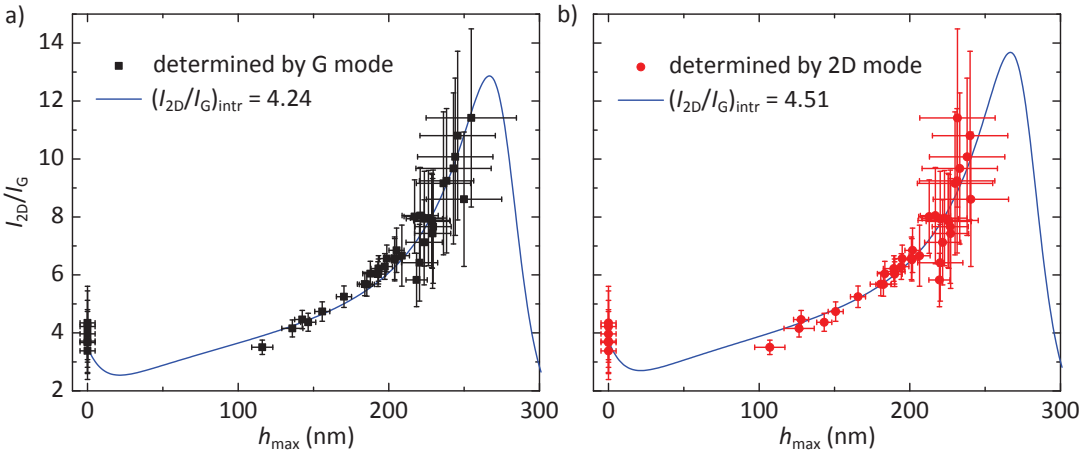

Figure 7.5: I_{2D}/I_G as a function of h_{max}, the distance between the membrane and the bottom of the trench, at the point of maximal deflection. h_{max} is extracted as described in the main text, by using the change in I_G **(a)** and I_{2D} **(b)** with V_g. The large error bars for high I_{2D}/I_G are caused by a poor Raman signal near $V_g = 0$, due to destructive interference. Blue lines are fits based on equation (7.1) with the fitting parameters $(I_{2D}/I_G)_{intr} = 4.2$ (a) and 4.5 (b).

7.2 Theory of graphene sheet deformation due to electrostatic pressure

In the previous section, we have successfully determined the gate induced deflection. The aim of this section is now to theoretically describe the gate induced evolution of h and then, in particular, find a way to predict the collapse of the membrane at high gate voltages.

The application of a gate voltage V_g induces a charge accumulation on the graphene membrane, because the (conducting) membrane and the highly doped silicon are separated by (non-conducting) dielectrics, *i.e.* air and SiO_2. The separation of charges is the origin of an electric field. If one charge is placed in vacuum, its electric field is determined, in its most general way, by Gauss's law [Landau60]:

$$\oint_S \boldsymbol{E} \cdot \mathrm{d}\boldsymbol{S} = \frac{Q}{\varepsilon_0}. \tag{7.2}$$

Here, S is a closed surface enclosing any volume, $\boldsymbol{E}$ is the electric field vector, $\mathrm{d}\boldsymbol{S}$ is a vector perpendicular to a small surface element $\mathrm{d}S$ with magnitude $\mathrm{d}S$, Q is the total charge enclosed within S and ε_0 is the electric constant. Furthermore, we remind that a charge q, which experiences the electric field $\boldsymbol{E}$, is subjected to the Lorentz force, $\boldsymbol{F}$, according to (without magnetic field) [Jackson62]:

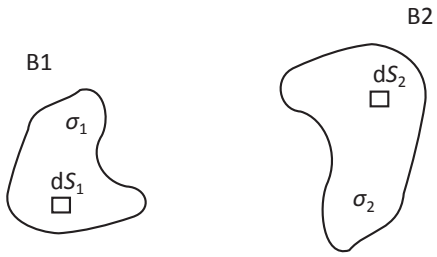

Figure 7.6: Sketch of the Lorentz force acting between two charged bodies B1 and B2 with surface charge densities σ_1 and σ_2, respectively.

$$\boldsymbol{F} = q\,\boldsymbol{E}. \tag{7.3}$$

This force, considered per area, acts as a pressure load on the graphene membrane and is responsible for its deflection. In the following subsection we will derive the relationship between this pressure load and the applied gate voltage, by taking into account the device geometry, in particular its capacitance.

7.2.1 Forces in electrostatic gating

Let us first consider two charged and arbitrarily shaped bodies B1 and B2 with a surface charge density σ_1 and σ_2, respectively, and divide them into small patches $\mathrm{d}S_1$ and $\mathrm{d}S_2$. The force with which B1 acts on B2 is obtained by considering the electric field strength $\boldsymbol{E}_1$ (caused by B1) at every patch $\mathrm{d}S_2$. Thus, one writes, according to the Lorentz force:

$$\boldsymbol{F}_{12} = \oint_{S2} \sigma_2 \,\mathrm{d}S_2\, \boldsymbol{E}_1. \tag{7.4}$$

Now, let B1 be a cylinder of radius R, placed in vacuum ($\varepsilon_\mathrm{r} = 1$), with a positive charge $+Q$ and a surface charge density $\sigma_1 = +\sigma$, and let the axis of that cylinder coincide with the z-axis. The electric field $\boldsymbol{E}_\mathrm{z}$ along the z-axis is given by [Griffiths99]

$$\boldsymbol{E}_\mathrm{z} = \frac{\sigma}{2\varepsilon_0} \frac{\sqrt{z^2+R^2} - z}{\sqrt{z^2+R^2}}\, \boldsymbol{e}_\mathrm{z}. \tag{7.5}$$

In the limit of $z \ll R$, *i.e.* considering the cylinder as an infinite plate, the second term tends to 1. Thus, the electric field at the position of B2 is

$$\boldsymbol{E}_1 = \frac{\sigma}{2\varepsilon_0}\, \boldsymbol{e}_\mathrm{z}. \tag{7.6}$$

Let B2 be a flat infinite plate with a negative charge $-Q$ and a surface charge density of $-\sigma$. The force with which B1 acts on B2 rewrites then as

$$\boldsymbol{F}_{12} = \int_S (-\sigma)\, \mathrm{d}S\, \boldsymbol{E}_1 = -Q\boldsymbol{E}_1. \tag{7.7}$$

The minus sign indicates that the force is attractive, as expected for oppositely charged plates. Using $Q = \sigma S$ one finally gets for the absolute value of the force:

$$F_{12} = \frac{\sigma^2 S}{2\varepsilon_0}. \tag{7.8}$$

The electrostatic pressure, labeled P_{el}, is obtained by dividing the force (equation (7.8)) by the surface. Furthermore, P_{el} can be expressed in terms of c, the capacitance per unit area, which is given by $c = \sigma/V_{\mathrm{g}}$. Hence, one gets

$$P_{\mathrm{el}} = \frac{c^2 V_{\mathrm{g}}^2}{2\varepsilon_0}. \tag{7.9}$$

We note that, if the plate is not flat, c is a function of the local distance at the position (x, y), thus it is $P_{\mathrm{el}}(x, y)$. Furthermore, media with $\varepsilon_{\mathrm{r}} \neq 1$ and, in particular, multilayer systems as air/SiO_2 between the silicon and the graphene membrane can be incorporated in c, which acts then as an effective capacitance.

7.2.2 Mechanical deformation

In the case of a suspended graphene membrane, the electrostatic pressure $P_{\mathrm{el}}(x, y)$ induces a deformation $\xi(x, y)$ of the membrane, because at the edges, it is supported by the substrate, or even clamped (see figure 7.1a). The deformation is determined by minimizing the total energy of the profile, as discussed in chapter 2 (see section 2.5). Here, apart from the bending and the stretching contribution of the elastic energy, also the electrostatic energy contributes to the total free energy. Thus, the equations of equilibrium write as [Medvedyeva11]

$$\begin{aligned} D\Delta^2\xi - \frac{\partial}{\partial x_\beta}\left(t\sigma_{\alpha\beta}\frac{\partial \xi}{\partial x_\alpha}\right) &= P_{\mathrm{el}}(x, y) \\ \frac{\partial \sigma_{\alpha\beta}}{\partial x_\beta} &= 0, \end{aligned} \tag{7.10}$$

in accordance with equation (2.34) in section 2.5. Let us consider our case of a graphene membrane exfoliated over a trench. If $W \gg L$ (see figure 7.1), the gate induced deformation of the membrane is homogeneous in the y-direction. Following Medvedyeva and Blanter, one can sup-

pose that the tension along the sheet is constant over the sheet, *i.e.* the tensor ($t\sigma_{\alpha\beta}$) can be replaced by $T\delta_{\alpha\beta}$ where $\delta_{\alpha\beta}$ is the Kronecker-delta [Medvedyeva11].

T can be written as the sum of two contributions to the stress: $T = T_0 + T_\mathsf{H}$. Here, T_0 is the residual built-in strain, whereas T_H is the strain induced by the relative elongation:

$$T_\mathsf{H} = \frac{Et}{1-\nu^2}\,\frac{\Delta L}{L}. \tag{7.11}$$

Thus, the relative elongation involves the solution of the equilibrium equations, $\xi(x)$, because the length of the membrane is found by according to

$$\Delta L + L = \int_{-L/2}^{+L/2} \sqrt{1+[\xi'(x)]^2}\,\mathrm{d}x. \tag{7.12}$$

Then, equation (7.10), together with the definition of T, rewrites as

$$D\,\frac{\partial^4\xi}{\partial x^4} - T(\xi'(x))\,\frac{\partial^2\xi}{\partial x^2} = P_\mathsf{el}(\xi(x)), \tag{7.13}$$

where T and P_el depend on x in a non-trivial manner. In section 2.5 (chapter 2) we already addressed the difficulty to solve this equation (see section 2.5), even when the y-direction is omitted. An analytical solution can be found only self-consistently.

Medvedyeva and Blanter considered a constant electrostatic pressure over the whole sheet. Nevertheless, $P_\mathsf{el}(x)$ is proportional to the square root of the total capacitance $c(x)$, and $c(x)$ is a function of the distance between the membrane and the SiO_2. For small deflections, P_el could be taken as constant because the difference in the distance between the edges and the middle of the trench is small. But in our experiments, the maximal deflection exceeds half of the value of the air thickness, which means that the effects of the profile shape on P_el have to be taken into account.

In the following, we assume that the profile of the membrane is parabolic. This assumption is *inter alia* based on *in situ* AFM measurements performed on gated graphene membranes [Schwarz15] and forms a first approximation. Furthermore, we derive a relationship between the maximal deflection in the center of the membrane, denoted ξ_max, and the electrostatic pressure. To do so, we consider P_el as a constant average value all over the sheet. The essential question, how to determine P_el, is addressed later.

Let $\xi(x) = a+bx+cx^2$ be the shape of the profile. With the boundary condition $\xi(\pm L/2) = 0$ and the differential equation (7.13) the coefficients a, b and c are determined. One gets

$$\xi(x) = \frac{P_\mathsf{el}}{2T}\left(\frac{L^2}{4} - x^2\right). \tag{7.14}$$

The condition $\xi'(x) = 0$ at $x = 0$ connects P_{el} and T to the maximal deflection:

$$\xi_{\text{max}} = \frac{P_{\text{el}} L^2}{8T}. \tag{7.15}$$

In order to eliminate T, we calculate it explicitly for the parabolic profile and insert the result in (7.15) in order to get an equation which relates ξ_{max} to P_{el}.

For small deflections, *i.e.* $\xi'(x) \ll 1$, the square root in equation (7.11) can be expanded so that T_H can be written as

$$T_H = \frac{Et}{2(1-\nu^2)L} \int_{-L/2}^{+L/2} [\xi'(x)]^2 \, \mathrm{d}x. \tag{7.16}$$

Integrating and using equation (7.15) in order to eliminate T leads then to the following result [Medvedyeva11, Bao12]:

$$P_{\text{el}} = \frac{8T_0}{L^2} \, \xi_{\text{max}} + \frac{64Et}{3(1-\nu^2)L^4} \, \xi_{\text{max}}^3. \tag{7.17}$$

We take notice of the fact that this result strongly resembles equation (2.39), where P is the sum of a term scaling linear with ξ_{max} and a term scaling as ξ_{max}^3. Indeed, the linear term contains the prestrain in the membrane, T_0. For $T_0 = 0$, P_{el} is proportional to ξ_{max}^3, as expected for an unstrained membrane without bending stiffness (compare also with the case of circular membranes [Hencky15, Wan95] (see chapter 6). The proportionality constant for the ξ_{max}^3-term includes again the Young's modulus E, the membrane thickness t and a geometry dependent parameter, which is here L. As expected, the length of the trench scales in the same manner as the blister radius, *i.e.* as $1/L^4$.

The intriguing question is how P_{el} can be determined to best describe the maximal displacement of the membrane. Medvedyeva and Blanter consider the distance between the bottom and the membrane as constant. Bao *et al.* measured the displacement of an *in situ* gated graphene membrane in a SEM by analyzing the SEM images. They compared the case of a constant distance (constant P_{el}) to a modified electrostatic pressure obtained by integrating c along a parabolic profile, before injecting it in the equation $P_{\text{el}} = c^2 V_{\text{g}}^2/(2\varepsilon_0)$ [Bao12].

Here, we will consider the following three cases and give the corresponding relationship between V_{g} and ξ_{max}:

Case 1: P_{el} is directly calculated via $P_{\text{el}} = c^2 V_{\text{g}}^2/(2\varepsilon_0)$. The capacitance c is constant over the sheet and does not depend on ξ_{max}, thus every displacement of the membrane is neglected. This case has been considered by Medvedyeva and Blanter and first by Bao *et*

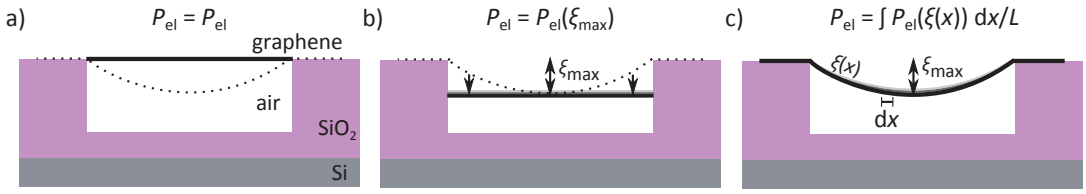

Figure 7.7: Sketch of the three cases to evaluate the electrostatic pressure P_{el}, with the following assumptions: The distance between the graphene membrane and the bottom **a)** does not change. **b)** changes but is constant along the sheet ("lift"-model). **c)** follows a parabolic profile, P_{el} depends on x and is then integrated along the sheet.

al. [Medvedyeva11, Bao12] (see figure 7.7a). Combining equation (7.17) and (7.9) with $c = (c_{air}^{-1} + c_{SiO_2}^{-1})^{-1}$ where $c_{air} = \varepsilon_0/d_{air}$ and $c_{SiO_2} = \varepsilon_0\varepsilon_r/d_{SiO_2}$, one gets

$$V_g^2 = \frac{2}{\varepsilon_0}\left(\frac{8T_0}{L^2}\,\xi_{max} + \frac{64Et}{3(1-\nu^2)L^4}\,\xi_{max}^3\right)\left(d_{air} + \frac{d_{SiO_2}}{\varepsilon_r}\right)^2. \tag{7.18}$$

Case 2: P_{el} is calculated via $P_{el}(\xi_{max}) = c(\xi_{max})^2 V_g^2/(2\varepsilon_0)$ where the capacitance c depends directly and only on ξ_{max} and is considered as constant over the sheet. This "lift"-model does not take into account the parabolic profile (see figure 7.7b). The distance between the membrane and the bottom is reduced by ξ_{max}, so that we get nearly the same expression as in case 1:

$$V_g^2 = \frac{2}{\varepsilon_0}\left(\frac{8T_0}{L^2}\,\xi_{max} + \frac{64Et}{3(1-\nu^2)L^4}\,\xi_{max}^3\right)\left(d_{air} - \xi_{max} + \frac{d_{SiO_2}}{\varepsilon_r}\right)^2. \tag{7.19}$$

Case 3: P_{el} takes into account the parabolic shape of the membrane and is the sum of every element $P_{el}(\xi(x))\mathrm{d}x$ contributing to the overall pressure (see figure 7.7c). Thus it is

$$P_{el}(\xi_{max}) = \frac{1}{2\varepsilon_0}\int_{-L/2}^{+L/2} c^2\left(\xi(x)\right) V_g^2\,\frac{\mathrm{d}x}{L}, \tag{7.20}$$

where $c(\xi(x)) = (c_{air}^{-1}(\xi_(x)) + c_{SiO_2}^{-1})^{-1}$ and $c_{air} = \varepsilon_0/(d_{air} - \xi(x))$ with the parabolic shape of the membrane: $\xi(x) = 4\xi_{max}((L/2)^2 - x^2)/L^2$.

The integral writes as

$$P_{el}(\xi_{max}) = A\int_{-L/2}^{+L/2} \frac{1}{(B + Cx^2)^2}\,\frac{\mathrm{d}x}{L}, \tag{7.21}$$

with

$$\begin{aligned} A &= \frac{V_{\mathsf{g}}^2 c_{\mathsf{SiO_2}}^2}{2\varepsilon_0} \\ B &= 1 + \frac{c_{\mathsf{SiO_2}}}{\varepsilon_0}\left(d_{\mathsf{air}} - \xi_{\mathsf{max}}\right) \\ C &= \frac{4 c_{\mathsf{SiO_2}} \xi_{\mathsf{max}}}{\varepsilon_0 L^2}. \end{aligned} \tag{7.22}$$

The primitive integral involves the point symmetric arc tangent function:

$$P_{\mathsf{el}}(\xi_{\mathsf{max}}) = \frac{A}{2L}\left[\frac{\arctan\left(\frac{\sqrt{C}x}{\sqrt{B}}\right)}{\sqrt{B^3 C}} + \frac{x}{B^2 + BCx^2}\right]_{-L/2}^{+L/2} \tag{7.23}$$

and finally gives the relationship between V_{g} and ξ_{max} (with B defined in (7.22)):

$$V_{\mathsf{g}}^2 = \frac{\frac{4\varepsilon_0}{c_{\mathsf{SiO_2}}^2}\left(\frac{8T_0}{L^2}\ \xi_{\mathsf{max}} + \frac{64Et}{3(1-\nu^2)L^4}\ \xi_{\mathsf{max}}^3\right)}{\sqrt{\frac{\varepsilon_0}{B^3 c_{\mathsf{SiO_2}} \xi_{\mathsf{max}}}}\ \arctan\left(\sqrt{\frac{c_{\mathsf{SiO_2}} \xi_{\mathsf{max}}}{\varepsilon_0 B}}\right) + \frac{1}{B^2 + \frac{c_{\mathsf{SiO_2}} \xi_{\mathsf{max}}}{\varepsilon_0} B}} \tag{7.24}$$

In the next section we will compare the three cases to our experimental data obtained on a gated suspended graphene device, as discussed in section 7.1.

7.2.3 Comparison of three models to determine the electrostatic pressure load

The exactitude of the determination of h_{max} is supported by the result of $(I_{\mathsf{2D}}/I_{\mathsf{G}})_{\mathsf{intr}}$ which is in very good agreement with the data obtained by analyzing the three graphene blisters (see section 6.2.2) and with recently published data [Froehlicher15a].

As already pointed out, the exact determination of h_{max} near $V_{\mathsf{g}} = 0$, *i.e.* the values of h near a minimum value of the enhancement factors is not possible and affected by large error bars in figure 7.5. Nevertheless, an upper bound for h_{max} can be estimated, since the evolution of I_{G} and I_{2D} is monotonic and does not exceed the local minimum (see also figure 7.3). For I_{G}, this bound is 246 nm whereas it is 240 nm for I_{2D}. In particular, knowing that d_{air} is 288 nm, this estimation implies that the graphene membrane is either initially deflected by ≈ 40 nm or that it is partially sticked to the edges of the trench, as it has been observed by AFM measurements on graphene blisters [Bunch08, Wang15]. Also, the ratio $I_{\mathsf{2D}}/I_{\mathsf{G}}$ confirms that $h_{\mathsf{max}}(V_{\mathsf{g}} = 0)$ is smaller than d_{air}, otherwise the ratio would start to decrease when V_{g} approaches 0.

In the following analysis, the deflection at the center of the membrane ξ_{max} is taken as the deflection with respect to its initial position at $V_{\text{g}} = 0$, *i.e.* $\xi_{\text{max}} = 246\,\text{nm} - h_{\text{max}}$ and $\xi_{\text{max}} = 240\,\text{nm} - h_{\text{max}}$ for the data extracted from I_{G} and I_{2D}, respectively.

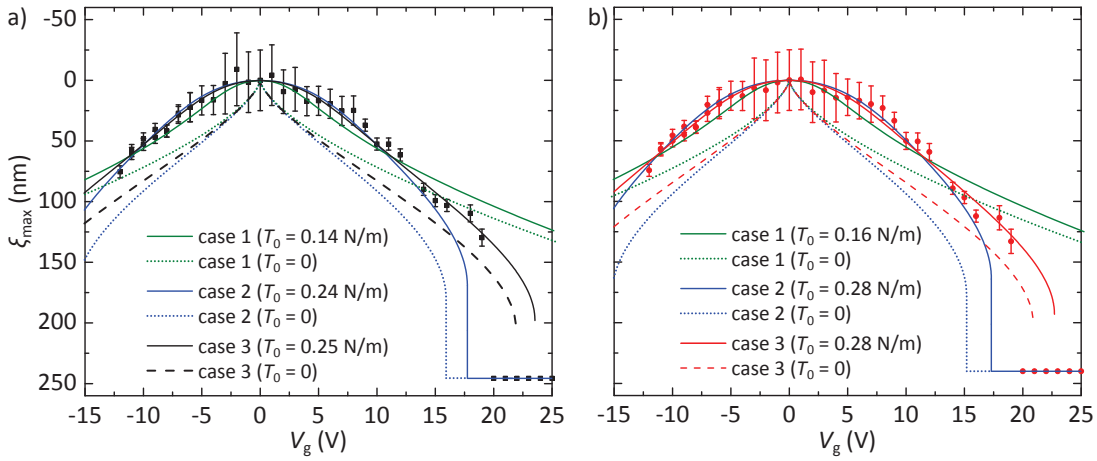

Figure 7.8: a) ξ_{max} as a function of V_{g}, extracted from I_{G} (black squares). The green, blue and black solid lines are fits to the data based on the models 1, 2 and 3 (equations (7.18), (7.19) and (7.24)*), respectively, leaving T_0 as free fitting parameter. The dotted and dashed lines correspond to the respective equations by fixing $T_0 = 0$. **b)** The same data as in (a), extracted from I_{2D} (red circles).

* Equation (7.19) can be solved with respect to ξ_{max} (polynomial of order 5). The real solution gives a collapse (constant ξ_{max} for increasing V_{g}, blue lines). However, equation (7.24) cannot be solved with respect to ξ_{max}. Thus, V_{g} is calculated from ξ_{max}. The result gives the black (red) curve which also predicts a decreasing V_{g} as ξ_{max} increases, when ξ_{max} exceeds the critical value of collapse. This part of the solution is not shown since it does not correspond to a physical solution.

Figure 7.8a and b show ξ_{max}, extracted from I_{G} and I_{2D}, respectively, as a function of V_{g}. Green, blue and black solid lines, which are fits to the data based on the models 1, 2 and 3 (equations (7.18), (7.19) and (7.24)), respectively, are added to the graph. Here, T_0 is used as a free fitting parameter.

The three models fit well the data up to an absolute value of $V_{\text{g}} = 12\,\text{V}$. For higher V_{g}, the discrepancy between the models becomes larger. In particular, case 1 (green straight line) is condemned to follow a smooth line without asymptote because the model includes a constant distance between the bottom of the trench and the graphene membrane. Thus, this model might fit the experimental data for small deflections, but is not valid for the case of large deflections in the vicinity of the breakdown. The data fit best for a value of $T_0 = 0.14\,\text{N/m}$.

We now consider the fit of model 2 (blue straight line), which, however, predicts a collapse of the membrane at $17.7\,\text{V}$, slightly below the actual measured value between 19 and $20\,\text{V}$. Model 3 then presumes a collapse at a higher voltage, *i.e.* $23.5\,\text{V}$. The obtained values for T_0 are 0.24 and $0.25\,\text{N/m}$, respectively.

The value of built-in strain T_0 seems to be particularly governed by the characteristics of the experimental data around $V_g = 0$. For $T_0 = 0$, no matter which model is employed, a direct change in the deflection is predicted. However, the deflection is retarded because the intrinsic strength of the strained graphene has to be overcome. The strain is indeed tensile, as T_0 is positive. In order to express T_0 in terms of the relative elongation with respect to unstrained graphene, we translate T_0 into ϵ using equation (7.11) and find for models 2 and 3:

$$\epsilon = \frac{T_0\,(1-\nu^2)}{Et} = \frac{0.25\,\mathrm{N/m}\,(1-0.16^2)}{351.75\,\mathrm{N/m}} \approx 0.07\,\%. \tag{7.25}$$

Interestingly, this value of ϵ is in strikingly good agreement with the built-in strain estimated by interpreting the Raman maps at room temperature, where a value of (0.06 ± 0.01) % has been found. The fact that we are able to estimate the built-in strain with a technique which does not involve the frequencies of the Raman G and 2D modes further validates the correctness of the vector decomposition model. In addition, the reference point (ω_G^0, ω_{2D}^0) might be different at 4 K, which would complicate a proper analysis.

However, it is not straightforward that the built-in strain at 4 K is the same as at room temperature, since the thermal expansion coefficients (TECs) play an important role for such a large temperature range [Bonini07]. If the TECs of graphene and Si or rather SiO_2 are different, this TEC mismatch would induce supplementary strain in the membrane.

Recent experimental investigations about the TEC of graphene even agree with an unusual negative TEC [Bao09, Chen09a, Singh10, Yoon11a] related to out-of-plane vibrational modes in the two dimensional graphene [Suleimanov93]. This negative TEC is $\approx -6 \times 10^{-6}\,\mathrm{K}^{-1}$. In contrast, the TEC of SiO_2 is positive and in the order of $0.6 \times 10^{-6}\,\mathrm{K}^{-1}$ [Reed91]. Hence, a rough estimate gives an additional tensile strain of 0.2 % when going from room temperature to 4 K. However, we do not observe any change in strain. This might be due to local displacements of the graphene flake, since the flake is not directly clamped at the borders of the trench. Furthermore, the subtle interplay between the substrate, the flake, the Ti/Au contacts and the neighboring 2LG and 4LG might play a role.

In conclusion, model 2 overestimates the electrostatic pressure, because this model assumes that the distance between the bottom of the trench and the membrane is ξ_{max} everywhere. The actual deflection is better described by model 3. It assumes an effective electrostatic pressure obtained by taking into account the parabolic profile of the membrane. Nevertheless, the collapse occurs at lower V_g as predicted. We point out that in the vicinity of collapse, the system is in a critical unstable state where only small perturbations can bring the membrane to break down. In particular, within the model, the membrane is considered as clamped at the borders, but in our device, the lateral distances to the nearest clamping contacts are 5 and $20\,\mu$m (see optical

micrograph in figure 7.2a). *I.e.* a large area is uncovered and might locally slip when the membrane is pulled downwards in the trench.

Based on these considerations, we will use model 3 in order to be able to predict at which V_g the membrane collapses for different device geometries. In other words, depending on the oxide thickness and the depth of the trench, the critical maximal deflection can be modeled. In addition, the gate induced charge carrier density can be evaluated.

7.3 Theory near collapse

Motivated by the results in the previous section, we generalize the application of model 3 to substrates with different d_{SiO_2} and varying air thickness d_{air}. In particular, we come back to the notation introduced in section 3.5 for the calculation of the Raman enhancement factors, where the multilayered system [Si - SiO_2 ($d_{SiO_2} = 285\,\text{nm} - d_{air}$) - vacuum ($d_{air} < 285\,\text{nm}$) - graphene] is called system 2 and [Si - SiO_2 ($d_{SiO_2} = 500\,\text{nm} - d_{air}$) - vacuum ($d_{air} < 500\,\text{nm}$) - graphene] is called system 3. For both systems we will first sketch the dependence of the deflection on the percentage of d_{air} in the initial oxide thickness and on the the applied backgate voltage. Second, the critical values $V_{g,crit}$ and $\xi_{max,crit}$ in the vicinity of collapse are evaluated. Furthermore we will set out in more detail the effect of the backgate voltage and the deflection on the charge carrier density.

For the subsequent analysis, the following assumptions hold:

- The graphene membrane is clamped to the substrate at the borders of the trench.
- The initial deflection of the membrane is zero.
- The profile of the membrane is parabolic with applied backgate voltage.
- Model 3 describes best the reality.
- If not stated differently, the built-in strain is neglected ($T_0 = 0$).

7.3.1 Maximal deflection and its critical value

In figure 7.9a we present a color plot of the maximal deflection at the center of the membrane, ξ_{max}, as a function of the percentage of d_{air} in the initial oxide thickness of $500\,\text{nm}$. The trench width here is $5\,\mu$m. The corresponding gate voltage V_g, which is necessary to reach ξ_{max}, is color-coded. This color plot has been calculated by means of a homemade Matlab program and is based on equation (7.24).

As an example, we take the case of $d_{air}/500\,\text{nm} = 75\,\%$, *i.e.* $d_{SiO_2} = 125\,\text{nm}$ and $d_{air} = 375\,\text{nm}$. ξ_{max} increases with increasing V_g (regime 2 in figure 7.9a). When V_g reaches the critical

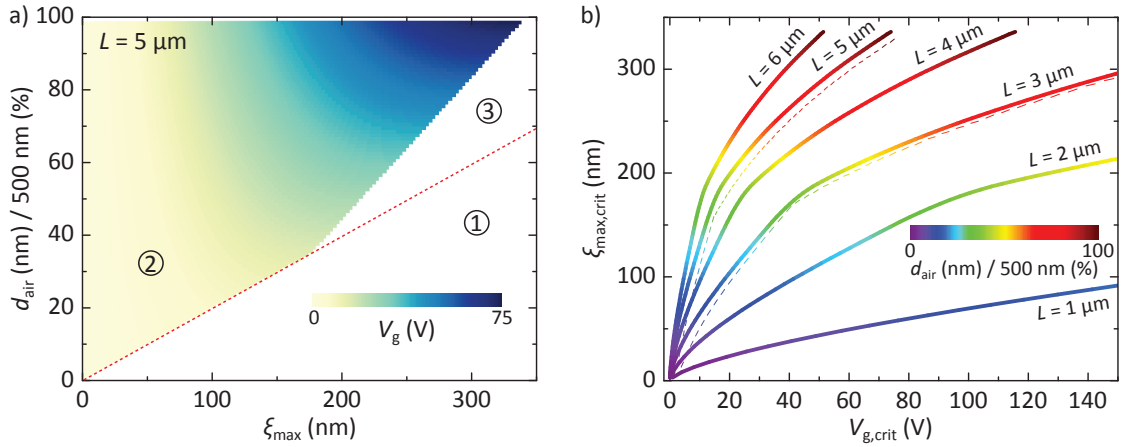

Figure 7.9: a) Modeling of the gate induced deflection ξ_{max} at the center of a $5\,\mu$m large trench, as a function of the percentage of d_{air} in the initial oxide thickness of 500 nm. The color bar indicates the gate voltage which is necessary to reach a certain deflection. The color plot is devided in three regions (see main text for detailed discussion). $T_0 = 0$. **b)** Critical maximal deflection as a function of the corresponding critical gate voltage, in the vicinity of collapse. The data are extracted from color plots as in (a) by going along the border of region 2 with region 1 and 3. The critical (straight) lines are shown for different trench widths L. The color code indicates the corresponding percentage of d_{air} in 500 nm oxide. For $L = 3$ and $5\,\mu$m, the critical (dashed) lines are added for $T_0 = 0.3$ N/m in order to estimate the impact of typical built-in strain.

value $V_{\text{crit}} = 45$ V, the corresponding deflection is $\xi_{\text{max,crit}} = 275$ nm. Going beyond 45 V leads to the collapse of the membrane. In particular, this collapse is abrupt and the membrane undergoes a sudden displacement of 100 nm. This displacement can directly be read by horizontally connecting $\xi_{\text{max,crit}}$ to the red dashed line in figure 7.9a.

This regime 3, corresponding to an abrupt collapse of the membrane, is not predicted for $d_{\text{air}}/500\,\text{nm} < 36\,\%$. On the contrary, the deposition of the membrane on the bottom of the trench is smooth. In particular, only low gate voltages (below 10 V) are necessary to make the membrane reach the bottom. Note that, of course, region 1 is never reached because it corresponds to the non-physical penetration of the membrane in the oxide[3].

An interesting question is now, which voltage does a device support until the membrane collapses. In figure 7.9b we figure out that the width of the trench L is in important parameter. The critical lines for different L are extracted from color maps as shown in figure 7.9a by going along the border of region 2 with region 1 and 3. Thus the lines correspond to the critical maximal deflection, $\xi_{\text{max,crit}}$, as a function of the corresponding critical gate voltage, $V_{\text{g,crit}}$, in the vicinity of

[3]We note that equation (7.24) cannot be solved with respect to ξ_{max}. Hence, in figure 7.9a we present the solution with respect to V_{g}. This solution gives in principle an analytical value for region 2. But since these values would correspond to a decrease of ξ_{max} with increasing V_{g}, which is not physical, we have whitened region 2. In particular, we further justify this step by the fact that a real solution of model 2 with respect to ξ_{max} can be found, because equation (7.19) is a pure polynomial of 5$^{\text{th}}$ order. In that case, the dependence of ξ_{max} on V_{g} is characterized by an asymptote, *i.e.* V_{g} is constant for increasing ξ_{max}, which is, in experiments, a collapse.

collapse. The rainbow color code indicates the corresponding percentage of d_{air} in 500 nm oxide. In order to estimate the impact of typical tensile built-in strain (see chapter 5), the critical (dashed) lines for $L = 3$ and $5\,\mu$m are added for $T_0 = 0.3$ N/m ($\epsilon \approx 0.08$ %). A built-in strain slightly shifts the curves to higher $V_{\text{g,crit}}$.

For completeness, we also give the theoretical results for a substrate of 285 nm (system 2) and 90 nm (see figures 7.10a and b). The reader should be aware of the assumptions made above, because in real experiments, the graphene membrane is either initially bent or not directly clamped at the borders. Also, the temperature might influence the critical state near collapse because of different TECs. But we think that our results can serve as a guideline for gated graphene membranes.

It is difficult to obtain data from literature, because, as stated above, the collapse of the device is often considered as an unintentional side effect when transport properties are examined. However, Bolotin *et al.* give a value of $V_{\text{g,crit}} = 20$ V for $d_{\text{air}} = 150$ nm, $d_{\text{SiO}_2} = 150$ nm and $L \approx 3\,\mu$m, and thus limited their measurement range to ± 5 V [Bolotin08b]. For these parameters our model predicts $V_{\text{g,crit}} = 18.3$ V (data not shown, only calculated), which is in excellent agreement. Berciaud *et al.* performed backgate measurements on suspended graphene for a trench of $L \approx 4\,\mu$m, etched in 285 nm oxide [Berciaud13]. The authors only estimate d_{SiO_2} to 130 nm by using the RIE etching rate, which is not a reliable enough information for a correct trench depth. Indeed, if one calculates with $d_{\text{SiO}_2} = 130$ nm and $d_{\text{air}} \approx 155$ nm, a value of $V_{\text{g,crit}} = 7.8$ V is predicted, which is significantly lower than the values of up to 20 V applied by the authors. This discrepancy might further be explained by the fact that the borders of their trenches are not straight but corrugated due to the fabrication process, which would locally lead to a smaller width and, consequently, to a higher $V_{\text{g,crit}}$.

7.3.2 Charge density and its maximal value

Now, we know the dependence of the maximal deflection ξ_{max} on the gate voltage, and we can extract the corresponding value of the charge carrier density in the middle of the trench, denoted n_{max}. The charges are inhomogeneously distributed on the membrane and we consider that there is no back coupling mechanism of the charges on the profile, which is a first approximation. One can write

$$n_{\text{max}} = c(\xi_{\text{max}})V_{\text{g}}(\xi_{\text{max}}) = \frac{\varepsilon_0\varepsilon_{\text{r}}V_{\text{g}}(\xi_{\text{max}})}{\varepsilon_{\text{r}}(d_{\text{air}} - \xi_{\text{max}}) + d_{\text{SiO}_2}}. \tag{7.26}$$

Note that, in general, n varies strongly along the trench width because of the parabolic shape of the membrane. Here, we consider the point of the membrane which is the nearest to the bottom and thus is severely sensed by the backgate, *i.e.* n_{max} is indeed the maximum value of n and drops when one approaches the borders of the trench.

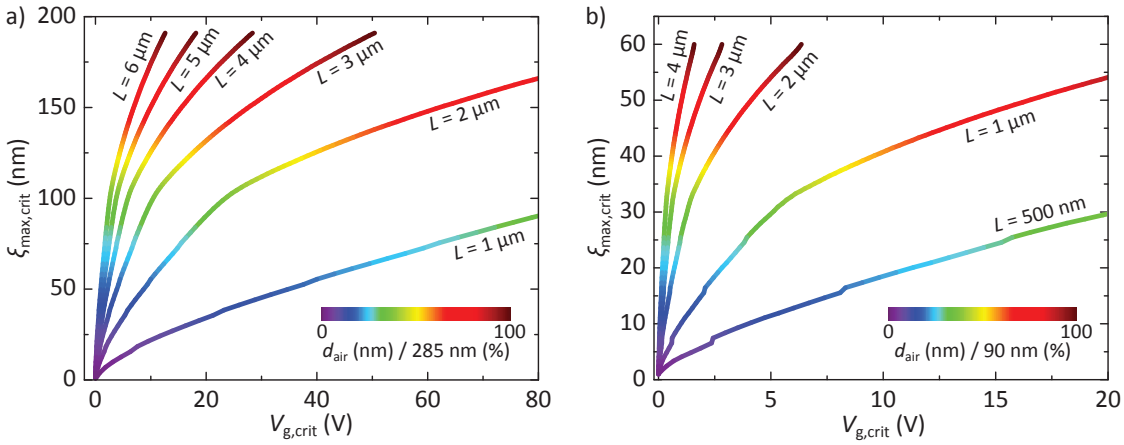

Figure 7.10: a) Critical maximal deflection as a function of the corresponding critical gate voltage, for an oxide thickness of 285 nm. The critical (color coded) lines, indicating the percentage of d_{air} in 285 nm oxide, are shown for different trench widths L. **b)** The same data for an oxide thickness of 90 nm. The data are plotted for smaller L since a low aspect ratio is difficult to achieve, experimentally.

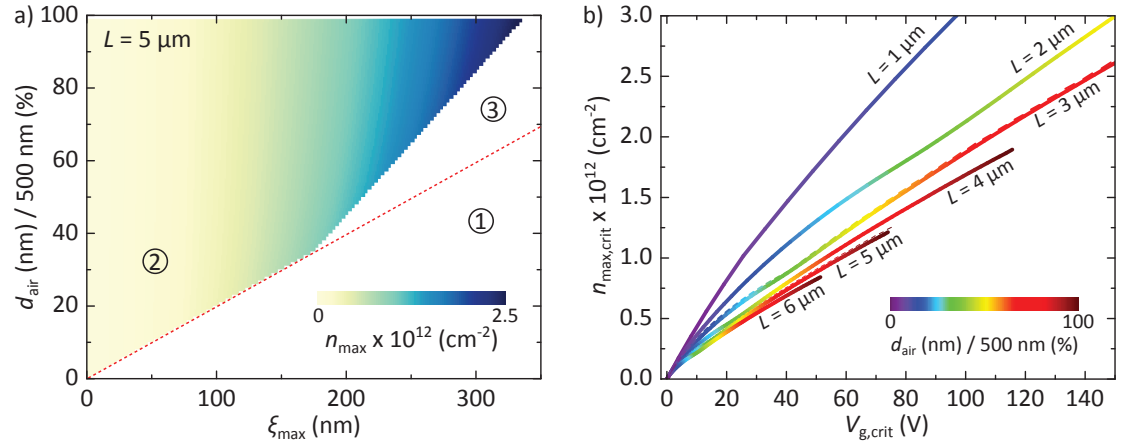

Figure 7.11: a) Modeling of the gate induced deflection ξ_{max} at the center of a $5\,\mu$m large trench, as a function of the percentage of d_{air} in the initial oxide thickness of 500 nm. The color bar indicates the charge carrier density n_{max} at the center of the trench. The corresponding backgate voltage is plotted in figure 7.9a. Region 3, corresponding to a sticked membrane, is left whitened to highlight the features of the suspended membrane. $T_0 = 0$. **b)** Critical maximal charge carrier density as a function of the corresponding critical gate voltage, in the vicinity of collapse. The data are extracted from color plots as in (a) by going along the border of region 2 with region 1 and 3. The critical (straight) lines are shown for different trench widths L. The color code indicates the corresponding percentage of d_{air} in 500 nm oxide. As in figure 7.9b, the critical (dashed) lines are added for $T_0 = 0.3$ N/m in order to estimate the impact of typical built-in strain ($L = 3$ and $5\,\mu$m).

In figure 7.11a, we show a color plot similar to that in the previous section, this time showing n_{max} as color code (for $L = 5\,\mu$m). Even if in region 3 a physical value can be given for the charge density (equation (7.26) becomes just $n_{\text{max}} = \varepsilon_0\varepsilon_r V_g/d_{SiO_2}$ without any dependence on ξ_{max} because the membrane is attached to the bottom), we do not plot the corresponding data in order to highlight the features of the suspended membrane. The gating would be more efficient because the air (or vacuum) layer with its relatively low permittivity is absent, leading to high values of n.

Reconsidering the exemplary case of $d_{\text{air}}/500\,\text{nm} = 75\,\%$, we see that n_{max} reaches a value of $\approx 1.9 \times 10^{12}\,\text{cm}^{-2}$ for $V_g = 45\,\text{V}$.

To get further insight in the values of charge densities which might be obtained in suspended graphene membranes, we go again along the critical line near the collapse and plot the corresponding data, $n_{\text{max,crit}}$ *vs.* V_{crit}, for different L. In the case of a large trench ($L = 5$ and $6\,\mu$m) the reachable values are around $10^{12}\,\text{cm}^{-2}$ in the case of all oxide taken away. For typical devices with $d_{\text{air}}/500\,\text{nm} = 50\,\%$, n_{max} does not exceed $\approx 1.5 \times 10^{12}\,\text{cm}^{-2}$. The narrower the trench is, the larger values n_{max} can reach because V_{crit} is pushed to very high values. Nevertheless, for very narrow trenches ($L = 2$ and $1\,\mu$m), the gating gets less efficient because the distance between the membrane and the bottom does not change much. Hence, the large thickness of the medium with a relatively low permittivity governs the gating and avoids large values of n.

We note that a typical built-in strain of $T_0 = 0.3\,\text{N/m}$ has a negligible impact of the charge carrier density (see dashed lines for $L = 3$ and $5\,\mu$m).

For completeness, we show the critical lines for substrates of 285 and $90\,\text{nm}$ oxide thickness in figures 7.12a and b respectively.

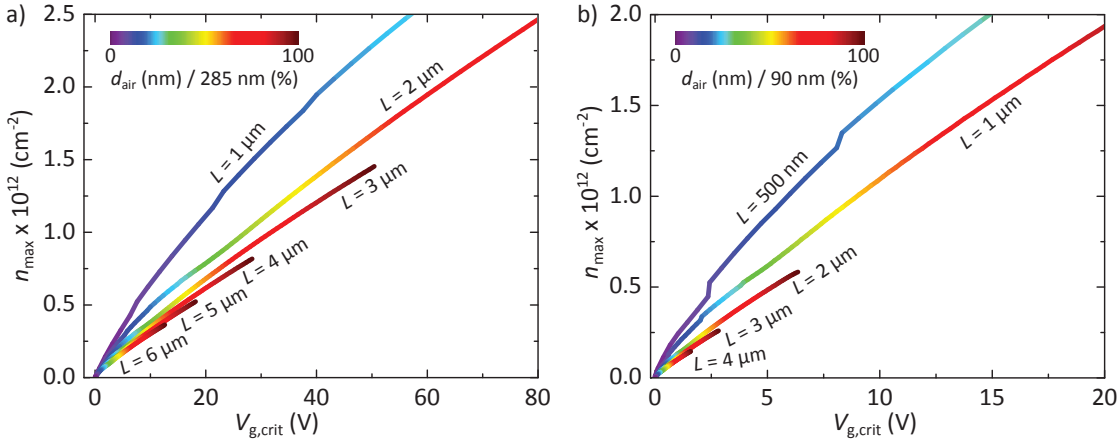

Figure 7.12: a) Critical charge carrier density as a function of the corresponding critical gate voltage, for $d_{SiO_2} = 285\,\text{nm}$. The critical lines, indicating the percentage of d_{air} in $285\,\text{nm}$ oxide by means of a color code, are shown for different trench widths L. **b)** The same data for $d_{SiO_2} = 90\,\text{nm}$. The kinks are artefacts due to the resolution of the color plots and the subsequent extraction of the critical lines.

Now we know which magnitude of charge carrier densities we might expect in suspended graphene devices. Hence, we can focus on the gate induced frequency shifts of the Raman G and 2D modes observed on the device introduced in section 7.1. The aim is to examine these frequency shifts with respect to both the charge carrier density and strain induced due to the strong deflection.

7.4 Analysis of phonon-softening

As mentioned above (see section 7.1), the suspended graphene device we present in this chapter showed the signatures of a low doping level at room temperature. In particular, the fwhm of the G mode ($\Gamma_\mathsf{G} \approx 16\,\mathrm{cm}^{-1}$) and the correlation of ω_2D and ω_G suggest that the charge carrier density is less than $3 \times 10^{11}\,\mathrm{cm}^{-2}$. We expect that cooling down the device does not have any influence on the doping level, on the contrary, the charge inhomogeneity has the tendency to decrease. Thus, our device builds an ideal platform to examine the introduction of additional charge carriers in the graphene and its consequence on the phonon modes.

In the following, we could represent our data in terms of the Fermi energy E_F. This representation would be more pleasant for the reader because E_F is proportional to $\sqrt{|n|}$ which would stretch the data in the regime of low doping. However, the conversion from n to E_F involves the Fermi velocity ν_F according to $E_\mathsf{F} = \mathrm{sgn}(n)\hbar\nu_\mathsf{F}\sqrt{\pi|n|}$. For graphene on SiO_2, where n is generally several $10^{12}\,\mathrm{cm}^{-2}$, ν_F has been measured to $1.1 \pm 0.10 \times 10^6$ m/s by a variety of techniques including the early transport experiments [Novoselov05a, Zhang05]. In contrast to standard metals, where Landau's Fermi-liquid theory holds, it turns out that in graphene near the neutrality point, the Fermi velocity diverges due to a vanishing charge carrier density [Elias11, Hwang12, Siegel13, Faugeras15]. The charge carriers cannot considered as a 2d electron gas anymore, and many body effects come into play [Mak14, Faugeras15]. Thus, in suspended graphene devices, where n can be finely tuned, several studies report about an logarithmic increase of the Fermi velocity when n is getting smaller than several $10^{11}\,\mathrm{cm}^{-2}$ [Elias11, Faugeras15].

By means of Raman spectroscopy, the accurate determination of n near the Dirac point is challenging because one has to account for the phonon renormalization, and the spatial resolution is limited to $\approx 1\,\mu\mathrm{m}^2$ (see figure A.1 in the Appendix). Hence, one can give only an upper limit of n (see also chapter 5). Since the effect of n on ν_F seems to be important below this upper limit[4] and we do not want to introduce artefacts of a conversion we are not sure of, we do not convert n into E_F.

The deflection at the center, which has been determined by means of the analysis of the Raman mode intensities, can be easily used to calculate the corresponding charge carrier density. To do so, we take equation (7.26) and plot the result in figure 7.13a. The hole and electron den-

[4] Elias *et al.* found $\nu_\mathsf{F} \geq 2.5 \times 10^6$ m/s at $n < 10^{10}\,\mathrm{cm}^{-2}$ and $\nu_\mathsf{F} \leq 1.5 \times 10^6$ for $n > 2 \times 10^{11}\,\mathrm{cm}^{-2}$.

sities are plotted as positive and negative n, respectively. With this calculation involving only the corresponding oxide and the air thickness for each gate voltage, a maximal hole density of 6.2×10^{11} cm^{-2} is reached for $V_g = +19$ V.

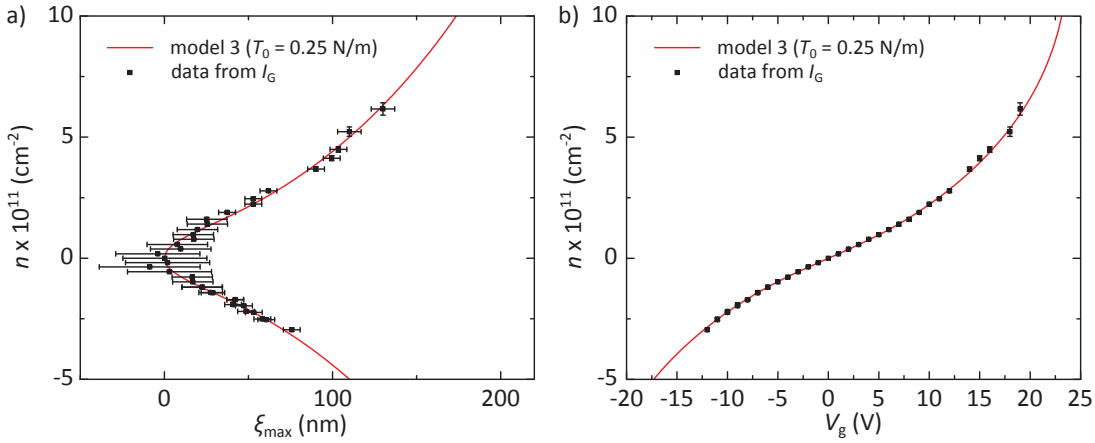

Figure 7.13: a) Charge carrier density n *vs.* maximal deflection at the center of the trench, ξ_{max}. The data set (black squares) is obtained by taking the deflection deduced from the Raman G mode intensity and by calculating n with the equation (7.26) for the corresponding gate voltage. Model 3, which fitted best the data in figure 7.8 for a built-in strain of $T_0 = 0.25$ N/m, is added (red line). Note that we suppose here that $n = 0$ at $V_g = 0$, which is a reasonable approximation because the charge carrier density at $V_g = 0$ is certainly $< 1 \times 10^{11}$ cm^{-2}. **b)** Charge carrier density n *vs.* applied gate voltage V_g for the same data (black squares) and model 3 (red line).

In figure 7.13a as well as in figure 7.13b, where n is plotted *vs.* V_g, we have added model 3 (red lines) with the value of $T_0 = 0.25$ N/m which best fitted the data in figure 7.8. The data nestle well against the model. This is a direct consequence of the good fit in figure 7.8 because both the data and the model are recalculated using the same equation (equation (7.26)) in order to obtain n.

These plots suggest that the charge carrier density covers roughly a range from -3×10^{11} cm^{-2} to $+6 \times 10^{11}$ cm^{-2}, starting from electron doping and ending with hole doping. These values correspond to Fermi energies of approximately -70 meV and $+100$ meV (using a Fermi velocity of 1.1×10^6 m/s). In theory, this range is sufficient to observe the phonon renormalization of the G mode at 4 K [Lazzeri06]. In particular, the packed distribution of ω_G and ω_{2D} as well as the large Γ_G indicates a low doping level and, notably, a low charge inhomogeneity. Thus, we now consider the gate induced frequency shifts of the Raman G and 2D mode.

In figure 7.14a and b, we plot the Raman shifts of the G and 2D modes as a function of V_g. Both the G and 2D mode soften with increasing absolute value of V_g. The data has been fitted with a parabolic profile in order to extract the initial values of the Raman frequencies at 4 K and $V_g = 0$. These values are 1582.6 cm^{-1} and 2669.4 cm^{-1} for the G and 2D mode, respectively. The

observed downshifts are symmetric with respect to $V_g = 0$ and reach values of $\Delta\omega_G = -5\,\text{cm}^{-1}$ and $\Delta\omega_{2D} = -11\,\text{cm}^{-1}$ at $V_g = +19$ V.

Prima facie, the ratio of these shift rates suggests that they are principally strain induced, because $\Delta\omega_{2D}/\Delta\omega_G = -11\,\text{cm}^{-1}/-5\,\text{cm}^{-1} = 2.2$. This shift rate has been confirmed to appear under biaxial and/or low level uniaxial strain (see chapters 5 and 6). The strain is a direct consequence of the electrostatic pressure acting on the membrane. Thus, the strain induced Raman shifts compete with an eventual charge carrier induced phonon softening or hardening.

We will now analyze if we are able to deconvolute these two contributions to the Raman shift on our sample.

In figure 7.14c we plot $\Delta\omega_G$ (with respect to the value of $1582.6\,\text{cm}^{-1}$ at $V_g = 0$, extracted from figure 7.14a) as a function of n. One might compare to the theoretical model taking into account the adiabatic and non-adiabatic contribution of the G mode phonon renormalization (see chapter 3), which we have plotted in figure 7.14d, for a temperature of 4 K and different values of charge inhomogeneities. These charge inhomogeneities correspond to fluctuations of the Fermi energy of 0, 10, 20 meV *etc.*, and are here expressed in terms of the charge carrier density, where we have used a value of[5] $v_F = 1.05 \times 10^6$ m/s. However, if one considers only the change in the G mode frequency and compares the data in figures 7.14c and d, the interpretation of the data as a charge carrier induced Raman shift seems likely, but is misleading. Indeed, in chapters 5 and 6 we have stressed the importance of considering the correlation of ω_G and ω_{2D} in order to identify the underlying mechanism which is responsible for the change in the Raman frequencies. For this reason, we show this correlation in figure 7.14e, where the first indication of strain induced Raman shifts is further confirmed, because the data points align on a slope of $\partial\omega_{2D}/\partial\omega_G = 2.2$.

What is the origin of these at first sight pure strain induced Raman shifts, since we expect a significant doping induced change at 4 K when the charge carrier densities are in the range of $6 \times 10^{11}\,\text{cm}^{-1}$? Several observations indicate that a non-negligible charge carrier density inhomogeneity is probed within our measurements.

First, in view of the theoretical prediction plotted in figure 7.14d, a charge inhomogeneity of roughly $1 \times 10^{11}\,\text{cm}^{-2}$ is in agreement with a smeared out phonon renormalization, *i.e.* only a very small change in ω_G with n.

Second, the fwhm of the G mode, Γ_G, shows a tendency to decrease slightly with increasing n. To illustrate this effect, we plot in figure 7.14f $\Delta\Gamma_G = \Gamma_G^0 - \Gamma_G$, where $\Gamma_G^0 = 13\,\text{cm}^{-1}$ is the value measured at $V_g = 0$. The theoretical prediction of the evolution of $\Delta\Gamma_G$ is added for different charge inhomogeneities. The slight decrease of Γ_G is in accordance with charge inhomogeneities in the same range as estimated previously, *i.e.* around $1 \times 10^{11}\,\text{cm}^{-2}$. In particular, the decrease is

[5] The choice of this value is justified because we will argue in the following that our sample suffers from a gate and deflection induced non-negligible charge inhomogeneity. Thus, the range of charge inhomogeneity is considerably higher than the one where a divergence of the Fermi velocity is observed [Elias11].

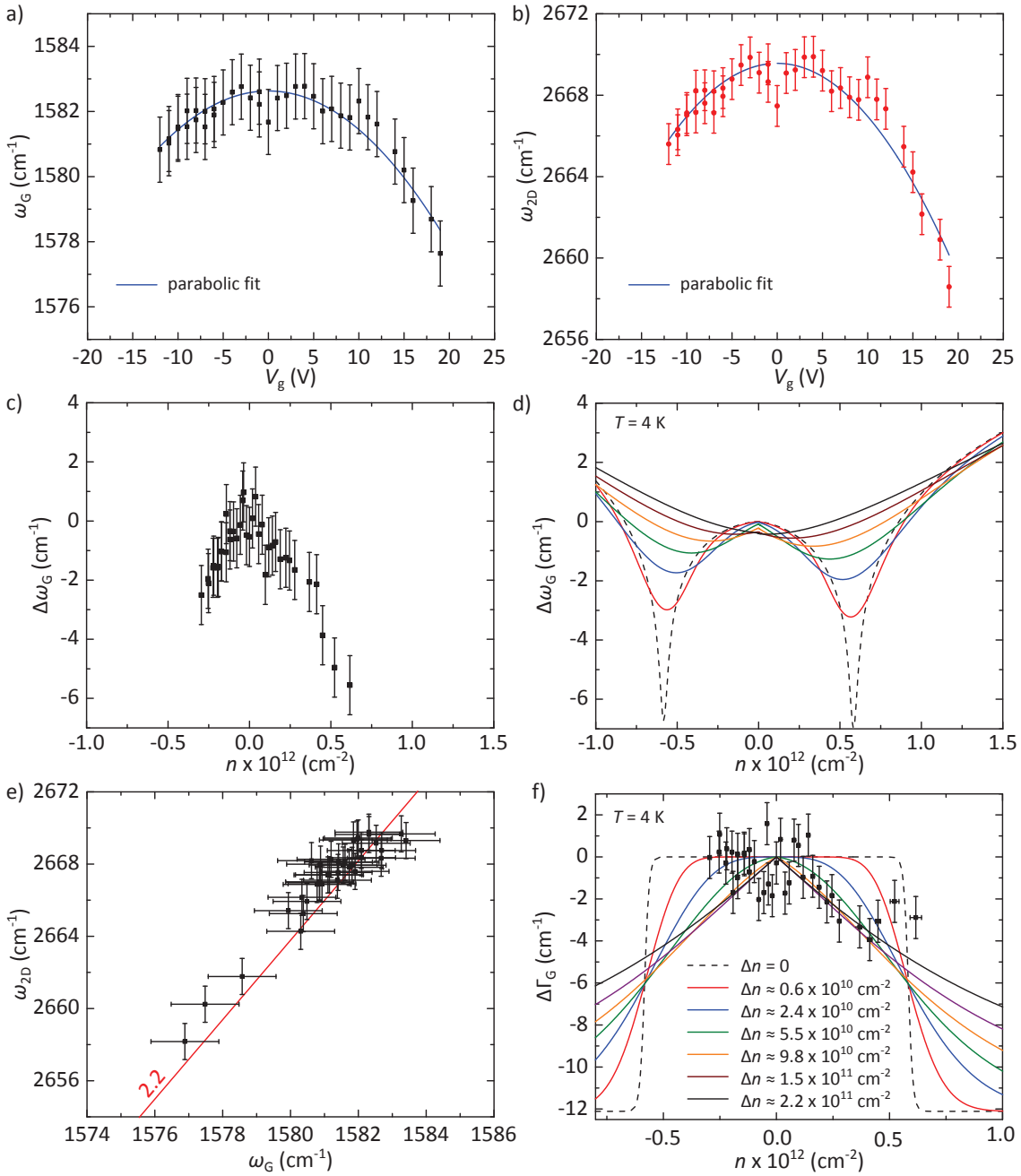

Figure 7.14: a) Measured ω_G as a function of V_g and fitted with a parabola (blue line, symmetric with respect to $V_g = 0$). **b)** Same data as in (a), plotted for ω_{2D}. **c)** Raman shift $\Delta\omega_G$ *vs.* n. $\Delta\omega_G$ is with respect to its initial value at $V_g = 0$, extracted from the parabolic fit in (a), *i.e.* $1582.6\,\text{cm}^{-1}$. n is calculated according to equation (7.26). **d)** Theoretical predictions [Lazzeri06] of the G mode Raman shift with varying n, at $T = 4\,\text{K}$, for different charge inhomogeneities, calculated for different Fermi energy fluctuations (0, 10, $20\,\text{meV}$ *etc.*) and expressed in terms of Δn using a Fermi velocity of 1.05×10^6 m/s. **e)** Correlation of ω_G and ω_{2D}. The red line is $\omega_{2D} = 2.2\,(\omega_G - 1582.6) + 2669.4$. **f)** $\Delta\Gamma_G = \Gamma_G - \Gamma_G^0$ as a function of n, where Γ_G^0 is $13\,\text{cm}^{-1}$ for the experimental data, and taken in such a way that Γ_G^0 with the experimental Γ_G^0 for the theoretical calculations.

in disagreement with a well-defined homogeneous charge distribution, where one would expect a constant value (see black dashed line in figure 7.14f).

Finally, and this issue is rather intuitive, the higher V_g gets, the more the charge is inhomogeneously distributed over the membrane because ξ_{max} increases and consequently the curvature of $\xi(x)$. In figure 7.15, we show a sketch of the suspended membrane device at the limit of collapse, *i.e.* at $V_g = +19$ V. Supposing a parabolic shape of the membrane, we can calculate the corresponding charge carrier density in each point. The obtained values of n are shown in figure 7.15b (black line). The graph shows a variation of n in the range between 3×10^{11} and 6×10^{11} cm^{-2}. Here comes into play the spatial resolution of our Raman measurements, which is first of all limited by the size of the laser spot ($0.7\,\mu$m^2, see figure A.1 in the Appendix). This resolution is marked with a vertical light green stripe in figure 7.15b. With a stable laser beam and fixed sample, this resolution accounts for a charge inhomogeneity in the range of 0.2×10^{11} cm^{-2}. Additionally, slight thermal shifts have been observed during the acquisition of the Raman spectra. Thus, a larger spatial area has to be considered. We observed lateral drifts in the range of $1\,\mu$m in variable directions. Consequently, a larger distribution of charge densities is probed (see light blue vertical stripe in figure 7.15b). This effect might then translate into an effective charge inhomogeneity, which is indicated by a horizontal light blue stripe in figure 7.15b[6].

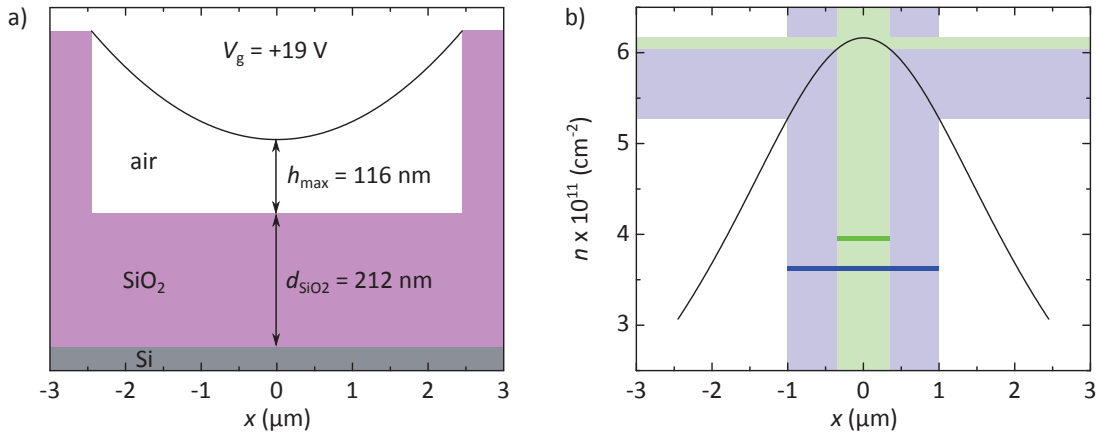

Figure 7.15: a) Schematic of the membrane profile at $V_g = +19$ V, approximated as parabolic. **b)** The corresponding charge carrier density for the parabolic profile in (a), calculated with a simple capacitor model. The laser spot size (green) and typical thermal drifts during the acquisition time (blue) are added, which leads to the probe of an effective charge inhomogeneity of $\approx 1 \times 10^{11}$ cm^{-2}.

We conclude that, even if our suspended graphene device forms initially an ideal platform for studies of the doping induced phonon renormalization, an unavoidable charge inhomogeneity is

[6]We note that n is proportional to V_g *and* to the distance of the capacitor. Thus, the back coupling mechanism can strongly enhance n very locally when V_g attains high values. In contrast, the height measurement does not follow this double proportionality and hence, the error in the height measurement is less affected by thermal drifts during the measurements.

introduced due to the device geometry. This charge inhomogeneity is estimated to 1×10^{11} cm^{-2} and smears out the expected phonon renormalization of the G mode, even at 4 K. Instead, we observe strain induced Raman shifts. These shifts follow a slope of $\partial\omega_{2D}/\partial\omega_G = 2.2$, a value which we have previously confirmed to stem from pure biaxial or slight uniaxial strain. Indeed, in view of the device geometry (see the optical image of the sample in figure 7.2), the induced strain is certainly a mixture of small biaxial and uniaxial strain. With the maximum shift of the G mode we observed with respect to its initial value at $V_G = 0$ (approximately 5 cm^{-1}), we estimate the maximal induced strain to 0.1 %, by using the Grüneisen parameter $\gamma_G = 1.8$.

7.5 Conclusion

As in the case of our study on graphene blisters in chapter 6, we have again proven the power of Raman spectroscopy for characterizing graphene samples. From a single Raman measurement series on a suspended graphene membrane as a function of the backgate voltage, one is able to extract *in situ* the electrostatically induced membrane deflection with the help of the interference modulated change of the Raman intensities. Furthermore, the analysis of the Raman frequencies gives an insight in the strain and charge carrier distribution. This issue is particularly interesting since suspended graphene is intrinsically undoped.

However, back coupling mechanisms between the gate induced deflection and the charge redistribution within the membrane strongly depend on the device geometry and hinder a clean observation of the theoretically predicted doping induced phonon renormalization. Notably, the convolution of the spatially inhomogeneous charge redistribution with the size of the laser spot and the magnitude of thermal drifts gives an average measurement afflicted with a charge inhomogeneity smearing out any intrinsic measurement, making this measurement run somehow equal to a gate measurement on supported graphene at room temperature.

Nonetheless, we have extracted important information about the mechanical response of the membrane, in particular we have compared our data to a model based on the theory of elasticity, which predicts a collapse of the device at high gate voltages. The observation of this irreversible collapse confirms the correctness of the model and led us to a detailed theoretical investigation of the regime of unstable deflections in the vicinity of the collapse, and that for different device geometries. This analysis is particularly interesting in view of transport measurement on suspended graphene, where the electrical conductivity is tuned via a backgate voltage. Our investigations give estimations about the maximal backgate voltage which can be applied to such devices before the membrane collapses. The regime of intermediate deflections, in turn, recently attracted the attention due to the possible precise distance control in order to finely tune distance dependent interactions on the nanoscale [Puller13, Cole15, Reserbat-Plantey15]. The keywords here are nano-positioning and graphene as a ruler on the nanoscale.

Finally, our theoretical investigations can serve as a guide for future suspended graphene device fabrication. Depending on the issue, *e.g.* strong charge carrier gradient, large deflections or flat graphene with low charge carrier gradient, the substrate, width and depth of the trenches can be adapted. Notably, our work opens the pathway for a device geometry allowing for lower charge inhomogeneities in order to be capable to cleanly resolve the doping induced phonon renormalization of the G mode.

Related publications

Paper:

- Dominik Metten, Guillaume Froehlicher and Stéphane Berciaud, *in preparation*.

Oral presentation:

- *In-situ probing of electrostatically induced deflection of suspended graphene by Raman scattering spectroscopy*, Annual meeting of the GDRI Graphene Nanotubes, 29th of November to 3rd of December 2015, Aussois (France)

8 Conclusion and perspectives

In this manuscript, we have thoroughly examined the mechanical response of monolayer graphene membranes to external pressure loads by purely optical means. The use of micro-Raman spectroscopy offers a deep insight in the studied material, because it is sensitive to the crystalline quality of the membrane, to the doping level and to strain, and it helps to unambiguously identify monolayer graphene.

In a first part, we have focused on a statistical evaluation of a bunch of suspended graphene samples by carefully analyzing the spatial distribution of the Raman G and 2D mode frequencies, both on the suspended and supported part of exfoliated graphene flakes. Since the Raman frequency shift rates upon doping and strain are different, we were able to estimate doping and, importantly, strain levels in suspended graphene devices. We have found that this pre-strain is strongly sample dependent and can achieve values of $0.1\,\%$. Additionally, the spatial strain-distribution within one membrane varies from sample to sample, in particular it can cover a range of $0.1\,\%$. The knowledge of the strain distribution down to a sub-micrometer resolution in such membrane devices is crucial for opto-mechanical applications. Notably, pre-strain influences the mechanical response when graphene membranes are subjected to a pressure load.

We have further found out that the doping level in suspended graphene does not exceed a few 10^{11} cm^{-2}, which is in contrast to doping levels in supported graphene, which is generally at least one order of magnitude higher. Thus, suspended graphene membranes form the ideal platform for fundamental studies, allowing for a clean probing of the physics in the vicinity of the Dirac point.

We took advantage of this kind of undoped samples in order to focus on the purely strain-induced Raman shifts. To do so, we considered graphene membranes exfoliated over micrometer-sized pits within a blister test configuration, which is feasible due to graphene's strong adhesion to the surrounding substrate and to its impermeability to standard gases [Bunch08, Koenig11]. We have recorded Raman spectra as a function of the applied air pressure load, which provides numerous information about the mechanical properties of graphene. By analyzing the observed changes in the Raman peak intensity, which is interference modulated due to a change in distance

between the membrane and the bottom of the pit, acting as a mirror, we have extracted the height of the pressurized blister. Together with the analysis of the corresponding Raman frequencies, we were able to extract the Grüneisen parameters of the G and 2D modes to $\gamma_{\mathsf{G}} = 1.8 \pm 0.2$ and $\gamma_{\mathsf{2D}} = 2.4 \pm 0.2$. The pure biaxial strain in the center of the blister induces a shift rate of these Raman modes of $\partial\omega_{\mathsf{2D}}/\partial\omega_{\mathsf{G}} = 2.2 \pm 0.1$. In addition, we focused on the microscopic mechanical response and confirmed that the deflection scales to the third power with the pressure load, as expected for thin membranes with vanishing bending stiffness [Hencky15, Campbell56, Landau70]. Interestingly, this relationship permitted us the extraction of the Young's modulus to $E = 1.05 \pm 0.10$ TPa.

We further investigated the approach of applying an electrostatic pressure load to suspended graphene by making advantage of the electric field effect geometry. Within this approach, the Fermi level of graphene can be finely tuned [Novoselov04]. Our Raman measurements, recorded as a function of the backgate voltage, are sensitive to the gate induced variation of the Fermi level, but also to strain, which originates from the electrostatic attraction of the membrane down to the gate electrode.

This deflection has been determined by analyzing the interference induced Raman intensity modulation with varying distance between the graphene membrane and the bottom of the trench. Interestingly, we observed an irreversible collapse of the membrane at high voltages. In order to understand the deflection and the collapse conditions of gated graphene membranes, we compared our data with a self-consistent model based on the theory of elasticity [Landau70, Medvedyeva11, Bao12]. Our study reveals that pre-strain is in fact an important parameter governing the deflection. Furthermore, our model answers to the question when a suspended graphene membrane, subjected to electrostatic pressure, is expected to enter a critical regime of instable deflections, leading to a collapse of the device. This issue is particular interesting because graphene membranes are often used in the electric field-effect geometry in order to modulate its electrical and optical conductivity, and one does not have an *in situ* information and control on the mechanical deflection.

Notably, the precise control of the deflection opens the pathway to more sophisticated devices [Federspiel15]. The well-defined and controllable properties of suspended graphene can be coupled to nanometer-sized systems, such as semiconducting nano-emitters, which interact with graphene membranes [Reserbat-Plantey15]. This interaction can be tuned with high precision and can be regarded as a ruler at the nano-scale.

However, applications are not limited to the application of DC voltages, on the contrary, recent investigations highlighted the strong potential of graphene based mechanical resonators [Bunch07, Chen09a, Barton11, Koppens14]. In particular, the mechanical actuation by coupling the resonators capacitively can be read out either electrically [Chen09a, Eichler11] or optically [Bunch07, Cole15]. The resonance frequency of such systems is very sensitive to external per-

turbations and, together with its ultra-light weight, its negligible bending stiffness and extremely high Young's modulus, graphene based mechanical systems are optimal for high precision sensing of various kinds [Wong10, Hill11, Puller13], such as mass [Chaste12] or force sensing [Bunch07]. Here, the resonance frequencies are in the range of several hundred MHz.

Recent studies have even established the potential of graphene for cavity opto-mechanics. Barton *et al.* have shown that the quality factor of the resonance can be influenced by the characteristics of the laser beam used to optically read out the resonance [Barton12]. This back-action of the light on the mechanical motion makes it possible to access the coupling of mechanical resonators to phenomena occurring in the quantum regime in graphene. In particular, such back-actions, *e.g.*, radiation pressure, has been used to cool down macroscopic systems to their quantum mechanical ground state [O'Connell10, Chan11, Teufel11]. Recent works attaining the microwave frequency vibration range opened the pathway for such investigations [Song14, Weber14]. Indeed, for these experiments, graphene as a 2d material is an excellent candidate because of its unique and well-defined electronic, optical and mechanical properties [Castellanos-Gomez15].

Raman spectroscopy is a well established tool for characterization of graphene [Malard09b, Ferrari13] and other potential 2d materials such as transition metal dichalcogenides [Carvalho15, Castellanos-Gomez15, Froehlicher15b, Lee15, Lorchat15, Zhang15], which are good candidates for opto-mechanical resonators and investigations of coupling mechanisms [Castellanos-Gomez13]. In particular, we have demonstrated in this manuscript that electron-phonon coupling can be precisely probed and allows for a spatial resolution of strain and doping level within an ultra-thin membrane. Therefore, we believe that Raman spectroscopy continues to be the key characterization tool when the issue arises to probe motion and stress in a time-resolved manner. In other words, time-resolved micro-Raman spectroscopy would be able to give at the same time information about the flexural motion of graphene resonators (in the MHz to GHz range) and the Raman active phonon modes (in the THz range). Local time-resolved stress probing, in particular in combination with the controlled excitation of different flexural modes, would be an appealing challenge [Jiang15].

Appendix

A Laser spot and defocusing influences

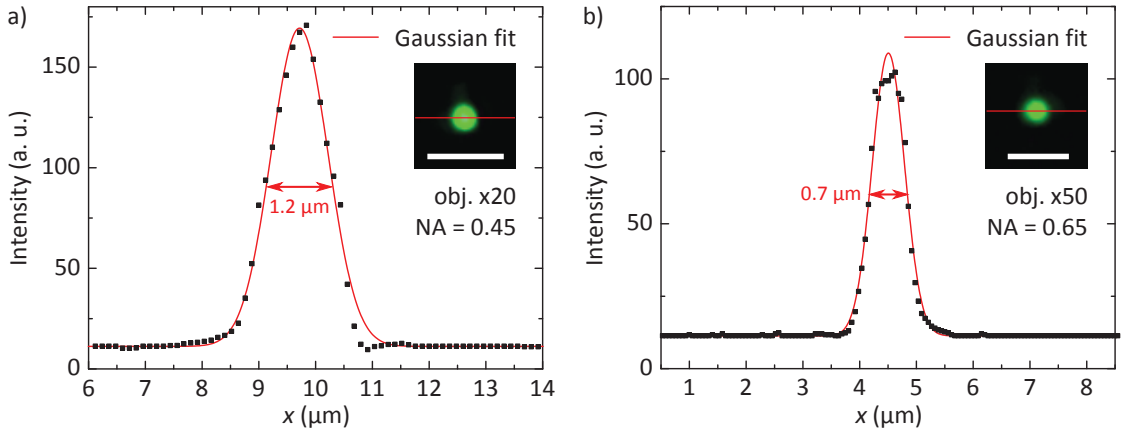

Figure A.1: a) Laser spot intensity as a function of the lateral distance x on a bare Si/SiO_2 substrate, for the $\times 20$ objective used for the measurements presented in chapters 5 and 6. The plotted data are extracted from an optical image (see red line in the inset image, the scale bar is $5\,\mu$m). This image has been taken under the measurement conditions in chapter 6, *i.e.* with the pumped cryostat (with quartz window, under vacuum and at ambient temperature). A measurement without quartz window gives the same full width at half maximum (fwhm), *i.e.* $\approx 1.2\,\mu$m, extracted from a Gaussian fit of the data. **b)** The same data for the $\times 50$ objective used in chapter 7. The scale bar in the inset image is $3\,\mu$m. A fwhm of $0.7\,\mu$m is extracted from a Gaussian fit of the data.

B Calibration of the pressure load

A key point in the analysis of chapter 6 is the calibration of the pressure load Δp. This measurement is not straightforward since the pit depth is on the same order of magnitude as the blister height ξ_{max}. We have therefore measured the blister topography (relate it to the text here, We make use of ...) and deduced the blister volume V_{B} at $p_{\text{ext}} \approx 10^{-2}$ Pa, starting from $p_{\text{int}} = (100 \pm 2)$ kPa. Bulging of the graphene provides a larger volume ($V_{\text{B}} + V_0$, where V_0 is the

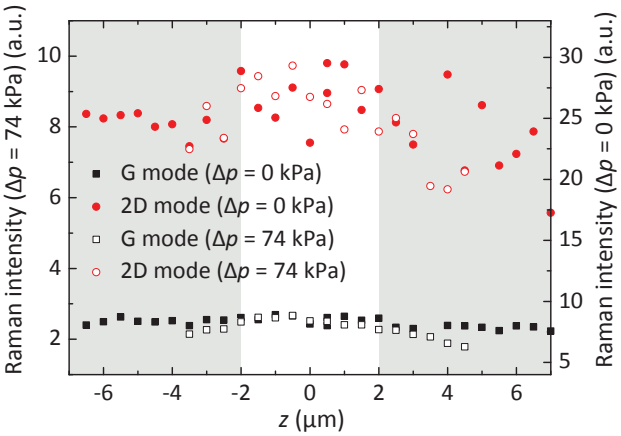

Figure A.2: Variations of I_{G} and I_{2D} as a function of the axial position z of the laser beam waist relative to the graphene membrane, for two extreme values of $\Delta p = 74$ kPa and $\Delta p = 0$ kPa. During a measurement run, the laser focus varies by less than $1\,\mu$m. Within a range of $\pm 2\,\mu$m, no appreciable changes in the Raman intensities could be observed. We therefore conclude that our results presented in chapter 6 are not affected by the focusing conditions and that the large changes in the Raman intensity are only due to optical interference effects.

volume of the cylindrical pit) for the air molecules trapped under the graphene blister. From the ideal gas law, we can then deduce the reduced inner pressure $p_{\mathrm{int}} = (74 \pm 5)$ kPa, considering the error bars in V_0 and in the atmospheric pressure. We then assume that, in the limit of low pressure loads $\Delta p = p_{\mathrm{int}} - p_{\mathrm{ext}}$, the downshifts of the Raman features scale lineraly with Δp [Zabel11]. Considering the two limiting cases of $p_{\mathrm{ext}} \approx 10^{-2}$ Pa and $p_{\mathrm{ext}} = 100$ kPa, we thus get an estimation of Δp with an error bar of a few kPa for each measurement. We note that very similar values of Δp are obtained from the downshifts of the G and 2D mode features.

In the main manuscript, we assumed that the number of gas molecules under the suspended graphene in sample A was constant, because the values of I_{G}, I_{2D}, ω_{G} and ω_{2D} at atmospheric pressure are the same before and after the measurement series as a function of Δp. Since the initial number of trapped molecules is not known for samples B and C, it is not possible to directly deduce a value for p_{int} at $p_{\mathrm{ext}} \approx 10^{-2}$ Pa, using the ideal gas law. In this case, we estimate Δp by making the following assumptions:

1. The maximum value of ω_{G} during a measurement run as a function of Δp corresponds to unstrained flat graphene. At this particular value, a nearly flat profile is found for I_{G} and I_{2D} over the blister.

2. ω_{G} and ω_{2D} are proportional to Δp. We then used the linear relationship between Δp and the Raman frequencies deduced from the measurements on sample A.

As a consequence, the pressure load Δp in samples B and C is determined with similar uncertainty but with a potentially greater systematic error than for sample A.

C Supplementary data of samples A

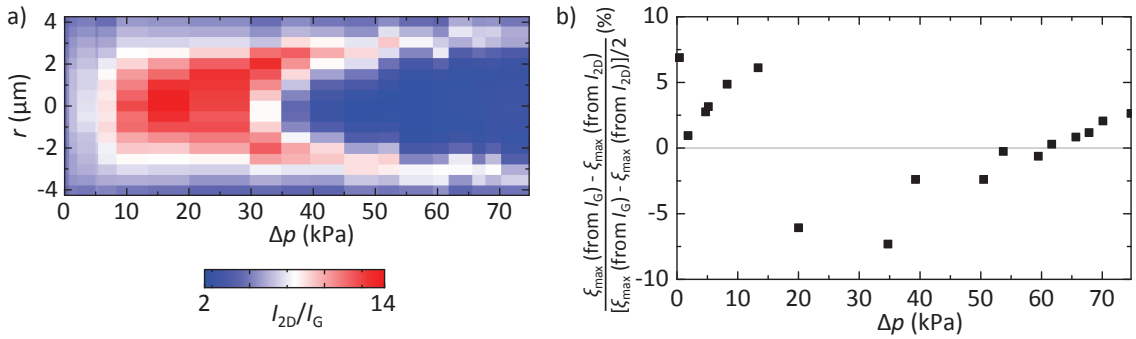

Figure C.3: a) Integrated intensity ratio I_{2D}/I_G, measured on sample A, as a function of the distance from the blister center r and the pressure load Δp. **b)** Relative difference between the maximal blister heights deduced from the G and 2D mode intensities.

D Data of samples B and C

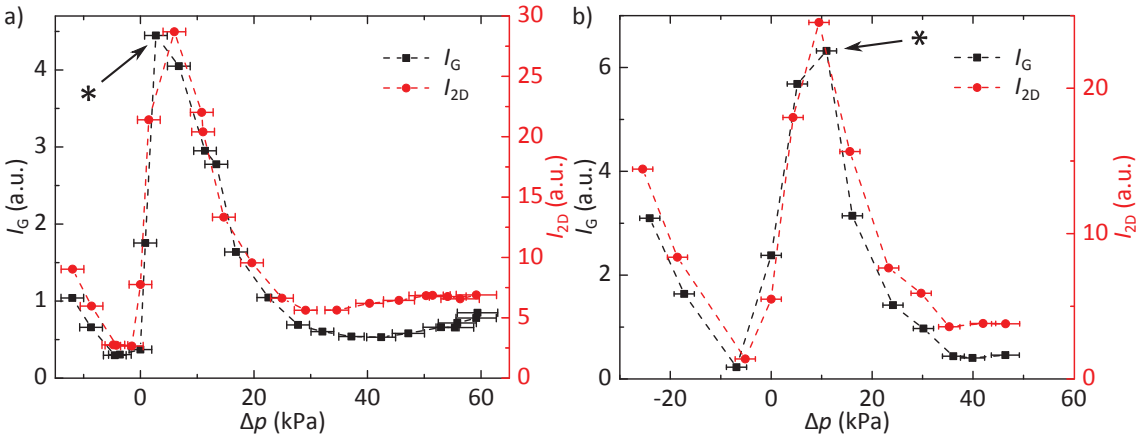

Figure D.4: a) Evolution of the integrated intensities of the G (black squares) and 2D (red circles) mode features measured at the center of sample B, as a function of the pressure load Δp. The black star marks the maximum value of I_G which corresponds to the local maximum in the enhancement factor pattern, *i.e.* here h_{max} is ≈ 416 nm. **b)** Same data for sample C. The dashed lines are a guides to the eye.

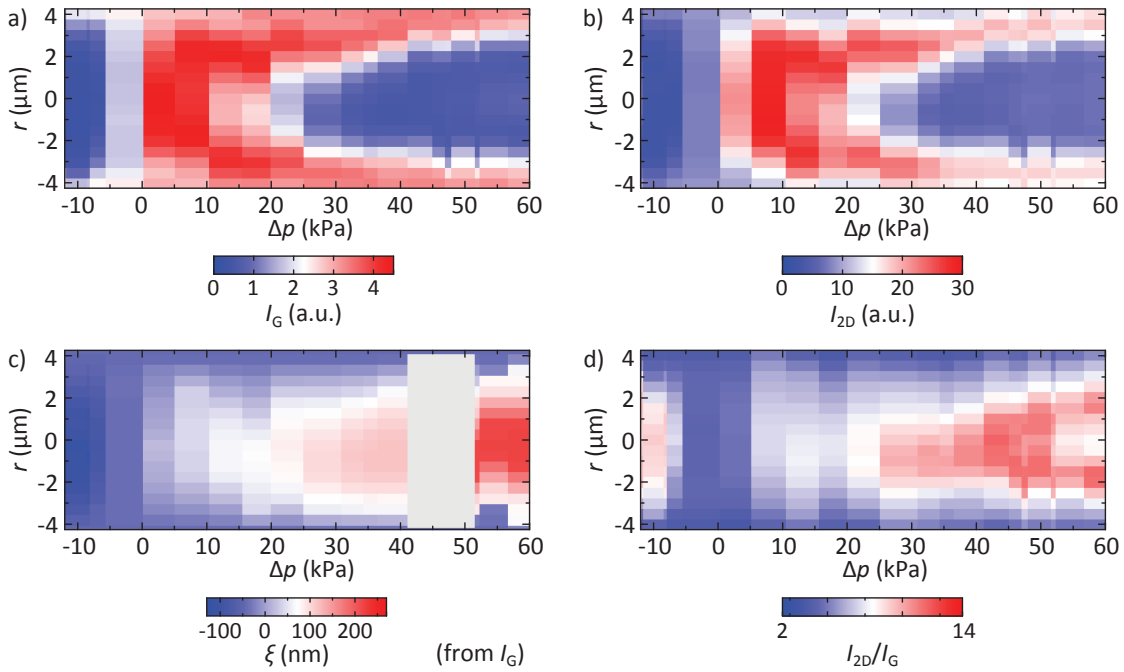

Figure D.5: Sample B: **a)** and **b)** Contour plots of the Raman G and 2D mode intensities I_{G} and I_{2D}, respectively, as a function r and Δp. **c)** Blister height $\xi(r) = h(r) - d_{\mathrm{air}}$ deduced from I_{G}, as a function of Δp. The area in light gray in corresponds to a regime of low Raman intensity, where the blister topography cannot be determined accurately. Note that, in particular, an inward bulging is observed when Δp goes from 0 to -15 kPa. **d)** Contour plot of the $I_{\mathrm{2D}}/I_{\mathrm{G}}$ ratio, showing a strong dependence on the blister height and the radial distance.

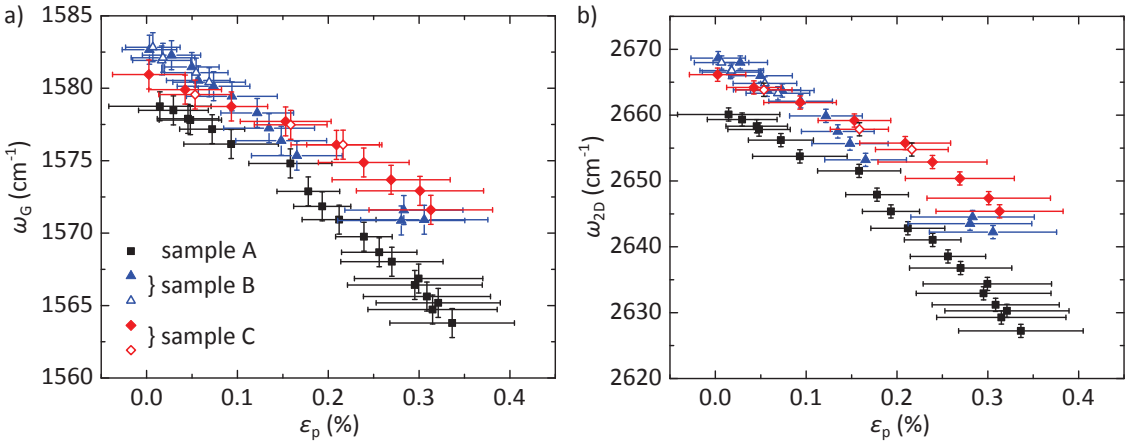

Figure D.6: Determination of the Grüneisen parameters. ω_{2D} **(a)** and ω_G **(b)** are plotted in dependence of ϵ_p, for samples A (black squares), B (blue triangles) and C (red lozenges). The filled symbols are acquired data on an outwardly bulged blister whereas the open symbols are obtained on an inwardly bulged blister (negative pressure load). Note that both filled and open symbols align well. In comparison to sample A, the data of samples B and C are shifted to higher frequencies by approximately $3\,\mathrm{cm}^{-1}$ for all ϵ_p, which is due to a slightly different prestrain in the samples. The shift rates obtained from linear fits are: $\partial\omega_G/\partial\epsilon_p = (-42 \pm 7)\,\mathrm{cm}^{-1}$/% strain and $\partial\omega_{2D}/\partial\epsilon_p = (-90 \pm 7)\,\mathrm{cm}^{-1}$/% strain (sample B), and $\partial\omega_G/\partial\epsilon_p = (-28 \pm 10)\,\mathrm{cm}^{-1}$/% strain and $\partial\omega_{2D}/\partial\epsilon_p = (-64 \pm 10)\,\mathrm{cm}^{-1}$/% strain (sample C)

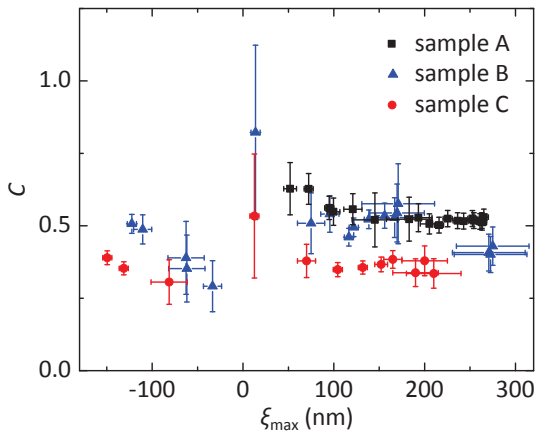

Figure D.7: The constant C relating the blister volume V_B to the maximal blister height ξ_{max} as a function of ξ_{max}, for samples A, B and C. The volume is obtained by integrating the blister profile over 2π. An average value of $C = 0.52 \pm 0.02$ can be extracted.

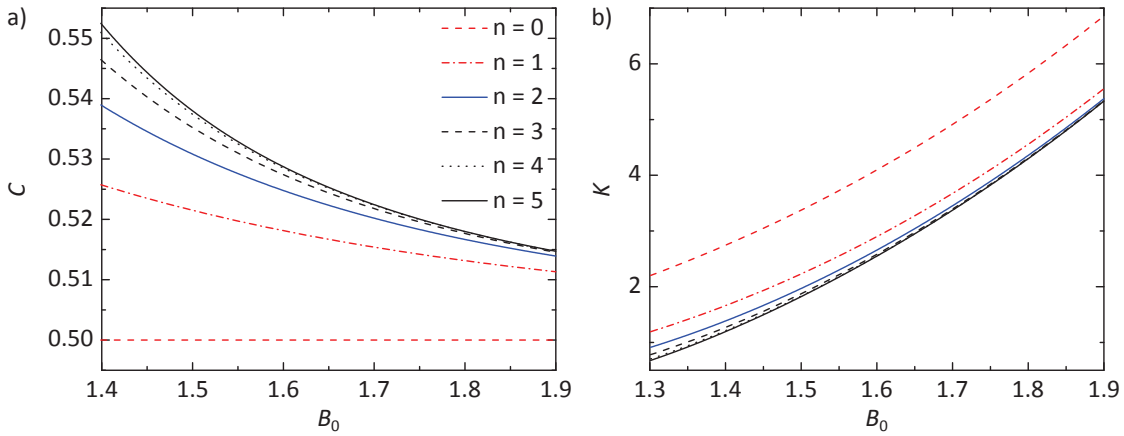

Figure D.8: a) C vs. B_0 according to the definition of $C(\nu)$ in equation (6.8) for different n. A value of $C(\nu = 0.16) \approx 0.52$ gives a value of $B_0 \approx 1.7$. **b)** This value then is coherent with a value of $K(\nu = 0.16) \approx 3$.

E Other supplementary data

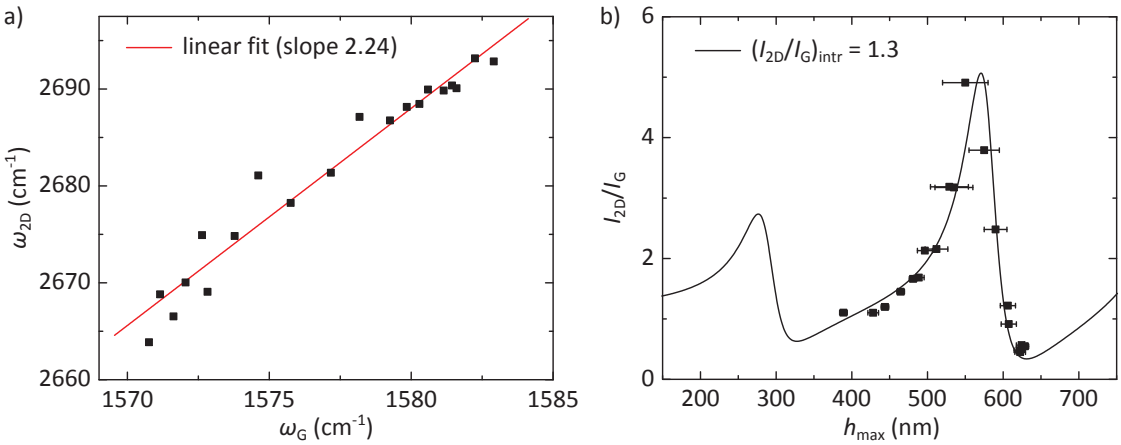

Figure E.9: a) Correlation of ω_G and ω_{2D} measured at the center of a pressuried 2L graphene blister. The data are recorded at different pressure loads. The pressure load induces a biaxial strain in the 2L graphene. The G mode feature as been fit with a single Lorentzian. The position of the 2D mode feature, which is a relatively complex composition of several sub-features [Herziger14], has been extracted using a single modified Lorentzian [Basko08] for convenience. The red line is a linear fit of the data; a slope of 2.24 ± 0.12 is found, which is in perfect agreement with the slope of 2.22, which can be extracted from the data on 2L graphene bubbles of Zabel *et al.* [Zabel11]. **b)** Evolution of the ratio of the integrated intensities of the 2D and G mode features, I_{2D}/I_G, as a function of h_{max}, the distance between the 2L graphene and the bottom of the pit. The data qualitatively resemble to the data shown in figure 6.8a, a 1L graphene on the same chip, with the same d_{air} of 395 ± 10 nm. As for the 1L graphene, an intrinsic value of the I_{2D}/I_G ratio can be extracted according to equation (6.1). We find 1.3 ± 0.1. Note that, in particular, I_{2D}/I_G of a 2L graphene can be, under certain interference conditions, much larger than the ratio of 1L graphene (≈ 5 as maximum value for 2L graphene *vs.* ≈ 2 as minimum value for 1L graphene measured on our samples).

List of Figures

1.1 Graphene as building block for sp2 carbon allotropes . . . 2
1.2 Overview of suspended graphene samples . . . 6

2.1 Crystal structure of graphene and first Brillouin zone . . . 10
2.2 Energy dispersion of π-electrons in graphene . . . 12
2.3 Density of states in graphene . . . 15
2.4 Field effect geometry and substrate influences on charge carrier density and mobility 18
2.5 Schematic of intra- and interband processes in graphene and optical transmittance measurements . . . 21
2.6 Correlation of the zone center vibrational modes of monolayer graphene and graphite . . . 23
2.7 Phonon dispersion of graphene (DFT model) and graphite (X-ray scattering data) 25
2.8 Schematic of a graphene blister used for delamination test . . . 27
2.9 Schematic of a bent plate . . . 30

3.1 Schematic of Raman scattering processes . . . 39
3.2 Raman spectra of first order Raman processes in mono- and few layer graphene . 41
3.3 Representation of the Raman G mode process . . . 44
3.4 Typical Raman spectrum of pristine and defected graphene . . . 45
3.5 Representation of the Raman 2D mode process . . . 46
3.6 Effects of trigonal warping in the 2D mode line shape . . . 50
3.7 Influence of uni- and biaxial strain on the Raman G and 2D modes . . . 55
3.8 Schematic of vector decomposition of the strain and doping component in the ω_G-ω_{2D}-plane . . . 57
3.9 G and 2D mode frequency correlation for doping and determination of the doping scaling factor . . . 59
3.10 Correlation of $\omega_{G^+}/\omega_{G^-}$ and ω_{2D} in the case of uniaxial strain . . . 60
3.11 Visibility of graphene on different Si/SiO_2-substrates . . . 63

3.12 Schematic of a one layer Fabry-Pérot 64
3.13 Schematic representation of the interference processes within a graphene layer . 66
3.14 Refractive indexes of graphene 68
3.15 Color plot of theoretical enhancement factors for the Raman G and 2D modes . . 70
3.16 Cuts of the enhancement factor color plots for different laser wavelengths 71

4.1 Exfoliation steps 74
4.2 Fabrication steps 75
4.3 Locating graphene monolayers and metal contact evaporation 77
4.4 Experimental micro-Raman setup 79

5.1 Built-in strain and ripple formation in suspended graphene devices 84
5.2 Raman spectra of suspended graphene 85
5.3 Hyperspectral Raman maps of a suspended graphene device 86
5.4 Correlation between $\langle\Gamma_{\mathrm{G}}\rangle$ and $\langle\omega_{\mathrm{G}}\rangle$ and $\langle\omega_{\mathrm{2D}}\rangle$ on suspended graphene devices . 87
5.5 Comparison of Raman frequency correlations on suspended samples 89
5.6 Example of hyperspectral Raman mapping for strain determination 92
5.7 Comparison of Raman frequency correlations: suspended *vs.* supported graphene 93

6.1 Graphene blister test: samples and measurement principle 99
6.2 Typical Raman spectra of a graphene blister for different pressure loads 100
6.3 Comparison of the evolution of the Raman frequencies and linewidths of a blister test with those doping induced 101
6.4 Raman frequency correlation as a function of the pressure load on graphene blisters 102
6.5 Influence of the pressure load on the Raman scattering intensity 104
6.6 Calculated Raman enhancement factors and corresponding intensity data on a graphene blister 106
6.7 Series of raw spectra on a graphene blister highlighting the change in $I_{\mathrm{2D}}/I_{\mathrm{G}}$ . . 107
6.8 Data and fits for the extraction of the intrinsic value of $I_{\mathrm{2D}}/I_{\mathrm{G}}$ 108
6.9 Contour plots of the determination of the blister height from the Raman scattering intensity 110
6.11 Determination of the Grüneisen parameters 113
6.12 Determination of the Young's modulus 115
6.13 Comparison of $\Delta p \propto \xi^3_{\mathrm{max}}$ dependence of several graphene blisters 117
6.14 Calculated Raman enhancement factors and corresponding intensity data on few layer graphene blister 118
6.15 Comparison of $\Delta p \propto \xi^3_{\mathrm{max}}$ dependence of 1 to 4L graphene 119
6.16 Correlation of ω_{G} and ω_{2D} in the case of biaxial strain 122

7.1 Schematic of a gated suspended graphene device 128
7.2 Optical micrograph and Raman spectra of a gated suspended graphene device . . 130
7.3 Raman intensity dependence on the gate voltage 133
7.4 SEM images of the gated device after gate-dependent Raman study 135
7.5 Determination of I_{2D}/I_G on a gated suspended graphene membrane 136
7.6 Schematic of the Lorentz force acting between two charged bodies 137
7.7 Three assumption for calculating electrostatic pressure 141
7.8 Maximal deflection of the membrane *vs.* gate voltage 143
7.9 Deflection modeling and critical values for 500 nm oxide (system 3) 146
7.10 Deflection modeling and critical values for 285 nm (system 2) and 90 nm oxide . . 148
7.11 Charge density modeling and critical values for 500 nm oxide (system 3) 148
7.12 Charge density modeling and critical values for 285 nm (system 2) and 90 nm oxide 149
7.13 Correlation between charge carrier density, maximal deflection and gate voltage for a specific device 151
7.14 Gate induced Raman shifts 153
7.15 Convolution of the membrane profile with the laser spot size and extent of thermal drifts 154

A.1 Laser spot calibration 161
A.2 influence of the focusing conditions 162
C.3 Variation of I_{2D}/I_G as a function of Δp and difference in height extraction between I_G and I_{2D}, for sample A 163
D.4 Evolution of I_G and I_{2D} for samples B and C 163
D.5 Additional data of I_G, I_{2D}, I_{2D}/I_G and ξ as function of Δp for sample B 164
D.6 Additional data for the determination of the Grüneisen parameters 165
D.7 Values of the constant C relating the blister volume to the deflection 165
D.8 Relationships between constants C, B_0 and K 166
E.9 Bilayer graphene: Raman G and 2D mode frequency correlation and intrinsic I_{2D}/I_G 167

List of Tables

2.1 Relation between dimensionality, dispersion relation and density of states 16

3.1 Overview: shift rates for doping 58

5.1 Strain and doping values on several suspended and supported graphene samples 94

6.1 Summary of the characteristics of graphene membrane devices used for blister tests 101

6.2 Overview: shift rates for biaxial strain and Grüneisen parameters 123

7.1 Strain and doping values of gated graphene device at room temperature 129

Bibliography

[Ager90] J. W. Ager, D. K. Veirs, and G. M. Rosenblatt. *Raman intensities and interference effects for thin films adsorbed on metals*. The Journal of Chemical Physics **92** (3), 2067-2076 (1990). 72

[Al-Jishi82] R. Al-Jishi and G. Dresselhaus. *Lattice-dynamical model for graphite*. Phys. Rev. B **26** (8), 4514-4522 (1982). 24, 44

[Ando98] T. Ando, T. Nakanishi, and R. Saito. *Berry's Phase and Absence of Back Scattering in Carbon Nanotubes*. J. Phys. Soc. Jpn. **67** (8), 2857-2862 (1998). 14

[Ando02] T. Ando, Y. Zheng, and H. Suzuura. *Dynamical conductivity and zero-mode anomaly in honeycomb lattices*. Journal of the Physical Society of Japan **71**, 1318-1324 (2002). 17

[Ando06] T. Ando. *Anomaly of Optical Phonon in Monolayer Graphene*. J. Phys. Soc. Jpn. **75** (12), 124701 (2006). xvi, 51, 52

[Annamalai12] M. Annamalai, S. Mathew, M. Jamali, D. Zhan, and M. Palaniapan. *Elastic and nonlinear response of nanomechanical graphene devices*. Journal of Micromechanics and Microengineering **22** (10), 105024 (2012). 98, 120, 124

[Annamalai13] M. Annamalai, S. Mathew, M. Jamali, D. Zhan, and M. Palaniapan. *Effects of annealing on the ripple texture and mechanical properties of suspended bilayer graphene*. Journal of Physics D: Applied Physics **46** (14), 145302 (2013). 120, 123

[Aoki07] M. Aoki and H. Amawashi. *Dependence of band structures on stacking and field in layered graphene*. Solid State Communications **142** (3), 123-127 (2007). 42

[Araujo12] P. T. Araujo, D. L. Mafra, K. Sato, R. Saito, J. Kong, and M. S. Dresselhaus. *Phonon Self-Energy Corrections to Nonzero Wave-Vector Phonon Modes in Single-Layer Graphene*. Phys. Rev. Lett. **109** (4), 046801 (2012). 51

[Ashcroft75] N. W. Ashcroft and N. D. Mermin. *Solid State Physics*. Thomsen Brooks/Cole, 1975. 16, 20

[Balandin11] A. A. Balandin. *Thermal properties of graphene and nanostructured carbon materials*. Nat. Mater. **10** (8), 569-581 (2011). 1

[Bao09] W. Bao, F. Miao, Z. Chen, H. Zhang, W. Jang, C. Dames, and C. N. Lau. *Controlled ripple texturing of suspended graphene and ultrathin graphite membranes*. Nat Nano **4** (9), 562-566 (2009). 4, 84, 121, 144

[Bao10] W. Bao, G. Liu, Z. Zhao, H. Zhang, D. Yan, A. Deshpande, B. Le Roy, and C. N. Lau. *Lithography-free fabrication of high quality substrate-supported and freestanding graphene devices*. Nano Research **3** (2), 98-102 (2010). 83

[Bao12] W. Bao, K. Myhro, Z. Zhao, Z. Chen, W. Jang, L. Jing, F. Miao, H. Zhang, C. Dames, and C. N. Lau. *In Situ Observation of Electrostatic and Thermal Manipulation of Suspended Graphene Membranes*. Nano Lett. **12** (11), 5470-5474 (2012). 140, 141, 158

[Baranov87] A. Baranov, A. N. Bekhterev, Y. S. Bobovich, and V. I. Petrov. *Interpretation of certain characteristics in Raman spectra of graphite and glassy carbon*. Optics and Spectroscopy **62**, 612-616 (1987). 45

[Barton11] R. A. Barton, B. Ilic, A. M. van der Zande, W. S. Whitney, P. L. McEuen, J. M. Parpia, and H. G. Craighead. *High, Size-Dependent Quality Factor in an Array of Graphene Mechanical Resonators*. Nano Lett. **11** (3), 1232-1236 (2011). xxii, xxvii, 83, 94, 116, 120, 127, 158

[Barton12] R. A. Barton, I. R. Storch, V. P. Adiga, R. Sakakibara, B. R. Cipriany, B. Ilic, S. P. Wang, P. Ong, P. L. McEuen, J. M. Parpia, and H. G. Craighead. *Photothermal self-oscillation and laser cooling of graphene optomechanical systems*. Nano Lett. **12** (9), 4681-4686 (2012). 159

[Basko07] D. M. Basko. *Effect of inelastic collisions on multiphonon Raman scattering in graphene*. Physical Review B **76** (8), 081405 (2007). 47

[Basko08] D. M. Basko. *Theory of resonant multiphonon Raman scattering in graphene*. Phys. Rev. B **78** (12), 125418 (2008). 43, 44, 47, 48, 51, 53, 86, 100, 109, 167

[Basko09a] D. M. Basko. *Calculation of the Raman G peak intensity in monolayer graphene: role of Ward identities*. New Journal of Physics **11** (9), 095011 (2009). xvi, 44, 53

[Basko09b] D. M. Basko, S. Piscanec, and A. C. Ferrari. *Electron-electron interactions and doping dependence of the two-phonon Raman intensity in graphene*. Phys. Rev. B **80** (16), 165413 (2009). xvi, 43, 53, 54, 107, 109, 134

[Beams95] J. W. Beams. *In structures and properties of thin films*. Wiley, New York, 1995. 34

[Bena05] C. Bena and S. A. Kivelson. *Quasiparticle scattering and local density of states in graphite*. Phys. Rev. B **72** (12), 125432 (2005). 14

[Berciaud09] S. Berciaud, S. Ryu, L. E. Brus, and T. F. Heinz. *Probing the intrinsic properties of exfoliated graphene: Raman spectroscopy of free-standing monolayers*. Nano Lett. **9** (1), 346-352 (2009). xviii, 3, 19, 22, 26, 48, 49, 53, 56, 83, 85, 86, 93, 100, 103

[Berciaud10] S. Berciaud, Melinda Y. Han, Kin Fai Mak, Louis E. Brus, Philip Kim, and Tony F. Heinz. *Electron and optical phonon temperatures in electrically biased graphene*. Phys. Rev. Lett. **104** (22), 227401 (2010). 38, 40

[Berciaud13] S. Berciaud, X. Li, H. Htoon, L.E. Brus, S.K. Doorn, and T.F. Heinz. *Intrinsic line shape of the Raman 2D-mode in freestanding graphene monolayers*. Nano Lett. **13** (8), 3517-3523 (2013). xv, 47, 49, 50, 53, 56, 85, 86, 87, 89, 90, 100, 147

[Berciaud14] S. Berciaud, M. Potemski, and C. Faugeras. *Probing electronic excitations in mono- to pentalayer graphene by micro magneto-Raman spectroscopy*. Nano Lett. **14**, 4548-4553 (2014). 38

[Berger04] C. Berger, Z. Song, T. Li, X. Li, A. Y. Ogbazghi, R. Feng, Z. Dai, A. N. Marchenkov, E. H. Conrad, P. N. First, and W. A. de Heer. *Ultrathin Epitaxial Graphite: 2D Electron Gas Properties and a Route toward Graphene-based Nanoelectronics*. J. Phys. Chem. B **108** (52), 19912-19916 (2004). 3

[Berry13] V. Berry. *Impermeability of graphene and its applications*. Carbon **62**, 1-10 (2013). 97

[Blake07] P. Blake, E. W. Hill, A. H. Castro Neto, K. S. Novoselov, D. Jiang, R. Yang, T. J. Booth, and A. K. Geim. *Making graphene visible*. Appl. Phys. Lett. **91** (6), 063124 (2007). xvii, 1, 38, 62, 63, 67, 68, 112

[Blakslee70] O. L. Blakslee, D. G. Proctor, E. J. Seldin, G. B. Spence, and T. Weng. *Elastic Constants of Compression-Annealed Pyrolytic Graphite*. Journal of Applied Physics **41** (8), 3373-3382 (1970). 1, 83

[Boddeti13] N. G. Boddeti, S. P. Koenig, R. Long, J. Xiao, J. S. Bunch, and M. L. Dunn. *Mechanics of Adhered, Pressurized Graphene Blisters*. J. of Appl. Mech. **80** (4), 40909 (2013). 97, 98, 115

[Boehm62] H. P. Boehm, A. Claus, G. O. Fischer, and U. Hofmann. *Dünnste Kohlenstoff-Folien*. Z. Naturforschg. **17b**, 150-153 (1962). xiii, 1, 9

[Boehm94] H. P. Boehm, R. Setton, and E. Stumpp. *Nomenclature and terminology of graphite intercalation compounds*. Pure Appl. Chem. **66**, 1893-1901 (1994). 1, 9

[Bolotin08a] K. I. Bolotin, K. J. Sikes, J. Hone, H. L. Stormer, and P. Kim. *Temperature-dependent transport in suspended graphene*. Phys. Rev. Lett. **101** (9), 096802 (2008). 19

[Bolotin08b] K. I. Bolotin, K. J. Sikes, Z. Jiang, M. Klima, G. Fudenberg, J. Hone, P. Kim, and H. L. Stormer. *Ultrahigh electron mobility in suspended graphene*. Solid State Commun. **146**, 351-355 (2008). xiv, 3, 4, 6, 17, 18, 19, 26, 27, 83, 94, 127, 147

[Bonaccorso10] F. Bonaccorso, Z. Sun, T. Hasan, and A. C. Ferrari. *Graphene photonics and optoelectronics*. Nat Photon **4** (9), 611-622 (2010). 19

[Bonini07] N. Bonini, M. Lazzeri, N. Marzari, and F. Mauri. *Phonon Anharmonicities in Graphite and Graphene*. Phys. Rev. Lett. **99**, 176802 (2007). 24, 43, 53, 144

[Bostwick07] A. Bostwick, T. Ohta, T. Seyller, K. Horn, and E. Rotenberg. *Quasiparticle dynamics in graphene*. Nat Phys **3** (1), 36-40 (2007). 12, 13

[Bruna09] M. Bruna and S. Borini. *Optical constants of graphene layers in the visible range*. Appl. Phys. Lett. **94** (3), 031901 (2009). 67, 68

[Budde15] H. Budde, N. Coca-López, X. Shi, R. Ciesielski, A. Lombardo, D. Yoon, A. C. Ferrari, and A. Hartschuh. *Raman Radiation Patterns of Graphene*. ACS Nano **10** (2), 1756 (2015). 109

[Bunch07] J. S. Bunch, A. M. van der Zande, S. S. Verbridge, I. W. Frank, D. M. Tanenbaum, J. M. Parpia, H. G. Craighead, and P. L. McEuen. *Electromechanical resonators from graphene sheets*. Science **315** (5811), 490-493 (2007). xxvii, 3, 5, 26, 27, 60, 83, 94, 121, 127, 158, 159

[Bunch08] J. S. Bunch, S. S. Verbridge, J. S. Alden, A. M. van der Zande, J. M. Parpia, H. G. Craighead, and P. L. McEuen. *Impermeable atomic membranes from graphene sheets*. Nano Lett. **8** (8), 2458-2462 (2008). xxii, 3, 6, 26, 27, 60, 62, 83, 94, 97, 98, 115, 142, 157

[Bunch12] J. S. Bunch and M. L. Dunn. *Adhesion mechanics of graphene membranes*. Solid State Commun. **152** (15), 1359-1364 (2012). 1, 98, 120, 124

[Calizo07] I. Calizo, A. A. Balandin, W. Bao, F. Miao, and C. N. Lau. *Temperature Dependence of the Raman Spectra of Graphene and Graphene Multilayers*. Nano Lett. **7** (9), 2645-2649 (2007). 3

[Campbell56] J. D. Campbell. *On the theory of initially tensioned circular membranes subjected to uniform pressure*. The Quarterly Journal of Mechanics and Applied Mathematics **9** (1), 84-93 (1956). 114, 158

[Cancado11] L. G. Cancado, A. Jorio, E. H. Martins Ferreira, F. Stavale, C. A. Achete, R. B. Capaz, M. V. O. Moutinho, A. Lombardo, T. S. Kulmala, and A. C. Ferrari. *Quantifying Defects in Graphene via Raman Spectroscopy at Different Excitation Energies*. Nano Lett. **11** (8), 3190-3196 (2011). 3, 22, 42

[Cardarelli08] F. Cardarelli. *Materials Handbook*. London, Springer-Verlag, 2008. 83

[Carvalho15] B. R. Carvalho, L. M. Malard, J. M. Alves, C. Fantini, and M. A. Pimenta. *Symmetry-Dependent Exciton-Phonon Coupling in 2D and Bulk* MoS_2 *Observed by Resonance Raman Scattering*. Phys. Rev. Lett. **114**, 136403 (2015). 159

[Casiraghi07a] C. Casiraghi, A. Hartschuh, E. Lidorikis, H. Qian, H. Harutyunyan, T. Gokus, K. S. Novoselov, and A. C. Ferrari. *Rayleigh Imaging of Graphene and Graphene Layers*. Nano Lett. **7** (9), 2711-2717 (2007). 38

[Casiraghi07b] C. Casiraghi, S. Pisana, K. S. Novoselov, A. K. Geim, and A. C. Ferrari. *Raman fingerprint of charged impurities in graphene*. Appl. Phys. Lett. **91** (23), 233108 (2007). 3

[Castellanos-Gomez13] A. Castellanos-Gomez, R. van Leeuwen, M. Buscema, Herre S. J. van der Zant, G. A. Steele, and W. J. Venstra. *Single-Layer MoS_2 Mechanical Resonators*. Adv. Mater. **25** (46), 6719-6723 (2013). 159

[Castellanos-Gomez15] A. Castellanos-Gomez, V. Singh, H. S. J. van der Zant, and G. A. Steele. *Mechanics of freely-suspended ultrathin layered materials*. Annalen der Physik **527** (1-2), 27-44 (2015). 4, 159

[Castro Neto09] A. H. Castro Neto, F. Guinea, N. M. R. Peres, K. S. Novoselov, and A. K. Geim. *The electronic properties of graphene*. Rev. Mod. Phys. **81** (1), 109-162 (2009). xiv, 1, 10, 11, 12, 14, 15, 42, 50

[Castro10] E. V. Castro, H. Ochoa, M. I. Katsnelson, R. V. Gorbachev, D. C. Elias, K. S. Novoselov, A. K. Geim, and F. Guinea. *Limits on Charge Carrier Mobility in Suspended Graphene due to Flexural Phonons*. Phys. Rev. Lett. **105** (26), 266601 (2010). 19

[Chae09] D.-H. Chae, B. Krauss, K. von Klitzing, and J. H. Smet. *Hot Phonons in an Electrically Biased Graphene Constriction*. Nano Lett. **10** (2), 466-471 (2009). 3, 40

[Chan11] J. Chan, T. P. Mayer Alegre, A. H. Safavi-Naeini, J. T. Hill, A. Krause, S. Groblacher, M. Aspelmeyer, and O. Painter. *Laser cooling of a nanomechanical oscillator into its quantum ground state*. Nature **478** (7367), 89-92 (2011). 159

[Chaste12] J. Chaste, A. Eichler, J. Moser, G. Ceballos, R. Rurali, and A. Bachtold. *A nanomechanical mass sensor with yoctogram resolution*. Nat Nano **7** (5), 301-304 (2012). 3, 35, 84, 159

[Chen09a] C. Chen, S. Rosenblatt, K. I. Bolotin, W. Kalb, P. Kim, I. Kymissis, H. L. Stormer, T. F. Heinz, and J. Hone. *Performance of monolayer graphene nanomechanical resonators with electrical readout*. Nature Nano **4** (12), 861-867 (2009). xxvii, 5, 27, 60, 83, 94, 127, 144, 158

[Chen09b] C.-C. Chen, W. Bao, J. Theiss, C. Dames, C. N. Lau, and S. B. Cronin. *Raman Spectroscopy of Ripple Formation in Suspended Graphene*. Nano Lett. **9** (12), 4172-4176 (2009). 4, 26, 84, 121

[Chen11] C.-F. Chen, C.-H. Park, B. W. Boudouris, J. Horng, B. Geng, C. Girit, A. Zettl, M. F. Crommie, R. A. Segalman, S. G. Louie, and F. Wang. *Controlling inelastic light scattering quantum pathways in graphene*. Nature **471** (7340), 617-620 (2011). xvi, 44, 52, 53

[Cheng11] Y. C. Cheng, Z. Y. Zhu, G. S. Huang, and U. Schwingenschlägl. *Grüneisen parameter of the G mode of strained monolayer graphene*. Phys. Rev. B **83** (11), 115449 (2011). 61, 123, 124

[Cheon14] S. Cheon, K. D. Kihm, H. G. Kim, G. Lim, J. S. Park, and J. S. Lee. *How to Reliably Determine the Complex Refractive Index (RI) of Graphene by Using Two Independent Measurement Constraints*. Sci. Rep. **4**, - (2014). 67, 68

[Chuvilin10] A. Chuvilin, U. Kaiser, E. Bichoutskaia, N. A. Besley, and A. N. Khlobystov. *Direct transformation of graphene to fullerene*. Nat Chem **2** (6), 450-453 (2010). 1

[Cole15] R. M. Cole, G. A. Brawley, V. P. Adiga, R. De Alba, J. M. Parpia, B. Ilic, H. G. Craighead, and W. P. Bowen. *Evanescent-Field Optical Readout of Graphene Mechanical Motion at Room Temperature*. Phys. Rev. Applied **3** (2), 024004 (2015). xxvii, 155, 158

[Das Sarma11] S. Das Sarma, S. Adam, E. H. Hwang, and E. Rossi. *Electronic transport in two-dimensional graphene*. Rev. Mod. Phys. **83** (2), 407-470 (2011). 1

[Das08] A. Das, S. Pisana, B. Chakraborty, S. Piscanec, S. K. Saha, U. V. Waghmare, K. S. Novoselov, H. R. Krishnamurthy, A. K. Geim, A. C. Ferrari, and A. K. Sood. *Monitoring dopants by Raman scattering in an electrochemically top-gated graphene transistor*. Nat Nano **3** (4), 210-215 (2008). xvi, 17, 22, 43, 51, 52, 53, 58, 59, 87, 88, 90, 101, 107, 128, 134

[Das09] A. Das, B. Chakraborty, S. Piscanec, S. Pisana, A. K. Sood, and A. C. Ferrari. *Phonon renormalization in doped bilayer graphene*. Phys. Rev. B **79** (15), 155417 (2009). 53, 58

[Davydov69] A. S. Davydov. *Theory of Molecular Excitons*. McGraw-Hill, New York, 1969. 22

[Deacon07] R. S. Deacon, K.-C. Chuang, R. J. Nicholas, K. S. Novoselov, and A. K. Geim. *Cyclotron resonance study of the electron and hole velocity in graphene monolayers*. Phys. Rev. B **76** (8), 081406 (2007). 11

[Dean10] C. R. Dean, A. F. Young, I. Meric, C. Lee, L. Wang, S. Sorgenfrei, K. Watanabe, T. Taniguchi, P. Kim, K. L. Shepard, and J. Hone. *Boron nitride substrates for high-quality graphene electronics*. Nat. Nano **5** (10), 722-726 (2010). 3, 19

[Dietl08] P. Dietl, F. Piéchon, and G. Montambaux. *New magnetic field dependence of Landau levels in a graphene-like structure*. Phys. Rev. Lett. **100** (23), 236405 (2008). 13

[Ding10] F. Ding, H. Ji, Y. Chen, A. Herklotz, K. Dörr, Y. Mei, A. Rastelli, and O. G. Schmidt. *Stretchable Graphene: A Close Look at Fundamental Parameters through Biaxial Straining*. Nano Lett. **10** (9), 3453-3458 (2010). 60, 61, 87, 123

[Dlubak12] B. Dlubak, M.-B. Martin, C. Deranlot, B. Servet, S. Xavier, R. Mattana, M. Sprinkle, C. Berger, W. A. De Heer, F. Petroff, A. Anane, P. Seneor, and A. Fert. *Highly efficient spin transport in epitaxial graphene on SiC*. Nat Phys **8** (7), 557-561 (2012). 1

[Dresselhaus] M. S. Dresselhaus. *Solid State Physics Part 2 - Optical properties of solids*. URL http://web.mit.edu/course/6/6.732/www/6.732-pt2.pdf. 20, 41

[Dresselhaus02] M. S. Dresselhaus and G. Dresselhaus. *Intercalation compounds of graphite*. Advances in Physics **51** (1), 1-186 (2002). 14

[Dresselhaus05] M. S. Dresselhaus, G. Dresselhaus, R. Saito, and A. Jorio. *Raman spectroscopy of carbon nanotubes*. Physics Reports **409** (2), 47-99 (2005). 43

[Du08] X. Du, I. Skachko, A. Barker, and E. Y. Andrei. *Approaching ballistic transport in suspended graphene*. Nat Nano **3** (8), 491-495 (2008). 3, 27

[Dubay03] O. Dubay and G. Kresse. *Accurate density functional calculations for the phonon dispersion relations of graphite layer and carbon nanotubes*. Phys. Rev. B **67** (3), 035401 (2003). 24

[Eckmann12] A. Eckmann, A. Felten, A. Mishchenko, L. Britnell, R. Krupke, K. S. Novoselov, and C. Casiraghi. *Probing the Nature of Defects in Graphene by Raman Spectroscopy*. Nano Lett. **12** (8), 3925-3930 (2012). 3, 22, 42

[Eichler11] A. Eichler, J. Moser, J. Chaste, M. Zdrojek, I. Wilson-Rae, and A. Bachtold. *Nonlinear damping in mechanical resonators made from carbon nanotubes and graphene*. Nat Nano **6** (6), 339-342 (2011). xxvii, 127, 158

[Elias11] D. C. Elias, R. V. Gorbachev, A. S. Mayorov, S. V. Morozov, A. A. Zhukov, P. Blake, L. A. Ponomarenko, I. V. Grigorieva, K. S. Novoselov, F. Guinea, and A. K. Geim. *Dirac cones reshaped by interaction effects in suspended graphene*. Nature Physics **7** (9), 701-704 (2011). 52, 90, 91, 150, 152

[Engel12] M. Engel, M. Steiner, A. Lombardo, A. C. Ferrari, H. v. Löhneysen, P. Avouris, and R. Krupke. *Light-matter interaction in a microcavity-controlled graphene transistor*. Nat. Comm. **3**, 906 (2012). 94

[Faugeras11] C. Faugeras, M. Amado, P. Kossacki, M. Orlita, M. Kühne, A. A. L. Nicolet, Yu. I. Latyshev, and M. Potemski. *Magneto-Raman Scattering of Graphene on Graphite: Electronic and Phonon Excitations*. Phys. Rev. Lett. **107**, 036807 (2011). 38

[Faugeras15] C. Faugeras, S. Berciaud, P. Leszczynski, Y. Henni, K. Nogajewski, M. Orlita, T. Taniguchi, K. Watanabe, C. Forsythe, P. Kim, R. Jalil, A.K. Geim, D.M. Basko, and M. Potemski. *Landau level spectroscopy of electron-electron interactions in graphene*. Phys. Rev. Lett. **114** (12), 126804 (2015). 52, 90, 150

[Federspiel15] F. Federspiel, G. Froehlicher, M. Nasilowski, S. Pedetti, A. Mahmood, B. Doudin, S. Park, J.-O. Lee, D. Halley, B. Dubertret, P. Gilliot, and S. Berciaud. *Distance Dependence of the Energy Transfer Rate from a Single Semiconductor Nanostructure to Graphene*. Nano Lett. **15** (2), 1252-1258 (2015). xxvii, 62, 158

[Ferrari06] A. C. Ferrari, J. C. Meyer, V. Scardaci, C. Casiraghi, M. Lazzeri, F. Mauri, S. Piscanec, D. Jiang, K. S. Novoselov, S. Roth, and A. K. Geim. *Raman Spectrum of Graphene and Graphene Layers*. Phys. Rev. Lett. **97** (18), 187401 (2006). xv, 3, 22, 40, 49

[Ferrari07] A. C. Ferrari. *Raman spectroscopy of graphene and graphite: Disorder, electron-phonon coupling, doping and nonadiabatic effects*. Solid State Commun. **143** (1–2), 47-57 (2007). 3, 22, 46

[Ferrari13] A. C. Ferrari and D. M. Basko. *Raman spectroscopy as a versatile tool for studying the properties of graphene*. Nature Nano **8** (4), 235-246 (2013). 1, 3, 22, 23, 39, 41, 43, 46, 56, 159

[Föppl07] A. Föppl. *Vorlesungen über technische Mechanik*. B. G. Teubner **5**, 132 (1907). 33

[Forster76] O. Forster. *Analysis 2*. Vieweg Studium, 1976. 30

[Forster13] F. Forster, A. Molina-Sanchez, S. Engels, A. Epping, K. Watanabe, T. Taniguchi, L. Wirtz, and C. Stampfer. *Dielectric screening of the Kohn anomaly of graphene on hexagonal boron nitride*. Phys. Rev. B **88** (8), 085419 (2013). 19

[Fox95] M. A. Fox and J. K. Whitesell. *Organische Chemie. Grundlagen, Mechanismen, bioorganische Anwendungen*. Springer, 1995. 9

[Frank07] I. W. Frank, D. M. Tanenbaum, A. M. van der Zande, and P. L. McEuen. *Mechanical properties of suspended graphene sheets*. Journal of Vacuum Science & Technology B **25** (6), 2558-2561 (2007). 19, 120

[Frank10] O. Frank, G. Tsoukleri, J. Parthenios, K. Papagelis, I. Riaz, R. Jalil, K. S. Novoselov, and C. Galiotis. *Compression Behavior of Single-Layer Graphenes*. ACS Nano **4** (6), 3131-3138 (2010). 60

[Frank11] O. Frank, M. Mohr, J. Maultzsch, C. Thomsen, I. Riaz, R. Jalil, K. S. Novoselov, G. Tsoukleri, J. Parthenios, K. Papagelis, L. Kavan, and C. Galiotis. *Raman 2D-Band Splitting in Graphene: Theory and Experiment*. ACS Nano **5** (3), 2231-2239 (2011). 49, 56, 122

[Freitag10] M. Freitag, H.-Y. Chiu, M. Steiner, V. Perebeinos, and P. Avouris. *Thermal infrared emission from biased graphene*. Nat Nano **5** (7), 497-501 (2010). 38

[Froehlicher15a] G. Froehlicher and S. Berciaud. *Raman spectroscopy of electrochemically-gated graphene field-effect transistor: Geometrical capacitance, electron-phonon, electron-electron and electron-defect scattering*. Phys. Rev. B **91**, 205413 (2015). xvi, 17, 45, 51, 52, 53, 54, 58, 59, 90, 92, 93, 101, 107, 109, 134, 142

[Froehlicher15b] G. Froehlicher, E. Lorchat, F. Fernique, C. Joshi, A. Molina-Sánchez, L. Wirtz, and S. Berciaud. *Unified Description of the Optical Phonon Modes in N-Layer MoTe2*. Nano Lett. **15** (10), 6481-6489 (2015). 26, 41, 159

[Fröhlich54] A. Fröhlich. *Electrons in electric fields*. Adv. in Phys. **3**, 325 (1954). 38

[Fromm13] F. Fromm, P. Wehrfritz, M. Hundhausen, and T. Seyller. *Looking behind the scenes: Raman spectroscopy of top-gated epitaxial graphene through the substrate*. New Journal of Physics **15** (11), 113006 (2013). 58

[Fuchs08] J.-N. Fuchs and M. O. Goerbig. *Introduction to the physical properties of graphene*. In *Lecture Notes*, (2008). 10, 11, 12, 13

[Gao14] W. Gao, P. Xiao, G. Henkelman, K. M. Liechti, and R. Huang. *Interfacial adhesion between graphene and silicon dioxide by density functional theory with van der Waals corrections*. J. Phys. D **47**, 255301 (2014). 26, 27, 62, 83, 97

[Geim07] A. K. Geim and K. S. Novoselov. *The rise of graphene*. Nat Mater **6** (3), 183-191 (2007). xiv, 1, 2, 17, 18

[Georgiou11] T. Georgiou, L. Britnell, P. Blake, R. V. Gorbachev, A. Gholinia, A. K. Geim, C. Casiraghi, and K. S. Novoselov. *Graphene bubbles with controllable curvature*. Appl. Phys. Lett. **99** (9), - (2011). 3, 6, 26, 61

[Godel13] F. Godel, E. Pichonat, D. Vignaud, H. Majjad, D. Metten, Y. Henry, S. Berciaud, J.-F. Dayen, and D. Halley. *Epitaxy of MgO magnetic tunnel barriers on epitaxial graphene*. Nanotechnology **24** (47), 475708 (2013). 80

[Goncher13] S. J. Goncher, L. Zhao, A. N. Pasupathy, and G. W. Flynn. *Substrate Level Control of the Local Doping in Graphene*. Nano Lett. **13** (4), 1386-1392 (2013). 19

[Graf07] D. Graf, F. Molitor, K. Ensslin, C. Stampfer, A. Jungen, C. Hierold, and L. Wirtz. *Spatially Resolved Raman Spectroscopy of Single- and Few-Layer Graphene*. Nano Lett. **7** (2), 238-242 (2007). xv, 3, 22, 42, 49

[Griffiths99] D. J. Griffiths. *Introduction to Electrodynamics*. Prentice Hall, 3 edition, 1999. 137

[Grüneis09] A. Grüneis, J. Serrano, A. Bosak, M. Lazzeri, S. L. Molodtsov, L. Wirtz, C. Attaccalite, M. Krisch, A. Rubio, F. Mauri, and T. Pichler. *Phonon surface mapping of graphite: Disentangling quasi-degenerate phonon dispersions*. Phys. Rev. B **80** (8), 085423 (2009). 24, 25, 26, 49

[Gupta06] A. Gupta, G. Chen, P. Joshi, S. Tadigadapa, and Eklund. *Raman Scattering from High-Frequency Phonons in Supported n-Graphene Layer Films*. Nano Lett. **6** (12), 2667-2673 (2006). xv

[Gupta15] S. Gupta, E. Heintzman, and J. Jasinski. *Multiphonon Raman spectroscopy properties and Raman mapping of 2d van der Waals solids: graphene and beyond*. J. Raman Spectrosc. **46** (2), 217-230 (2015). 43

[Han07] M. Y. Han, B. Özyilmaz, Y. Zhang, and P. Kim. *Energy Band-Gap Engineering of Graphene Nanoribbons*. Phys. Rev. Lett. **98** (20), 206805 (2007). 17

[Hanfland89] M. Hanfland, H. Beister, and K. Syassen. *Graphite under pressure: Equation of state and first-order Raman modes*. Phys. Rev. B **39** (17), 12598-12603 (1989). 61

[Hasegawa06] Y. Hasegawa, R. Konno, H. Nakano, and M. Kohmoto. *Zero modes of tight-binding electrons on the honeycomb lattice*. Phys. Rev. B **74** (3), 033413 (2006). 13

[Hecht02] E. Hecht. *Optics*. Addison Wesley, 4 edition, 2002. 38

[Heinecke76] R. A. H. Heinecke. *Plasma reactor design for the selective etching of SiO2 on Si*. Solid-State Electronics **19**, 1039-1040 (1976). 74

[Hencky15] H. Hencky. *Über den Spannungszustand in kreisrunden Platten mit verschwindender Biegungssteifigkeit*. Z. angew. Math. Phys. **63**, 311-317 (1915). xxii, 27, 98, 114, 115, 140, 158

[Hernandez08] Y. Hernandez, V. Nicolosi, M. Lotya, F. M. Blighe, Z. Sun, S. De, McGovernI. T., B. Holland, M. Byrne, Y. K. Gun'Ko, J. J. Boland, P. Niraj, G. Duesberg, S. Krishnamurthy, R. Goodhue, J. Hutchison, V. Scardaci, A. C. Ferrari, and J. N. Coleman. *High-yield production of graphene by liquid-phase exfoliation of graphite*. Nat Nano **3** (9), 563-568 (2008). 3

[Herziger12] F. Herziger, P. May, and J. Maultzsch. *Layer-number determination in graphene by out-of-plane phonons*. Phys. Rev. B **85** (23), 235447 (2012). 42, 117

[Herziger14] F. Herziger, M. Calandra, P. Gava, P. May, M. Lazzeri, F. Mauri, and J. Maultzsch. *Two-Dimensional Analysis of the Double-Resonant 2D Raman Mode in Bilayer Graphene*. Phys. Rev. Lett. **113** (18), 187401 (2014). 42, 167

[Hill11] E. W. Hill, A. Vijayaragahvan, and K. Novoselov. *Graphene Sensors*. Sensors Journal, IEEE **11** (12), 3161-3170 (2011). xxvii, 3, 35, 84, 159

[Hobson53] J. P. Hobson and W. A. Nierenberg. *The Statistics of a Two-Dimensional, Hexagonal Net*. Phys. Rev. **89** (3), 662 (1953). 14

[Huang09] M. Huang, H. Yan, C. Chen, D. Song, T. F. Heinz, and J. Hone. *Phonon softening and crystallographic orientation of strained graphene studied by Raman spectroscopy*. Proceedings of the National Academy of Sciences **106** (18), 7304-7308 (2009). 43, 54, 60, 103, 122, 134

[Huang10] M. Huang, H. Yan, T. F. Heinz, and J. Hone. *Probing Strain-Induced Electronic Structure Change in Graphene by Raman Spectroscopy*. Nano Lett. **10** (10), 4074-4079 (2010). 3, 49, 54, 56, 122

[Huang11] M. Huang, T. A. Pascal, H. Kim, W. A. Goddard, and J. R. Greer. *Electronic-Mechanical Coupling in Graphene from in situ Nanoindentation Experiments and Multiscale Atomistic Simulations*. Nano Lett. **11** (3), 1241-1246 (2011). 83, 94

[Hwang12] C. Hwang, D. A. Siegel, S.-K. Mo, W. Regan, A. Ismach, Y. Zhang, A. Zettl, and A. Lanzara. *Fermi velocity engineering in graphene by substrate modification*. Scientific Reports **2**, 590 (2012). 52, 90, 150

[Iijima80] S. Iijima. *Direct observation of the tetrahedral bonding in graphitized carbon black by high resolution electron microscopy*. Journal of Crystal Growth **50** (3), 675-683 (1980). 1

[Iijima93] S. Iijima and T. Ichihashi. *Single-shell carbon nanotubes of 1-nm diameter*. Nature **363** (6430), 603-605 (1993). 1

[Jackson62] J. D. Jackson. *Classical electrodynamics*. John Wiley & Sons, Ltd., 1962. 136

[Jiang09] J.-W. Jiang, J.-S. Wang, and B. Li. *Young's modulus of graphene: A molecular dynamics study*. Phys. Rev. B **80** (11), 113405 (2009). 98, 123, 124

[Jiang15] J.-W. Jiang, B.-S. Wang, J.-S. Wang, and H. S. Park. *A review on the flexural mode of graphene: lattice dynamics, thermal conduction, thermal expansion, elasticity and nanomechanical resonance*. Journal of Physics: Condensed Matter **27** (8), 083001 (2015). 159

[Jorio02] A. Jorio, A. G. Souza Filho, G. Dresselhaus, M. S. Dresselhaus, A. K. Swan, M. S. Ünlü, B. B. Goldberg, M. A. Pimenta, J. H. Hafner, C. M. Lieber, and

R. Saito. *G-band resonant Raman study of 62 isolated single-wall carbon nanotubes*. Phys. Rev. B **65** (15), 155412 (2002). 43

[Jung14] W. Jung, J. Park, T. Yoon, T.-S. Kim, S. Kim, and C.-S. Han. *Prevention of water permeation by strong adhesion between graphene and SiO_2 substrate*. Small **10** (9), 1704-1711 (2014). 27

[Kalbac10] M. Kalbac, A. Reina-Cecco, H. Farhat, J. Kong, L. Kavan, and M. S. Dresselhaus. *The Influence of Strong Electron and Hole Doping on the Raman Intensity of Chemical Vapor-Deposition Graphene*. ACS Nano **4** (10), 6055-6063 (2010). xvi, 43, 44, 52, 53

[Karimi97] A. Karimi, O. R. Shojaei, T. Kruml, and J. L. Martin. *Characterisation of TiN thin films using the bulge test and the nanoindentation technique*. Thin Solid Films **308-309**, 334-339 (1997). 34

[Kármán10] T. von Kármán. *Festigkeitsproblem im Maschinenbau*. Encyk. d. math. Wiss. **4**, 311-385 (1910). 33, 128

[Karssemeijer11] L. J. Karssemeijer and A. Fasolino. *Phonons of graphene and graphitic materials derived from the empirical potential LCBOPII*. Surface Science **605** (17–18), 1611-1615 (2011). 26

[Kashuba09] O. Kashuba and V. I. Falko. *Signature of electronic excitations in the Raman spectrum of graphene*. Phys. Rev. B **80** (24), 241404 (2009). 38

[Kim09] K. S. Kim, Y. Zhao, H. Jang, S. Y. Lee, J. M. Kim, K. S. Kim, J.-H. Ahn, P. Kim, J.-Y. Choi, and B. H. Hong. *Large-scale pattern growth of graphene films for stretchable transparent electrodes*. Nature **457** (7230), 706-710 (2009). 3

[Kim15a] S. J. Kim, T. Choi, B. Lee, S. Lee, K. Choi, J. B. Park, J. M. Yoo, Y. S. Choi, J. Ryu, P. Kim, J. Hone, and B. H. Hong. *Ultraclean Patterned Transfer of Single-Layer Graphene by Recyclable Pressure Sensitive Adhesive Films*. Nano Lett. **15** (5), 3236-3240 (2015). 83

[Kim15b] Y. D. Kim, H. Kim, Y. Cho, J. H. Ryoo, C.-H. Park, P. Kim, Y. S. Kim, S. Lee, Y. Li, S.-N. Park, Y. Shim Yoo, D. Yoon, V. E. Dorgan, E. Pop, T. F. Heinz, J. Hone, S.-H. Chun, H. Cheong, S. W. Lee, M.-H. Bae, and Y. D. Park. *Bright visible light emission from graphene*. Nat Nano **10** (8), 676-681 (2015). 38

[Kitt13] A. L. Kitt, Z. Qi, S. Rémi, H. S. Park, A. K. Swan, and B. B. Goldberg. *How graphene slides: Measurement and theory of strain-dependent frictional forces between graphene and SiO_2*. Nano Lett. **13** (6), 2605-2610 (2013). 60, 61, 122, 123, 130

[Klintenberg09] M. Klintenberg, S. Lebègue, C. Ortiz, B. Sanyal, J. Fransson, and O. Eriksson. *Evolving properties of two-dimensional materials: from graphene to graphite*. J. Phys.: Condens. Matter **21** (33), 335502 (2009). 67, 68

[Koenig11] S. P. Koenig, N. G. Boddeti, M. L. Dunn, and J. S. Bunch. *Ultrastrong adhesion of graphene membranes*. Nat Nano **6** (9), 543-546 (2011). xxii, 3, 26, 27, 60, 62, 83, 97, 98, 99, 115, 120, 121, 124, 157

[Koenig13] S. P. Koenig. *Graphene Membranes: Mechanics, Adhesion, and Gas Separations*. PhD thesis, University of Colorado, (2013). 114

[Kohn59] W. Kohn. *Image of the Fermi surface in the vibration spectrum of a metal*. Phys. Rev. Lett. **2** (9), 393-394 (1959). 26

[Komaragiri05] U. Komaragiri, M. R. Begley, and J. G. Simmonds. *The Mechanical Response of Freestanding Circular Elastic Films Under Point and Pressure Loads*. Journal of Applied Mechanics **72** (2), 203-212 (2005). 34

[Koningstein73] J. A. Koningstein. *Raman Spectroscopy Involving Electronic Levels*. Annual Review of Physical Chemistry **24**, 121-134 (1973). 38

[Koppens14] F. H. L. Koppens, T. Mueller, Ph. Avouris, A. C. Ferrari, M. S. Vitiello, and M. Polini. *Photodetectors based on graphene, other two-dimensional materials and hybrid systems*. Nat Nano **9** (10), 780-793 (2014). 158

[Kürti02] J. Kürti, V. Zólyomi, A. Grüneis, and H. Kuzmany. *Double resonant Raman phenomena enhanced by van Hove singularities in single-wall carbon nanotubes*. Phys. Rev. B **65** (16), 165433 (2002). 49

[Kuzmenko08] A. B. Kuzmenko, E. van Heumen, F. Carbone, and D. van der Marel. *Universal Optical Conductance of Graphite*. Phys. Rev. Lett. **100** (11), 117401 (2008). 20

[Lafkioti10] M. Lafkioti, B. Krauss, T. Lohmann, U. Zschieschang, H. Klauk, K. v. Klitzing, and J. H. Smet. *Graphene on a Hydrophobic Substrate: Doping Reduction and Hysteresis Suppression under Ambient Conditions*. Nano Lett. **10** (4), 1149-1153 (2010). 19

[Lambert60] J. H. Lambert. *Photometria sive de mensura et gradibus luminis, colorum et umbrae*. Eberhardt Klett, 1760. 19

[Land92] T.A. Land, T. Michely, R.J. Behm, J.C. Hemminger, and G. Comsa. *STM investigation of single layer graphite structures produced on Pt(111) by hydrocarbon decomposition*. Surf. Sci. **264** (3), 261-270 (1992). 3

[Landau60] L. D. Landau and E. M. Lifshitz. *Electrodynamics of continuous media*, volume 8. Pergamon Press, 1 edition, 1960. 136

[Landau70] L. D. Landau and E. M. Lifshitz. *Theory of elasticity*, volume 7. Pergamon Press, 2 edition, 1970. xvii, 28, 31, 33, 34, 158

[Lazzeri06] M. Lazzeri and F. Mauri. *Nonadiabatic Kohn Anomaly in a Doped Graphene Monolayer*. Phys. Rev. Lett. **97** (26), 266407 (2006). xvi, xxv, 4, 44, 51, 52, 59, 151, 153

[Lazzeri08] M. Lazzeri, C. Attaccalite, L. Wirtz, and F. Mauri. *Impact of the electron-electron correlation on phonon dispersion: Failure of LDA and GGA DFT functionals in graphene and graphite*. Phys. Rev. B **78** (8), 081406 (2008). xv, 24, 25, 26, 48, 92

[Lee08] C. Lee, X. Wei, J. W. Kysar, and J. Hone. *Measurement of the elastic properties and intrinsic strength of monolayer graphene*. Science **321** (5887), 385-388 (2008). xxiii, 1, 3, 6, 83, 94, 98, 120, 123, 124

[Lee09] C. Lee, X. Wei, Q. Li, R. Carpick, J. W. Kysar, and J. Hone. *Elastic and frictional properties of graphene*. Phys. Status Solidi B **246** (11-12), 2562-2567 (2009). 120

[Lee12a] J. E. Lee, G. Ahn, J. Shim, Y. S. Lee, and S. Ryu. *Optical separation of mechanical strain from charge doping in graphene*. Nature Communications **3**, 1024 (2012). xvii, xix, xxii, 3, 4, 22, 56, 61, 87, 92, 93, 103, 122, 128, 129

[Lee12b] J.-U. Lee, D. Yoon, and H. Cheong. *Estimation of Young's modulus of graphene by Raman spectroscopy*. Nano Lett. **12** (9), 4444-4448 (2012). xxii, xxiii, 48, 60, 61, 83, 87, 98, 103, 121, 122, 123, 124, 127

[Lee14] J. H. Lee, J. Y. Tan, C.-T. Toh, S. P. Koenig, V. E. Fedorov, A. H. Castro Neto, and B. Azyilmaz. *Nanometer Thick Elastic Graphene Engine*. Nano Lett. **14** (5), 2677-2680 (2014). 98

[Lee15] J.-U. Lee, M. Kim, and H. Cheong. *Raman Spectroscopic Studies on Two-Dimensional Materials*. Applied Microscopy **45** (3), 126-130 (2015). 159

[Li09] X. Li, W. Cai, J. An, S. Kim, J. Nah, D. Yang, R. Piner, A. Velamakanni, I. Jung, E. Tutuc, S. K. Banerjee, L. Colombo, and R. S. Ruoff. *Large-Area Synthesis of High-Quality and Uniform Graphene Films on Copper Foils*. Science **324** (5932), 1312-1314 (2009). 3

[Li12] S.-L. Li, H. Miyazaki, H. Song, H. Kuramochi, S. Nakaharai, and K. Tsukagoshi. *Quantitative Raman Spectrum and Reliable Thickness Identification for Atomic Layers on Insulating Substrates*. ACS Nano **6** (8), 7381-7388 (2012). 62

[Liao15] P. Liao and P. Xu. *Effect of initial tension on mechanics of adhered graphene blisters*. Appl. Phys. A **120** (4), 1503-1509 (2015). 83, 98

[Liu11] H. Liu, Y. Liu, and D. Zhu. *Chemical doping of graphene*. J. Mater. Chem. **21** (10), 3335-3345 (2011). 17

[Lorchat15] E. Lorchat, G. Froehlicher, and S. Berciaud. *Splitting of interlayer shear modes and photon energy dependent anisotropic Raman response in N-layer $ReSe_2$ and ReS_2*. arXiv **-**, 151203842 (2015). 159

[Loudon64] C. Loudon. *The Raman effect in crystals*. Advances in Physics **13**, - (1964). 22, 41

[Lu04] C. Lu, Q. Fu, S. Huang, and J. Liu. *Polymer Electrolyte-Gated Carbon Nanotube Field-Effect Transistor*. Nano Lett. **4** (4), 623-627 (2004). 17

[Lu10] Z. Lu and M. L. Dunn. *Van der Waals adhesion of graphene membranes*. Journal of Applied Physics **107** (4), 044301 (2010). xxii, 98, 116, 120

[Lucchese10] M. M. Lucchese, F. Stavale, E. H. Martins Ferreira, C. Vilani, M. V. O. Moutinho, R. B. Capaz, C. A. Achete, and A. Jorio. *Quantifying ion-induced defects and Raman relaxation length in graphene*. Carbon **48** (5), 1592-1597 (2010). 3, 42, 46

[Lui10] C. H. Lui, K. F. Mak, J. Shan, and T. F. Heinz. *Ultrafast Photoluminescence from Graphene*. Phys. Rev. Lett. **105** (12), 127404 (2010). 22, 38

[Lui12] C. H. Lui, L. M. Malard, S. H. Kim, G. Lantz, F. E. Laverge, R. Saito, and T. F. Heinz. *Observation of Layer-Breathing Mode Vibrations in Few-Layer*

Graphene through Combination Raman Scattering. Nano Lett. **12** (11), 5539-5544 (2012). 38, 42

[Lui13] C. H. Lui and T. F. Heinz. *Measurement of layer breathing mode vibrations in few-layer graphene*. Phys. Rev. B **87** (12), 121404 (2013). 26

[Lui14] C. H. Lui, Z. Ye, C. Keiser, X. Xiao, and R. He. *Temperature-Activated Layer-Breathing Vibrations in Few-Layer Graphene*. Nano Lett. **14** (8), 4615-4621 (2014). 23, 42

[Luo12] Z. Luo, C. Cong, J. Zhang, Q. Xiong, and T. Yu. *Direct observation of inner and outer G' band double-resonance Raman scattering in free standing graphene*. Applied Physics Letters **100** (24), 243107 (2012). 48

[Mafra11] D. L. Mafra, E. A. Moujaes, S. K. Doorn, H. Htoon, R. W. Nunes, and M. A. Pimenta. *A study of inner process double-resonance Raman scattering in bilayer graphene*. Carbon **49** (5), 1511-1515 (2011). 49

[Mahmood15] A. Mahmood, C.-S. Yang, J.-F. Dayen, S. Park, M. V. Kamalakar, D. Metten, S. Berciaud, J.-O. Lee, and B. Doudin. *Room temperature dry processing of patterned CVD graphene devices*. Carbon **86**, 256-263 (2015). 80

[Mak08] K. F. Mak, M. Y. Sfeir, Y. Wu, C. H. Lui, J. A. Misewich, and T. F. Heinz. *Measurement of the Optical Conductivity of Graphene*. Phys. Rev. Lett. **101** (19), 196405 (2008). 17, 20

[Mak12] K. F. Mak, L. Ju, F. Wang, and T. F. Heinz. *Optical spectroscopy of graphene: From the far infrared to the ultraviolet*. Solid State Commun. **152** (15), 1341-1349 (2012). 17, 22

[Mak14] K. F. Mak, F. H. da Jornada, K. He, J. Deslippe, N. Petrone, J. Hone, J. Shan, S. G. Louie, and T. F. Heinz. *Tuning Many-Body Interactions in Graphene: The Effects of Doping on Excitons and Carrier Lifetimes*. Phys. Rev. Lett. **112** (20), 207401 (2014). 150

[Malard09a] L. M. Malard, M. H. D. Guimarães, D. L. Mafra, M. S. C. Mazzoni, and A. Jorio. *Group-theory analysis of electrons and phonons in N-layer graphene systems*. Phys. Rev. B **79** (12), 125426 (2009). 22, 23, 24

[Malard09b] L. M. Malard, M. A. Pimenta, G. Dresselhaus, and M. S. Dresselhaus. *Raman spectroscopy in graphene*. Physics Reports **473** (5–6), 51-87 (2009). 3, 22, 41, 42, 117, 159

[Malitson65] I. H. Malitson. *Interspecimen Comparison of the Refractive Index of Fused Silica*. J. Opt. Soc. Am. **55** (10), 1205-1208 (1965). 67

[Martin08] J. Martin, N. Akerman, G. Ulbricht, T. Lohmann, J. H. Smet, K. von Klitzing, and A. Yacoby. *Observation of electron-hole puddles in graphene using a scanning single-electron transistor*. Nat Phys **4** (2), 144-148 (2008). 3, 18, 19, 26, 27, 53, 93

[Martin15] S. C. Martin, S. Samaddar, B. Sacépé, A. Kimouche, J. Coraux, F. Fuchs, B. Grévin, H. Courtois, and C. B. Winkelmann. *Disorder and screening in decoupled graphene on a metallic substrate*. Phys. Rev. B **91** (4), 041406 (2015). 19

[Martins Ferreira10] E. H. Martins Ferreira, M. V. O. Moutinho, F. Stavale, M. M. Lucchese, R. B. Capaz, C. A. Achete, and A. Jorio. *Evolution of the Raman spectra from single-, few-, and many-layer graphene with increasing disorder*. Phys. Rev. B **82** (12), 125429 (2010). 46

[Martins13] L. G. P. Martins, Y. Song, T. Zeng, M. S. Dresselhaus, J. Kong, and P. T. Araujo. *Direct transfer of graphene onto flexible substrates*. Proceedings of the National Academy of Sciences **110** (44), 17762-17767 (2013). 3

[Maultzsch04a] J. Maultzsch, S. Reich, and C. Thomsen. *Double-resonant Raman scattering in graphite: Interference effects, selection rules, and phonon dispersion*. Physical Review B **70** (15), 155403 (2004). 47, 86

[Maultzsch04b] J. Maultzsch, S. Reich, C. Thomsen, H. Requardt, and P. Ordejón. *Phonon Dispersion in Graphite*. Phys. Rev. Lett. **92** (7), 075501 (2004). xv, 24, 25, 26

[Medvedyeva11] M. V. Medvedyeva and Y. M. Blanter. *Piezoconductivity of gated suspended graphene*. Phys. Rev. B **83**, 045426 (2011). xxiv, 34, 83, 116, 128, 138, 139, 140, 141, 158

[Metten13] D. Metten, F. Federspiel, M. Romeo, and S. Berciaud. *Probing built-in strain in freestanding graphene monolayers by Raman spectroscopy*. Phys. Status Solidi B **250**, 2681-2688 (2013). 95

[Metten14] D. Metten, F. Federspiel, M. Romeo, and S. Berciaud. *All-optical blister test of suspended graphene using micro-Raman spectroscopy*. Phys. Rev. Applied **2** (5), 054008 (2014). 125

[Metten15] D. Metten, G. Froehlicher, and S. Berciaud. *Doping- and interference-free measurement of I_{2D}/I_G in suspended monolayer graphene blisters*. Phys. Status Solidi B **252** (11), 2390-2394 (2015). 125

[Metzger09] C. Metzger, S. Rémi, M. Liu, S. V. Kusminskiy, A. H. Castro Neto, A. K. Swan, and B. B. Goldberg. *Biaxial Strain in Graphene Adhered to Shallow Depressions*. Nano Lett. **10** (1), 6-10 (2009). xxii, 4, 54, 61, 87, 123

[Meyer07] J. C. Meyer, A. K. Geim, M. I. Katsnelson, K. S. Novoselov, T. J. Booth, and S. Roth. *The structure of suspended graphene sheets*. Nature **446** (7131), 60-63 (2007). 3, 6, 19, 27

[Miller09] D. L. Miller, K. D. Kubista, G. M. Rutter, M. Ruan, W. A. de Heer, P. N. First, and J. A. Stroscio. *Observing the Quantization of Zero Mass Carriers in Graphene*. Science **324** (5929), 924-927 (2009). 38

[Mizuno13] Naomi Mizuno, Bent Nielsen, and Xu Du. *Ballistic-like supercurrent in suspended graphene Josephson weak links*. Nat Commun **4**, - (2013). 4

[Mohiuddin09] T. M. G. Mohiuddin, A. Lombardo, R. R. Nair, A. Bonetti, G. Savini, R. Jalil, N. Bonini, D. M. Basko, C. Galiotis, N. Marzari, K. S. Novoselov, A. K. Geim, and A. C. Ferrari. *Uniaxial strain in graphene by Raman spectroscopy: G peak splitting, Gruneisen parameters, and sample orientation*. Phys. Rev. B **79** (20), 205433 (2009). xvi, xxii, 3, 22, 43, 54, 55, 60, 61, 84, 103, 104, 122, 123, 124, 134

[Mohr07] M. Mohr, J. Maultzsch, E. Dobardžić, S. Reich, I. Milošević, M. Damnjanović, A. Bosak, M. Krisch, and C. Thomsen. *Phonon dispersion of graphite by inelastic x-ray scattering*. Phys. Rev. B **76** (3), 035439 (2007). xv, 24, 25

[Mohr09] M. Mohr, K. Papagelis, J. Maultzsch, and C. Thomsen. *Two-dimensional electronic and vibrational band structure of uniaxially strained graphene from ab initio calculations*. Phys. Rev. B **80** (20), 205410 (2009). 1, 43, 54

[Mohr10] M. Mohr, J. Maultzsch, and C. Thomsen. *Splitting of the Raman 2D band of graphene subjected to strain*. Phys. Rev. B **82** (20), 201409 (2010). 49, 84, 134

[Mounet05] N. Mounet and N. Marzari. *First-principles determination of the structural, vibrational and thermodynamic properties of diamond, graphite, and derivatives*. Phys. Rev. B **71** (20), 205214 (2005). 24

[Nair08a] R. R. Nair, P. Blake, A. N. Grigorenko, K. S. Novoselov, T. J. Booth, T. Stauber, N. M. R. Peres, and A. K. Geim. *Fine Structure Constant Defines Visual Transparency of Graphene*. Science **320** (5881), 1308 (2008). 20, 21

[Nair08b] R. R. Nair, P. Blake, A. N. Grigorenko, K. S. Novoselov, T. J. Booth, T. Stauber, N. M. R. Peres, and A. K. Geim. *Universal Dynamic Conductivity and Quantized Visible Opacity of Suspended Graphene*. arXiv **-**, 0803.3718 (2008). 1, 21

[Narula14] R. Narula and S. Reich. *Graphene band structure and its 2D Raman mode*. Phys. Rev. B **90** (8), 085407 (2014). 1, 86

[Neek-Amal10] M. Neek-Amal and F. M. Peeters. *Nanoindentation of a circular sheet of bilayer graphene*. Phys. Rev. B **81** (23), 235421 (2010). 120

[Nemanich77] R.J. Nemanich, G. Lucovsky, and S.A. Solin. *Infrared active optical vibrations of graphite*. Solid State Communications **23** (2), 117-120 (1977). 1, 22, 23

[Nemanich79] R. J. Nemanich and S. A. Solin. *First- and second-order Raman scattering from finite-size crystals of graphite*. Phys. Rev. B **20** (2), 392-401 (1979). 44

[Nemanich80] R. J. Nemanich, C. C. Tsai, and G. A. N. Connell. *Interference-Enhanced Raman Scattering of Very Thin Titanium and Titanium Oxide Films*. Phys. Rev. Lett. **44** (4), 273-276 (1980). 72

[Neumann15a] C. Neumann, S. Reichardt, M. Drögeler, B. Terrés, K. Watanabe, T. Taniguchi, B. Beschoten, S. V. Rotkin, and C. Stampfer. *Low B Field Magneto-Phonon Resonances in Single-Layer and Bilayer Graphene*. Nano Lett. **15** (3), 1547-1552 (2015). 38

[Neumann15b] C. Neumann, S. Reichardt, P. Venezuela, M. Drogeler, L. Banszerus, M. Schmitz, K. Watanabe, T. Taniguchi, F. Mauri, B. Beschoten, S. V. Rotkin, and C. Stampfer. *Raman spectroscopy as probe of nanometre-scale strain variations in graphene*. Nat Commun **6**, 8429 (2015). 38, 94

[Ni07] Z. H. Ni, H. M. Wang, J. Kasim, H. M. Fan, T. Yu, Y. H. Wu, Y. P. Feng, and Z. X. Shen. *Graphene Thickness Determination Using Reflection and Contrast Spectroscopy*. Nano Lett. **7** (9), 2758-2763 (2007). 3, 67, 68, 83

[Ni09] Z. H. Ni, T. Yu, Z. Q. Luo, Y. Y. Wang, L. Liu, C. P. Wong, J. Miao, W. Huang, and Z. X. Shen. *Probing charged impurities in suspended graphene using Raman spectroscopy*. ACS Nano **3** (3), 569-574 (2009). 19, 56, 106

[Ni10] Z. H. Ni, H. M. Wang, Z. Q. Luo, Y. Y. Wang, T. Yu, Y. H. Wu, and Z. X. Shen. *The effect of vacuum annealing on graphene*. J. Raman Spectrosc. **41** (5), 479-483 (2010). 93

[Nicholl15] R. J. T. Nicholl, H. J. Conley, N. V. Lavrik, I. Vlassiouk, Y. S. Puzyrev, V. P. Sreenivas, S. T. Pantelides, and K. I. Bolotin. *The effect of intrinsic crumpling on the mechanics of free-standing graphene*. Nat. Commun. **6**, 8789 (2015). 120, 123

[Nicklow72] R. Nicklow, N. Wakabayashi, and H. G. Smith. *Lattice Dynamics of Pyrolytic Graphite*. Phys. Rev. B **5** (12), 4951-4962 (1972). 1, 24

[Novoselov04] K. S. Novoselov, A. K. Geim, S. V. Morozov, D. Jiang, Y. Zhang, S. V. Dubonos, I. V. Grigorieva, and A. A. Firsov. *Electric Field Effect in Atomically Thin Carbon Films*. Science **306** (5696), 666-669 (2004). 1, 17, 74, 158

[Novoselov05a] K. S. Novoselov, A. K. Geim, S. V. Morozov, D. Jiang, M. I. Katsnelson, I. V. Grigorieva, S. V. Dubonos, and A. A. Firsov. *Two-dimensional gas of massless Dirac fermions in graphene*. Nature **438** (7065), 197-200 (2005). xiii, 17, 150

[Novoselov05b] K. S. Novoselov, D. Jiang, F. Schedin, T. J. Booth, V. V. Khotkevich, S. V. Morozov, and A. K. Geim. *Two-dimensional atomic crystals*. Proc. Natl. Acad. Sci. U. S. A. **102** (30), 10451-10453 (2005). 1, 74

[O'Connell10] A. D. O'Connell, M. Hofheinz, M. Ansmann, R. C. Bialczak, M. Lenander, E. Lucero, M. Neeley, D. Sank, H. Wang, M. Weides, J. Wenner, J. M. Martinis, and A. N. Cleland. *Quantum ground state and single-phonon control of a mechanical resonator*. Nature **464** (7289), 697-703 (2010). 159

[Oshima88] C. Oshima, T. Aizawa, R. Souda, Y. Ishizawa, and Y. Sumiyoshi. *Surface phonon dispersion curves of graphite (0001) over the entire energy region*. Solid State Communications **65** (12), 1601-1604 (1988). 24

[Park07] C.-H. Park, F. Giustino, M. L. Cohen, and S. G. Louie. *Velocity Renormalization and Carrier Lifetime in Graphene from the Electron-Phonon Interaction*. Phys. Rev. Lett. **99** (8), 086804 (2007). 22

[Peres06] N. M. R. Peres, A. H. Castro Neto, and F. Guinea. *Conductance quantization in mesoscopic graphene*. Phys. Rev. B **73** (19), 195411 (2006). 17

[Pietronero81] L. Pietronero and S. Strässler. *Bond-Length Change as a Tool to Determine Charge Transfer and Electron-Phonon Coupling in Graphite Intercalation Compounds*. Phys. Rev. Lett. **47** (8), 593-596 (1981). 51

[Pimenta07] M. A. Pimenta, G. Dresselhaus, M. S. Dresselhaus, L. G. Cancado, A. Jorio, and R. Saito. *Studying disorder in graphite-based systems by Raman spectroscopy*. Phys. Chem. Chem. Phys. **9** (11), 1276-1290 (2007). 22, 42, 46

[Pisana07] S. Pisana, M. Lazzeri, C. Casiraghi, K. S. Novoselov, A. K. Geim, A. C. Ferrari, and F. Mauri. *Breakdown of the adiabatic Born-Oppenheimer approximation in graphene*. Nat. Mater. **6** (3), 198-201 (2007). xvi, xxv, 3, 51, 52, 86, 87

[Piscanec04] S. Piscanec, M. Lazzeri, Francesco Mauri, A. C. Ferrari, and J. Robertson. *Kohn Anomalies and Electron-Phonon Interactions in Graphite*. Phys. Rev. Lett. **93** (18), 185503 (2004). 24, 26, 59

[Piscanec07] S. Piscanec, M. Lazzeri, J. Robertson, A. C. Ferrari, and F. Mauri. *Optical phonons in carbon nanotubes: Kohn anomalies, Peierls distortions, and dynamic effects*. Phys. Rev. B **75** (3), 035427 (2007). 43, 52

[Pócsik98] I. Pócsik, M. Hundhausen, M. Koós, and L. Ley. *Origin of the D peak in the Raman spectrum of microcrystalline graphite*. Journal of Non-Crystalline Solids **227-230, Part 2**, 1083-1086 (1998). 44, 56

[Poilane00] C. Poilane, P. Delobelle, C. Lexcellent, S. Hayashi, and H. Tobushi. *Analysis of the mechanical behavior of shape memory polymer membranes by nanoindentation, bulging and point membrane deflection tests*. Thin Solid Films **379** (1–2), 156-165 (2000). 34

[Polyzos15] I. Polyzos, M. Bianchi, L. Rizzi, E. N. Koukaras, J. Parthenios, K. Papagelis, R. Sordan, and C. Galiotis. *Suspended monolayer graphene under true uniaxial deformation*. Nanoscale **7** (30), 13033-13042 (2015). 43, 56, 60, 84, 134

[Poncharal99] P. Poncharal, Z. L. Wang, D. Ugarte, and W. A. de Heer. *Electrostatic Deflections and Electromechanical Resonances of Carbon Nanotubes*. Science **283** (5407), 1513-1516 (1999). 127

[Pop12] E. Pop, V. Varshney, and A. K. Roy. *Thermal properties of graphene: Fundamentals and applications*. MRS Bulletin **37** (12), 1273-1281 (2012). 1

[Popov13] V. N. Popov and P. Lambin. *Theoretical 2D Raman band of strained graphene*. Phys. Rev. B **87** (15), 155425 (2013). 56, 84, 107, 134

[Proctor09] J. E. Proctor, E. Gregoryanz, K. S. Novoselov, M. Lotya, J. N. Coleman, and M. P. Halsall. *High-pressure Raman spectroscopy of graphene*. Phys. Rev. B **80** (7), 073408 (2009). 61

[Puller13] V. Puller, B. Lounis, and F. Pistolesi. *Single molecule detection of nanomechanical motion*. Phys. Rev. Lett. **110** (12), 125501 (2013). xxvii, 155, 159

[Raman28] C. V. Raman. *A new radiation*. Indian J. Phys. **2**, 387-398 (1928). 3, 38

[Rao11] R. Rao, D. Tishler, J. Katoch, and M. Ishigami. *Multiphonon Raman scattering in graphene*. Phys. Rev. B **84** (11), 113406 (2011). 43

[Reed91] W. P. Reed. *Standard Reference Material 739*. Certificate, National Institue of Standards and Technology, Gaithersburg, (1991). 144

[Reich02] S. Reich, J. Maultzsch, C. Thomsen, and P. Ordejón. *Tight-binding description of graphene*. Phys. Rev. B **66** (3), 035412 (2002). xiv, 11

[Reich04] S. Reich and C. Thomsen. *Raman spectroscopy of graphite*. Philosophical Transactions of the Royal Society of London A: Mathematical, Physical and Engineering Sciences **362** (1824), 2271-2288 (2004). 1, 40

[Reina09] A. Reina, X. Jia, J. Ho, D. Nezich, H. Son, V. Bulovic, M. S. Dresselhaus, and J. Kong. *Large area, few-layer graphene films on arbitrary substrates by chemical vapor deposition*. Nano Lett. **9** (1), 30-35 (2009). 3

[Reserbat-Plantey12] A. Reserbat-Plantey, L. Marty, O. Arcizet, N. Bendiab, and V. Bouchiat. *A local optical probe for measuring motion and stress in a nanoelectromechanical system*. Nature Nano **7** (3), 151-155 (2012). 112, 127

[Reserbat-Plantey13] A. Reserbat-Plantey, S. Klyatskaya, V. Reita, L. Marty, O. Arcizet, M. Ruben, N. Bendiab, and V. Bouchiat. *Time- and space-modulated Raman signals in graphene-based optical cavities*. Journal of Optics **15** (11), 114010 (2013). 4, 62, 94

[Reserbat-Plantey15] A. Reserbat-Plantey, K. G. Schädler, L. Gaudreau, G. Navickaite, J. Güttinger, D. Chang, C. Toninelli, A. Bachtold, and F. H. L. Koppens. *Electro-mechanical control of an optical emitter using graphene*. arXiv preprint **-**, arXiv:1504.08275 (2015). xxvii, 35, 127, 155, 158

[Ryu08] S. Ryu, M. Y. Han, J. Maultzsch, T. F. Heinz, P. Kim, M. L. Steigerwald, and L. E. Brus. *Reversible Basal Plane Hydrogenation of Graphene*. Nano Lett. **8** (12), 4597-4602 (2008). 88

[Ryu10] S. Ryu, L. Liu, S. Berciaud, Y.-J. Yu, H. Liu, P. Kim, G. W. Flynn, and L. E. Brus. *Atmospheric Oxygen Binding and Hole Doping in Deformed Graphene on a SiO2 Substrate*. Nano Lett. **10** (12), 4944-4951 (2010). 19, 88, 93

[Saha08] S. K. Saha, U. V. Waghmare, H. R. Krishnamurthy, and A. K. Sood. *Phonons in few-layer graphene and interplanar interaction: A first-principles study*. Phys. Rev. B **78** (16), 165421 (2008). 24, 41

[Sahoo05] S. Sahoo, T. Kontos, C. Schönenberger, and C. Sürgers. *Electrical spin injection in multiwall carbon nanotubes with transparent ferromagnetic contacts*. Applied Physics Letters **86** (11), 112109 (2005). 1

[Sakhaee-Pour08] A. Sakhaee-Pour, M.T. Ahmadian, and A. Vafai. *Applications of single-layered graphene sheets as mass sensors and atomistic dust detectors*. Solid State Commun. **145** (4), 168-172 (2008). 84

[Sandler03] J. Sandler, M. S. P. Shaffer, A. H. Windle, M. P. Halsall, M. A. Montes-Moran, C. A. Cooper, and R. J. Young. *Variations in the Raman peak shift as a function of hydrostatic pressure for various carbon nanostructures: A simple geometric effect*. Phys. Rev. B **67** (3), 035417 (2003). 61

[Sato11] K. Sato, J. S. Park, R. Saito, C. Cong, T. Yu, C. H. Lui, T. F. Heinz, G. Dresselhaus, and M. S. Dresselhaus. *Raman spectra of out-of-plane phonons in bilayer graphene*. Phys. Rev. B **84** (3), 035419 (2011). 38, 42

[Schwarz15] C. Schwarz. *Oral communication*. Institut Néel, Grenoble, (2015). 139

[Shafraniuk15] S. Shafraniuk. *Graphene - Fundamental, Devices and Applications*. Pan Stanford Publishing, 2015. 51

[Shang11] J. Shang, T. Yu, J. Lin, and G. G. Gurzadyan. *Ultrafast Electron-Optical Phonon Scattering and Quasiparticle Lifetime in CVD-Grown Graphene*. ACS Nano **5** (4), 3278-3283 (2011). 38

[Shi09] Y. Shi, X. Dong, P. Chen, J. Wang, and L.-J. Li. *Effective doping of single-layer graphene from underlying SiO_2 substrates*. Phys. Rev. B **79** (11), 115402 (2009). 19

[Shi14] J.-X. Shi, T. Natsuki, X.-W. Lei, and Q.-Q. Ni. *Equivalent Young's modulus and thickness of graphene sheets for the continuum mechanical models*. Applied Physics Letters **104** (22), 223101 (2014). 121

[Shivaraman09] S. Shivaraman, R. A. Barton, X. Yu, J. Alden, L. Herman, M. V. S. Chandrashekhar, J. Park, P. L. McEuen, J. M. Parpia, H. G. Craighead, and M. G. Spencer. *Free-Standing Epitaxial Graphene*. Nano Lett. **9** (9), 3100-3105 (2009). 6

[Siebentritt97] S. Siebentritt, R. Pues, K.-H. Rieder, and A. M. Shikin. *Surface phonon dispersion in graphite and in a lanthanum graphite intercalation compound*. Phys. Rev. B **55** (12), 7927-7934 (1997). 24

[Siegel13] D. A. Siegel, W. Regan, A. V. Fedorov, A. Zettl, and A. Lanzara. *Charge-Carrier Screening in Single-Layer Graphene*. Phys. Rev. Lett. **110**, 146802 (2013). 52, 150

[Singh10] V. Singh, S. Sengupta, H. S. Solanki, R. Dhall, A. Allain, S. Dhara, P. Pant, and M. M. Deshmukh. *Probing thermal expansion of graphene and modal dispersion at low-temperature using graphene nanoelectromechanical systems resonators*. Nanotechnology **21** (16), 165204 (2010). 35, 84, 144

[Singh14] V. Singh, S. J. Bosman, B. H. Schneider, Y. M. Blanter, A. Castellanos-Gomez, and G. A. Steele. *Optomechanical coupling between a multilayer graphene mechanical resonator and a superconducting microwave cavity*. Nat Nano **9** (10), 820-824 (2014). 94

[Smekal23] A. Smekal. *Zur Quantentheorie der Dispersion*. Naturwissenschaften **11**, 873-875 (1923). 38

[Sommer15] B. Sommer, J. Sonntag, A. Ganczarczyk, D. Braam, G. Prinz, A. Lorke, and M. Geller. *Electron-beam induced nano-etching of suspended graphene*. Sci. Rep. **5**, 7781 (2015). 4

[Song10] Y. J. Song, A. F. Otte, Y. Kuk, Y. Hu, D. B. Torrance, P. N. First, W. A. de Heer, H. Min, S. Adam, M. D. Stiles, A. H. MacDonald, and J. A. Stroscio. *High-*

resolution tunnelling spectroscopy of a graphene quartet. Nature **467** (7312), 185-189 (2010). 38

[Song14] X. Song, M. Oksanen, J. Li, P. J. Hakonen, and M. A. Sillanpää. *Graphene Optomechanics Realized at Microwave Frequencies*. Phys. Rev. Lett. **113** (2), 027404 (2014). 159

[Stampfer07] C. Stampfer, F. Molitor, D. Graf, K. Ensslin, A. Jungen, C. Hierold, and L. Wirtz. *Raman imaging of doping domains in graphene on SiO2*. Applied Physics Letters **91** (24), 241907 (2007). 3

[Strutt99] J. Strutt. *On the transmission of light through an atmosphere containing small particles in suspension, and on the origin of the blue of the sky*. Philosophical Magazine **5** (47), 375-394 (1899). 38

[Suk11] J. W. Suk, A. Kitt, C. W. Magnuson, Y. Hao, S. Ahmed, J. An, A. K. Swan, B. B. Goldberg, and R. S. Ruoff. *Transfer of CVD-Grown Monolayer Graphene onto Arbitrary Substrates*. ACS Nano **5** (9), 6916-6924 (2011). 3

[Suleimanov93] R. A. Suleimanov and N. A. Abdullaev. *The nature of negative linear expansion of graphite crystals*. Carbon **31** (7), 1011-1013 (1993). 144

[Sun08] D. Sun, Z.-K. Wu, C. Divin, X. Li, C. Berger, W. A. de Heer, P. N. First, and T. B. Norris. *Ultrafast Relaxation of Excited Dirac Fermions in Epitaxial Graphene Using Optical Differential Transmission Spectroscopy*. Phys. Rev. Lett. **101** (15), 157402 (2008). 38

[Tan98] P. H. Tan, Y. M. Deng, and Q. Zhao. *Temperature-dependent Raman spectra and anomalous Raman phenomenon of highly oriented pyrolytic graphite*. Phys. Rev. B **58** (9), 5435-5439 (1998). 43

[Tan07] Y.-W. Tan, Y. Zhang, K. Bolotin, Y. Zhao, S. Adam, E. H. Hwang, S. Das Sarma, H. L. Stormer, and P. Kim. *Measurement of Scattering Rate and Minimum Conductivity in Graphene*. Phys. Rev. Lett. **99** (24), 246803 (2007). 17

[Tan12] P. H. Tan, W. P. Han, W. J. Zhao, Z. H. Wu, K. Chang, H. Wang, Y. F. Wang, N. Bonini, N. Marzari, N. Pugno, G. Savini, A. Lombardo, and A. C. Ferrari. *The shear mode of multilayer graphene*. Nat. Mater. **11** (4), 294-300 (2012). 26, 41, 117

[Tan13] X. Tan, J. Wu, K. Zhang, X. Peng, L. Sun, and J. Zhong. *Nanoindentation models and Young's modulus of monolayer graphene: A molecular dynamics study*. Appl. Phys. Lett. **102** (7), - (2013). 1, 98, 123, 124

[Teufel11] J. D. Teufel, T. Donner, Dale Li, J. W. Harlow, M. S. Allman, K. Cicak, A. J. Sirois, J. D. Whittaker, K. W. Lehnert, and R. W. Simmonds. *Sideband cooling of micromechanical motion to the quantum ground state*. Nature **475** (7356), 359-363 (2011). 159

[Thomsen00] C. Thomsen and S. Reich. *Double Resonant Raman Scattering in Graphite*. Phys. Rev. Lett. **85** (24), 5214-5217 (2000). xv, 45, 49

[Thomsen02] C. Thomsen, S. Reich, and P. Ordejón. *Ab initio determination of the phonon deformation potentials of graphene*. Phys. Rev. B **65** (7), 073403 (2002). xxii, 61, 123, 124

[Thomsen04] C. Thomsen, S. Reich, and J. Maultzsch. *Carbon Nanotubes: Basic Concepts and Physical Properties*. Wiley Subscription Services, Inc., A Wiley Company, 2004. 11, 16

[Tiberj13] A. Tiberj, M. Rubio-Roy, M. Paillet, J. R. Huntzinger, P. Landois, M. Mikolasek, S. Contreras, J. L. Sauvajol, E. Dujardin, and A. A. Zahab. *Reversible optical doping in graphene*. Sci. Rep. **3**, 2355 (2013). 58

[Timoshenko59] S. Timoshenko and S. Woinowsky-Krieger. *Theory of plates and shells*. McGraw-Hill, 1959. 34

[Tombros07] N. Tombros, C. Jozsa, M. Popinciuc, H. T. Jonkman, and B. J. van Wees. *Electronic spin transport and spin precession in single graphene layers at room temperature*. Nature **448** (7153), 571-574 (2007). 1

[Tombros11] N. Tombros, A. Veligura, J. Junesch, M. H. D. Guimaraes, I. J. Vera-Marun, H. T. Jonkman, and B. J. van Wees. *Quantized conductance of a suspended graphene nanoconstriction*. Nat. Phys. **7** (9), 697-700 (2011). 17

[Tsakalakos81] T. Tsakalakos. *The bulge test: A comparison of the theory and experiment for isotropic and anisotropic films*. Thin Solid Films **75** (3), 293-305 (1981). 34

[Tsukagoshi99] K. Tsukagoshi, B. W. Alphenaar, and H. Ago. *Coherent transport of electron spin in a ferromagnetically contacted carbon nanotube*. Nature **401** (6753), 572-574 (1999). 1

[Tuinstra70] F. Tuinstra and J. L. Koenig. *Raman Spectrum of Graphite*. The Journal of Chemical Physics **53** (3), 1126-1130 (1970). 1, 40, 44

[Tyborski15] C. Tyborski, F. Herziger, R. Gillen, and J. Maultzsch. *Beyond double-resonant Raman scattering: Ultraviolet Raman spectroscopy on graphene, graphite, and carbon nanotubes*. Phys. Rev. B **92** (4), 041401 (2015). 47, 49

[Varchon07] F. Varchon, R. Feng, J. Hass, X. Li, B. Ngoc Nguyen, C. Naud, P. Mallet, J.-Y. Veuillen, C. Berger, E. H. Conrad, and L. Magaud. *Electronic Structure of Epitaxial Graphene Layers on SiC: Effect of the Substrate*. Phys. Rev. Lett. **99** (12), 126805 (2007). 12

[Venezuela11] P. Venezuela, M. Lazzeri, and F. Mauri. *Theory of double-resonant Raman spectra in graphene: Intensity and line shape of defect-induced and two-phonon bands*. Phys. Rev. B **84** (3), 035433 (2011). 25, 26, 46, 47, 49, 50

[Vidano78] R. P. Vidano and D. B. Fischbach. *New Lines in the Raman Spectra of Carbons and Graphite*. Journal of the American Ceramic Society **61** (1-2), 13-17 (1978). 1, 44

[Vidano81] R. P. Vidano, D. B. Fischbach, L. J. Willis, and T. M. Loehr. *Observation of Raman band shifting with excitation wavelength for carbons and graphites*. Solid State Communications **39** (2), 341-344 (1981). 44

[Vlassak92] J. J. Vlassak and W. D. Nix. *A new bulge test technique for the determination of Young's modulus and Poisson's ratio of thin films*. Journal of Materials Research **7** (12), 3242-3249 (1992). 34

[Vuye93] G. Vuye, S. Fisson, V. Nguyen Van, Y. Wang, J. Rivory, and F. Abelès. *Temperature dependence of the dielectric function of silicon using in situ spectroscopic ellipsometry*. Thin Solid Films **233** (1–2), 166-170 (1993). 68

[Wallace47] P. R. Wallace. *The Band Theory of Graphite*. Phys. Rev. **71** (9), 622-634 (1947). xiv, 1, 11, 14

[Wan95] K.-T. Wan and Y.-W. Mai. *Fracture mechanics of a new blister test with stable crack growth*. Acta Metallurgica et Materialia **43** (11), 4109-4115 (1995). 114, 115, 140

[Wan03] K.-T. Wan, S. Guo, and D. A. Dillard. *A theoretical and numerical study of a thin clamped circular film under an external load in the presence of a tensile residual stress*. Thin Solid Films **425** (1–2), 150-162 (2003). 34

[Wang07] F. Wang, W. Liu, Y. Wu, M. Y. Sfeir, L. Huang, J. Hone, S. O'Brien, L. E. Brus, T. F. Heinz, and Y. R. Shen. *Multiphonon Raman Scattering from Individual Single-Walled Carbon Nanotubes*. Phys. Rev. Lett. **98** (4), 047402 (2007). 43

[Wang08a] X. Wang, Y. P. Chen, and D. D. Nolte. *Strong anomalous optical dispersion of graphene: complex refractive index measured by Picometrology*. Opt. Express **16** (26), 22105-22112 (2008). 67, 68

[Wang08b] X. Wang, Y. Ouyang, X. Li, H. Wang, J. Guo, and H. Dai. *Room-Temperature All-Semiconducting Sub-10-nm Graphene Nanoribbon Field-Effect Transistors*. Phys. Rev. Lett. **100** (20), 206803 (2008). 17

[Wang08c] Y. Y. Wang, Z. H. Ni, Z. X. Shen, H. M. Wang, and Y. H. Wu. *Interference enhancement of Raman signal of graphene*. Applied Physics Letters **92** (4), 043121 (2008). 72

[Wang08d] Y. Y. Wang, Z. H. Ni, T. Yu, Z. X. Shen, H. M. Wang, Y. H. Wu, W. Chen, and Andrew T. Shen W. *Raman Studies of Monolayer Graphene: The Substrate Effect*. J. Phys. Chem. C **112** (29), 10637-10640 (2008). 19

[Wang08e] Z. K. Wang, H. S. Lim, S. C. Ng, B. Özyilmaz, and M.H. Kuok. *Brillouin scattering study of low-frequency bulk acoustic phonons in multilayer graphene*. Carbon **46** (15), 2133-2136 (2008). 26

[Wang10a] H. Wang, J. H. Strait, P. A. George, S. Shivaraman, V. B. Shields, M. Chandrashekhar, J. Hwang, F. Rana, M. G. Spencer, C. S. Ruiz-Vargas, and J. Park. *Ultrafast relaxation dynamics of hot optical phonons in graphene*. Applied Physics Letters **96** (8), 081917 (2010). 38

[Wang10b] Z. Wang, Z. Zhang, H. Xu, L. Ding, S. Wang, and L.-M. Peng. *A high-performance top-gate graphene field-effect transistor based frequency doubler*. Appl. Phys. Lett. **96** (17), 173104 (2010). 17

[Wang12] L. Wang, J. J. Travis, A. S. Cavanagh, X. Liu, S. P. Koenig, P. Y. Huang, S. M. George, and J. S. Bunch. *Ultrathin Oxide Films by Atomic Layer Deposition on Graphene*. Nano Lett. **12** (7), 3706-3710 (2012). 83, 94

[Wang15] X. Wang, H. Tian, W. Xie, Y. Shu, W.-T. Mi, M. Ali Mohammad, Q.-Y. Xie, Y. Yang, J.-B. Xu, and T.-L. Ren. *Observation of a giant two-dimensional band-piezoelectric effect on biaxial-strained graphene*. NPG Asia Mater **7**, e154 (2015). 142

[Weber10] J. W. Weber, V. E. Calado, and M. C. M. van de Sanden. *Optical constants of graphene measured by spectroscopic ellipsometry*. Appl. Phys. Lett. **97** (9), 091904 (2010). 67, 68

[Weber14] P. Weber, J. Güttinger, I. Tsioutsios, D. E. Chang, and A. Bachtold. *Coupling graphene mechanical resonators to superconducting microwave cavities*. Nano Lett. **14** (5), 2854-2860 (2014). 159

[Williams97] J. G. Williams. *Energy release rates for the peeling of flexible membranes and the analysis of blister tests*. Int. Journal of Fracture **87**, 265-288 (1997). 34

[Wirtz04] L. Wirtz and A. Rubio. *The phonon dispersion of graphite revisited*. Solid State Communications **131** (3–4), 141-152 (2004). 24

[Wong10] C.-L. Wong, M. Annamalai, Z.-Q. Wang, and M. Palaniapan. *Characterization of nanomechanical graphene drum structures*. Journal of Micromechanics and Microengineering **20** (11), 115029 (2010). xxvii, 159

[Wu14] J.-B. Wu, X. Zhang, M. Ijäs, W.-P. Han, X.-F. Qiao, X.-L. Li, D.-S. Jiang, A. C. Ferrari, and P.-H. Tan. *Resonant Raman spectroscopy of twisted multilayer graphene*. Nature Communications **5**, - (2014). 41

[Xiang15] L. Xiang, S. Y. Ma, F. Wang, and K. Zhang. *Nanoindentation models and Young's modulus of few-layer graphene: a molecular dynamics simulation*. Journal of Physics D: Applied Physics **48** (39), 395305 (2015). 121

[Xue11] J. Xue, J. Sanchez-Yamagishi, D. Bulmash, P. Jacquod, A. Deshpande, K. Watanabe, T. Taniguchi, P. Jarillo-Herrero, and B. J. LeRoy. *Scanning tunnelling microscopy and spectroscopy of ultra-flat graphene on hexagonal boron nitride*. Nat Mater **10** (4), 282-285 (2011). 3, 19, 26, 53

[Yan07] J. Yan, Y. Zhang, P. Kim, and A. Pinczuk. *Electric Field Effect Tuning of Electron-Phonon Coupling in Graphene*. Phys. Rev. Lett. **98** (16), 166802 (2007). 3, 51, 52, 53, 86, 87

[Yan08a] J. Yan, E. A. Henriksen, P. Kim, and A. Pinczuk. *Observation of Anomalous Phonon Softening in Bilayer Graphene*. Phys. Rev. Lett. **101** (13), 136804 (2008). 51, 52, 88

[Yan08b] J.-A. Yan, W. Y. Ruan, and M. Y. Chou. *Phonon dispersions and vibrational properties of monolayer, bilayer, and trilayer graphene: Density-functional perturbation theory*. Phys. Rev. B **77** (12), 125401 (2008). 24

[Yan09] J. Yan. *Raman spectroscopy in graphene*. PhD thesis, Columbia University, (2009). 23, 24

[Yanagisawa05] H. Yanagisawa, T. Tanaka, Y. Ishida, M. Matsue, E. Rokuta, S. Otani, and C. Oshima. *Analysis of phonons in graphene sheets by means of HREELS measurement and ab initio calculation*. Surf. Interface Anal. **37** (2), 133-136 (2005). 24

[Yoon09] D. Yoon, H. Moon, Y.-W. Son, J. S. Choi, B. H. Park, Y. H. Cha, Y. D. Kim, and H. Cheong. *Interference effect on Raman spectrum of graphene on SiO2/Si*. Phys. Rev. B **80** (12), 125422 (2009). 62, 78, 105

[Yoon11a] D. Yoon, Y.-W. Son, and H. Cheong. *Negative Thermal Expansion Coefficient of Graphene Measured by Raman Spectroscopy*. Nano Lett. **11** (8), 3227-3231 (2011). 144

[Yoon11b] D. Yoon, Y.-Woo Son, and H. Cheong. *Strain-Dependent Splitting of the Double-Resonance Raman Scattering Band in Graphene*. Phys. Rev. Lett. **106** (15), 155502 (2011). 49, 56, 84, 122, 124, 134

[Yoon12] T. Yoon, W. C. Shin, T. Y. Kim, J. H. Mun, T.-S. Kim, and B. J. Cho. *Direct Measurement of Adhesion Energy of Monolayer Graphene As-Grown on Copper and Its Application to Renewable Transfer Process*. Nano Lett. **12** (3), 1448-1452 (2012). 27, 83, 97

[Yue12] K. Yue, W. Gao, R. Huang, and K. M. Liechti. *Analytical methods for the mechanics of graphene bubbles*. Journal of Applied Physics **112** (8), 083512 (2012). 34, 98

[Zabel11] J. Zabel, R. R. Nair, A. Ott, T. Georgiou, A. K. Geim, K. S. Novoselov, and C. Casiraghi. *Raman spectroscopy of graphene and bilayer under biaxial strain: Bubbles and balloons*. Nano Lett. **12** (2), 617-621 (2011). xxii, 22, 54, 55, 60, 61, 87, 103, 117, 121, 122, 123, 162, 167

[Zandiatashbar14] A. Zandiatashbar, G.-H. Lee, S. J. An, S. Lee, N. Mathew, M. Terrones, T. Hayashi, C. R. Picu, J. Hone, and N. Koratkar. *Effect of defects on the intrinsic strength and stiffness of graphene*. Nat Commun **5**, 3186 (2014). 83

[Zhang05] Y. Zhang, Y.-W. Tan, H. L. Stormer, and P. Kim. *Experimental observation of the quantum Hall effect and Berry's phase in graphene*. Nature **438** (7065), 201-204 (2005). 17, 150

[Zhang08] L. M. Zhang, Z. Q. Li, D. N. Basov, M. M. Fogler, Z. Hao, and M. C. Martin. *Determination of the electronic structure of bilayer graphene from infrared spectroscopy*. Phys. Rev. B **78** (23), 235408 (2008). 42

[Zhang15] X. Zhang, X.-F. Qiao, W. Shi, J.-B. Wu, D.-S. Jiang, and P.-H. Tan. *Phonon and Raman scattering of two-dimensional transition metal dichalcogenides from monolayer, multilayer to bulk material*. Chem. Soc. Rev. **44** (9), 2757-2785 (2015). 159

[Ziegler14] K. Ziegler, A. Hill, and A. Sinner. *Graphene optoelectronics*. Wiley-VCH Verlag GmbH & Co. KGaA, 2014. 20

[Ziman60] J. M. Ziman. *Electrons and phonons*. Oxford University Press, 1960. 38

Dominik METTEN

Probing the opto-electronic and mechanical properties of suspended graphene membranes by Raman spectroscopy

Résumé

Ce travail présente une étude par diffusion micro-Raman de membranes de graphène suspendu. La spectroscopie Raman est présentée comme un outil rapide et peu invasif pour estimer les contraintes natives dans du graphène suspendu et est utilisée pour en sonder quantitativement la déflection, induite soit par une différence de pression d'air soit électrostatiquement.
Dans des bulles de graphène pressurisées, une analyse minutieuse des intensités et fréquences des principaux modes Raman permet une détermination tout-optique de la topographie de la bulle, du module de Young et des paramètres de Grüneisen du graphène.
Une grille électrostatique offre une manière élégante d'introduire à la fois des contraintes et du dopage dans le graphène. Des mesures Raman permettent une détermination précise de la déflection induite par la force électrostatique (jusqu'à l'effondrement irréversible), en très bon accord avec un modèle électromécanique.

Mots-clés : graphène, suspendu, membrane, contrainte, dopage, Raman, spectroscopie

Abstract

This work presents a micro-Raman scattering study of undoped suspended graphene membranes. Raman spectroscopy is introduced as a fast and minimally invasive tool to estimate sample-dependent built-in strain in suspended graphene, and is further employed to quantitatively probe the membrane deflection, which may be induced either by an air pressure difference or electrostatically.
In pressurized graphene blisters, an all-optical determination of the blister topography, the Young's modulus and the Grüneisen parameters of graphene is achieved by a thorough analysis of the intensity and frequency of the main Raman modes.
Electrostatic gating offers an elegant way to simultaneously strain and dope graphene. Raman measurements allow an accurate determination of the electrostatically-induced graphene deflection (up to irreversible collapse), in very good agreement with an electromechanical model.

Keywords: graphene, suspended, membrane, strain, doping, Raman, spectroscopy